ON THE EFFECTS OF STRESS STATE AND MICROSTRUCTURE INDUCED ANISOTROPIES ON DUCTILE FRACTURE

A Dissertation

by

NITHIN THOMAS

Submitted to the Office of Graduate and Professional Studies of
Texas A&M University
in partial fulfillment of the requirements for the degree of

DOCTOR OF PHILOSOPHY

Chair of Committee,	Ahmed Amine Benzerga
Committee Members,	Ramesh Talreja
	Ibrahim Karaman
	Mohammad Naraghi
Head of Department,	Rodney Bowersox

December 2016

Major Subject: Aerospace Engineering

ABSTRACT

A major challenge that is currently facing the mechanics of materials community is the accurate prediction of fracture in advanced ductile materials. The intertwined effects of intrinsic and extrinsic factors make ductile fracture one of the most complex phenomena in materials mechanics. Intrinsic factors include large plastic deformations, induced anisotropies, microstructural evolution, and stress state effects. Extrinsic factors relate to the effect of boundary conditions and to the onset of plastic instabilities, either material (e.g., shear bands) or structural (e.g., necking). This dissertation sheds light on three fundamental topics - effect of non proportional loadings, anisotropic ductile fracture and failure by shear localization. First, by means of a simple fracture model, a generic shape of the fracture strain versus average triaxiality locus and previously published experimental results are rationalized. Then, a more elaborate ductile fracture model is utilized to carry out three-dimensional finite element simulations of damage accumulation to failure in initially crack-free specimens under certain symmetry considerations. The results reveal an emerging competition between intrinsic and structural effects imparted by plastic anisotropy. Finally, full 3D simulations are carried out when the triads of loading and plastic anisotropy are misoriented. The simulations reveal, for the first time, failure by shear band formation in initially round notched bars, reminiscent of experimental observations in Al or Mg alloys. These insights have practical and theoretical consequences and will aid the implementation of improved models of ductile fracture with accurate predictive capabilities and the design of safer structural components in the aerospace, automotive and energy industries.

DEDICATION

This dissertation is dedicated to my loving wife Dr. Litty Thomas, my dear parents Mr. Thomas Xavier and Ms. Mollykutty Francis, and to all my other teachers who helped me become who I am.

ACKNOWLEDGEMENTS

This dissertation was made possible due to the timely support extended by many great personalities. First I would like to extend my sincere gratitude to my advisor Professor Amine Benzerga for the great guidance and financial support he offered all through my doctoral life. I admire him for his superior research and scientific outlook, extensive knowledge and teaching skills. I have learned quite a lot from discussions with him and have grown as a student and researcher under his guidance. The scientific writing training I had from him was priceless.

Next, I would like to thank my committee members for the valuable time they spent serving on my dissertation committee. The interactions I had with Profs. Ramesh Talreja, Ibrahim Karaman and Mohammad Naraghi were quite insightful and I am grateful for their encouragement, support and suggestions for improvements.

I am greatly thankful to Dr. Soondo Kweon and Dr. Shyam Mohan Keralavarma for the valuable discussions we had in understanding the model and UMAT employed in the study. A special thank you to dear Ms. Karen Knabe for the wonderful moral support she provided all through my Ph.D. Whenever we met, her radiating happiness and peacefulness had a profoundly positive impact on my state of mind. I am also grateful to Miriam Brown, Ashley McCoy, Gail Rowe, Michelle Newton, James Munnerlyn and Todd Pollard of the Aerospace Department for all their kind gestures and support through my time at Texas A&M University.

I would like to thank all my friends for their support and encouragement. In particular, I would like to thank Sidharth Somanathan, Shinu Baby, Vishnu Venugopal, Francy Varghese, Dhanesh Yeganantham, Aswathi Sudhir, Josef Sebastian, Xavier

Poulain, Babak Kondori and Sangil Lee for all they have done to support me. I will always cherish our valuable interactions and moments of friendship.

Special thanks to my parents and brothers for their amazing love, support and prayers. Words cannot express my sincere gratitude to my wife Litty for supporting me through the challenging period in the doctoral life. I am immensely thankful for her kindness, endless love, patience and for the sacrifices she had made towards supporting me.

Financial support I received from the Department of Aerospace Engineering, the National Science Foundation and Lawrence Livermore National Lab, through my advisor, is gratefully acknowledged.

CONTRIBUTORS AND FUNDING SOURCES

Contributors

This work was supported by a dissertation committee consisting of Professors A. A. Benzerga (advisor), Ramesh Talreja and Mohammad Naraghi of the Department of Aerospace Engineering and Professor Ibrahim Karaman of the Department of Materials Science and Engineering.

The experimental results included in Chapter 3 were conducted by Dr. Shamik Basu of the Department of Materials Science and Engineering. All other work conducted for the dissertation was completed by the student independently.

Funding Sources

Graduate study was supported partly by teaching assistantship from the department of Aerospace Engineering of Texas A&M University and partly by support from the National Science Foundation and the Lawrence Livermore National Security, LLC.

TABLE OF CONTENTS

Page

LIST OF FIGURES

FIGURE Page

LIST OF TABLES

TABLE Page

1. INTRODUCTION AND MOTIVATION

1.1 Introduction

Predicting material failure is essential to many applications impacting national security, the nation's infrastructure such as pipelines and power plants as well as the aerospace, automotive and metal forming industries. For example, the development of strong and tough lightweight materials in transportation vehicles will ultimately lead to less fuel consumption and reduced emissions with a positive impact on the environment. Recognizing this important role of advanced materials in supporting an innovation-driven U.S. manufacturing sector, President Barack Obama introduced the Materials Genome Initiative (MGI) in June 2011 with this aim: discover, develop, manufacture, and deploy advanced materials twice as fast, at a fraction of the cost. Important components of the materials innovation infrastructure will be the development of advanced simulation tools that are validated through experimental data. A key characteristic that defines efforts in support of MGI is an integrated, collaborative workflow that draws simultaneously from experiments, computation, and theory.

A major challenge that is currently facing the mechanics of materials community is the accurate prediction of fracture/failure in advanced, technologically important ductile materials such as Magnesium, Aluminum which are attractive candidates for the aerospace and automotive applications. In such porous ductile materials, fracture may take place due to the nucleation, growth and coalescence of voids that initiate from inclusions and second phase particles [43]. Another mode of ductile fracture is by shear localization or the mechanical instability of the specimen involved and as such localization plays a major role in the ductile fracture process often contributing

to reduced ductility. This mode of failure usually involves one or more shear bands inside of which the deformation concentrates. These two modes of failure can exist concurrently in a material and may support each other. For example, under certain circumstances, accumulation of intense stresses and strains in a shear band may drive or accelerate the void nucleation, growth and coalescence inside the band, thereby leading to failure. And in some other cases, void nucleation/growth/coalescence induced softening can lead to localization.

The accumulation of large plastic strains and the inherent path dependency of plastic deformation causes the strain to failure in ductile materials to depend on the initial microstructure, strain history and the state of stress. The relevant micro structural variables which influence ductile failure are the void volume fraction, void shape, void orientation and void spacing [21, 44, 51, 67, 100]. Strain history effects prevail through pre-strain, residual strains and strain path change induced effects. Instantaneous stress states may be completely characterized by two parameters: the stress triaxiality, T and the Lode parameter L (related to the first and third invariant of the stress tensor respectively and will be defined formally in Chapter 2), for the general three dimensional state of loading. The former which involves the first stress invariant, has no effect in standard plasticity but is critical in porous metal plasticity [20].

The pioneering work by Orowan [101] on notched specimens shed light on the importance of plastic constraint which can be characterized by the stress triaxiality parameter. Bridgman [29] through his experiments demonstrated that the hydrostatic stress plays a crucial role in the ductile fracture. Higher strain to failures were obtained in tension by carrying out the test under hydrostatic pressure effecting a reduction of stress triaxiality near the neck region. This was further confirmed by McClintock [91] and Rice and Tracey [108], through their study on the growth

of cylindrical and spherical voids. Hancock and MacKenzie [54] and Hancock and Brown [53] through their work on notched specimens, demonstrated that the strain to failure in ductile fracture was a monotonically decreasing function of the stress triaxiality.

Although the influence of stress triaxiality on ductile fracture was clearly established by previous studies, whether it is sufficient to characterize the failure in ductile materials is studied in detail recently. The effect of Lode parameter on void growth in the case of isotropic matrices is not negligible and plastic anisotropy may aggravate or alleviate the effect depending upon the type of anisotropy and material [16]. The Lode parameter has more pronounced effect on the mode of void coalescence as reported by Gologanu et al. [48, 49]. The effect of Lode parameter explored by the few experimental studies available to date are conflicting. Some studies [8, 9] have shown a non monotonous fracture locus with strain to failure reaching its minimum in shear (L = 0) while others have revealed a monotonous fracture locus [52, 82]. Although the extent of Lode effect remains unsettled despite much work over the past decade; see [36] for an overview of the recent literature, similar works by [41, 42, 70] indicate that Lode effect is prominent in low triaxiality and shear dominated loadings, causing significant reduction in ductility.

Another important aspect affecting the fracture behavior is the strain history effects. Enami [38], Enami [39] who investigated the effects of compressive and tensile prestrain on ductile fracture initiation in steels found that compressive prestrain led to cleavage cracking and reduced ductility. Although [34, 111] found that the general effect of prestrain is to reduce fracture toughness, [4] reported that fracture toughness increased significantly for straining upto 2%. [132], using stress controlled axisymmetric cell models demonstrated that a prestrain history significantly reduced the void coalescence strain especially at high stress triaxialities in addition to inducing

strain hardening and void shape changes. [71, 89] observed that the work hardening capacity of the material decreased as the pre strain is increased, even for small prestrains, with the effect more prominent in materials with high work hardening rate [86]. [110] found that prestrain at lower/higher triaxiality led to a lower/higher void growth rate and increased/decreased ductility in high strength structural steels. Based on experiments and computational modeling, [32] also observed a decrease in failure strain of structural steel HY-100 caused by prestraining at higher triaxiality. [78] found that biaxial prestraining reduced the uniaxial ductility of steel, when compared with its ductility in continuous uniaxial tensile deformation. Zhalehfar et al. [130] investigated the effect of strain path change on the Forming Limit Diagram (FLD) and observed that prestaining in biaxial tension reduced the limit curve and shifted it to the right-hand side of the FLD, whereas prestraining in uniaxial tension raised the FLC and shifted it to the left-hand side of the FLD.

In reality, industrial operations usually takes place in multiple stages consisting various loading paths thereby making the material undergo different stress states and strain histories. However, in literature, fracture strains are reported assuming proportional loading paths. This is also true in the case of Forming limit diagrams (FLD) which are used to characterize the formability of sheet metals wherein proportional loading paths are assumed, and hence a constant stress ratio effecting an assumption of constant triaxiality. So the question arises as in how much is the fracture locus determined through a non-proportional loading path different from that determined through a proportional loading path. This was explored by using finite element cell model calculations by [14, 129] and they demonstrated that strain to failure can be much smaller than under proportional loading. The results of [14] were confirmed experimentally by [11] for one family of load path changes and for fixed Lode parameter.

On the modeling side, several frameworks are developed in the past few decades which are still being improved upon. Uncoupled models [25, 63, 108] although simple in structure, presents with some limitations. On the other hand, coupled models [2, 16, 51, 67, 85, 95, 96, 106**?**] seamlessly combine plasticity and damage resulting in comparatively complex set of equations and are usually supplemented with the evolution equations for microstructural parameters.

Gurson model [51] is the most widely known, homogenization based model for growth of voids in ductile material. Gurson type modeling framework combines limit analysis with homogenization (under appropriate approximations), of some assumed shape of representative volume element (RVE) having embedded voids assumed to be of shapes amenable to ease of tackling the fundamentally complex underlying mathematics. Notable improvements of the Gurson model include, [33, 121, 122, 125], resulting in the GTN model and has been used extensively in analysis of practical problems. Void shape effects were also added to these improvements by [44–46] and [31]. [16] included the effect of anisotropy of the matrix material by considering spherical voids in a Hill type matrix which was further extended by [67] for spheroidal voids in anisotropic matrix. Quite recently [85] has come up with further improvements including ellipsoidal void shapes. For a detailed overview of the models and the various strategies followed, see the comprehensive reviews by [20, 26, 105].

Models for coalescence of voids in a ductile medium was initiated by Thomason [117] who analyzed cylindrical voids in a rigid plastic matrix. Benzerga and Leblond [21], recently revisited the void coalescence problem for normal stress dominated stress states and presented the first analytical void coalescence criterion for those condition. This was extended to shear dominated loadings by [118]. Very recently, [65] came up with void coalescence criterion for voids in anisotropic matrix following the similar framework adopted by [21]. Although the above presented

void coalescence models are in itself quite advanced, practical applications of these models warrants the thorough understanding of microstructural evolutions leading to void coalescence and also their inherent coupled effects, which opens up avenues for further improvements.

1.2 Motivation

Early experimental studies [53, 54] had established the strain to failure as a monotonically decreasing function of stress triaxiality. This was in alignment with the classical models of [108], [91], [51] etc. On the other hand, low triaxiality experiments conducted in the past decade [8, 9], reported fracture strains which were significantly lower at low stress triaxialities (Fig.2.1). The low triaxiality regime is technologically important since, it is the stress state existing in applications such as metal forming, stretching of thin sheets for automotive and aerospace applications etc. So for the safe design of structural members against fracture, the question arises as in which of these strain to failures needs to be adopted for design purposes?

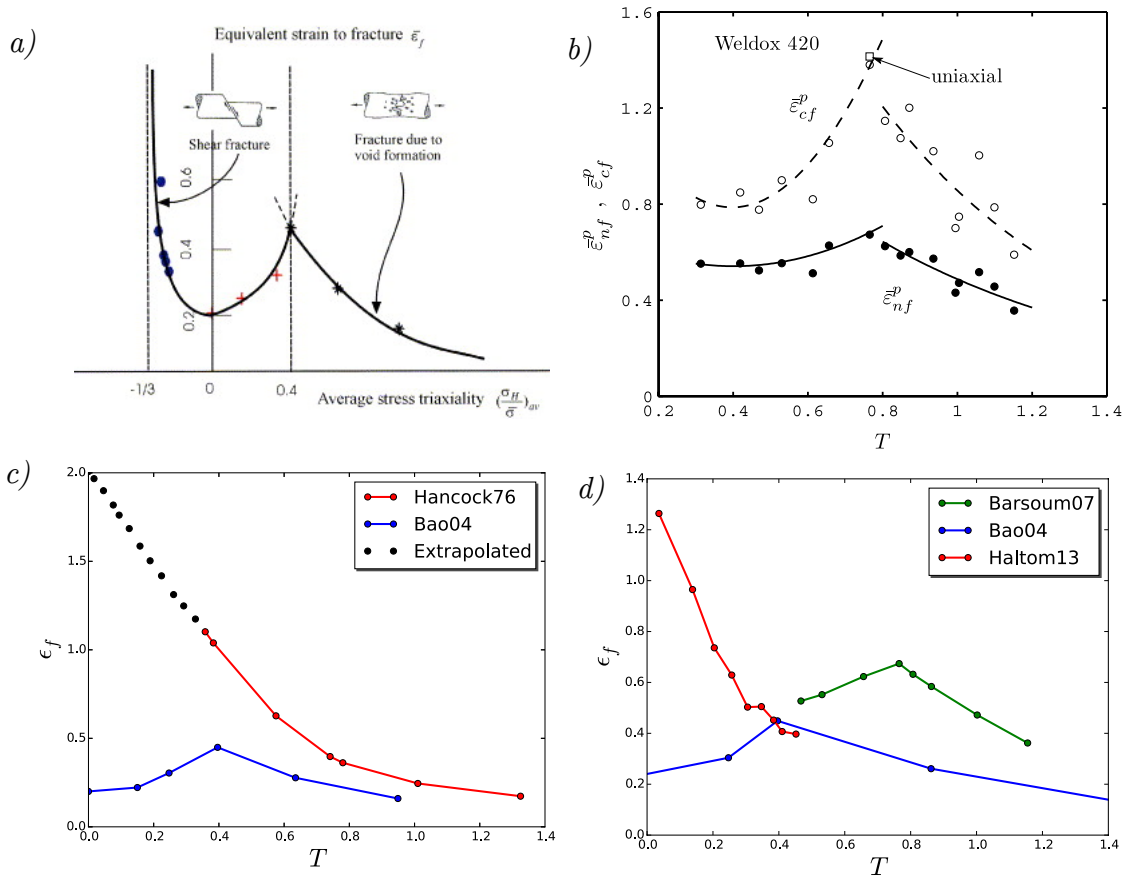

Figure 1.1: a) Equivalent strain to fracture vs average stress triaxiality [8] b) Effective plastic strain at failure vs. stress triaxiality [9] c) Effective plastic strain to failure initiation vs. stress triaxiality [54] d) Experimental results of Barsoum, Bao and Haltom replotted

To the above challenge, the research community has so far responded in two ways. Many groups have developed macroscopic, often stress-based, fracture criteria that incorporate the effect of the third stress invariant $J3$, (conventionally captured by the Lode parameter, L) in addition to that of T [7, 42]. The variant formulations account for the basic properties of isotropic scalar-valued tensor functions. The major drawback of these models is that they discuss fracture in macroscopic terms

and so their predictive abilities are quite limited. Also their model is based on the assumption of isotropic stress state which might not be a reasonable assumption at low triaxiality regimes where significant deformations and void distortions are present, leading to void shape induced anisotropies. Another approach initiated in [97] and followed by others consists of a modification of the Gurson-Tvergaard-Needleman void growth model to account for the effects of the third stress invariant $J3$. While useful, this modification is heuristic and tacitly assumes that the Lode effect is rooted in the void growth process. However, micromechanical cell model calculations [41, 131] have shown that the effect of the Lode parameter on void growth is not strong enough to explain the experimental findings in [8, 9]. As noted by [97], the only internal variable representing damage in the modified model has no longer the meaning of a void volume fraction. In fact, it loses its microstructural character of being measurable and observable. Connecting the Lode effect exclusively with void growth, or more generally void distortion, and the absence of observables in the modified model, or variants thereof, constitute their major shortcomings. Yet, both the macroscopic stress-based criteria in [7, 8, 36] and the modified Gurson model [97] have already had a major impact in the field of ductile fracture. This reflects the impending need in the mechanics of materials community for improved models. On the other hand, the above-mentioned shortcomings of these models elicit the gap that remains to be filled.

The results of previous studies clearly show that the fracture locus can be represented as a two dimensional surface as $\varepsilon_f = f(T, L)$. It is emphasized that this surface constitutes an intrinsic fracture locus provided that the loading is proportional, i.e., when both T and L remain constant during the loading up to failure. An important corrolary is that the intrinsic locus is not accessible to experimental measurement for it is impossible, in general, to impose constant-T and constant-L loadings. From the

experiments by [8], fracture maps represented by stress triaxiality and Lode parameter were constructed through experiments supplemented with numerical simulations. One cannot emphasize enough that what is measured therein is some apparent, not the intrinsic, fracture locus. The apparent locus may be affected by extrinsic factors such as the occurrence of **plastic instabilities**, either material (e.g., shear bands) or structural (e.g., necking). It is to be noted that at low triaxiality regimes where large deformations and void distortions are present, significant effects of **void shape induced anisotropies** prevail which makes the isotropic assumption used in the above models for formulating the fracture criterion, a restrictive one. It is worth noting that so-called butterfly specimens were used in [8], double-notched torsion specimens in [9] and another design in [52]. Also, the experiments were carried out for three different materials making comparisons difficult.

Another difference between the intrinsic and apparent fracture loci lies in the potential effect of **nonproportional loading**, which remains poorly quantified. In general, the stress triaxiality and Lode parameter are functions of some monotonically increasing parameter, say the effective strain ε. To account for nonproportional loading effects, some authors [7, 36] proposed to use strain- weighted averages of T and L in formulating their failure criteria. Averages are defined as:

$$\bar{T} = \frac{1}{\varepsilon_f} \int_0^{\varepsilon_f} T \, \mathrm{d}\varepsilon; \quad \bar{L} = \frac{1}{\varepsilon_f} \int_0^{\varepsilon_f} L \, \mathrm{d}\varepsilon \tag{1.1}$$

The premise in the above studies is that either nonproportional loading will lead to mild deviations or that the effect can be captured by averaging the variations of T and L with strain. It will be shown in Chapter 3 that this premise is questionable.

1.3 Objectives

The intertwined effects of intrinsic and extrinsic factors makes ductile fracture one of the most complex phenomena in materials mechanics. Intrinsic factors include large plastic deformations, induced anisotropies, microstructural evolution, and stress state effects. Extrinsic factors relate to the effect of boundary conditions and to the onset of plastic instabilities, either material (e.g., shear bands) or structural (e.g., necking). **The overall goal of this research is to elucidate the inevitably coupled effects of stress state, strain/load history and material microstructure on the ductile fracture of structural materials, by means of theory and simulations.** This, in turn, will enable the apportioning of intrinsic and extrinsic contributions to experimentally determined fracture loci and will aid the development of improved models of ductile fracture. The following are the objectives of this dissertation that feed into the overall goal.

1. **Quantify the deviations from the intrinsic fracture locus due to non proportional loadings (Chapter 3)**

   For complex stress states and under strictly proportional loadings, the fracture locus is a two dimensional surface. Deviations from that locus under non-proportional loadings have received little attention from experimentalists and modelers alike. Motivated by a series of finite-element cell model studies and experiments under both proportional and non- proportional stressing histories, the quantitative effect of loading path on the fracture locus is examined theoretically. Focus is laid on axisymmetric loadings and on ductile materials that fail by void growth to coalescence. To illustrate the key ideas, a simple damage model which captures the essence of findings from numerical and real experiments is adopted. It incorporates an internal state variable and is sup-

plemented with a critical void growth ratio criterion. In a first step, it is shown that the predictions of the model are in keeping with the exact finite-element calculations. Then the model predictive capabilities are used to explore the parameter space in ways that are not easily accessible to experiments. Two types of non-proportional loadings are examined and maximum deviations from the proportional fracture locus are quantified for the loadings considered. It is shown that neither the average values of T and L nor their terminal values would be appropriate in developing a failure criterion.

2. **Analyze the effect of microstructure induced anisotropy on the ductile fracture at low and moderate stress triaxialities. (Chapter 4)**

   In general, ductile failure may occur mainly in two modes; by micro void growth and coalescence or by instability [20, 105]. Failure by micro void coalescence consists of microscale localization happening in the ligament joining voids. This localization then leads to coalescence of voids and hence to predict ductile fracture quantitatively, modeling of void coalescence is a key step. An important ingredient in modeling void coalescence is to account for the evolution of microstructure prior to localization.

   Keralavarma and Benzerga [67] developed an anisotropic model (KB model) of void growth in a porous elasto-plastic or viscoplastic continuum subjected to arbitrary large deformations. Their model takes explicit account of the material anisotropy due to texturing in structural materials and the initial or induced anisotropy due to void shape, thus allowing for greater accuracy in predicting the initiation and propagation of cracks. A closed form yield function, flow rule and evolution equations for the microstructural variables were developed for the effective material using an approach based on classical homogenization theory

and limit-analysis. Void shape effects are more prominent in the regime of moderate triaxialities ($2/3 \leq T \leq 1.5$) such as those prevailing in notched bars. Cell model studies [69] in this regime report that the sensitivity to initial void shape is influenced greatly by the matrix material anisotropy. Although the KB model contains rich micro structure information and predicts accurate results, as of now, it lacks a void coalescence part. The KB model is implemented in ABAQUS as a UMAT subroutine [77]. As a first step towards modeling void coalescence, the KB model will be used to investigate the combined effects of plastic deformation, matrix anisotropy and void shape/orientation on the evolution of damage in notched bars.

3. **Examine through simulations, the development of shear bands caused by plastic anisotropy with or without damage.(Chapter 5)**

   This study will concentrate on the combined effects of plastic deformation and matrix anisotropy on plane strain bars (2D analysis) and smooth bars (3D analysis) so as to investigate the conditions favoring/inhibiting the development of macroscopic shear localization. Shear localization can be understood as a bifurcation in the incremental problem caused by the loss of ellipticity of the governing equations [107]. The necessary condition for shear localization is singular state of the acoustic tensor. Steinmann et. al [112] had studied the localization within orthotropic Hill type elastoplastic solids following along the classical work of Hill [57]. His analysis had shown an intriguing influence of certain types of orthotropy on macro scale localization. Towards investigating this further, the KB model will be used to study conditions favoring shear localization in notched bars.

2. BACKGROUND

2.1 Stress state measures

For general multi axial loadings, the scalar invariants of the stress tensor are employed, usually in the measures of ratios to describe ductile fracture. Among them, the effect of stress triaxiality on ductile fracture is well established. Stress triaxiality is defined as the ratio of mean normal stress σ_{m} to the Von Mises effective stress, σ_{e}, and involves the ratio of the first invariant of stress tensor to the second invariant.

$$T = \frac{\sigma_{\mathrm{m}}}{\sigma_{\mathrm{e}}} \equiv \frac{I_1}{3\sqrt{3J_2}} \tag{2.1}$$

with

$$\sigma_{\mathrm{m}} = \frac{\sigma_1 + \sigma_2 + \sigma_3}{3} \tag{2.2}$$

and

$$\sigma_{\mathrm{e}} = \frac{[(\sigma_1 - \sigma_2)^2 + (\sigma_2 - \sigma_3)^2 + (\sigma_3 - \sigma_1)^2]^{1/2}}{\sqrt{2}} \tag{2.3}$$

where $\sigma_1 \geq \sigma_2 \geq \sigma_3$ denote the principal stresses.

Although, by definition $-\infty < T < +\infty$, the value of T varies from $-2/3$ in biaxial compression to zero in pure shear and an initial value of $1/3$ in round smooth bars (increases subsequent to the onset of necking) to infinity in hydrostatic tension. The higher the strain-hardening capacity of the material, larger the triaxiality. T may not exceed about 4.0 under practical circumstances. This can be attributed to the decrease in the strain-hardening rate of all materials at large plastic strains. In notched round bars, T varies from 0.6 to 2 whereas higher values are found in cracked specimens such as the compact tension (CT) bars with maxima expected

to be around 3.0 ahead of the crack tip of a strain-hardening material under plane strain conditions [92].

The Lode parameter brings in the influence of the third invariant of the stress tensor and is defined as the ratio,

$$L = \frac{2\sigma_2 - \sigma_1 - \sigma_3}{\sigma_1 - \sigma_3}, \qquad -1 \leq L \leq 1 \tag{2.4}$$

In the case of axisymmetric stress states, only one *instantaneous* descriptor of the state of loading is sufficient since for them, $L = \pm 1$ depending on whether the major stress is axial or lateral. In axisymmetric tension, with one positive axial stress and two negative lateral stresses, $L = -1$. For axisymmetric compression with one negative axial stress and two positive lateral stresses, $L = +1$.

With the Lode parameter kept constant, if in addition, the triaxiality is also kept constant, the loading path is a constant slope-radial line starting from the origin in a $\sigma_m - \sigma_e$ plot and is known as a radial loading path. When loading follows such a path, the components of the stress tensor increase proportionally with any monotonically increasing loading variable (time). For this reason radial paths are also known as *proportional* loading paths. When the triaxiality is varied over the loading cycle, the slope is not constant and hence such paths are known as non-radial or *non-proportional* loading paths.

2.2 Notion of fracture locus

It is important to recognize that the stress measures T and L are evolving fields which are functions of stress state and accumulated plastic strain. It is advantageous to employ T and L in the context of proportional loadings since they remain constant throughout the history and thus helps in quantifying measures of ductility. However, when strong variations are present in their evolution over the straining history, as is

usually found in real experiments, such fracture strain measures in general lose their meaning. It should be kept in mind that the only fracture locus that is intrinsic to a material is that obtained under proportional loading. However, when the relevant loading parameters vary in the course of deformation, the loading is non-proporional and one can think of a locus of strain-to-failure versus average values of the loading parameters over the entire loading history up to the point of failure as $\varepsilon_f = f(T, L)$ as is often done in literature [7]. An understated fact in literature is that, in experiments it is impossible in general to keep the triaxiality and Lode parameter constant, all the way up to fracture and thus the intrinsic fracture locus of a ductile material is not accessible to experimental measurement. Hence, significant deviations can happen in the case of reported fracture strains under non-proportional loadings between experimental measurements depending upon the severity of non-proportionality. More details on this will be provided in the next chapter.

2.3 Uncoupled and coupled models of fracture

Constitutive models which are derived under the assumption that the stress and strain state existing in a material are independent of the evolution of damage are known as uncoupled models. In these models, attainment of a critical damage parameter is indicative of failure. Isolated void models such as the Rice and Tracey [108], the Johnson-Cook-Bermin model [25, 63] and the McClintock model [91] are examples of such models. Although from a physical point of view, coupling between damage and plasticity are expected and is natural, these models are appealing due to their simplicity in representation and ease of application in predicting material failure. However, to accurately and quantitatively capture the fracture behavior coupled models are the obvious choice. These are also the key to capture the competition between dominant modes of failure as an outcome of solution process. For example,

only a coupled model can predict failure by instability if it is propelled by damage itself. These models in general connect plasticity and damage and their evolution is interdependent. Porous metal plasticity models based on the homogenization framework such as the GTN model [51], Gologanu model [46, 47], Keralavarma Benzerga model [67] and the Madou-Leblond model [85] are good examples of these types of models.

2.4 Homogenization based models of ductile fracture

The backbone of continuum models of porous ductile solids rests on homogenization. The relationship between stress and strain at the macro scale is derived for a given constitutive description at the microscale; ie at the scale of voids. This results in a class of models in which the microstructural information seamlessly enter the macroscopic constitutive law and then they are usually supplemented with their evolution equations which makes them capable of modeling material failure all the way upto complete failure. Under this framework, models are derived based on the Hill-Mandel homogenization theory [58, 87]. The basic procedure followed is as follows. Initially a representative volume element (RVE) of the porous ductile solid consisting of voids embedded in a matrix is considered. This RVE can be assumed to be of different shapes such as spherical, cylindrical, spheroidal and is often adopted depending upon the ease of tackling the mathematical problem at hand without losing the essence of physics. There are two kinds of approach followed in general; the kinematic and the static with the difference between them rooted in the kind of boundary conditions considered. In the kinematic approach, uniform rate of deformations are imposed on the RVE boundary whereas in the static approach, static (for example a uniform stress) boundary conditions are applied on the RVE. Then adopting a matrix plasticity rule, relevant shapes of voids and under minimalistic

assumptions and approximations the effective properties of the homogeneous material is derived from the initially non-homogeneous material by the application of homogenization theory. Then these models are refined and validated by rigorously comparing them with numerically derived upper bounds for given microstructures through limit-analysis using a large family of trial deformation fields.

In the next few sections, a basic background on homogenization followed by the Keralavarma-Benzerga (KB) yield function which was derived based on this framework is presented. Then the finite element implementation of the KB model is presented in Section 2.7 followed by synopsis of the Benzerga-Leblond (BL) coalescence yield function which describes the effective coalescence process and can serve as an indicator of initiation of failure under normal stress dominated loading conditions. Then in section 2.10, the procedure for identifying the material parameters required for solving three dimensional boundary value problems (until crack initiation) using these models are presented.

2.5 A brief background on homogenization

The stress and the deformation rate at the macroscopic RVE scale are expressed as the volume average of their microscopic counterparts following standard homogenization procedure.

$$D_{ij} = \langle d_{ij} \rangle_\Omega, \qquad \Sigma_{ij} \equiv \langle \sigma_{ij} \rangle_\Omega, \tag{2.5}$$

where the notation $\langle \cdot \rangle_\Omega$ is for volume averaging over Ω.

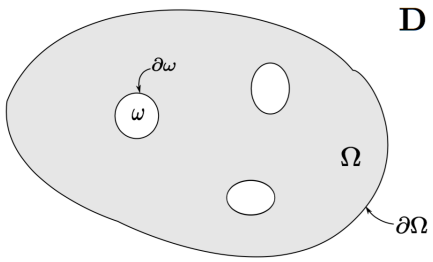

Figure 2.1: Sketch of a porous representative volume element, Ω, containing voids occupying volume ω

The effective, yield surface in stress space for a perfectly plastic matrix material with normality obeyed is determined according to the limit-analysis theorem [113], and is defined by

$$\Sigma_{ij} = \frac{\partial \Pi}{\partial D_{ij}}(\mathbf{D}) \tag{2.6}$$

Physically, equation (2.6) means that among all microscopic diffuse modes of plastic deformation, those that result in the smallest average dissipation over the cell will define macroscopic yielding. Here, $\Pi(\mathbf{D})$ is the macroscopic plastic dissipation defined below:

$$\Pi(\mathbf{D}) = \inf_{\mathbf{d}\in\mathcal{K}(\mathbf{D})} \langle \pi(\mathbf{d}) \rangle_{\Omega} \tag{2.7}$$

where $\mathcal{K}(\mathbf{D})$ denotes the set of kinematically admissible microscopic deformations:

$$\mathcal{K}(\mathbf{D}) = \{\mathbf{d} | \exists \mathbf{v}, \forall \mathbf{x} \in \Omega,\, d_{ij} = \frac{1}{2}(v_{i,j} + v_{j,i}) \,\text{and}\, \forall \mathbf{x} \in \partial\Omega,\, v_i = D_{ij} x_j\} \tag{2.8}$$

For a given deviator $\mathbf{d}$, the microscopic plastic dissipation is defined as

$$\pi(\mathbf{d}) = \sup_{\boldsymbol{\sigma}^* \in \mathcal{C}} \sigma^*_{ij}\, d_{ij} \tag{2.9}$$

the supremum being taken over all microscopic stresses that fall within the microscopic convex $\mathcal{C}$ of elasticity.

2.6 Keralavarma Benzerga (KB) growth yield function

For the actual derivation of the effective yield function following the above variational formulation, the following is adopted:

1. Geometry:

   The RVE is a hollow spheroid containing a confocal spheroidal cavity. Porosity f, void aspect ratio, W, and void axis, $\mathbf{e}_3$, are the microstructural variables.

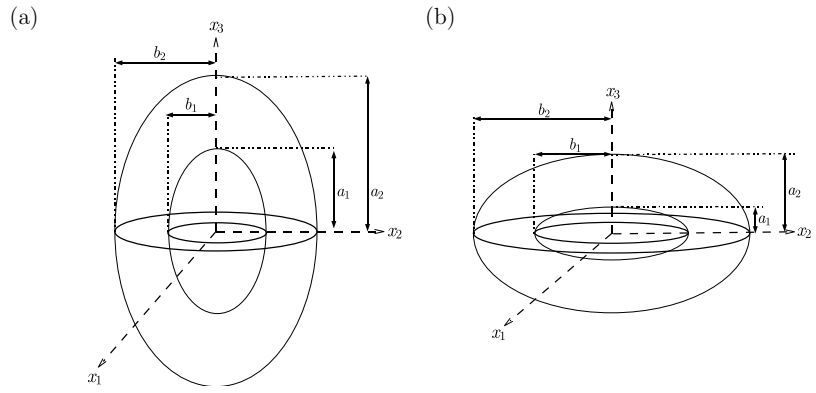

Figure 2.2: Porous representative volume elements used in the derivation of the analytical yield criterion. The cases of prolate (a), and oblate (b) voids require separate treatments.

2. Micro scale plasticity model:

   The orthotropic, associated Hill flow theory is used for the matrix.

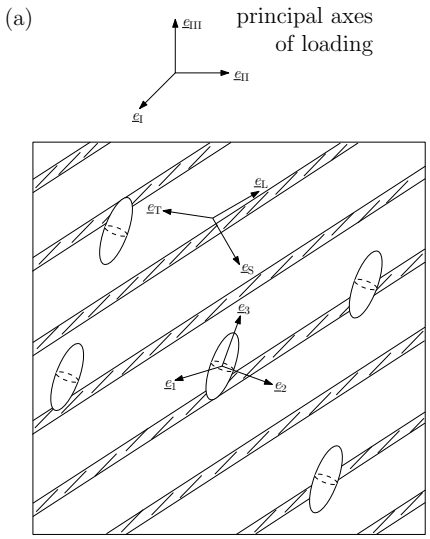

Figure 2.3: Schematic diagram of microstructure that consists of an aggregate of aligned spheroidal voids surrounded by the anisotropic matrix

3. Velocity fields:

$$\forall \mathbf{x} \in \Omega \backslash \omega, \quad v_i(\mathbf{x}) = A v_i^A(\mathbf{x}) + \beta_{ij} x_j, \tag{2.10}$$

As above, scalar A and symmetric tensor $\boldsymbol{\beta}$ are parameters (with $\beta_{kk} = 0$). Here, $\boldsymbol{\beta}$ is not necessarily axisymmetric if one admits the ensuing approximations.

The void is modeled as a spheroid with the main axis represented by $\mathbf{e}_3$ and the other two orthogonal directions by $\mathbf{e}_1$ and $\mathbf{e}_2$. Anisotropy of the matrix is represented by hatched bands in the schematic drawing with their orthogonal bases vectors denoted by $\mathbf{e}_L$, $\mathbf{e}_S$ and $\mathbf{e}_T$. Note that the bases of the matrix anisotropy and those of voids do not necessarily match, indicating the two types of anisotropy that can play a role in the material's overall constitutive response. Note as well that in general the principal loading direction is not aligned to either one of the bases of matrix

anisotropy and void orientation.

The deformation of the combined material, void and matrix, is captured by additive decomposition of the symmetric part of velocity gradient as done in other homogeneous materials and the hypoelastic law is employed for a finite strain formulation.

$$\mathbf{D} = \mathbf{D}^{\mathrm{e}} + \mathbf{D}^{\mathrm{p}}, \quad \mathbf{D}^{\mathrm{e}} = \mathbb{C}^{\mathrm{e}-1} : \overset{\triangledown}{\boldsymbol{\Sigma}} \tag{2.11}$$

where $\mathbb{C}^{\mathrm{e}}$ is the isotropic elastic tensor and $\overset{\triangledown}{\boldsymbol{\Sigma}}$ is the Jaumann stress rate defined by:

$$\overset{\triangledown}{\boldsymbol{\Sigma}} = \dot{\boldsymbol{\Sigma}} + \boldsymbol{\Sigma}\boldsymbol{\Omega} - \boldsymbol{\Omega}\boldsymbol{\Sigma}, \quad \boldsymbol{\Omega} = \frac{1}{2}(\boldsymbol{\nabla}\mathbf{v} - \boldsymbol{\nabla}\mathbf{v}^T), \tag{2.12}$$

where $\boldsymbol{\Omega}$ is the skew symmetric part of the velocity gradient $\boldsymbol{\nabla}\mathbf{v}$.

The void aspect ratio is defined as

$$w = \frac{a_1}{b_1}, \quad S = \ln(w) \tag{2.13}$$

where a_1 and b_1 represent the lengths of the axial($\mathbf{e}_3$) and transverse semi-axes($\mathbf{e}_1$ and $\mathbf{e}_2$) of the spheroidal void, respectively.

The KB yield criterion for a plastically anisotropic material of the Hill type [55] is written as $\mathcal{F}(\boldsymbol{\Sigma}) = 0$ with

$$\mathcal{F}(\boldsymbol{\Sigma}) = C\frac{3}{2}\frac{\boldsymbol{\Sigma} : \mathbb{H} : \boldsymbol{\Sigma}}{\bar{\sigma}^2} + 2(g+1)(g+f)\cosh\left(\kappa\frac{\boldsymbol{\Sigma} : \mathbf{X}}{\bar{\sigma}}\right) - (g+1)^2 - (g+f)^2 \tag{2.14}$$

where $\mathbb{H}, \mathbf{Q}$ and $\mathbf{X}$ are given by

$$\mathbb{H} \equiv \mathbb{p} + \eta(\mathbf{X}\otimes\mathbf{Q} + \mathbf{Q}\otimes\mathbf{X}), \quad \mathbb{p} \equiv \mathbb{J} : \mathbb{h} : \mathbb{J}, \quad \mathbb{J} \equiv \mathbb{I} - \frac{1}{3}\mathbf{I}\otimes\mathbf{I} \tag{2.15}$$

$$\mathbf{Q} \equiv -\frac{1}{2}(\mathbf{e}_1 \otimes \mathbf{e}_1 + \mathbf{e}_2 \otimes \mathbf{e}_2) + \mathbf{e}_3 \otimes \mathbf{e}_3, \ \mathbf{X} \equiv \alpha_2(\mathbf{e}_1 \otimes \mathbf{e}_1 + \mathbf{e}_2 \otimes \mathbf{e}_2) + (1 - 2\alpha_2)\mathbf{e}_3 \otimes \mathbf{e}_3 \quad (2.16)$$

$\bar{\sigma}$ is the yield strength of the material in a reference direction. In general, $\bar{\sigma}$ is selected as the yield strength in one of the orthotropic directions of the matrix material and the components of the anisotropy tensors $\mathbb{p}$ and $\mathbb{h}$ are scaled accordingly. $\mathbb{J}$ denotes the deviatoric projection operator and $\mathbb{h}$ dentoes the anisotropy tensor in the deviatoric stress space. $\mathbb{I}$ and $\mathbf{I}$ are the fourth and second order identity tensors, respectively. $\mathbf{e}_3$ is the main axis of the spheroidal void and $\mathbf{e}_1$ and $\mathbf{e}_2$ are the rest two orthogonal basis vectors. f is the porosity.

The matrix is considered to obey the power-law strain-hardening law as follows.

$$\bar{\sigma} = \sigma_{\mathrm{S}}(1 + \bar{\epsilon}/\epsilon_0)^N \quad (2.17)$$

where $\bar{\sigma}$ and $\bar{\epsilon}$ are work-conjugate measures of matrix effective stress and plastic strain, respectively. $\bar{\epsilon}$ is defined as the cumulative plastic strain.

The evolution of porosity is given by:

$$\dot{f} = (1 - f)\Lambda \frac{\partial \mathcal{F}}{\partial \Sigma_{\mathrm{m}}} \quad (2.18)$$

where Λ is the plastic multiplier.

The evolution of the plastic strain of the matrix $\bar{\epsilon}$ is obtained considering the plastic work equivalence between the macroscopic homogeneous material and the microstructure(matrix); the work done on voids is zero.

$$\mathbf{\Sigma} : \mathbf{D}^{\mathrm{p}} = (1 - f)\bar{\sigma}\dot{\bar{\epsilon}} \quad (2.19)$$

The evolution of void shape is described as

$$\dot{S} = \frac{3}{2} D^{\mathrm{p}'}_{33} + 3 \left[\frac{1 - 3\alpha_1}{f} + 3\alpha_2 - 1 \right] D^{\mathrm{p}}_{\mathrm{m}} \tag{2.20}$$

where $'$ indicates the deviatoric component of a second order tensor. Note this equation includes an implicit dependence upon matrix anisotropy through the macroscopic rate of plastic deformation, $\mathbf{D}^{\mathrm{p}}$, which is derived from the yield criterion (2.14) by normality.

Introducing the adjusting factor in [18, 45] into Eq.(2.20) leads to

$$\dot{S} = \mathbf{Q} : \left[h\mathbf{D}^{\mathrm{p}} + 3 \left(\frac{1}{f} \mathbf{X}^{v} - \mathbf{X} \right) D^{\mathrm{p}}_{\mathrm{m}} \right] \tag{2.21}$$

where tensor $\mathbf{X}^{v}$ is defined similar to $\mathbf{X}$. The adjusting factor h is defined as follows.

$$h = 1 + h_{\mathrm{e}} h_{\mathrm{f}} h_{\mathcal{T}} \tag{2.22}$$

$$h_{\mathrm{e}}(e_1) = \frac{9}{2} \frac{\alpha_1 - \alpha_1^{\mathrm{Gar}}}{1 - 3\alpha_1}, \qquad \alpha_1^{\mathrm{Gar}} = \begin{cases} \dfrac{1}{3 - e_1^2} & \text{(p)} \\ \dfrac{1 - e_1^2}{3 - 2e_1^2} & \text{(o)} \end{cases} \tag{2.23}$$

$$h_{\mathrm{f}}(f) = (1 - \sqrt{f})^2 \tag{2.24}$$

$$h_{\mathcal{T}}(\mathcal{T}, \epsilon) = \begin{cases} 1 - \dfrac{\mathcal{T}^2 + \mathcal{T}^4}{9} & \text{for} \quad \epsilon = +1 \\ 1 - \dfrac{\mathcal{T}^2 + \mathcal{T}^4}{18} & \text{for} \quad \epsilon = -1 \end{cases}, \qquad \epsilon \equiv \mathrm{sgn}(\Sigma_{\mathrm{m}} \Sigma'_{33}) \tag{2.25}$$

$$\mathcal{T} = \frac{\Sigma_{kk}/3}{\sqrt{\frac{3}{2} \boldsymbol{\Sigma}' : \boldsymbol{\Sigma}'}} \tag{2.26}$$

$\mathcal{T}$ is stress triaxiality. e_1 is the eccentricity of the void, and h_{e}, h_{f} and $h_{\mathcal{T}}$ correct the mismatch due to eccentricity, porosity and stress triaxiality, respectively, between unit cell simulation results and the model prediction.

The void orientation evolves following the macroscopic spin of the material and

the local plastic distortion, which was derived by Kailasam and Ponte Castaneda [64] as follows

$$\boldsymbol{\Omega}^v = \boldsymbol{\Omega} - \mathbb{C} : \mathbf{D}^{\mathrm{p}} \tag{2.27}$$

where $\boldsymbol{\Omega}$ and $\boldsymbol{\Omega}^v$ represent the continuum and void spin tensors respectively. $\mathbb{C}$ is the fourth order spin concentration tensor, which is given by

$$\mathbb{C} = -(1-f)\mathit{\Pi} : \mathbb{A}, \qquad \mathbb{A} = [\mathbb{I} - (1-f)\mathbb{S}]^{-1} \tag{2.28}$$

where $\mathbb{A}$ is the strain concentration tensor and $\mathit{\Pi}$ and $\mathbb{S}$ are the Eshelby tensors [40] for a spheroidal inclusion in an incompressible linear matrix. Then, the evolution of the void orientation is obtained using the following kinematical relationship

$$\dot{\mathbf{e}}_3 = \boldsymbol{\omega} \cdot \mathbf{e}_3, \qquad \boldsymbol{\omega} = \boldsymbol{\Omega}^v + \boldsymbol{\Omega}^l \tag{2.29}$$

where $\boldsymbol{\Omega}^l$ is an antisymmetric tensor given by

$$\Omega^l_{12} = 0, \quad \Omega^l_{i3} = \frac{w^2+1}{w^2-1} D^v_{i3} \qquad (i = 1, 2, \quad w \neq 1) \tag{2.30}$$

$$\mathbf{D}^v = \mathbb{A} : \mathbf{D}^{\mathrm{p}} \tag{2.31}$$

Combining Eq.(2.27) and (2.29)-2 leads to

$$\boldsymbol{\omega} = \boldsymbol{\Omega} - \mathbb{C} : \mathbf{D}^{\mathrm{p}} + \frac{1}{2} \sum_{i \neq j,\, w_i \neq w_j} \frac{w_i^2 + w_j^2}{w_i^2 - w_j^2} (\mathbf{e}_i \otimes \mathbf{e}_j + \mathbf{e}_j \otimes \mathbf{e}_i) : \mathbb{A} : \mathbf{D}^{\mathrm{p}} \mathbf{e}_i \otimes \mathbf{e}_j \tag{2.32}$$

The plastic spin tensor is defined as $\mathbf{W}^{\mathrm{p}} = \boldsymbol{\Omega} - \boldsymbol{\omega}$. It is evaluated as follows.

$$\mathbf{W}^{\mathrm{p}} = \mathbb{C} : \mathbf{D}^{\mathrm{p}} - \frac{1}{2} \sum_{i \neq j,\, w_i \neq w_j} \frac{w_i^2 + w_j^2}{w_i^2 - w_j^2} (\mathbf{e}_i \otimes \mathbf{e}_j + \mathbf{e}_j \otimes \mathbf{e}_i) : \mathbb{A} : \mathbf{D}^{\mathrm{p}} \mathbf{e}_i \otimes \mathbf{e}_j \tag{2.33}$$

2.7 Finite element formulation

The model presented in the previous section is implemented in the commercial finite element software [1] as a user material subroutine (UMAT). The constitutive relations are expressed in an intermediate rotated configuration, which is obtained from the current one by rotating with $\mathbf{R}^*$. $\mathbf{R}^*$ is the rotation tensor that results from the polar decomposition of the incremental deformation gradient $\Delta\mathbf{F}$

$$\Delta\mathbf{F} = \mathbf{R}^*\mathbf{U}^* \tag{2.34}$$

In this formulation, incremental objectivity is preserved by using a Jaumann rate in the hypoelastic equation. Quantities defined in the rotated configuration are indicated by the ($\tilde{}$) symbol. Constitutive descriptions need to be written only for the stretch part of deformations since the rotation part is taken care of by rotating quantities to the intermediate configuration.

Rotated tensors are indicated by a tilde and follow standard transformation rules

$$\tilde{\mathbf{A}} = \mathbf{R}^{*T}\mathbf{A}\mathbf{R}^*; \qquad \tilde{B}_{ijpq} = {R^*}_{ki}{R^*}_{lj}{R^*}_{mp}{R^*}_{nq}B_{klmn}. \tag{2.35}$$

The constitutive equations are then rewritten in the rotated configuration. For example, the hypoelastic law, which is written in the current configuration is converted to

$$\tilde{\mathbf{D}}^{\mathrm{e}} = \mathbb{C}^{\mathrm{e}-1} : \dot{\tilde{\mathbf{\Sigma}}} \tag{2.36}$$

in the rotated configuration.

Note that $\hat{\mathbb{C}}^{\mathrm{e}} = \mathbb{C}^{\mathrm{e}}$ in the case of isotropic elasticity, which is assumed in this

study. The objective rate $\overset{\nabla}{\boldsymbol{\Sigma}}$ is replaced by $\dot{\tilde{\boldsymbol{\Sigma}}}$, which is the main advantage of utilizing the corotational formulation. In other words, the constitutive updating is done without using any objective rate in the formulation. The flow rule based upon the normality is recast using the same way as follows.

$$\tilde{\mathbf{D}}^{\mathrm{p}} = \Lambda \frac{\partial \mathcal{F}}{\partial \tilde{\boldsymbol{\Sigma}}}(\tilde{\boldsymbol{\Sigma}}) \tag{2.37}$$

Differentiating the yield criterion with respect to $\tilde{\boldsymbol{\Sigma}}$ leads to

$$\tilde{\mathbf{D}}^{\mathrm{p}} = \Lambda \left[3C \frac{\tilde{\mathbb{H}} : \tilde{\boldsymbol{\Sigma}}}{\bar{\sigma}^2} + 2(g+1)(g+f)\kappa \sinh\left(\kappa \frac{\tilde{\boldsymbol{\Sigma}} : \tilde{\mathbf{X}}}{\bar{\sigma}} \right) \frac{\tilde{\mathbf{X}}}{\bar{\sigma}} \right] \tag{2.38}$$

The yield criterion, (2.14), is simply re-written with tilde quantities instead of non-tilde quantities.

$$\mathcal{F}(\tilde{\boldsymbol{\Sigma}}) = C\frac{3}{2}\frac{\tilde{\boldsymbol{\Sigma}} : \tilde{\mathbb{H}} : \tilde{\boldsymbol{\Sigma}}}{\bar{\sigma}^2} + 2(g+1)(g+f)\cosh\left(\kappa \frac{\tilde{\boldsymbol{\Sigma}} : \tilde{\mathbf{X}}}{\bar{\sigma}} \right) - (g+1)^2 - (g+f)^2 \tag{2.39}$$

2.8 Time integration method

To integrate the above constitutive equations, a semi-implicit integration algorithm is employed. The state variables in the rotated configuration are described as a vector set as follows,

$$[\mathbf{X}]^T = \left[\tilde{\boldsymbol{\Sigma}}',\ \tilde{\Sigma}_{\mathrm{m}},\ f,\ \bar{\epsilon},\ \bar{\sigma},\ \Lambda,\ S \right] \tag{2.40}$$

where the deviatoric-volumetric decomposition is applied to the Cauchy stress $\boldsymbol{\Sigma}$ to facilitate the convergence in the Newton-Raphson procedure employed below. This coupled system is solved using an implicit method following a backward Euler scheme.

The residual equations are expressed in the following vector set.

$$[\mathbf{R}]^T = \left[\mathbf{R}_{\tilde{\mathbf{\Sigma}}'},\ R_{\tilde{\Sigma}_\mathrm{m}},\ R_f,\ R_{\bar{\epsilon}},\ R_{\bar{\sigma}},\ R_{\mathcal{F}(\tilde{\mathbf{\Sigma}})},\ R_S\right]. \tag{2.41}$$

The state variables at the beginning of the increment are denoted by $\mathbf{X}_0$, and the variables at the end of the increment by $\mathbf{X}$. The iterative Newton-Raphson procedure is employed to solve the above equation set $[\mathbf{R}]^T = \mathbf{0}$

$$[\mathbf{X}]_{i+1} = [\mathbf{X}]_i - \left[\frac{\partial[\mathbf{R}]}{\partial[\mathbf{X}]_i}\right]^{-1}[\mathbf{R}] \tag{2.42}$$

where the subscript 'i' represents iteration number.

The consistent tangent matrix ($\mathbb{L} = \dfrac{\partial\tilde{\mathbf{\Sigma}}}{\partial\tilde{\mathbf{D}}}$) must be calculated for the global solution solving procedure, where the displacement of nodes are obtained. Computing $\mathbb{L}$ involves the following steps

$$\left[\frac{\partial\mathbf{X}}{\partial\tilde{\mathbf{D}}}\right] = -\left[\frac{\partial[\mathbf{R}]}{\partial[\mathbf{X}]}\right]^{-1}\left[\frac{\partial\mathbf{R}}{\partial\tilde{\mathbf{D}}}\right] \tag{2.43}$$

where

$$\left[\frac{\partial\mathbf{X}}{\partial\tilde{\mathbf{D}}}\right]^T = \left[\frac{\partial\tilde{\mathbf{\Sigma}}'}{\partial\tilde{\mathbf{D}}},\ \frac{\partial\tilde{\Sigma}_\mathrm{m}}{\partial\tilde{\mathbf{D}}},\ \frac{\partial f}{\partial\tilde{\mathbf{D}}},\ \frac{\partial\bar{\epsilon}}{\partial\tilde{\mathbf{D}}},\ \frac{\partial\bar{\sigma}}{\partial\tilde{\mathbf{D}}},\ \frac{\partial\Lambda}{\partial\tilde{\mathbf{D}}},\ \frac{\partial S}{\partial\tilde{\mathbf{D}}}\right] \tag{2.44}$$

and

$$\left[\frac{\partial\mathbf{R}}{\partial\tilde{\mathbf{D}}}\right]^T = \left[\frac{\partial\mathbf{R}_{\tilde{\mathbf{\Sigma}}'}}{\partial\tilde{\mathbf{D}}},\ \frac{\partial R_{\tilde{\Sigma}_\mathrm{m}}}{\partial\tilde{\mathbf{D}}},\ \frac{\partial R_f}{\partial\tilde{\mathbf{D}}},\ \frac{\partial R_{\bar{\epsilon}}}{\partial\tilde{\mathbf{D}}},\ \frac{\partial R_{\bar{\sigma}}}{\partial\tilde{\mathbf{D}}}\ \frac{\partial R_{\mathcal{F}(\tilde{\mathbf{\Sigma}})}}{\partial\tilde{\mathbf{D}}},\ \frac{\partial R_S}{\partial\tilde{\mathbf{D}}}\right] \tag{2.45}$$

Note that the same Jacobian matrix $\partial[\mathbf{R}]/\partial[\mathbf{X}]$ in Eq. (2.42) is used again in Eq. (2.43). $\mathbb{L}$ is obtained from (2.43) as:

$$\mathbb{L} = \frac{1}{\Delta t}\left(\frac{\partial\tilde{\mathbf{\Sigma}}'}{\partial\tilde{\mathbf{D}}} + \mathbf{I}\otimes\frac{\partial\tilde{\Sigma}_\mathrm{m}}{\partial\tilde{\mathbf{D}}}\right) \tag{2.46}$$

The algorithm used in the implementation is summarized in Fig 2.4.

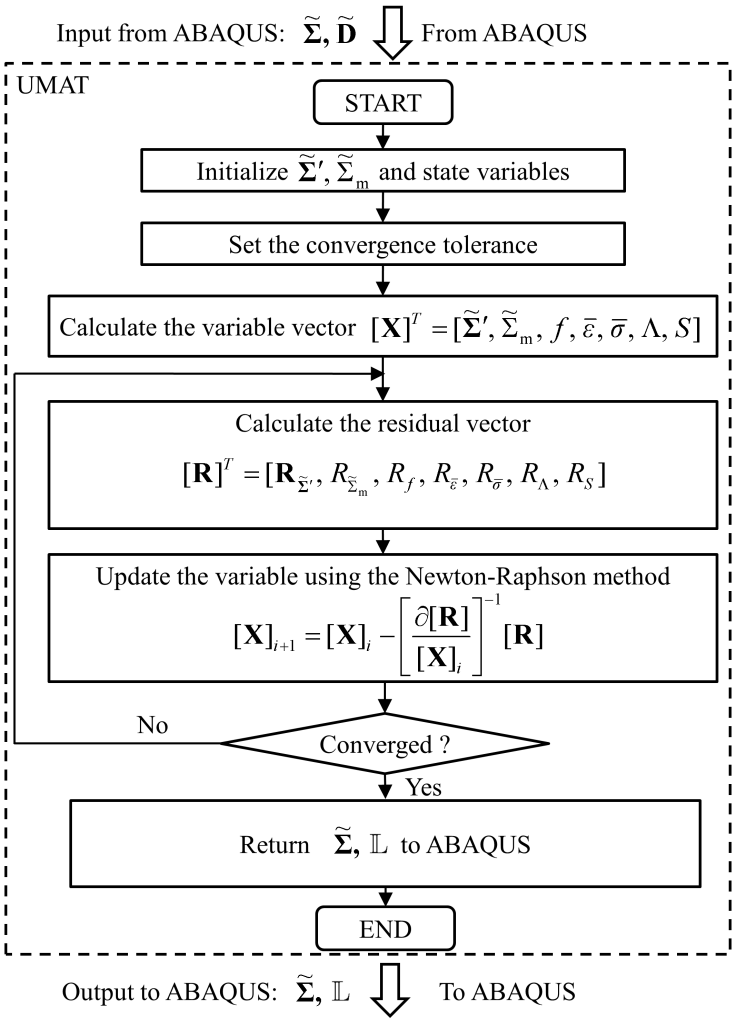

Figure 2.4: Flowchart of the integration algorithm in the user defined material subroutine (UMAT).

2.9 Benzerga Leblond (BL) coalescence yield function

Towards deriving the effective yield function the following framework is adopted (Only the relevant details from [21] is reproduced here. For the original derivation,

the reader is directed to [21]):

1. Geometry:

   The RVE is a cylindrical cell containing a coaxial cylindrical void. The various microstructural variables related to the geometry are the void aspect ratio $W \equiv h/R$, the cell aspect ratio $\lambda \equiv H/L$ and the one which represent the relative ligament size, the ligament parameter $\chi \equiv R/L$. This geometry is reported to a cylindrical coordinate system with local basis ($\mathbf{e}_r$, $\mathbf{e}_\theta$, $\mathbf{e}_z$) and a global Cartesian basis ($\mathbf{e}_1$, $\mathbf{e}_2$, $\mathbf{e}_3$) with $\mathbf{e}_3 = \mathbf{e}_z$. The cell is subjected to some triaxial axisymmetric loading. Void coalescence is inherently directional. It is assumed to take place in the $\mathbf{e}_1$–$\mathbf{e}_2$ plane with the major applied normal stress being along $\mathbf{e}_3$ ($\Sigma_{33} > \Sigma_{11} = \Sigma_{22}$). Note that the cell diameter $2L$ represents the void spacing transverse to the major stress. The cell is further divided into two parts: the central region Ω_{lig} containing the intervoid ligament and the part $\Omega \setminus \Omega_{\text{lig}}$ comprising the regions above and below the void (Fig. 2.5a). There are two interfaces between these two parts, S_{top} and S_{bot}, with S_{int} denoting their union.

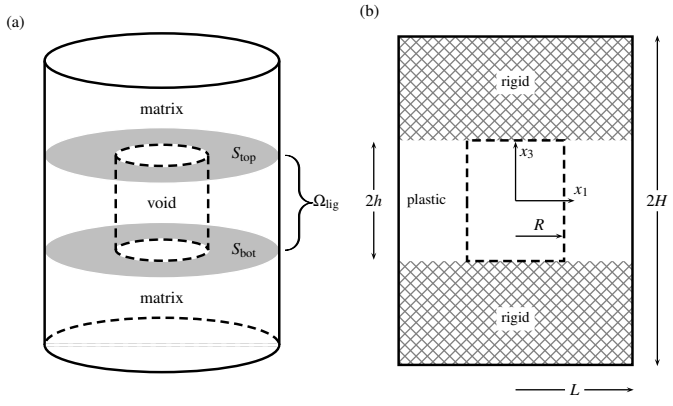

Figure 2.5: Geometry of cylindrical RVE

2. Micro scale plasticity model:

   The matrix is assumed to be rigid perfectly plastic. For the region Ω_{lig} containing the inter void ligament, the J_2 flow theory is used, with the regions above and below the void taken to be rigid (Fig. 2.5b).

3. Velocity fields:

   From the presence of rigid regions above and below the void follow the overall constraints $D_{11} = D_{22} = 0$ as well as interface conditions. Thus, boundary conditions on the velocity field include:

$$\forall \mathbf{x} \in \partial\Omega, \quad v_r(\mathbf{x}) = 0 \tag{2.47}$$

$$\forall \mathbf{x} \in \partial\Omega \setminus \partial\Omega_{\text{lig}}, \quad v_z(\mathbf{x}) = v_z(0, \pm h) \tag{2.48}$$

   with $v_\theta = 0$ everywhere from axial symmetry. It is (2.48) that makes these boundary conditions not of the uniform strain-rate type. In addition, interface conditions are:

$$\forall \mathbf{x} \in S_{\text{int}}, \quad v_r(\mathbf{x}) = 0, \quad v_z(\mathbf{x}) = v_z(0, \pm h) \tag{2.49}$$

A family of axially symmetric velocity fields that satisfy incompressibility was used by Tracey [119] who studied the growth of an isolated void. Their expression is:

$$\begin{aligned} v_r(r) =& \frac{A}{r} - \frac{Br}{2} \\ v_z(z) =& Bz \end{aligned} \tag{2.50}$$

where A and B are parameters. Gurson [51] used a subfamily of such fields to

derive an effective yield function for a material containing cylindrical voids. In [51] parameters A and B were set by homogeneous boundary conditions. Benzerga and Besson [16] used the same fields in their extension of the Gurson cylindrical void model to transversely isotropic matrix materials.

In the derivation by Benzerga and Leblond [21], another subfamily of velocity fields (2.50) is used in which constants A and B are related by boundary conditions (2.47)-(2.48), which are more appropriate to void coalescence. For the cylindrical cell, the boundary conditions specialize to

$$v_r(L) = 0 \quad \Rightarrow \quad A = \frac{BL^2}{2} \tag{2.51}$$

$$v_z(\pm h) = \pm Bh \quad \Rightarrow \quad B \text{ arbitrary} \tag{2.52}$$

B is related to D_{33}. Since by $(2.50)_2$ $d_{33} = B$ and by definition $D_{33} = c\langle d_{33}\rangle_{\Omega_{\text{lig}}}$ one has $B = D_{33}/c$. Thus, the admissible velocity fields used are:

$$\begin{aligned} v_r(r,z) =& \frac{D_{33}}{2c}\left(\frac{L^2}{r} - r\right) \\ v_z(z) =& D_{33}z/c \end{aligned} \tag{2.53}$$

where dependence of v_r upon z is included to emphasize that the expression is only valid for $-h < z < h$. Interface condition $(2.49)_2$ is automatically verified whereas $(2.49)_1$ specializes to:

$$v_r(r, \pm h) = 0 \quad \text{for} \quad R \leq r \leq L \tag{2.54}$$

Clearly, velocity field (2.53) does not satisfy this interface condition since v_r is independent of z in the intervoid ligament. It can still be used in searching for an upper bound to the yield locus. In doing so, the contribution to the effective dissi-

pation associated with the velocity discontinuity at the plastic–rigid interface must be accounted for.

The sought yield function Φ for the effective porous medium can only be a function of the axial (macroscopic) stress Σ_{33}. Indeed, since the normality rule is assumed at the microscale, it also holds for the effective behavior; see e.g., [20]:

$$D_{ij} \propto \frac{\partial \Phi}{\partial \Sigma_{ij}}.$$

Thus, from the overall constraints $D_{11} = D_{22} = 0$, it follows that

$$\frac{\partial \Phi}{\partial \Sigma_{11}} = \frac{\partial \Phi}{\partial \Sigma_{22}} = 0 \tag{2.55}$$

The effective dissipation computed above is homogeneous of degree 1 in $\mathbf{D}$, as it should be. Hence, from (2.6) the axial stress causing flow in the ligaments alone is obtained as:

$$\Sigma_{33} = \frac{\partial \Pi}{\partial D_{33}} = \frac{\Pi}{D_{33}} \tag{2.56}$$

The effective yield criterion for the material may be expressed as:

$$\begin{aligned} \Phi(\Sigma; \chi, W) = \frac{|\Sigma_{33}|}{\bar{\sigma}} - \frac{1}{\sqrt{3}} \Bigg[& 2 - \sqrt{1+3\chi^4} + \ln \frac{1+\sqrt{1+3\chi^4}}{3\chi^2} \\ & + \frac{\chi^3 - 3\chi + 2}{3\chi W} \Bigg] \\ & \equiv \frac{\Sigma_{33}}{\bar{\sigma}} - \frac{\Sigma_{33}^{\text{coal}}}{\bar{\sigma}}(\chi, W) \end{aligned} \tag{2.57}$$

2.10 Material parameter identification for application of models

In the modeling framework outlined in the above sections, initiation of fracture and its propagation(if supplemented with a void coalescence law with evolution equations all the way to final fracture) is an outcome of the the boundary value problem solution and microstructural evolution. The stress state effects, history effects, microstructural effects all are contained and captured in this single framework. It is worth noting that there are no fitting parameters in the above micro mechanically based models. The input parameters needed for the KB model are : the Young's modulus, Poisson's ratio, components of the macroscopic anisotropy tensor $\mathbb{h}$, the initial values of microstructural parameters such as initial porosity f_0, initial aspect ratio w_0, initial orientation of the void axis n_3 and the components of R^* matrix specifying the initial orientation of the matrix anisotropy. Hence the parameters needed for using these models in solving practical boundary value problems are basically those describing the elasto-plastic behavior and those characterizing the initial microstructure. Also it should be noted that although ductile fracture takes place due to void nucleation, growth and coalescence of voids, the above models assume that voids are present in the material from the beginning of plastic deformation. Thus as such, they don't consider nucleation of new voids. This can be a good assumption for materials with weak inclusion interfaces or elongated inclusions. For other materials this can be far from truth. However this can be remedied by using an appropriate void nucleation law, either as a stress controlled or as a strain controlled one or the predicted ductility should be modified to account for amount of nucleation. For further details on this see: [20]

In characterizing the material behavior, as a first step, the yield stress in a particular direction of orthotropy and the hardening response can be determined by

conducting a uniaxial tension test on a smooth bar. Then by conducting six uniaxial tension tests, the anisotropy ratios and the yield stresses can be characterized and these can be used to completely characterize the plastic anisotropy. The anisotropy of the matrix material can be characterized completely by identifying the components of the macroscopic Hill anisotropy tensor. Although a brief description of identification procedure is outlined below, more details can be found in [15] and [72].

For an orthotropic material when expressed using the Voigt's notation, the anisotropic Hill tensor has the form:

$$\mathbb{h} = \begin{bmatrix} h_L & h_{LT} & h_{LS} & 0 & 0 & 0 \\ h_{TL} & h_T & h_{TS} & 0 & 0 & 0 \\ h_{SL} & h_{ST} & h_S & 0 & 0 & 0 \\ 0 & 0 & 0 & h_{TS} & 0 & 0 \\ 0 & 0 & 0 & 0 & h_{LS} & 0 \\ 0 & 0 & 0 & 0 & 0 & h_{LT} \end{bmatrix} \tag{2.58}$$

For this case, the equivalent stress can be calculated as:

$$\begin{aligned} \sigma_{eq}^2 = \quad & h_L {\sigma_L^{'}}^2 + h_T {\sigma_T^{'}}^2 + h_S {\sigma_S^{'}}^2 + 2h_{TS} {\sigma_{TS}^{'}}^2 + 2h_{LS} {\sigma_{LS}^{'}}^2 + 2h_{LT} {\sigma_{LT}^{'}}^2 + \\ & (2h_{LT}\sigma_L^{'}\sigma_T^{'} + 2h_{LS}\sigma_L^{'}\sigma_S^{'} + 2h_{TS}\sigma_T^{'}\sigma_S^{'}) \end{aligned} \tag{2.59}$$

For a material with tension compression symmetry, the Hill tensor reduces to reduces to :

$$\mathbb{h} = \begin{bmatrix} h_L & 0 & 0 & 0 & 0 & 0 \\ 0 & h_T & 0 & 0 & 0 & 0 \\ 0 & 0 & h_S & 0 & 0 & 0 \\ 0 & 0 & 0 & h_{TS} & 0 & 0 \\ 0 & 0 & 0 & 0 & h_{LS} & 0 \\ 0 & 0 & 0 & 0 & 0 & h_{LT} \end{bmatrix} \tag{2.60}$$

and the corresponding equivalent stress reduces to

$$\sigma_{eq}^2 = h_L \sigma_L^{'2} + h_T \sigma_T^{'2} + h_S \sigma_S^{'2} + 2h_{TS} \sigma_{TS}^{'2} + 2h_{LS} \sigma_{LS}^{'2} + 2h_{LT} \sigma_{LT}^{'2} \tag{2.61}$$

Thus for an orthotropic material with tension compression symmetry the orthotropy of the matrix material can be completely characterized by the six Hill coefficients. These coefficients can be calculated from experiments using either six yield strengths or anisotropy ratios. For example, using anisotropy ratios, Hill coefficients can be calculated as follows:

$$\frac{h_T}{h_L} = 1 - \frac{3(R^L R^T - 1)}{R^L R^T - 2R^L - 2} \tag{2.62}$$

$$\frac{h_S}{h_L} = 1 - \frac{3R^L(R^T - 1)}{R^L R^T - 2R^L - 2} \tag{2.63}$$

$$\frac{h_{TS}}{h_L} = -\frac{1}{2}\frac{(2R^{TS} + 1)(R^L + 1)}{R^L R^T - 2R^L - 2} \tag{2.64}$$

$$\frac{h_{LS}}{h_L} = -\frac{1}{2}\frac{(2R^{LS} + 1)(R^L + 1)R^L}{R^L R^T - 2R^L - 2} \tag{2.65}$$

$$\frac{h_{LT}}{h_L} = -\frac{1}{2}\frac{(2R^{LT} + 1)(R^L R^T + 1)}{R^L R^T - 2R^L - 2} \tag{2.66}$$

The hill coefficients can also be calculated by using using yield strengths along different directions (L, T, S, LT, LS and TS) obtained from experiments, and by taking $\bar{\sigma} = \sigma_L$ and σ to be a general stress state. In this case $4h_L + h_T + h_S = 6$. Using equation 2.60:

$$\begin{aligned} h_L(2\sigma h_L - \sigma_T - \sigma_S)^2 + h_T(-\sigma_L + 2\sigma_T - \sigma_S)^2 + h_S(-\sigma_L - \sigma_T + 2\sigma_S)^2 \\ +18h_{TS}\sigma_{TS}^2 + 18h_{LS}\sigma_{LS}^2 + 18h_{LT}\sigma_{LT}^2 = 6(\sigma_L)^2 \end{aligned} \tag{2.67}$$

Effect of anisotropy can be quantified by introducing the factor h which is an scalar invariant of tensor $\mathbf{h}$. In axes pointing toward the principal directions of orthotropy of the matrix, h admits the following expression [16]:

$$h = 2\left[\frac{2}{5}\frac{h_L + h_T + h_S}{h_L h_T + h_T h_S + h_S h_L} + \frac{1}{5}\left(\frac{1}{h_{TS}} + \frac{1}{h_{LS}} + \frac{1}{h_{LT}}\right)\right]^{\frac{1}{2}} \tag{2.68}$$

After characterizing the elasto-plastic behavior and also the plastic flow anisotropy, exploratory experiments should be conducted to identify failure initiation sites. This step is crucial in also identifying the shapes of inclusions and thus the characteristics of voids and their shapes existing in the material. To determine the initial void volume fraction, aspect ratio, relative spacing in an average sense, optical microscopy can be used in unison with image analysis. These inputs can then be used as the initial values for the state of microstructures entering the constitutive equations. Further details can be found in [20]

3. ON FRACTURE LOCI OF DUCTILE MATERIALS UNDER NON-PROPORTIONAL LOADING

3.1 Introduction

Ductile fracture is one of the most complex phenomena in materials mechanics where intrinsic and extrinsic factors are intertwined. Intrinsic factors relate to effects of stress state and induced anisotropies, which manifest in significant microstructural evolution, particularly at large strains. Extrinsic factors relate to the effect of boundary conditions, especially on the onset of plastic instabilities, either material (e.g., shear bands), structural (e.g., necking) or a combination of both; see [20, 105] for recent overviews. In general, *instantaneous* (or current) states of loading are quantified in terms of the stress triaxiality ratio, T, and the Lode parameter, L, with:

$$T \equiv \frac{\Sigma_{\mathrm{m}}}{\Sigma_{\mathrm{eq}}}; \quad L = \frac{2\Sigma_{\mathrm{II}} - \Sigma_{\mathrm{I}} - \Sigma_{\mathrm{III}}}{\Sigma_{\mathrm{I}} - \Sigma_{\mathrm{III}}} \tag{3.1}$$

where $\Sigma_{\mathrm{m}} \equiv I_1/3$ is the mean normal (or hydrostatic) stress, $\Sigma_{\mathrm{eq}} \equiv \sqrt{3J_2}$ is the von Mises equivalent stress and $\Sigma_{\mathrm{I}} \geq \Sigma_{\mathrm{II}} \geq \Sigma_{\mathrm{III}}$ are the principal stresses. The notation $\boldsymbol{\Sigma}$ is used instead of $\boldsymbol{\sigma}$ to indicate that the attempt is usually to control T and L at macroscopic scales, whether in experiments [8, 9, 18, 63] or in cell model calculations [37, 74, 127]. An intrinsic fracture locus may be defined in terms of a consistent strain-to-failure ϵ_{f} viewed as a function of T and L; see e.g., [105]. It is emphasized that this surface is well defined provided that the loading is proportional, implying that both T and L remain constant during the loading up to failure. An important

Reprinted with permission from "On fracture loci of ductile materials under non-proportional loading" by N. Thomas, S. Basu and A. A. Benzerga. International Journal of Mechanical Sciences, 117:135 – 151, October 2016, Copyright [2016] Elsevier Ltd.

corrolary is that the intrinsic locus is *not* accessible to experimental measurement for it is impossible, in general, to impose constant-T and L loadings. Deviations from proportionality in real experiments are more prominent at very low (e.g., simple tension or shear) or very high (crack tip) triaxiality.

Quite a few experimental studies have probed into the effect of nonproportional loading on ductile fracture. In one category of investigations, abrupt triaxiality changes are imparted by a two-step loading procedure [6, 11, 32, 39, 89, 110] keeping the principal loading directions fixed. A notched bar is typically prestrained up to ϵ^* then a sharper (respectively shallower) notch is machined inside the initial notch to generate a step jump (respectively drop) in triaxiality. Marini et al. [89], who considered step jumps in T, concluded that a simple linear damage accumulation rule does not apply. They attributed this to (i) the triaxiality-dependence of void nucleation and (ii) the reduction in work hardening due to prestrain. Dahl and co-workers [6, 110] considered both jumps and drops in triaxiality. Defining a failure limit curve based on smooth and notched bar experiments without strain path change, they found that a prestrain at lower (respectively higher) triaxiality leads to an increase (respectively decrease) in ductility relative to the limit curve. While they argued that a single parameter fracture criterion is inadequate, they did not offer a physical explanation for the observed trends. Chae et al. [32], who considered triaxiality drops, also obtained a decrease in failure strain due to prestraining at higher triaxiality, consistent with findings in [6, 110]. However, they attributed the decrease in ductility to the propensity for void-sheet formation. Also, Enami [39] investigated the effect of compressive as well as tensile prestrain on ductile fracture initiation. His loading paths constitute a special case of triaxiality jumps. The author was overly concerned with the observation of cleavage when compressive prestrain was applied. He argued for the existence of an intrinsic ductile limit curve,

irrespective of prestrain or the occurrence of cleavage. Recently, Basu and Benzerga [11] considered step jumps in triaxiality, complementary of those in [6, 32, 89, 110]. Specifically, their loading paths are similar to Enami's but only for a tensile prestrain. They found that the strains to failure meet or exceed the limit curve, consistent with the trend in [6, 110]. Basu and Benzerga [11] also discussed various definitions of the fracture locus and showed that when the strain to failure is plotted against a strain-weighted average triaxiality, the fracture locus takes a peculiar shape, which is robust with respect to the various definitions. In such plots, the strain to failure appears to decrease dramatically, in some cases, compared with that obtained under porportional loading. Even more recently, Papasidero et al. [102] explored a regime of triaxialities lower than considered in [6, 11, 32, 39, 89, 110] using combined tension and torsion experiments. They argued for a nonlinear damage accumulation rule to quantitatively predict fracture.

In metal forming, one is usually concerned with establishing forming limit diagrams (FLD). The literature on nonproportional loading effects on formability is too vast to be duly surveyed here, since the chief concern of this work is fracture. Nevertheless, it is generally found that prestraining in uniaxial tension increases formability limits in the right portion of the FLD whereas prestraining in biaxial tension lowers the entire FLD [50, 78, 130]. In addition, when the principal loading directions are rotated, prestraining in uniaxial tension reduces the forming limits in most cases [50]. The effect of plastic anisotropy was investigated for example in [76] in the context of plastic flow localization. Quite recently, Martins et al. [90] reviewed fracture modes and criteria in sheet as well as bulk forming. Although they did not specifically discuss deviations under nonproportional loadings, they indicated that a criterion of constant effective strain at fracture is incorrect.

On the computational side, analyses of nonproportional loading effects on ductile

failure are scarce. Of particular interest are those that used the finite-element voided cell model [74]. In such calculations, failure is associated with an abrupt drop in stress carrying capacity due to strain concentration in ligaments, a phenomenon that begins to be modeled analytically based on sound micromechanics [22]. Zhang et al. [132] studied the effect of prestrain on ductile failure by means of the cell model. They showed that a prestrain can precipitate void coalescence, especially at high prestrain triaxialities. They also discussed the effect of initial void shape. More recently, Benzerga et al. [14] used a similar approach and showed that under non-proportional loading the strain to failure can be much smaller than under proportional loading at fixed average loading triaxiality. Their theoretical predictions have recently been corroborated by experimental results on mild steel [11]. Even more recently, Yu et al. [129] have extended the analyses of Benzerga et al. [14] to three-dimensional cells and thus explored more general loading paths in terms of stress state descriptors L and T. Their conclusions were essentially in keeping with those in [14], although for so-called continuous loading paths (no triaxiality jumps) the deviations from the intrinsic (i.e. proportional) locus were found to be less severe for the conditions they investigated.

This work addresses generic aspects of nonproportional loading effects in ductile fracture in order to shed light on past and recent experiments and simulations on this topic. The concept of a fracture locus under proportional loading is straightforward, although its realization is difficult in pratice outside of narrow ranges of stress and strain states. In conceiving nonproportional loading paths, however, the choices are infinite and the issue of completeness of any investigation arises. Both the FE simulations in [14] and the experiments in [11] were restricted to one kind of non-proportional loading, namely a step-jump in triaxiality with a single value of the pre-loading triaxiality corresponding to uniaxial loading. The objective of this paper

is to investigate more general types of non-proportional loading and their effect on various representations of the fracture loci. The wide range of conditions considered warrants the use of analytical damage models supplemented with a simple fracture criterion. The damage model is based on void growth theory [108] and is motivated by more sophisticated void growth models that incorporate void shape effects [20, 105]. While a similar methodology could be applied to the regime of combined tension and shear [102], focus is laid on tensile fracture where the fundamental damage and fracture mechanisms are much better established.

The chapter is organized as follows. Section 3.2 introduces a class of simple fracture models, one of which is used in most analyses. Section 3.3 presents the nonproportional loading paths analyzed, including some that are borrowed from the experimental literature. Analyses are then presented in Section 3.4, first for generic loadings then for actual experiments, and discussed in Section 3.5.

3.2 A simple fracture theory

Any uncoupled fracture model may be described by a criterion of the type:

$$\int_0^{\varepsilon_f} g(T, L)\, \mathrm{d}\varepsilon = C \tag{3.2}$$

where C is a material-dependent critical damage parameter, ε and ε_f are the current effective strain and failure strain, respectively, and g is a memory function that embodies the stress state sensitivity of the underlying damage process. Hence, g is viewed as a functional of loading parameters $T(\varepsilon)$ and $L(\varepsilon)$ defined by (3.1) and fully defines the (uncoupled) damage theory. Upon suitable calibration of C, equation (3.2) provides the implicit unknown ε_f given a fracture theory. The fundamental simplifying assumptions here are two-fold. First, the theory is uncoupled in that the damage, whose evolution is represented by g, does not affect plastic flow. This pre-

cludes the theory from being used in failure by shear band formation or other types of plastic instabilities induced by damage accumulation itself. Second, the critical damage parameter C is taken to be stress state independent. This, in general, precludes the theory from being quantitative over a wide range of stress states [105]. Yet, the simple structure of the theory enables qualitative trends to be discussed, particularly in the present context where a large number of loading paths are considered.

For proportional loadings, integration of (3.2) provides an explicit representation of the fracture locus as:

$$\varepsilon_f = C/g(T, L) \tag{3.3}$$

Cross-sections of the surface $\varepsilon_f(T, L)$ are illustrated in Fig. 3.1.

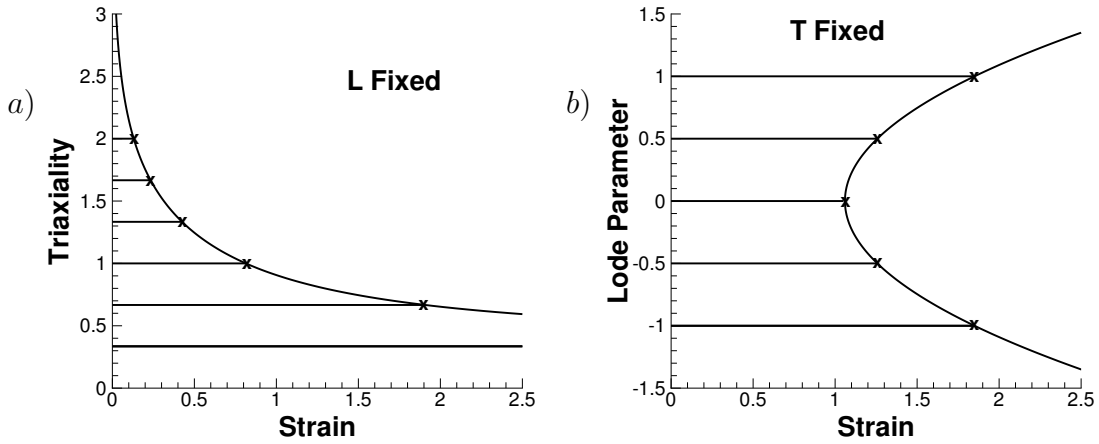

Figure 3.1: Cross-sections of the intrinsic fracture locus (a) At fixed Lode parameter L; (b) At fixed triaxiality T. Section (a) is known with some fidelity for materials failing by void growth to coalescence and T $\in]1/3, \infty[$. That in (b) is only illustrative, based on [42] for T ~ 0.5

For example, for axisymmetric loadings one has $L = \pm 1$, depending on whether the major stress is axial or radial, and $L = 0$ in shear. The value of T practically found in round smooth bars is initially $1/3$ and increases subsequent to the onset of necking. Higher levels of T values are found in notched and cracked specimens. In Fig. 3.1, section (a) is known with high-fidelity for materials failing by the growth to coalescence of pre-existing voids and $T \in [1/3, \infty[$. In this analysis, focus is laid on constant L loadings. Also, in this context low triaxiality means $T \to 1/3$.

Here, among the family of fracture models described by (3.2), only mechanism-based criteria are considered. This involves using void growth theory, e.g., [60, 108] to define the memory function $g(T(\varepsilon), L(\varepsilon))$ supplemented with a failure criterion. For the latter, the attainment of a critical void growth ratio is used here for simplicity [105]. For spherical voids at sufficiently high triaxialities, the void growth rate is approximately given by:

$$\frac{\dot{R}}{R} = a \exp\left(\frac{3}{2}T\right) \dot{\varepsilon} \tag{3.4}$$

where R is the current radius of the void, and a a prefactor equal to 0.283 in the original Rice & Tracey model [108] and 0.427 in Huang's revisited analysis [60]. Denoting the void growth ratio as (R/R_0) with R_0 the initial void radius, and $(R/R_0)_{\mathrm{c}}$ its critical value at failure initiation, a fracture model as in (3.2) is specified using:

$$g(T) = 0.427 \exp\left(\frac{3}{2}T\right); \quad C = \ln\left(\frac{R}{R_0}\right)_{\mathrm{c}} \tag{3.5}$$

This model is referred to as the Johnson-Cook-Beremin (JC-B) model [25, 63]. It involves no dependence upon the Lode parameter, although the original Rice and Tracey equations show some rather small dependence; see [105] for a recent overview and [80] for a rationale.

At low stress triaxialities, typically $T < 1$, void shape changes become significant and equation (3.4) becomes increasingly inaccurate. For instance, the latter predicts some significant void growth under uniaxial loading ($T = 1/3$), which is contrary to exact finite element solutions, e.g., using the computational cell model [20]. To account for this, void growth models have been developed which account for void shape evolution [44, 46, 67]. These models are fully coupled, hence not particularly fitting the class of models (3.2). However, one can obtain uncoupled forms as follows. For axisymmetric loading, the rate of increase of porosity, f, associated with such models can be simplified to [20]:

$$\frac{\dot{f}}{(1-f)\dot{\varepsilon}} = (g+f)\frac{\kappa\bar{\sigma}}{\Sigma_e}\sinh\left[\kappa(T-\beta)\frac{\Sigma_e}{\bar{\sigma}}\right] + D\eta + O(f^2) \tag{3.6}$$

where $\bar{\sigma}$ is the flow stress of the undamaged material, and g, κ, β, η and D are scalar-valued functions of micro-structural parameters f and the void aspect ratio w.

Fig. 3.2 illustrates the variations of the two most important of these functions, κ and β. In the dilute limit ($f \ll 1$ and $\dfrac{\Sigma_e}{\bar{\sigma}} \approx 1$) the above equation is further simplified for prolate voids as:

$$\frac{\dot{f}}{f} = \frac{3\dot{R}}{R} = \kappa\sinh\left[\kappa(T-\beta)\right]\dot{\varepsilon} \tag{3.7}$$

where R stands here for the mean void radius.

Eq. (3.7), while not encompassing general stress states, generalizes the Rice–Tracey void growth law (3.4). One key difference, however, is that even under proportional loading, Eq. (3.7) cannot be rigorously integrated without further assumptions. The reason for this is microstructure evolution, which is more prominent at

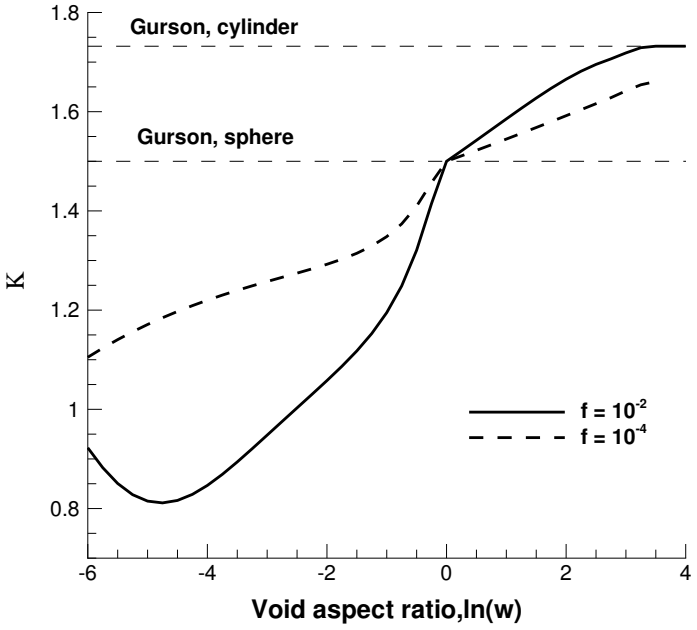

(a)

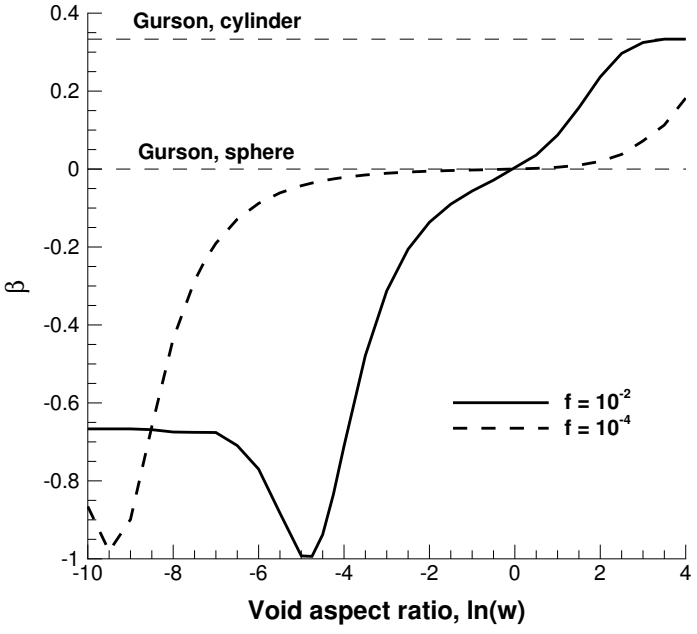

(b)

Figure 3.2: Dependence of (a) κ and (b) β on the void aspect ratio, w, over two orders of magnitude in void volume fraction, f. Adapted from [20].

low triaxiality and reflects in the non-constancy of $\kappa(f, w)$ and $\beta(f, w)$. This, in passing, points to a fundamental limitation of the class of models (3.2). For simplicity, κ and β may be chosen as fixed, for example by biasing the prediction toward high triaxiality data ($\kappa \to 3/2$ and $\beta \to 0$), low triaxiality data ($\kappa \to \sqrt{3}$ and $\beta \to 1/3$) [20] or as a matter of fact any intermediate triaxiality (see Fig. 3.2). Under such circumstances, integrating Eq. (3.7) for proportional loadings yields a criterion of type (3.2) with:

$$g(T) = 2a \sinh\left[\kappa(T - \beta)\right]; \quad C = \ln\left[\frac{R}{R_0}\right]_c \tag{3.8}$$

where the prefactor $2a = 0.854$ is used, as in (3.4), instead of $\kappa/3$ to account for Huang's correction[1]. In the high triaxiality limit, the function g in (3.8) reduces to that of the JC-B model in (3.5). In the low triaxiality limit, the resulting radial fracture locus given by (3.3) admits an asymptote at $T = 1/3$, which is the exact solution in the absence of void-particle interactions [105]. For illustration, typical fracture loci under proportional loading obtained with the two models above are shown in Fig. 3.3.

[1]As discussed in Ref. [105], the improved models that incorporate void shape effects [44, 46, 67] do not remedy the inaccuracy of isotropic models [51] in the high-triaxiality limit.

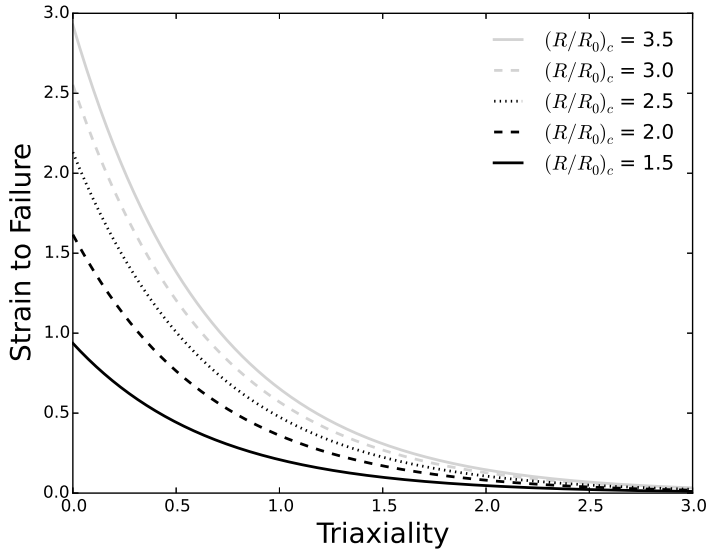

(a)

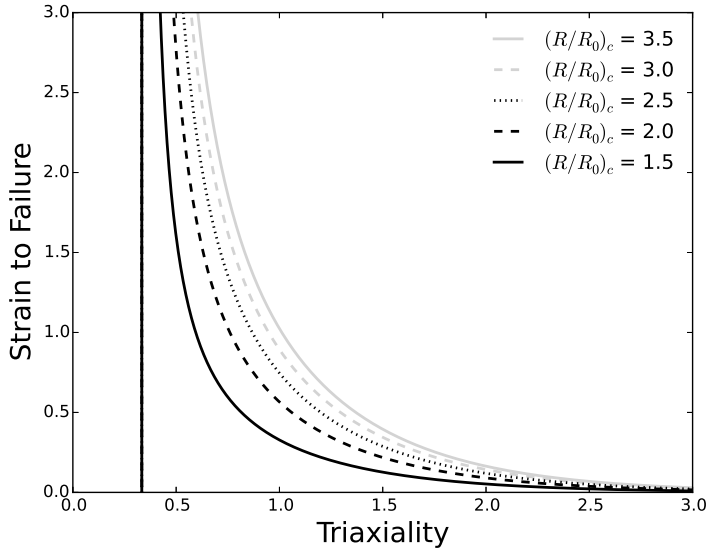

(b)

Figure 3.3: Typical failure loci for (a) Modified JC-B model (b) Extended model with $\kappa = \sqrt{3}$ and $\beta = \dfrac{1}{3}$

3.3 Problem formulation

Under radial loadings, equation (3.2) may be integrated to obtain a unique fracture locus given by (3.3). Under non-radial loadings, however, the fracture strain will depend on the specific loading path. Here, various loading paths are considered, some are purely theoretical and enable to thoroughly probe the space of possible loading paths, whereas others are taken from the experimental literature. In either case, the integral in equation (3.2) can be evaluated along the prescribed path, given a fracture theory, i.e., a choice of function g and parameter C (or equivalently $(R/R_0)_c$.) The wide range of loading paths considered warrants the use of the simple analytical damage models presented in Section 3.2.

For a given family of loading paths, two kinds of fracture loci are generated, as in [11]. In the first, the stress triaxiality is plotted against a monotonically increasing variable, namely some effective plastic strain, up to fracture as in Fig. 3.1a. Such a locus will be referred to as the T–ε plot. In the second, the fracture strain is plotted against the strain-weighted average triaxiality:

$$\bar{T} = \frac{1}{\varepsilon_f} \int_0^{\varepsilon_f} T \, \mathrm{d}\varepsilon \tag{3.9}$$

That will be referred to as the ε_f–$\bar{T}$ locus. The two fracture loci reduce to one for radial loadings, but are generally different for nonradial ones.

3.3.1 Theoretical loading paths

Analyses were carried out for two families of non-proportional loadings as depicted in Fig. 3.4. Implicit to both is that the principal directions of loading remain fixed throughout.

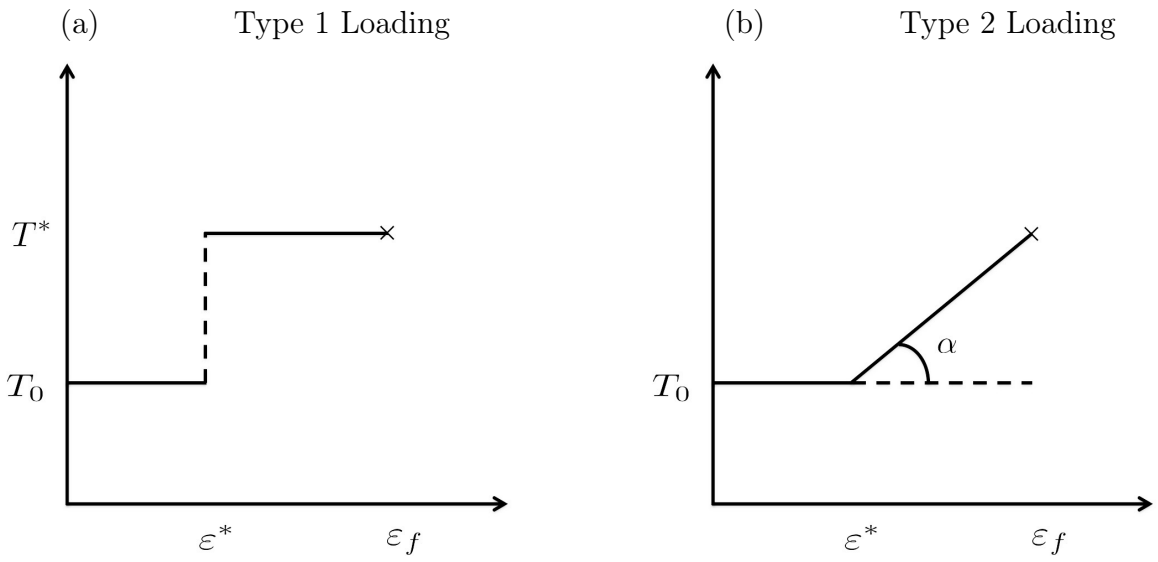

Figure 3.4: (a) A family of nonradial loading paths parameterized by the prestraining triaxiality T_0, the prestrain ε^* and the reloading triaxiality T^* (Type 1 Loading) (b) A family of nonradial loading paths parameterized by the prestraining triaxiality T_0, the prestrain ε^* and the slope α (Type 2 Loading)

3.3.1.1 Type 1 loading:

This family features an abrupt change in the loading path, Fig. 3.4a. Initially, loading at a constant triaxiality T_0 is applied until a strain ε^*, followed by a constant triaxiality T^* till failure. This may correspond to a triaxiality jump ($T_0 < T^*$) or drop ($T_0 > T^*$). In previous analyses by Benzerga et al. [14], triaxiality jumps were considered for only $T_0 = 1/3$ and three values of ε^*. Here, a much wider range of conditions is investigated using pre-loading triaxialities T_0 between 1/3 and 2. Note that the value of ε^* is limited by the maximum failure strain under radial loading at a given pre-loading triaxiality T_0. This limit value is given by $C/g(T_0)$ from equation (3.3). In practice, this type of loading idealizes situations encountered in multi-step sheet or bulk metal forming processes, as well as prestrained structures.

3.3.1.2 Type 2 loading:

This family of nonradial loadings allows for a gradual change in loading path in that the triaxiality is taken as a continuous function of the time-like parameter ε, Fig. 3.4b. Specifically, a constant triaxiality loading is applied until $\varepsilon = \varepsilon^*$, as for Type 1, then the triaxiality is linearly increased up to failure. This family of loading is then parametrized by the preloading triaxiality, T_0, prestrain, ε^*, and slope α. Here too, the value of ε^* must be smaller than $C/g(T_0)$. Values of T_0 between 1/3 and 2 and values of α between 0° and 90° have been considered. One example of such loading is the path experienced by a material point inside the neck of an initially smooth bar, in which case $T_0 = 1/3$, $\varepsilon^* = \epsilon_{\mathrm{n}}$ is the necking strain, and α depends on strain hardening.

3.3.2 Experimental loading paths

Four sets of published experiments have been analyzed using the simple fracture theory of Section 3.2. The first three are taken from Refs. [32, 89, 110] while the fourth set is from our recent experiments [11]. The loading paths considered in the first three studies are schematically shown in Fig. 3.5. All authors investigated loadings of Type 1, as per the above classification. In addition, Schiffmann et al. [110] considered mixed loadings reminiscent of a combination of Type 1 and Type 2.

3.3.2.1 Type 1 loading:

Marini et al. [89] investigated step jumps in nominal triaxiality (Fig. 3.5a) whereas Schiffmann et al. [110] and Chae et al. [32] studied step drops of triaxiality (Fig. 3.5b and d). In experiments, as the triaxiality is not directly controlled, such paths were imparted using notched bars as follows. Marini et al. [89] prestrained a shallow notched bar ($T_0 > 1/3$) to various levels of (effective) prestrain ϵ^*. This

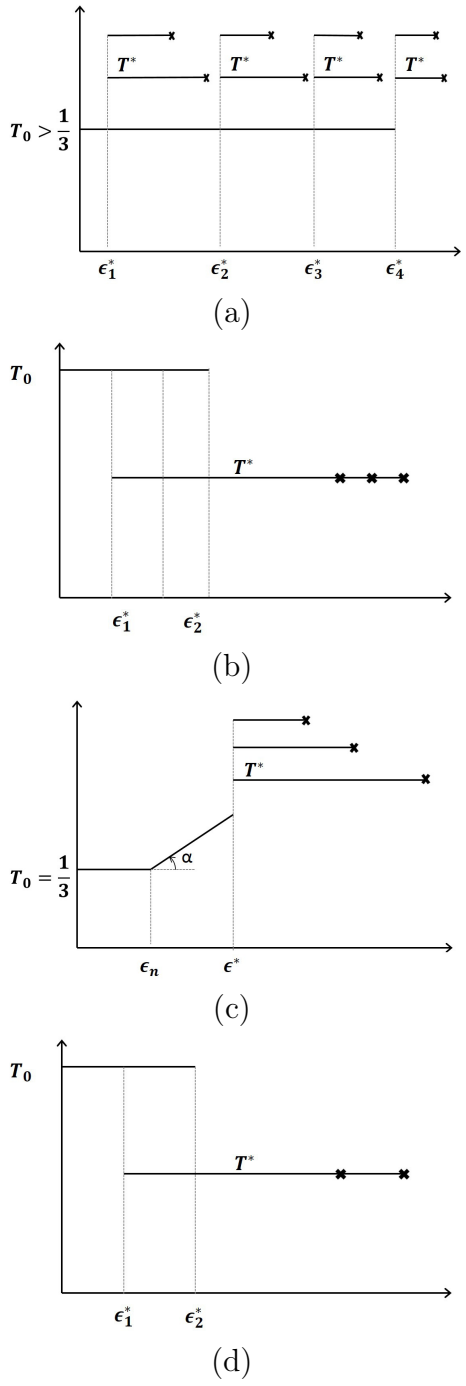

Figure 3.5: Schematics of experimental loading paths considered by (a) Marini et al. [89]; (b),(c) Schiffmann et al. [110]; and (d) Chae et al. [32]. Details are provided in Table 3.1

Material	ζ_0	**prestrain** ϵ^*	ζ^*	**Source**
A508	10	0.07	4	Marini et al. [89]
	10	0.31	4	
	10	0.46	4	
	10	0.55	4	
	10	0.07	2	
	10	0.31	2	
	10	0.46	2	
	10	0.55	2	
FeE690	2	0.13	5.3	Schiffmann et al. [110]
	2	0.17	5.3	
	2	0.22	5.3	
	∞	0.55	2	
	∞	0.55	4	
	∞	0.55	8.6	
HY-100	2.5	0.03	10	Chae et al. [32]
	2.5	0.07	10	
A572	∞	0.23	10.4	Basu and Benzerga [11]
	∞	0.23	3.9	
	∞	0.23	1.7	
	∞	0.23	0.9	

Table 3.1: Summary of experiments from the literature.

was followed by two different step jumps using sharper notches ($T^* > T_0 > 1/3$), and the specimens were then loaded to failure, as depicted in Fig. 3.5a. The strains to failure were reported in [89]. In practice, each notched bar is defined by a notch acuity parameter ζ equal to ten times the notch radius to notch root diameter. The parameters defining their experiments are reported in Table 3.1.

Schiffmann et al. [110] started with a sharp notch ($\zeta = 2$ so that $T_0 > 1/3$), pre-strained to three different strain levels then machined smaller bars with a shallower notch (Table 3.1) so that $1/3 < T^* < T_0$ (Fig. 3.5d). The experiments of Chae et al. [32] were essentially similar, albeit for a different material (Table 3.1). For the sake of brevity, the analyses of their experiments are omitted here. Finally, the recent

experiments of Basu and Benzerga [11] complements the above three sets by exploring the case of lowest preloading triaxiality $T_0 = 1/3$ and four different reloading triaxialities T^* but for a single value of the prestrain (Table 3.1). In all studies, a set of standard notch bar experiments were also carried out with no path change. The resulting fracture loci serve as reference.

3.3.2.2 Type 2 loading:

Every standard tensile testing of an initially smooth bar may fit in this category for materials whose plastic hardening can be approximated by a power-law. In the above cited works, such data was reported in [110] and [11]. In both, $T_0 = 1/3$ and $\varepsilon^* = \epsilon_{\rm n}$. Such paths are not included in Table 3.1.

3.3.2.3 Mixed Loading:

Schiffmann et al. [110] also considered the loading path depicted in Fig. 3.5c. It is realized in two steps. In the first, a smooth bar is loaded beyond necking so that $T_0 = 1/3$ and $\varepsilon^* > \epsilon_{\rm n}$. In the second step, notched bars with three different notch geometries were machined inside the neck of the predeformed bar and loaded to failure, thus leading to step jumps in triaxiality. This loading path is also included in Table 3.1 where $\zeta \to \infty$ refers to the smooth bar and ζ^* is for the machined notches. Note that the first step of loading itself is amenable to a Type 2 loading with induced ε^* equal to the necking strain.

3.3.3 Finite element analyses

In the theoretical loading paths of Section 3.3.1 triaxiality variations are imposed by design. However, in the experimental loading paths (Section 3.3.2) they need to be determined with some level of accuracy. To achieve this, finite element calculations were carried out to simulate the actual load path changes in the various

experiments in Table 3.1 using ABAQUS. The plastic behavior was modeled using rate-independent J_2 flow theory with isotropic hardening. Any potential effect of kinematic hardening due to load path change is neglected. The calculations were terminated when the remotely imposed displacement, as reported by the various authors, reached a value corresponding to the onset of failure. In all experiments, failure is assumed to have initiated at the center of the specimen, as was explicitly mentioned in some of the sources.

For the experiments by Basu and Benzerga [11] the hardening curve was supplied as tabulated data following an iterative procedure to account for large strain corrections beyond necking. More details are provided in [11]. In the simulation of the experiments with path change, the effect of prestrain on hardening is readily accounted for by disregarding the tabulated stress–strain data for effective strain values lower than ϵ^* for the data in [11]. This is straightforward since all material points in the predeformed smooth bar undergo the same loading path prior to necking.

For other experiments in the literature, the best power-law fit to the hardening curve was used, as the data provided in [32, 89, 110] was not sufficient to extract more accurate hardening laws at large strains. Nevertheless, the implication of such imperfections on the evolution of triaxiality is expected to be small. A more important issue is that in these experiments the first step involves deforming a notched bar so that the distribution of plastic strain in the specimen at the instant of load path change is nonuniform. The effect of predeformation on the hardening law to be used in the reloading step simulation must therefore be obtained in some approximate way. The following procedure was followed, which is represented schematically in Fig. 3.6.

At the instant of load path change (i.e., when $\varepsilon = \varepsilon^*$) the distribution of effective plastic strain p is known. An accurate method would consist of projecting the fields at

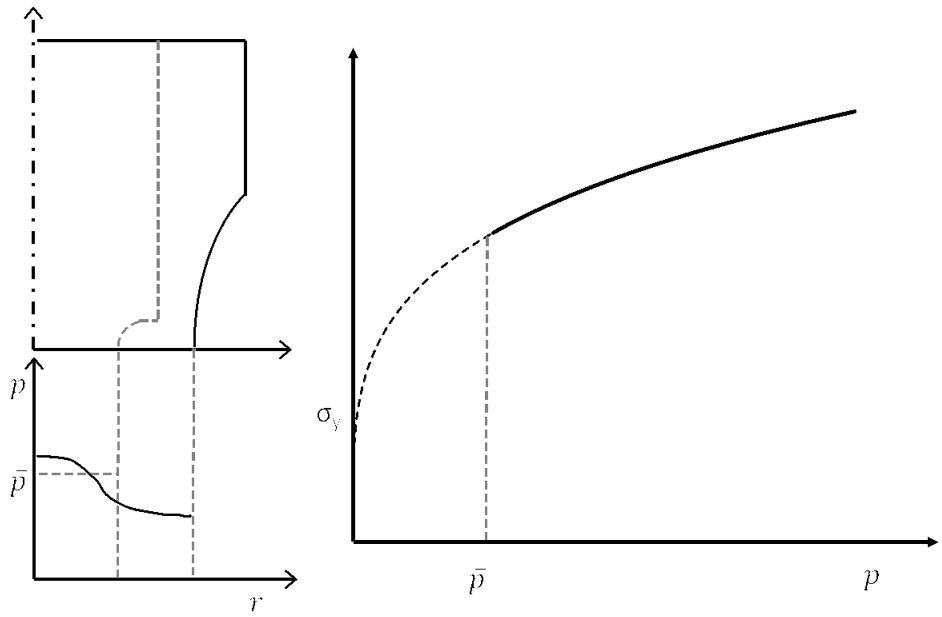

Figure 3.6: Procedure to account for prestrain effects on hardening in the finite element simulations.

that instant onto the smaller notched specimen (shown in dashed). This would enable among other things to keep any residual stress field that would have resulted from the first loading step. For simplicity however, the effective plastic strain averaged over the minimal section of the smaller bar was retained as an indication of an average, supposedly uniform, plastic strain, $\bar{p}$, with no associated residual stress. Thus, in the second step, the portion of the hardening curve past $\bar{p}$ is retained for subsequent analysis. This procedure allows to account for the natural loss in hardening capacity that follows prestraining.

3.4 Results

3.4.1 Model calibration

The JC-B fracture model defined by equations (3.2) and (3.5) involves one parameter, $(R/R_0)_c$. On the other hand, the extended model defined by (3.2) and (3.8)

involves three parameters, $(R/R_0)_c$, κ and β. In all rigour, parameters κ and β are not independent as they are set by assumed void volume and shape, see Fig. 3.2. Their typical range of variation is 0.8 to $\sqrt{3}$ for κ and -1 to 1/3 for β.

In what follows, when theoretical loading paths are analyzed the predictive capability of the approach is first tested by comparing with previously published cell model results [14]. In order to do so, the models are calibrated on cell results without path change.

Fig. 3.7a compares the radial fracture locus determined by the cell model from [14] with four radial loci obtained using the extended model for various parameter sets. Parameters κ and β are selected so as to represent the average void shape corresponding to a given triaxiality. Then the parameter $(R/R_0)_c$ is set by prescribing that the fracture locus passes through the data point for that triaxiality. For instance, if the choice is biased toward low triaxiality data, precisely capturing the behavior in the $T \to 1/3$ limit, then the fracture locus exhibits an asymptotic behavior near uniaxial tension, as obtained from the cell model. Otherwise, the model predicts fracture for $T = 1/3$.

Fig. 3.7b shows the best fits to the cell model data obtained using the extended and JC-B models. The fit with the extended model was obtained by biasing the prediction toward low-T data, as inferred from the above discussion. Therefore, using $\kappa = \sqrt{3}$ and $\beta = 1/3$, only one parameter, $(R/R_0)_c$, is used to obtain the best fit. One consequence of this is that the high-triaxiality portion of the fracture locus is not well captured, as shown in the inset. This is not surprising since it is generally impossible for any uncoupled model to capture the exact results over the full range of triaxialities.

On the other hand, the best fit obtained using the JC-B model is in agreement with the FE data at high triaxialities, but considerably overestimates (respec-

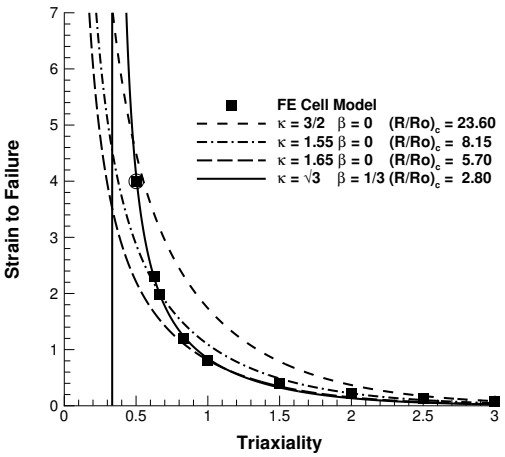

(a)

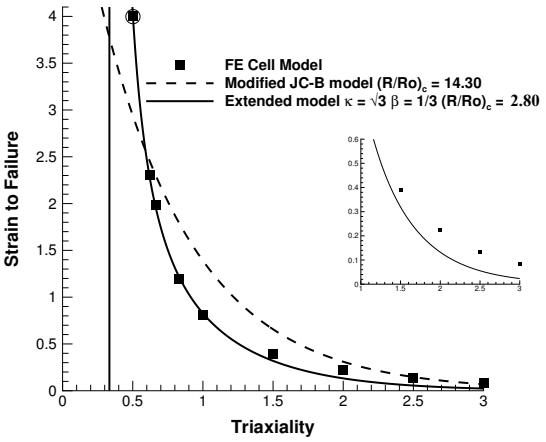

(b)

Figure 3.7: (a) Fracture loci obtained using the extended model versus those obtained by the cell model. (b) Calibration of the JC-B and extended models on cell model results.

tively underestimates) the fracture strain at intermediate (respectively low) triaxiality. Also, as explained earlier, it does not demonstrate the asymptotic behavior for $T = 1/3$. Yet, in what follows we shall work with these models, in particular the extended one while acknowledging their imperfections. It is emphasized that the current study is aimed at qualitatively assessing the deviations in failure locus corresponding to non-proportional loading paths. On strategies for developing a better quantitative prediction of ductile fracture, the reader is referred to the recent overview by Pineau et al. [105].

When the experimental loading paths are analyzed, model calibration is again performed using the (nominally) radial locus, namely the data with no path change. Table 3.2 reports the values so obtained for each set of experiments. Preference was given to the extended model when possible. Note, however, that for the data in [11] a better fit was obtained using the JC-B model. The quality of the fits will be shown further below, in context.

Data from	$(R/R_0)_c$	Fracture model	σ_y	N
Marini et al. [89]	2.13	extended		
Schiffmann et al. [110]	1.97	extended		
Basu and Benzerga [11]		JC-B		

Table 3.2: Fracture parameter, $(R/R_0)_c$, used in calibrating the fracture models for three sets of experiments. The last two columns also report the yield stress, σ_y, and hardening exponent, N, used in the finite element analyses of Section 3.3.3

3.4.2 Theoretical paths

3.4.2.1 Type 1 loading

Fig. 3.8a shows the radial and non-radial ε_f–$\bar{T}$ fracture loci obtained by Benzerga et al. [14] using the finite element cell model for type 1 loading with $T_0 = 1/3$ and $\varepsilon^* = 0.28$. By way of comparison, Figs. 3.8b and c represent the corresponding loci obtained using the JC-B and extended models, respectively. The procedure for obtaining the nonradial loci is explained in Appendix. Both models capture qualitatively well the trends of the cell model in Fig. 3.8a. In particular, they both predict the characteristics noted in [14], namely: (i) lack of one-to-one correspondence between fracture strain and average triaxiality; (ii) large deviation from the radial locus for large values of the reloading triaxiality T^*; and (iii) existence of an upturn in the locus at some characteristic value $\bar{T}_c$ of the average triaxiality. Recall that the models were calibrated using the radial loci (shown dashed in the figure). The extended model is quantitatively better. Not only it predicts that $\bar{T}_c \lesssim 1$, in keeping with cell model results, its prediction of the nonradial locus is nearly perfect although it is incapable of representing well the high-triaxiality portion of the radial locus, as discussed above. In other words, its imperfection at high triaxialities is inconsequential here.

With confidence gained from this comparison, the extended model is now used to explore the parameter space more thoroughly. This saves considerable computational time compared to the cell model.

(a)

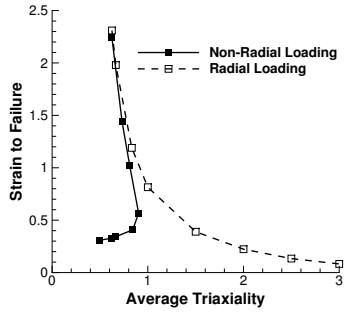

(b)

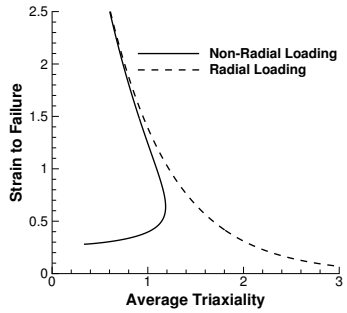

(c)

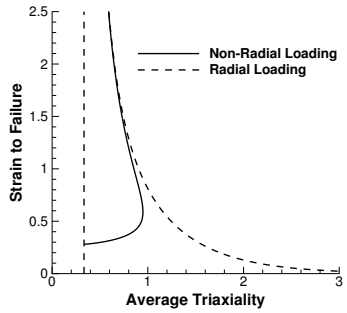

Figure 3.8: Comparison of radial and non-radial curves for step jump in loading for $T_0 = \frac{1}{3}$ with $\varepsilon^* = 0.28$ (a) FE cell model (b) Modified JC-B model (R/Ro)c = 14.30 (c) Extended model (R/Ro)c = 2.70 with $\kappa = \sqrt{3}$ and $\beta = \frac{1}{3}$

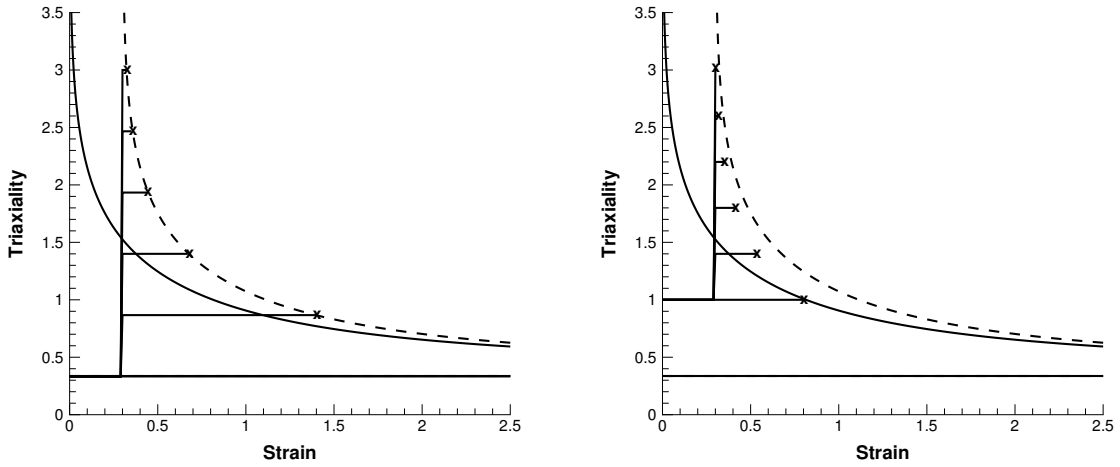

Figure 3.9: Predicted T–ε paths to fracture for Type 1 loading with $\varepsilon^* = 0.28$, $T^* > T_0$ and (a) $T_0 = 1/3$; (b) $T_0 = 1$.

Fig. 3.9a depicts some T–ε plots corresponding to the loci shown in Fig. 3.8b while Fig. 3.9b shows results for $T_0 = 1$ and the same prestrain. The 'x' at the end of each loading path indicates when fracture criterion (3.2) is met using (3.8). In the case $T_0 = T^* = 1/3$, which corresponds to uniaxial tension, failure is not predicted. Clearly, for both values of T_0, fracture occurs much beyond the point when the loading path meets the radial fracture locus (solid lines). Interestingly, in the $T_0 = 1/3$ case fracture is predicted when the loading path meets a locus translated from the radial one by an amount equal to the prestrain. This locus is depicted dashed in Fig. 3.9a. However, in the general case of $T_0 > 1/3$ the actual fracture locus is neither the radial locus nor the translated one, as ilustrated in Fig. 3.9b for $T_0 = 1$. The reason the fracture points lie on the translated locus for $T_0 = 1/3$ is that uniaxial tension does not lead to any damage growth according to the damage function g used in the extended model.

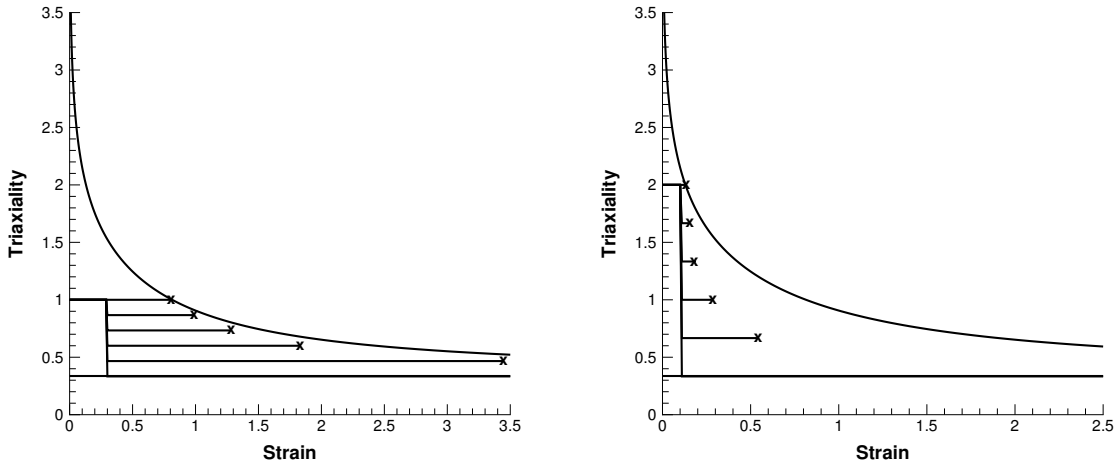

Figure 3.10: Type 1 loading paths (a) For $T_0 = 1$, with $T^* < T_0$, $\varepsilon^* = 0.3$ (b) For $T_0 = 2$ with $T^* < T_0$, $\varepsilon^* = 0.1$

Next, consider a step drop in triaxiality. Typical results are shown in Fig. 3.10. When $T^* = T_0$ the fracture point must lie on the radial locus. For any other value $1/3 < T^* < T_0$ fracture occurs well before the loading path meets the radial locus. This is because a high-triaxiality preloading is always damaging. The higher the initial triaxiality T_0 the larger the deviation from the radial locus (compare Fig. 3.10b with Fig. 3.10a). However, note that even for $T_0 = 1$ the fracture points still lie far from the radial locus, although this may not be so obvious by mere visual inspection of Fig. 3.10a. Also, note that for the special case $T^* = 1/3$ fracture is not predicted. Even if the prestraining triaxiality leads to some damage (void growth) reloading in uniaxial tension cannot (in theory) lead to final coalescence.

An alternative way of displaying the results is by plotting the fracture strain as a function of the triaxiality averaged over the entire loading history, as is sometimes done in the literature. The resulting ε_f–$\bar{T}$ fracture loci are more comprehensive in that they allow to show many more results in a single summary plot, as in Figs. 3.8b,c.

Details of how such plots are generated are described in Appendix. In particular, the non-radial curves are defined using implicit relation (3.13).

On that basis, Fig. 3.11 summarizes all that needs to be known about fracture loci under Type 1 loading, encompassing both jumps and drops in stress triaxiality. For reference, about a hundred cell model calculations would be needed to obtain enough points describing the overall trends exhibited in the figure. The locus corresponding to a prestrain $\varepsilon^* = 0.3$ in Fig. 3.11a is essentially close to that already shown in Fig. 3.8c. First, consider the case of triaxiality step jumps ($T^* > T_0$). It is evident that in the limit $T^* \to T_0$ the non-radial locus merges into the radial one and matches it for $T^* = T_0$. In the special case of $T_0 = 1/3$ both loci exhibit an asymptotic behavior in that limit. It is shown in Appendix that in the other limit, $T^* \to \infty$, the fracture strain must converge to ε^*. In that limit, it is straightforward to see that $\bar{T} \to T_0$ necessarily. Hence, the average triaxiality $\bar{T}$ must converge to T_0 in both limits $T^* \to T_0$ and $T^* \to \infty$, which implies that it must be bounded (viewed as a continuous function of T^*) and that the ε_f–$\bar{T}$ locus must be non-monotonic. The bound $\bar{T}_c$ is dependent upon the value of prestrain ε^* (see Appendix). This explains the general shape of the loci in Fig. 3.11 for stress triaxiality jumps.

To complete the picture, consider now triaxiality step drops ($T^* < T_0$). This regime is identified with the portion $\bar{T} \in [1/3, T_0]$ of the fracture loci in Fig. 3.11. This portion degenerates to a point with infinite ductility in the special case $T_0 = 1/3$ (Fig. 3.11a). Otherwise, for the prestraining triaxialities of 1 and 2 in Figs. 3.11b and c, respectively, this portion corresponds to the upper part of the locus. In the $T_0 = 1$ case this portion is essentially fused with the radial locus, irrespective of prestrain (Fig. 3.11b). This identifies a sub-family of non-proportional loadings that result in no deviation from the radial locus, a fact worthy of note. On the other hand, in the $T_0 = 2$ case the portion corresponding to triaxiality drops is clearly identified as

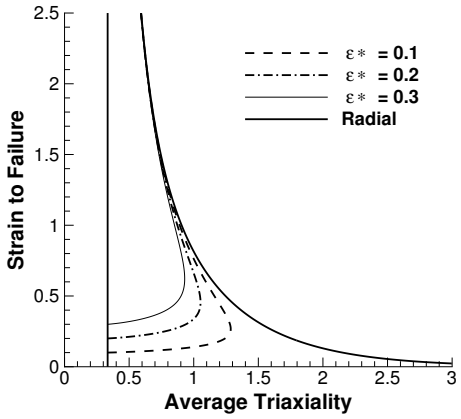

(a)

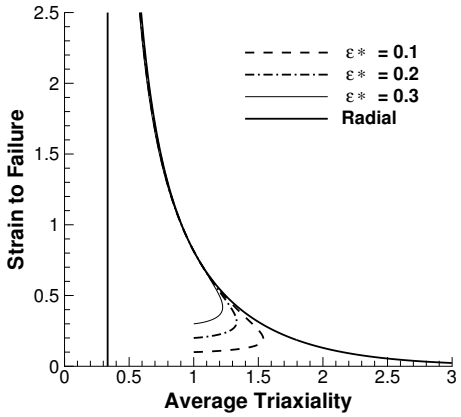

(b)

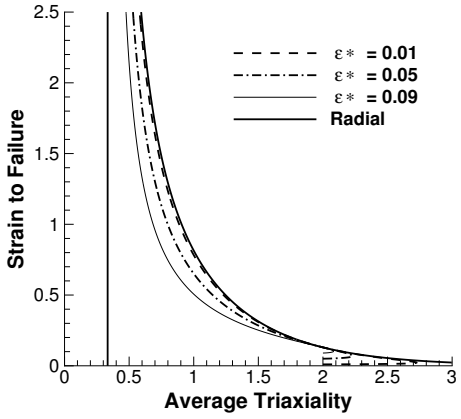

(c)

Figure 3.11: Radial and non radial loci for Type 1 loading (a) For $T_0 = 1/3$ with $T^* > T_0$ (b) For $T_0 = 1$, $T^* > T_0$ & $T^* < T_0$ (c) For T_0= 2, $T^* > T_0$ & $T^* < T_0$

deviating from the radial locus (Fig. 3.11c). The larger the prestrain the larger the deviation, unlike in the case of triaxiality jumps.

3.4.2.2 Type 2 loading

For Type 2 loading (see Fig. 3.4b) fracture criterion (3.2) may be integrated along the path to yield an expression for the fracture strain ε_f in terms of parameters T_0, α and ε^* characterizing the path. This expression is given by equation (3.15) in Appendix. Typical loading paths to failure are shown in Fig. 3.12 for $T_0 = 1/3$ and various values of α, with or without prestrain. The failure point is marked by 'x' as above. In all cases but $\alpha = 0$, fracture occurs significantly beyond the radial fracture locus. Similar trends (not shown for brevity) are obtained using other values of T_0.

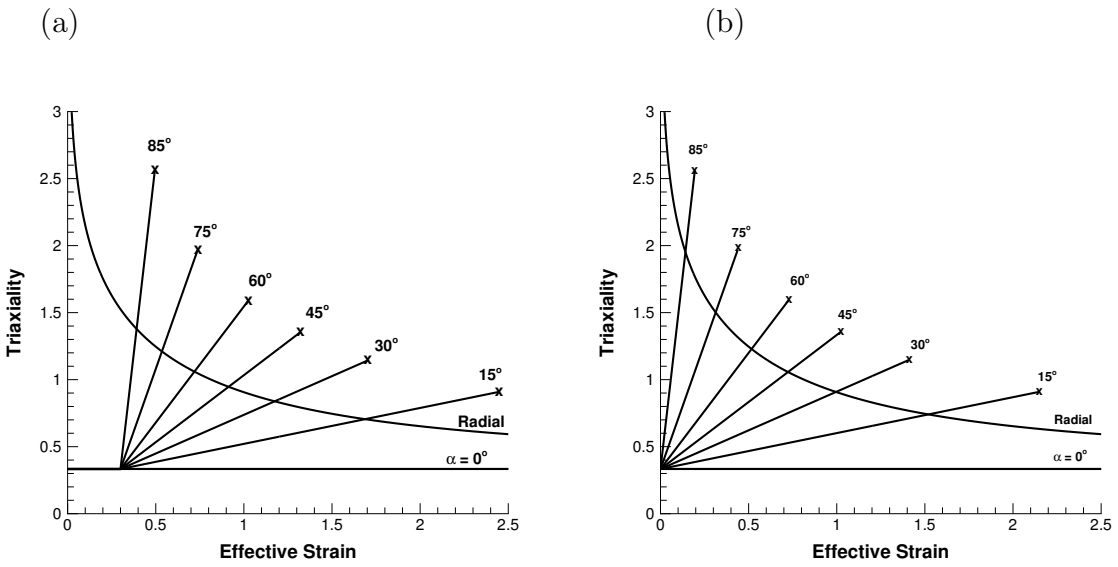

Figure 3.12: (a) Type-2-Loading-path-plots $T_0 = 1/3$ $\varepsilon^* = 0.3$ (b) Type-2-Loading-path-plots $T_0 = 1/3$ $\varepsilon^* = 0$

Just like for Type 1 loading, the dual fracture loci giving ε_f versus $\bar{T}$ are of interest. An implicit equation defining the nonradial locus is not straightforward in

this case. However, for each loading path, the average triaxiality may be evaluated using equation (3.16) of the appendix once ε_f is computed using (3.15). The so-obtained ε_f–$\bar{T}$ fracture loci are reported in Fig. 3.13.

Each part in this figure corresponds to one value of the preloading triaxiality T_0. In each part, three values of the prestrain ε^* are considered. In each plot, a given point corresponds to a specific value of the angle α defining how abrupt the path change is. The values used for α include those reported in Fig. 3.12 as well as additional points corresponding to $\alpha = 89$, 89.9 and 89.9999. The last three values were selected to exhibit limit behavior.

It can be shown that the ε_f–$\bar{T}$ loci for Type 2 loading have properties similar to those illustrated in Fig. 3.11 for Type 1 loading. These are recalled in Appendix It is noted that for $\alpha = 15$ and 30, the deviation from the radial fracture locus is negligible. Also, in the case of no prestrain ($\varepsilon^* = 0$), the loading path is basically a linear variation of triaxiality and the deviations from the radial locus remain small, including for large values of α. Note, however, the degenerate case of $\alpha \to 90$ for which the fracture strain must tend toward $\varepsilon^* = 0$ and the average triaxiality must tend toward T_0 by virtue of (3.16). As a result the point ($\bar{T} = T_0, \varepsilon_f = 0$) belongs to the each locus in Fig. 3.13 for $\varepsilon^* = 0$ even if it is not shown.

3.4.3 Experimental paths

Experimental nonradial loading paths described in Section 3.3.2 were analyzed using the simple fracture theory of Section 3.2. For each set of experiments, actual loading paths were determined using the finite element calculations described in Section 3.3.3 and the fracture parameter $(R/R_0)_c$ was calibrated as explained in Section 3.4.1 above.

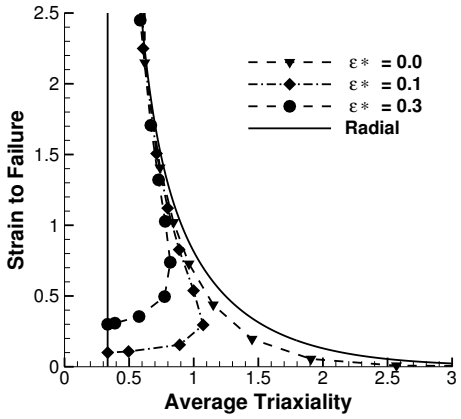

(a)

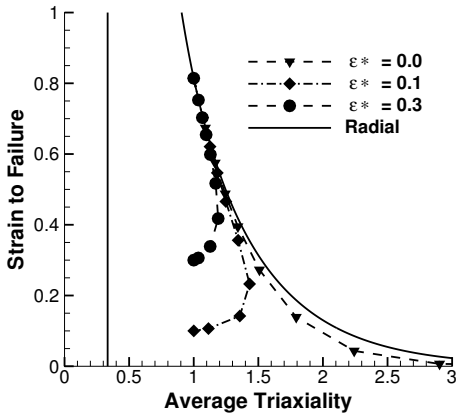

(b)

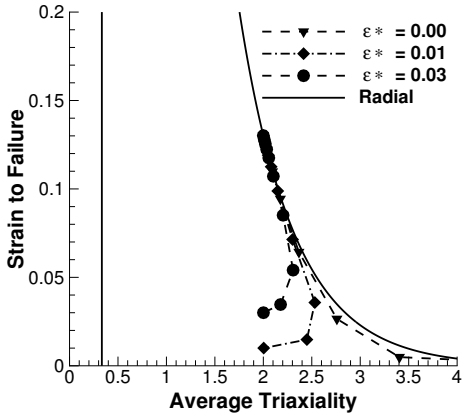

(c)

Figure 3.13: Radial and non radial loci for Type 2 Loading (a) $T_0 = 1/3$ (b) $T_0 = 1$ (c) $T_0 = 2$

3.4.3.1 Experiments of Marini et al.

Marini et al. [89] considered Type 1 loading, as sketched in Fig. 3.5a. Calculated triaxiality versus effective strain paths experienced by a material point at the location of failure initiation are shown in Fig. 3.14a for their experiments. The characteristics of these paths were given in Table 3.1. The 'X' symbol here denotes the onset of failure as inferred from the experiments. The results in Fig. 3.14a are consistent with those of similar calculations in [89]. In particular, some anomalies in the data are to be noted. While reloading at a high triaxiality leads to lowering the fracture strain for most prestrain values, the data corresponding to $\varepsilon^* = 0.47$ seems inconsistent. No information was provided on neither the repeatability of this trend nor the applied strain rates. Also included in the figure are the three data points (squares) corresponding to experiments with no path change. These nominally define the radial fracture locus from Marini et al.

On plotting their findings on a strain to failure versus average stress triaxiality locus (Fig. 3.14b) it is observed that there are deviations from the radial locus. However, no overall trend can be deduced.

In order to shed more light on this, the data is analyzed in Fig. 3.15 on the basis of lessons drawn from the theoretical analyses of Section 3.4.2. One approach would consist of unrolling the uncoupled fracture criterion in the finite element calculations and determining when it is met while following the exact paths shown in Fig. 3.14a. As stated above, the goal here is not to predict quantitatively fracture in the experiments, rather to rationalize the trends in these and other experiments in order to draw more general, if only qualitative, conclusions about the effects of nonproportional loadings in ductile fracture. With this in mind, the loading paths in Fig. 3.14a are idealized as Type 1 loadings (strictly step jumps) as in Section 3.4.2

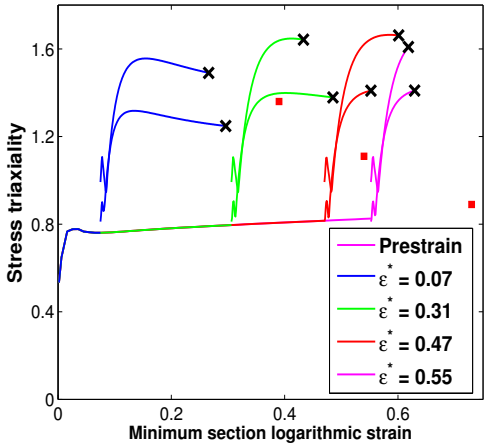

(a)

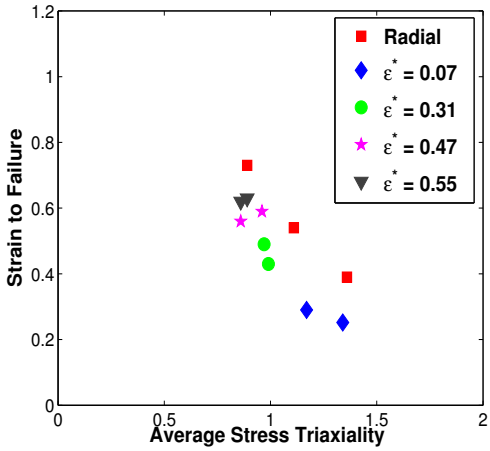

(b)

Figure 3.14: (a) Stress triaxiality, T, vs strain for a few load paths realized by [89]. Different prestrain levels are denoted by different colors and there are two different values of step jump in stress triaxiality at each prestrain. (b) Strain to fracture versus the strain weighted triaxiality $\bar{T}$ for the two sets of experiments described in Fig 3.14(a).

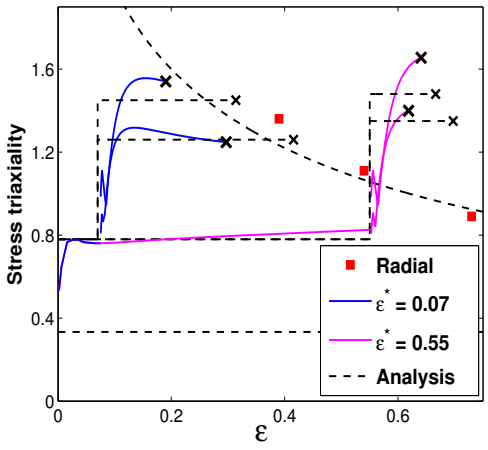

(a)

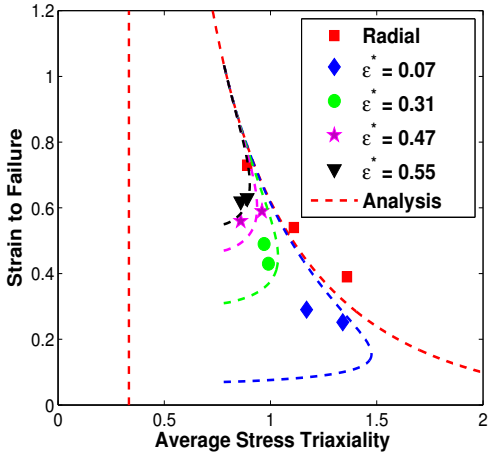

(b)

Figure 3.15: (a) Evolution of stress triaxiality with strain for a few loading paths for [89] with the analysis data superimposed on the experimental plots as dashed lines. Each path comprises of a step jump to 2 different values of stress triaxiality ratio after a prestrain to different values of ϵ^*. Each color represents the different prestrain levels under step 1 of loading. (b) Failure loci for proportional and non-proportional loading paths shown in fig. 3.14(a)

and the onset of fracture is determined using the simple theory. Fig. 3.15a illustrates the so-predicted fracture initiation plots. Only two loading paths corresponding to the two extreme values of prestrain are shown for clarity. Putting aside the discrepancies, which will be further discussed in Section 3.5, the results are consistent with the theoretical analyses in that the fracture strains lie between the radial fracture locus and the one translated by the amount of prestrain (not shown for clarity). The most important message, however, is conveyed in the ε_f–$\bar{T}$ plot of Fig. 3.15b. There, predictions based on the simple theory are superposed onto the experimental data previously shown in Fig. 3.14b. On the sole basis of the data, it is difficult to uncover the fundamental trend, since for a given prestrain value there are only two data points and such experiments are scarce and costly. The model, on the other hand, rationalizes the data. It also predicts that larger deviations would be expected if the specimens were reloaded at higher triaxialities (that is using notches sharper than $\zeta = 2$).

3.4.3.2 Experiments of Schiffmann et. al

Schiffmann et al. [110] considered Type 1 loading of the triaxiality step drop kind, as sketched in Fig. 3.5b. Calculated T–ε paths at the location of failure initiation are shown in Fig. 3.16a where the large 'X' symbol again stands for failure from their experiments; also see Table 3.1 for path parameters. Also included in the figure are four data points (squares) corresponding to experiments with no path change as reported in [110]. The loading paths shown dashed in the figure are idealized paths (strict T step drops). The small 'x' symbol in these corresponds to onset of failure as predicted by the model. Discrepancies aside (see Section 3.5 for related discussion), the results are consistent with the theoretical analyses of Section 3.4.2 in that the fracture strains lie below the radial fracture locus for this kind of Type 1 loading

(see Fig. 3.10.)

Schiffmann et al. [110] also considered the mixed type loading sketched in Fig. 3.5c. Calculated T–ε paths at the location of failure initiation are shown in Fig. 3.16b along with idealized paths shown in dashed. As above, the large 'X' and small 'x' symbols stand for measured [110] and predicted fracture strains (extended model); also see Table 3.1 for path parameters and Table 3.2 for model parameters. As in Fig. 3.16a, the four experimental data points (squares) defining the nominal radial locus are included. The discrepancies here between measured and fracture strains are much smaller. Here, the key observation is that the results are consistent with the theoretical analyses of Section 3.4.2 for either Type 1 with a step increase in T or Type 2, in that the fracture strains lie above the radial fracture locus (see Figs. 3.9 and 3.12.)

When the results of Schiffmann et al. [110] for both types of loading are plotted on a ε_f–$\bar{T}$ locus (Fig. 3.16c) deviations from the radial locus are noted, just like for the data of Marini et al. in Fig. 3.14b. However, once again no overall trend stands out. On the other hand, when predictions based on the simple theory are superposed onto the experimental data, it is possible to rationalize the trends, although the unavoidable quantitative discrepancies come in the way of a clearer picture. We emphasize that solely based on the data, it is difficult to uncover the fundamental trend because the data is limited for a given choice of prestrain.

3.4.3.3 Experiments of Basu & Benzerga

Basu and Benzerga [11] considered Type 1 loading that complements the experiments in [89, 110]. The paths they studied are sketched in Fig. 3.5d. Calculated T–ε paths at the location of failure initiation for some of their experiments are shown in Fig. 3.17a (solid lines). Path and model parameters were provided in Tables 3.1

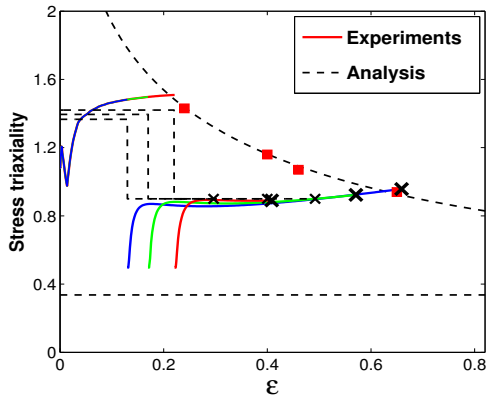

(a)

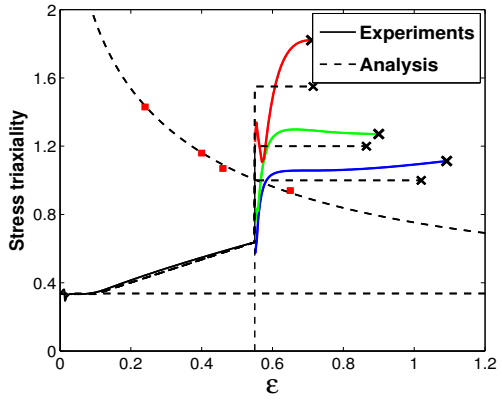

(b)

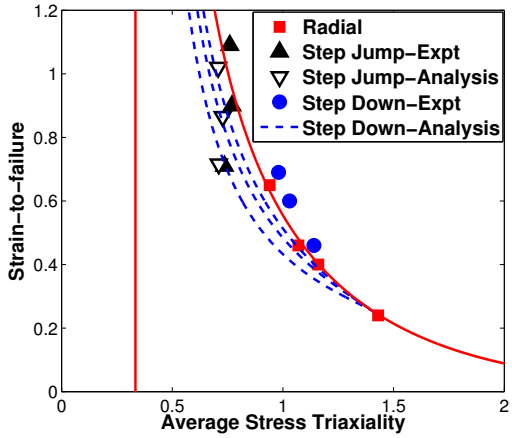

(c)

Figure 3.16: Load paths for loadings adopted by [110] (a) Step jump & (b) Step decrease. (c) Failure loci in the strain to fracture versus the strain-weighted triaxiality $\bar{T}$ for the data shown in Fig 3.16(a)&(b).

and 3.2. Idealized paths used in fracture prediction are shown dashed as above and the square data points correspond to experiments with no path change from [11]. Also, the 'X' and 'x' symbols bear the same meanining as in preceding figures. On the basis of the theoretical analyses of Section 3.4.2, specifically the results for $T_0 = 1/3$ in Fig. 3.9a, the predicted fracture points 'x' are expected to lie on a curve translated from the radial locus by the amount of prestrain, here 0.23. This holds, albeit approximately due to model imperfections to be further discussed below.

Here too, if the data are represented in the ε_f–$\bar{T}$ plot (Fig. 3.17b) then the following is observed. First, the deviations from the radial locus are much clearer than in previously published experiments; for reference see Fig. 3.14b and Fig. 3.16c for the data in [89] and [110], respectively. This is due to the consideration of very sharp notches ($\zeta < 2$) upon load path change in [11]; see Table 3.1. In addition, the simple fracture theory rationalizes the trend (solid line in Fig. 3.17b) inspite of the quantitative discrepancy.

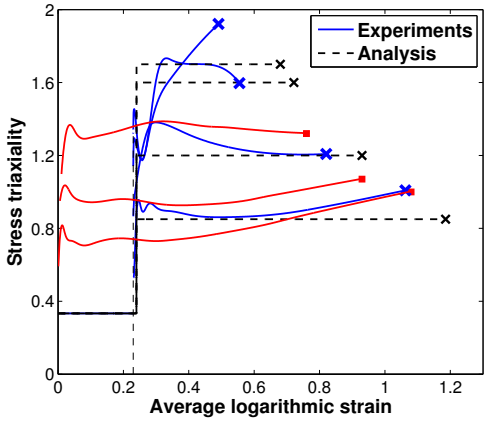

(a)

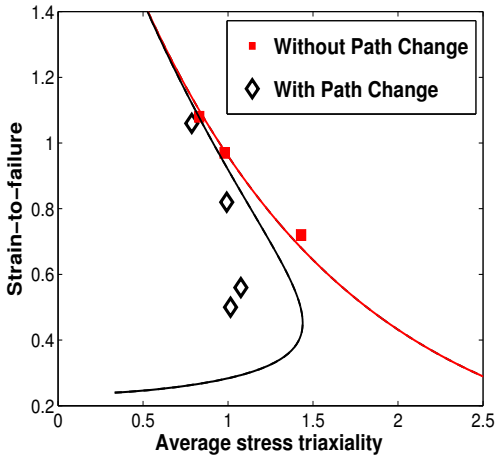

(b)

Figure 3.17: (a) Evolution of stress triaxiality with global strain in representative experiments up to crack initiation by [11]. The solid line refers to the data from the experiments while dashed lines are obtained superimposing the model predictions on the experimental data. (b) Fracture loci of the loadings shown in Fig.3.17(a) with the results of the model plotted in solid lines

3.5 Discussion

Using a simple fracture theory for ductile materials, generic trends have been uncovered when non-proportional loadings are considered. The trends pertain to two distinct but related definitions of the fracture locus, which are identical in the special case of proportional loading. Exact results for, say materials with initial voids, could have been obtained using the finite element cell model as in [14, 129]. Reproducing the theoretical results summarized for instance in Figs. 3.11 and 3.13 using the cell model would have required about 200 finite element calculations, most of which include two separate boundary value problem solutions. The method used is thus appropriate to tackle the stated problem with high-throughput analyses. The efficiency of the method is based on the uncoupled character of the damage model and the assumption of a constant critical damage parameter. This approach has well documented limitations [105] but is fully justified in the present context.

Nearly three decades after the publication of the first experiments on this topic by Marini et al. [89] it is fair to say that the picture on nonproportional loading effects in ductile fracture was at best cloudy. On the one hand, the various investigators indicate that the nonproportional loading paths do not end on the radial fracture locus [11, 32, 89, 110]. On the other hand, interpretations of the various experiments have remained elusive and sometimes conflicting. For example, Mohr and Marcadet [94] have recently suggested that a linear damage accumulation rule applies, contrary to what Marini et al. [89] reported earlier. Even more recently, Papasidero et al. [102] argued that while a linear rule works fine a nonlinear rule is quantitatively better. It is important to note that any criterion cast in the format used in this paper, equation (3.2), represents a linear damage accumulation rule. It is clear that if the strain to void nucleation is not negligible compared with the total strain to

failure, then deviations occur as argued in [89]. However, the imperfections reported in [89, 102] are not necessarily due to the inapplicability of a linear rule, rather to the imperfections in the damage model itself. This includes the inability of an uncoupled damage function to capture all regimes of triaxiality, let alone more complex loading situations. It also includes the fact that a constant critical damage parameter C is generally not quantitative.

In addition, when the fracture strain ε_f is plotted versus the strain-weighted average triaxiality, previously published data appears so clustered that the trends are inconclusive; see for instance Fig. 3.14b and Fig. 3.16c. Here again, the simple theory proved useful in providing a rationale for the experimental trends, some of which were reported in this paper (Figs. 3.15b, 3.16c and 3.17b.) In fact, the theoretical analyses suggest ways in which prior experiments could be augmented so as to make the trends unequivocal. Consider for instance the experiments of Marini et al. [89]. What would have been useful is an additional one or two experiments with $\zeta < 2$ (sharper notches) for the second step of loading. This could be done for a single condition of prestrain. Similarly, in the step drop experiments of Schiffmann et al. [110] the data nearly lie on the radial locus (Fig. 3.16c), which seems fortuitous. Indeed, mere examination of the theoretical trends in Fig. 3.11b clearly indicates that the nonradial and radial fracture loci are identified with each other for $T_0 = 1$ for step drops in triaxiality (that part lies to the left of the locus). One way to exhibit strong deviations would have consisted of using a sharper notch during the first step of loading and a much shallower notch (if not simply a smooth bar) in the second step, as inferred from the results in Fig. 3.11c. Evidently, the more recent experiments of Basu and Benzerga [11] were in part guided by theory and hence produced more sensible deviations in ε_f–$\bar{T}$ diagrams (Fig. 3.17b.)

In general, effects of nonproportional loading can manifest in various ways. The

general scenario is quite complex because of unavoidably intertwined history effects on both damage-free *plasticity* and plasticity-induced *damage*. Even when kinematic hardening is small, as is probably the case in the steels used in the experiments [6, 11, 32, 89, 110], the loss of isotropic strain hardening capacity due to prestraining must be accounted for in any quantitative prediction. The simple fracture theory above is insensitive to strong hardening effects since the term $\Sigma_e/\bar{\sigma}$, which involves the matrix flow stress, is lumped into the triaxiality. In part, this explains the discrepancy noted between the measured and predicted fracture strains in the various results reported above. Another factor is that the idealized loading paths impart some additional errors compared with the actual paths calculated by finite elements. Finally, as discussed under model calibration along with Fig. 3.7, the uncoupled model cannot be quantitative over the full range of stress triaxiality, even for ideal configurations considered in the cell model involving initial voids in a von Mises hardenable matrix. By focusing on the plasticity induced damage, the present paper depicts a clean picture for the overall qualitative trends in what concerns nonproportional loading effects.

Another aspect that is worth mentioning in the context of nonradial loading experiments on steels is potential complications associated with the onset of cleavage, as reported for example by Enami [39]. In the experimental results from the cited literature [6, 32, 89, 110] it was not clear whether the authors had maintained the same nominal strain rate in the notched region upon reloading in step 2. For example, Basu and Benzerga carefully rescaled the remote displacement rates in their experiments so as to ensure the same nominal strain rate prior to and after path change. This is important because if the remote displacement rate is kept the same, then the strain rate inside the notch would be much higher, thus possibly leading to fracture by cleavage. This is illustrated in Fig. 3.18 showing fractographs from

additional experiments not reported in [11]. In turn, such spurious strain rate effects may also explain some inconsistencies in the data found in the literature. In all experiments reported in [11] cleavage was avoided when extremely sharp notches were used in the reloading step.

The present findings have both conceptual and practical implications. Critical strain fracture criteria are often used, which are written in terms of stress invariants or ratios thereof. To the extent that isotropic fracture criteria are appropriate (the ductile damage process is inherently anisotropic [18, 19]) it is important to understand when and how they can be used. Most notable among these is the Johnson–Cook model, which also includes strain rate and temperature effects on the flow strength. If such a model is used in integrated form, as usually practiced, then fracture is predicted when the loading path meets the radial fracture locus. In the case of nonproportional loading involving either a step increase or gradual increase in triaxiality, it is clear from Figs. 3.9 and 3.12 that fracture occurs well beyond the radial locus. Hence, in such situations the Johnson–Cook model would be overly conservative. On the other hand, for loadings involving a decrease in triaxiality along the path, fracture would occur below the radial locus; see Fig. 3.10. Such situations warrant special care. Obviously, a fracture criterion of the type $\varepsilon_f(T, L)$ is conceptually incorrect. To remedy this, a rate form of the criterion involving integration of a damage function along the path should be used. Nevertheless, from the practical point of view, the question arises as to how large the deviations from the radial locus can be for commonly encountered loading paths. The results here can serve as basis to measure the errors implied by using critical strain fracture criteria in integrated form.

(a)

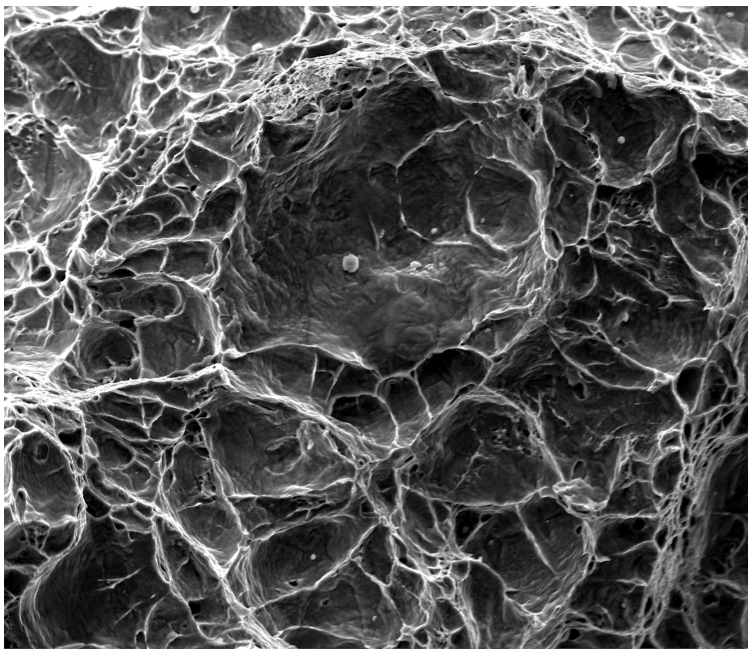

(b)

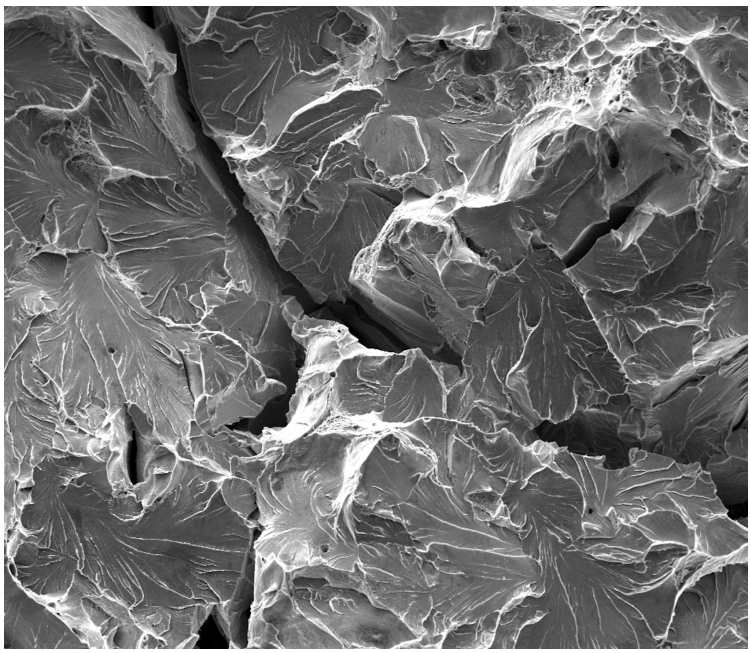

Figure 3.18: Fracture surfaces of A572 steel specimens with notch acuity $\zeta = 0.9$ prestrained in tension (see Table 3.1) and reloaded at a strain rate of (a) $\dot{\varepsilon} \sim 10^{-3} s^{-1}$; and (b) $\dot{\varepsilon} \sim 2 \times 10^{-2} s^{-1}$

3.6 Conclusions

A simple fracture theory has been employed which supplements an uncoupled damage model with a constant critical damage parameter in order to investigate ductile fracture under nonproportional loading. Emphasis was laid on that part of the deviations that are related to plasticity-induced damage. When first compared with exact finite-element cell model simulations, the predictions of the theory were shown to be excellent when a variant of the damage model that approximately accounts for void shape effects is used. Then the theory was employed to explore the parameter space. Two representative families of loading have been investigated. The main conclusions are as follows:

- When the nonproportional loading path involves an increase in stress triaxiality, fracture is invariably found to set beyond the fracture limit curve defining proportional loading. This holds for both a step jump and gradual increase in triaxiality and is thus likely to hold irrespective of the detailed shape of the loading path.

- On the other hand, when the loading path involves a decrease in stress triaxiality, fracture is found to set before the path intersects the (proportional) fracture limit curve. This situation indicates that one should be concerned about employing critical fracture strain criteria in integrated form.

- A generic shape of the fracture strain versus average triaxiality locus has been rationalized, irrespective of loading type. With this as basis, previously published experimental results have been rationalized without recourse to ad hoc explanations. In addition, the results provide insight into ways to improve the experimental programs previously attempted to tackle this problem.

- Ductile fracture is inherently anisotropic, particularly at low stress triaxialities. The fracture theory accounts only partially and approximately for some effects of anisotropy. Although the authors do not advocate using the model as is to make fracture predictions, it is remarkable that the projections are qualitatively robust for changes in the constitutive damage laws used.

3.7 Nonradial loci of type 1

For Type 1 loading, a relationship between the average triaxiality $\bar{T}$ and the fracture strain ε_f is derived as follows. First, specializing equation (3.2) for the loading path of interest then rearranging gives:

$$g(T^*) = \frac{C - \varepsilon^* g(T_0)}{\varepsilon_f - \varepsilon^*} \tag{3.10}$$

From the definition (3.9) of $\bar{T}$ one gets:

$$\varepsilon_f \bar{T} = \varepsilon^* T_0 + (\varepsilon_f - \varepsilon^*) T^* \tag{3.11}$$

Once T_0 and ε^* are specified the value of T^* sets the residual strain to failure $\varepsilon_f - \varepsilon^*$ via the fracture condition. Inverting (3.10) then substituting for T^* in (3.11) one obtains $\bar{T}$ as:

$$\bar{T} = \frac{\varepsilon^* T_0 + (\varepsilon_f - \varepsilon^*) g^{-1}\left[\dfrac{C - \varepsilon^* g(T_0)}{\varepsilon_f - \varepsilon^*}\right]}{\varepsilon_f} \tag{3.12}$$

Equation (3.12) provides an explicit expression of $\bar{T}$ in terms of ε_f given a damage function g and a critical parameter C.

In case of the extended model, for example, the damage or memory function $g(T)$ is given by (3.8) so that the nonradial fracture locus for Type 1 loading is fully

specified through:

$$\bar{T} = \frac{\varepsilon^* T_0 + (\varepsilon_f - \varepsilon^*) \left\{ \beta + \frac{1}{\kappa} \sinh^{-1} \left[\frac{C - \varepsilon^* g(T_0)}{2a(\varepsilon_f - \varepsilon^*)} \right] \right\}}{\varepsilon_f} \tag{3.13}$$

For ease of reference, $\bar{T}$ is the average triaxiality, ε^* is the pre-strain, ε_f is the strain-to-failure, T_0 is the pre-straining triaxiality and T^* is the reloading triaxiality. Equation (3.13) is used to generate all ε_f–$\bar{T}$ plots in Figs. 3.8c and 3.11 for various values of the parameters.

Note that relationship (3.13) is *not* invertible over the full range of fracture strains. Up to two values of ε_f may be obtained for the same value of $\bar{T}$. This explains the peculiar shape of the loci in Figs. 3.8c and 3.11.

Next, consider asymptotic behavior. To this end, specializing equation (3.9) for the loading path of interest then inverting gives:

$$T^* = \frac{\varepsilon_f \bar{T} - \varepsilon^* T_0}{\varepsilon_f - \varepsilon^*} \tag{3.14}$$

which could also be obtained from (3.11) above. In the limit $T^* \to \infty$, it can be seen that the fracture strain must converge to ε^* since both ε_f and $\bar{T}$ are finite. Incidentally, the average triaxiality also converges to T_0. Therefore, the point (T_0, ε^*) must lie on the locus.

Finally, the existance of a bound $\bar{T}_c$ on the average triaxiality was established in the text. Its expression may be obtained by differentiating $\bar{T}$ in (3.13) viewed as a function of ε_f. The result is a complex expression of $\bar{T}_c$ in terms of ε^*, T_0 and damage model parameters.

3.8 Nonradial loci of type 2

In case of type 2 loading, an implicit relation such as (3.13) giving the fracture strain ε_f in terms of $\bar{T}$ does not seem feasible. Instead, a parametric representation of the locus is obtained by integrating along the path the fracture condition (3.2) and the definition of $\bar{T}$, equation (3.9). This leads to:

$$\varepsilon_f = \varepsilon^* + \frac{1}{\tan\alpha}\left[(\beta - T_0) + \frac{1}{\kappa}\cosh^{-1}\left[\frac{\kappa\tan\alpha\,(C - g(T_0)\varepsilon^*)}{2a} + \cosh\left(\kappa(T_0 - \beta)\right)\right]\right] \tag{3.15}$$

and

$$\bar{T} = T_0 + \frac{\tan\alpha}{2\varepsilon_f}(\varepsilon_f - \varepsilon^*)^2 \tag{3.16}$$

where the load path characteristics T_0, ε^* and α play the role of parameters. Note that because ε_f explicitly appears in (3.16) making parametric plots is cumbersome. For this reason, the fracture loci based on equations (3.15) and (3.16) (see Fig. 3.13) are made point by point given a set of parameters.

The type 2 fracure loci enjoy properties similar to those of type 1. For example, in the limit $\alpha \to \pi/2$, the second term in (3.15) vanishes and $\varepsilon_f \to \varepsilon^*$. Likewise, the second term in (3.16) vanishes because the square term dominates and $\bar{T} \to T_0$. Therefore, the point (T_0, ε^*) must lie on the locus.

3.9 Acknowledgements

Partial support from the Lawrence Livermore National Security, LLC under Master Task Agreement No. B575363, LLNL under Contract DE-AC52-07NA27344 and the National Science Foundation under grant CMMI-0748187 is gratefully acknowledged.

4. THREE DIMENSIONAL SIMULATIONS OF ANISOTROPIC DUCTILE FRACTURE

4.1 Introduction

Accurate concurrent modeling of void growth to coalescence and strain localization in shear bands as a function of imposed deformation and stress state is important to predict limits to ductility in structural materials. The inherent non-proportional loadings associated with most industrial forming operations exacerbates this challenge of accurate quantitative prediction of fracture. The onset of strain localization and macroscopic cracking in ductile materials depend on microstructural details such as the size, shape and distribution of the voids. For better predictive capabilities and to account for path dependency, thus, a fracture model must incorporate internal state variables in the form of micro structural information. For large scale simulations of ductile failure aimed towards the development of damage tolerant microstructures, these models also need to be implemented in large deformation finite element codes.

The fundamental mechanisms underlying ductile fracture is extensively researched and well understood and advanced models of ductile fracture are being developed and improved upon using insights from experiments, computation and theory; see the recent reviews by [20, 26, 105] for an overview of the literature. Uncoupled models of void growth [25, 63, 108] although simple in their constitutive structure and use, have some limitations. On the other hand, coupled models [2, 16, 46, 51, 67, 85, 95, 96, 106] seamlessly combine plasticity and damage resulting in comparatively complex set of equations and are usually supplemented with the evolution equations for microstructural parameters. Once the models are developed, they are thoroughly assessed both

computationally and experimentally. Usually, the model predictions are compared against results from finite element cell model studies [41, 69, 74, 75, 98, 103, 114, 115, 122, 131] and heuristic corrections needed if any, are added to the models towards improving them. As a next step, predictions are compared to experimental observations [13, 19, 59]. Then simulations using models of real experimental geometries (smooth bars, notched bars, cracked specimen and plane strain specimens) are done towards exploring the parameter space not reachable via real experiments.

Initially crack free specimens of smoothbars, notched bars and plane strain specimens are typically employed in fracture investigations probing the influence of stress state and strain. Among them, notched bars, introduced by [54] constitute ideal tools for studying damage initiation and accumulation and have some advantages over other geometries. Material parameters in fracture models are usually fit by conducting tensile tests on notched specimens. One key advantage is that the fracture process in them is believed to be uncoupled from instabilities such as necking and shear banding. In addition, by varying the notch radius, various stress triaxiality values can be realized and in general triaxiality at the centre of the notched bars tend to remain roughly constant [23] making them ideal constant triaxiality specimens.

[54, 83] conducted experimental studies on notched bars and showed that stress triaxiality is a governing factor controlling ductility in structural materials which was later confirmed by [53] who in addition found out that fracture in cylindrical notched specimens initiated at the centre where the stress triaxiality was maximum. [100], following the lines of [30] conducted analyses of axisymmetric and plane strain notched bars using the GTN model [125] incorporating both stress and strain controlled nucleation to investigate the roles of high strains and triaxiality on failure. [13] used the notched bar experiments to conduct a thorough assessment of the [51] model. Some of the other notable works using notched bars were carried out by

[3, 28, 124] and [59]. [19] employed a void growth model incorporating both material and morphological anisotropy supplemented with a void coalescence model towards predicting fracture in notched bars of low alloy steel. Model predictions were thoroughly compared to experimental ones [18] and accurate quantitative prediction of damage accumulation and crack initiation in notched bars without any adjustable parameters was demonstrated. Recently, [73] reported higher ductility in notched bars than in smooth bars of magnesium alloy AZ31 and this was attributed to a change of fracture mechanism from twinning induced fracture under uniaxial case to micro void coalescence under triaxial case.

In general, ductile failure may occur mainly in two modes; by micro void growth and coalescence or by instability [20, 105]. Failure by micro void coalescence consists of microscale localization happening in the ligament joining voids. This localization then leads to coalescence of voids and hence to predict ductile fracture quantitatively, modeling void coalescence is key. Initial models of void coalescence were either heuristic or empirical. Initial models assumed that coalescence occurred when a critical value of void growth ratio [24] or critical porosity [125] were attained. However, since these critical values were functions of stress state [104, 132], they do not represent material parameters by themselves. [21] revisited the problem of coalescence by internal necking resorting to a limit analysis approach on a rigid-plastic cylindrical cell of coaxial voids as first posed by [117] and derived the first analytical void coalescence model for isotropic materials. This model was then extended for remote shear loadings by [118] and then for plastically anisotropic matrix materials by [65].

An important ingredient to modeling void coalescence is to account for the evolution of microstructure prior to microscale localization. This involves accounting for the influence of anisotropies; initial and induced. Initial anisotropies pertain to

that existing in the undamaged material due to texture (referred to here as *plastic anisotropy*). Anisotropy can also be deformation induced; i.e via the evolution of void shape and orientation and this is refereed to as *morphological anisotropy*. Models aimed at tackling the effect of morphological anisotropies (which has prominent effect mainly in the low to moderate triaxiality regimes) were proposed initially by [46] and later by [84, 85, 95]. On the other hand, the effect of plastic anisotropy was found to persist at all values of triaxiality in the cell model calculations of [69] and this has significant implications in the evolution of microstructure in the pre-coalescence regime. [16, 66] developed models to incorporate the plastic anisotropy of the matrix material in addition to that of morphological anisotropy. However the above models conjectured that the combined effect can be obtained by superposition of individual ones. To mathematically model the strong coupling between plastic anisotropy and void shape effects, [67] developed an anisotropic model of void growth and coalescence in a porous elasto-plastic or viscoplastic continuum subjected to arbitrary large deformations. Very recently, this was extended to the case of general ellipsoid cavities in Hill matrix by [96].

[67] model takes explicit account of the material anisotropy due to texturing in structural materials and the initial or induced anisotropy due to void shape changes and rotation, thus allowing for greater accuracy in predicting the initiation and propagation of cracks. A closed form yield function, flow rule and evolution equations for the microstructural variables were developed for the effective material using an approach based on classical homogenization theory and limit-analysis. The analytical yield criterion was validated by developing a numerical method to derive rigorous upper bounds to the yield criterion for given microstructures using a large family of trial deformation fields in computational limit analysis [68]. The evolution equations for the microstructural variables were validated by comparison to direct finite-element

simulations of porous unit cells subjected to radial loading with constant stress triaxiality. Based on the unit cell results, heuristic extensions were proposed for the microstructure evolution equations to account for effects neglected in the analytical derivations so that the model provides accurate estimates of the damage evolution in structural analysis. This model was implemented in a finite element code by following a co-rotational formulation of the constitutive relations [77].

The goal of this study is to investigate the combined effects of void shape and matrix anisotropy on damage evolution to crack initiation in ductile materials. Focus is laid on ductile fracture through void growth and coalescence and not by macroscopic strain localization. Towards this, the [67] model, supplemented with the [21] void coalescence model is used to conduct three dimensional computational analyses of boundary value problems on notched bars.

4.2 Formulation

The Keralavarma Benzerga [67] constitutive model used here describes the elastoplastic deformation coupled with damage, as outlined in Chapter 2. These relations can also be applied to rate-dependent elasto-viscoplastic materials by using the analytical yield functions as plastic potentials, as for example done by Tvergaard and Needleman [125] for the Gurson model. Here, the constitutive relations are recalled for completeness. For further details, see Refs. [67, 77].

4.2.1 Keralavarma Benzerga void growth model

The deformation of the combined material, void and matrix, is captured by additive decomposition of the symmetric part of velocity gradient as done in other homogeneous materials and the hypoelastic law is employed for a finite strain formulation.

$$\mathbf{D} = \mathbf{D}^{\mathrm{e}} + \mathbf{D}^{\mathrm{p}} \tag{4.1}$$

where the elastic part is given by:

$$\mathbf{D}^{\mathrm{e}} = \mathbb{L}^{-1} : \overset{\triangledown}{\boldsymbol{\sigma}} \tag{4.2}$$

with $\mathbb{L}$ the isotropic tensor of elastic moduli and $\overset{\triangledown}{\boldsymbol{\sigma}}$ is the Jaumann stress rate defined by:

$$\overset{\triangledown}{\boldsymbol{\sigma}} = \dot{\boldsymbol{\sigma}} + \boldsymbol{\sigma}\boldsymbol{\Omega} - \boldsymbol{\Omega}\boldsymbol{\sigma}, \quad \boldsymbol{\Omega} = \frac{1}{2}(\boldsymbol{\nabla}\mathbf{v} - \boldsymbol{\nabla}\mathbf{v}^{T}), \tag{4.3}$$

where $\boldsymbol{\Omega}$ is the skew symmetric part of the velocity gradient $\boldsymbol{\nabla}\mathbf{v}$. The plastic part of $\mathbf{D}$ is given by normality to a yield surface $\mathcal{F}(\boldsymbol{\sigma}) = 0$

$$\mathbf{D}^{\mathrm{p}} = \Lambda \frac{\partial \mathcal{F}}{\partial \boldsymbol{\sigma}} \tag{4.4}$$

The Keralavarma Benzerga flow potential for a plastically anisotropic material of the Hill type is written as $\mathcal{F}(\boldsymbol{\sigma}) = 0$ with

$$\mathcal{F}_G(\boldsymbol{\sigma}) = C\frac{\sigma_{\mathrm{eq}}^2}{\bar{\sigma}^2} + 2q_{\mathrm{w}}(g+1)(g+f)\cosh\left(\kappa\frac{\boldsymbol{\sigma} : \mathbf{X}}{\bar{\sigma}}\right) - (g+1)^2 - q_{\mathrm{w}}^2(g+f)^2 \tag{4.5}$$

where σ_{eq} is an equivalent stress that could be based on advanced anisotropic plasticity in the absence of porosity. Here, yielding in the matrix is taken to obey Hill's criterion [55] and σ_{eq} is defined as:

$$\sigma_{\mathrm{eq}}^2 = \frac{3}{2}\boldsymbol{\sigma} : \mathbb{H} : \boldsymbol{\sigma} \tag{4.6}$$

where $\mathbb{H}$ is related to Hill's anisotropy tensor $\mathbb{p}$ through:

$$\mathbb{H} \equiv \mathbb{p} + \eta(\mathbf{X} \otimes \mathbf{Q} + \mathbf{Q} \otimes \mathbf{X}), \quad \mathbb{p} \equiv \mathbb{J} : \mathbb{h} : \mathbb{J}, \quad \mathbb{J} \equiv \mathbb{I} - \frac{1}{3}\mathbf{I} \otimes \mathbf{I} \tag{4.7}$$

Here $\mathbf{Q}$ is a constant tensor and $\mathbf{X}$ a void shape dependent tensor which are both transversely isotropic in the frame associated with the void are are given by:

$$\mathbf{Q} \equiv -\frac{1}{2}(\mathbf{n}_1 \otimes \mathbf{n}_1 + \mathbf{n}_2 \otimes \mathbf{n}_2) + \mathbf{n}_3 \otimes \mathbf{n}_3 \tag{4.8}$$

$$\mathbf{X} \equiv \alpha_2(\mathbf{n}_1 \otimes \mathbf{n}_1 + \mathbf{n}_2 \otimes \mathbf{n}_2) + (1 - 2\alpha_2)\mathbf{n}_3 \otimes \mathbf{n}_3 \tag{4.9}$$

where $\mathbf{n}_3$ is the void axis and $\mathbf{n}_1$ and $\mathbf{n}_2$ are orthogonal base vectors arbitrarily chosen in the transverse plane. Also, in 4.5, $\bar{\sigma}$ is the flow stress of the matrix material in a reference direction. In practice, $\bar{\sigma}$ is selected as the yield strength in one of the principal directions of orthotropy and the components of the anisotropy tensor $\mathbb{p}$ are scaled accordingly. In addition, f denotes the porosity and the criterion parameters C, g, κ in 4.5 as well as η in 4.7 and α_2 in 4.9 are functions of f and eventually the void aspect ratio w and the components of $\mathbb{p}$. In 4.7, $\mathbb{J}$ denotes the deviatoric projection operator and $\mathbb{h}$ denotes the anisotropy tensor in the deviatoric stress space and $\mathbb{I}$ and $\mathbf{I}$ are the fourth and second order identity tensors, respectively. Finally, q_{w} in in 4.5 is a void shape dependent factor that was determined by [46] to fit unit cell results:

$$q_{\mathrm{w}} = 1 + (q - 1)/\cosh S \tag{4.10}$$

where $q = 1.6$ is the value taken by q_{w} for a spherical void. The matrix is considered to obey the power-law strain-hardening law as follows.

$$\bar{\sigma} = \sigma_{\mathrm{S}}(1 + \bar{\epsilon}/\epsilon_0)^N \tag{4.11}$$

where $\bar{\sigma}$ and $\bar{\epsilon}$ are work-conjugate measures of matrix effective stress and plastic strain, respectively. $\bar{\epsilon}$ is defined as the cumulative plastic strain. The evolution of porosity is given by plastic incompressibility of the matrix as follows.

$$\dot{f} = (1-f)\Lambda\frac{\partial \mathcal{F}}{\partial \boldsymbol{\sigma}} \tag{4.12}$$

where Λ is the plastic multiplier. The evolution of the plastic strain of the matrix $\bar{\epsilon}$ is obtained considering the plastic work equivalence between the macroscopic homogeneous material and the microstructure (matrix); the work done on voids is zero.

$$\boldsymbol{\sigma} : \mathbf{D}^{\mathrm{p}} = (1-f)\bar{\sigma}\dot{\bar{\epsilon}} \tag{4.13}$$

The evolution of void shape is described as

$$\dot{S} = \frac{3}{2}D^{\mathrm{p}'}_{33} + 3\left[\frac{1-3\alpha_1}{f} + 3\alpha_2 - 1\right]D^{\mathrm{p}}_{\mathrm{m}} \tag{4.14}$$

where $'$ indicates the deviatoric component of a second order tensor. Note this equation includes an implicit dependence upon matrix anisotropy through the macroscopic rate of plastic deformation, $\mathbf{D}^{\mathrm{p}}$, which is derived from the yield criterion (4.5) by normality. Introducing the adjusting factor in [18, 45] into Eq.(4.14) leads to

$$\dot{S} = \mathbf{Q} : \left[h\mathbf{D}^{\mathrm{p}} + 3\left(\frac{1}{f}\mathbf{X}^{v} - \mathbf{X}\right)D^{\mathrm{p}}_{\mathrm{m}}\right] \tag{4.15}$$

where tensor $\mathbf{X}^{v}$ is defined similar to $\mathbf{X}$. The adjusting factor h is defined as follows.

$$h = 1 + h_{\mathrm{e}}h_{\mathrm{f}}h_{\mathcal{T}} \tag{4.16}$$

$$h_{\mathrm{e}}(e_1) = \frac{9}{2}\frac{\alpha_1 - \alpha_1^{\mathrm{Gar}}}{1 - 3\alpha_1}, \qquad \alpha_1^{\mathrm{Gar}} = \begin{cases} \dfrac{1}{3 - e_1^2} & \text{(p)} \\ \dfrac{1 - e_1^2}{3 - 2e_1^2} & \text{(o)} \end{cases} \tag{4.17}$$

$$h_{\mathrm{f}}(f) = (1 - \sqrt{f})^2 \tag{4.18}$$

$$h_{\mathcal{T}}(\mathcal{T}, \epsilon) = \begin{cases} 1 - \dfrac{\mathcal{T}^2 + \mathcal{T}^4}{9} & \text{for} \quad \epsilon = +1 \\ 1 - \dfrac{\mathcal{T}^2 + \mathcal{T}^4}{18} & \text{for} \quad \epsilon = -1 \end{cases}, \qquad \epsilon \equiv \mathrm{sgn}(\Sigma_{\mathrm{m}}\Sigma'_{33}) \tag{4.19}$$

$$\mathcal{T} = \frac{\Sigma_{kk}/3}{\sqrt{\frac{3}{2}\boldsymbol{\Sigma}' : \boldsymbol{\Sigma}'}} \tag{4.20}$$

where $\mathcal{T}$ represents stress triaxiality and e_1 is the eccentricity of the void. h_{e}, h_{f} and $h_{\mathcal{T}}$ correct the mismatch due to eccentricity, porosity and stress triaxiality, respectively, between unit cell simulation results and the model prediction.

The void orientation evolves following the macroscopic spin of the material and the local plastic distortion, which was derived by Kailasam and Ponte Castaneda [64] as follows

$$\boldsymbol{\Omega}^v = \boldsymbol{\Omega} - \mathbb{C} : \mathbf{D}^{\mathrm{p}} \tag{4.21}$$

where $\boldsymbol{\Omega}$ and $\boldsymbol{\Omega}^v$ represent the continuum and void spin tensors respectively. $\mathbb{C}$ is the fourth order spin concentration tensor, which is given by

$$\mathbb{C} = -(1 - f)\mathit{\Pi} : \mathbb{A}, \qquad \mathbb{A} = [\mathbb{I} - (1 - f)\mathbb{S}]^{-1} \tag{4.22}$$

where $\mathbb{A}$ is the strain concentration tensor and $\mathit{\Pi}$ and $\mathbb{S}$ are the Eshelby tensors [40] for a spheroidal inclusion in an incompressible linear matrix. Then, the evolution of the void orientation is obtained using the following kinematical relationship

$$\dot{\mathbf{e}}_3 = \boldsymbol{\omega} \cdot \mathbf{e}_3, \qquad \boldsymbol{\omega} = \boldsymbol{\Omega}^v + \boldsymbol{\Omega}^l \tag{4.23}$$

where $\mathbf{\Omega}^l$ is an antisymmetric tensor given by

$$\Omega^l_{12} = 0, \quad \Omega^l_{i3} = \frac{w^2+1}{w^2-1} D^v_{i3} \qquad (i = 1, 2, \quad w \neq 1) \tag{4.24}$$

$$\mathbf{D}^v = \mathbb{A} : \mathbf{D}^{\mathrm{p}} \tag{4.25}$$

Combining Eq.(4.21) and (4.23)-2 leads to

$$\boldsymbol{\omega} = \mathbf{\Omega} - \mathbb{C} : \mathbf{D}^{\mathrm{p}} + \frac{1}{2} \sum_{i \neq j,\, w_i \neq w_j} \frac{w_i^2 + w_j^2}{w_i^2 - w_j^2} (\mathbf{e}_i \otimes \mathbf{e}_j + \mathbf{e}_j \otimes \mathbf{e}_i) : \mathbb{A} : \mathbf{D}^{\mathrm{p}} \mathbf{e}_i \otimes \mathbf{e}_j \tag{4.26}$$

The plastic spin tensor is defined as $\mathbf{W}^{\mathrm{p}} = \mathbf{\Omega} - \boldsymbol{\omega}$. Utilizing Eq.(4.26), $\mathbf{W}^{\mathrm{p}}$ is written as follows.

$$\mathbf{W}^{\mathrm{p}} = \mathbb{C} : \mathbf{D}^{\mathrm{p}} - \frac{1}{2} \sum_{i \neq j,\, w_i \neq w_j} \frac{w_i^2 + w_j^2}{w_i^2 - w_j^2} (\mathbf{e}_i \otimes \mathbf{e}_j + \mathbf{e}_j \otimes \mathbf{e}_i) : \mathbb{A} : \mathbf{D}^{\mathrm{p}} \mathbf{e}_i \otimes \mathbf{e}_j \tag{4.27}$$

4.2.2 Benzerga Leblond void coalescence model

As explained in Chapter 2, the Benzerga Leblond flow potential for void coalescence used in this study is given by:

$$\begin{aligned} \mathcal{F}_C(\sigma, \chi, W) = \frac{|\sigma_{33}|}{\bar{\sigma}} - \frac{1}{\sqrt{3}} \Bigg[& 2 - \sqrt{1+3\chi^4} + \ln \frac{1+\sqrt{1+3\chi^4}}{3\chi^2} \\ & + \frac{\chi^3 - 3\chi + 2}{3\chi W} \Bigg] \\ & \equiv \frac{\sigma_{33}}{\bar{\sigma}} - \frac{\sigma_{33}^{\mathrm{coal}}}{\bar{\sigma}}(\chi, W) \end{aligned} \tag{4.28}$$

4.2.3 Finite element model

The following material property is used for the simulations in this study. $\sigma_S = 420$ MPa is the initial yield stress of the matrix material along $\mathbf{e}_S$. $N = 0.1$ is the hardening exponent and $\epsilon_0 = 0.002$ is a constant strain offset. Table.4.1 shows the parameters used for simulations. For the results shown here, the following materials are selected – isotropic, transversely isotropic material ib (representative of Aluminum alloys) which is weak in shear, transversely isotropic material iii (representative of Zirconium alloys) which is shear resistant and material AZ31(representative of Magnesium alloys) which is an anisotropic material. The isotropic, ib and iii are materials that have equal yield stresses in tension along the principal directions of orthotropy which leads to roughly similar values of effective yield stresses. This can be beneficial while comparing different materials. In order to explore the more general cases of materials commonly observed experimentally [18], an instance of transversely isotropic material which has unequal yield stress in tension along principal directions of orthotropy is also considered. All Hill coefficients for the isotropic matrix has a value of 1. The transverse isotropy of Mat ib is characterized by the equal values of the hill coefficients h_{TS} and h_{SL} with the direction of transverse isotropy along $\mathbf{e}_S$. For the anisotropic AZ31, all the hill coefficients have different values. In all the results shown here, the void axis is initially aligned along the $\mathbf{e}_S$ or $\mathbf{e}_L$direction.

The typical range of porosities existing in real materials are between 10^{-4} and 10^{-2}. Although, nowadays, the effective initial porosities existing in various processed alloys can be less than 10^{-4}, for the simulations conducted in this study an initial porosity of $f_0 = 10^{-4}$ is assumed and is thought to be representative of actual porosities existing in typical structural materials.

The values of initial void shapes explored are from $w_0 = 1/6$, 1 and 6, respectively

corresponding to oblate, spherical and prolate voids. These are representative of void shapes existing in real materials with the void shape as oblate when they grow from cleavage cracks nucleated by particle cracking; represented as spherical in the case of equiaxed voids, and prolate when they are originate from inclusions previously elongated by a manufacturing process. As an example, prolate voids with aspect ratios even greater than 20 can be found in rolled steel plates with MnS inclusions, see ref: [19]. Another basis for selecting the above values of initial aspect ratios are for enabling relevant comparisons with the existing cell model results whenever possible, which utilized the same values [103].

3D calculations in ABAQUS using the UMAT was carried out on notched bars denoted by RNζ with ζ representing the notch severity parameter as explained in Chapter 3. The mesh (Fig.4.1) consists of the 20-noded quadratic quadrilateral elements (C3D20R) with reduced integration (2 x 2 x 2 integration points). The boundary conditions are specified as follows. Due to symmetries (loading along the principal axes of orthotropy with voids aligned along the same), only 1/8 of the notched bar is modeled. Symmetry boundary conditions are applied on the lateral surfaces. A uniform displacement U is prescribed on the top surface in the Y direction and the Y displacement of the centre surface of the bar is arrested. Initially flat elements are used in the regions where necking is expected since the elements therein would undergo significant elongation in the direction of major axial stress.

Table 4.1: Parameters used in this study

Calculation	h_{L}	h_{T}	h_{S}	h_{TS}	h_{SL}	h_{LT}	h		f_0	w_0
Isotropic	1.000	1.000	1.000	1.000	1.000	1.000	2.000		0.0001	1/6, 1, 6
Mat ib (trans.iso)	1.000	1.000	1.000	2.333	2.333	1.000	1.757		0.0001	1/6, 1, 6
Mat ie (trans.iso)	2.500	2.500	0.250	1.375	1.375	1.000	1.757		0.0001	1/6, 1, 6
Mat iii (trans.iso)	1.000	1.000	1.000	0.5	0.5	1.000	2.366		0.0001	1/6, 1, 6
AZ31(anisotropic)	1.170	0.920	0.400	1.780	1.600	1.030	2.090		0.0001	1/6, 1, 6

The simulations presented here enable to probe the spatial variation of various microstructural variables as well as their evolution at local integration points of interests. In the following sections, results in terms of both the spatial as well as the local evolutions are presented. All the calculations presented here are stopped when the first instance of void coalescence is met as predicted by the [21] coalescence criterion. The onset of void coalescence may not be regarded as an adequate criterion for failure, and the numerical simulation of fracture warrants the use of models representing complete loss of stress carrying capacity. In the case of notched bars, the strain to failure at complete loss of stress carrying capacity ε_f can be substantially different from that at initiation of void coalescence ε_c [20]. However, this methodology of quantifying initiation of fracture enables the comparison of various model materials as well as revealing qualitative trends and couplings between effects of different microstructural variables.

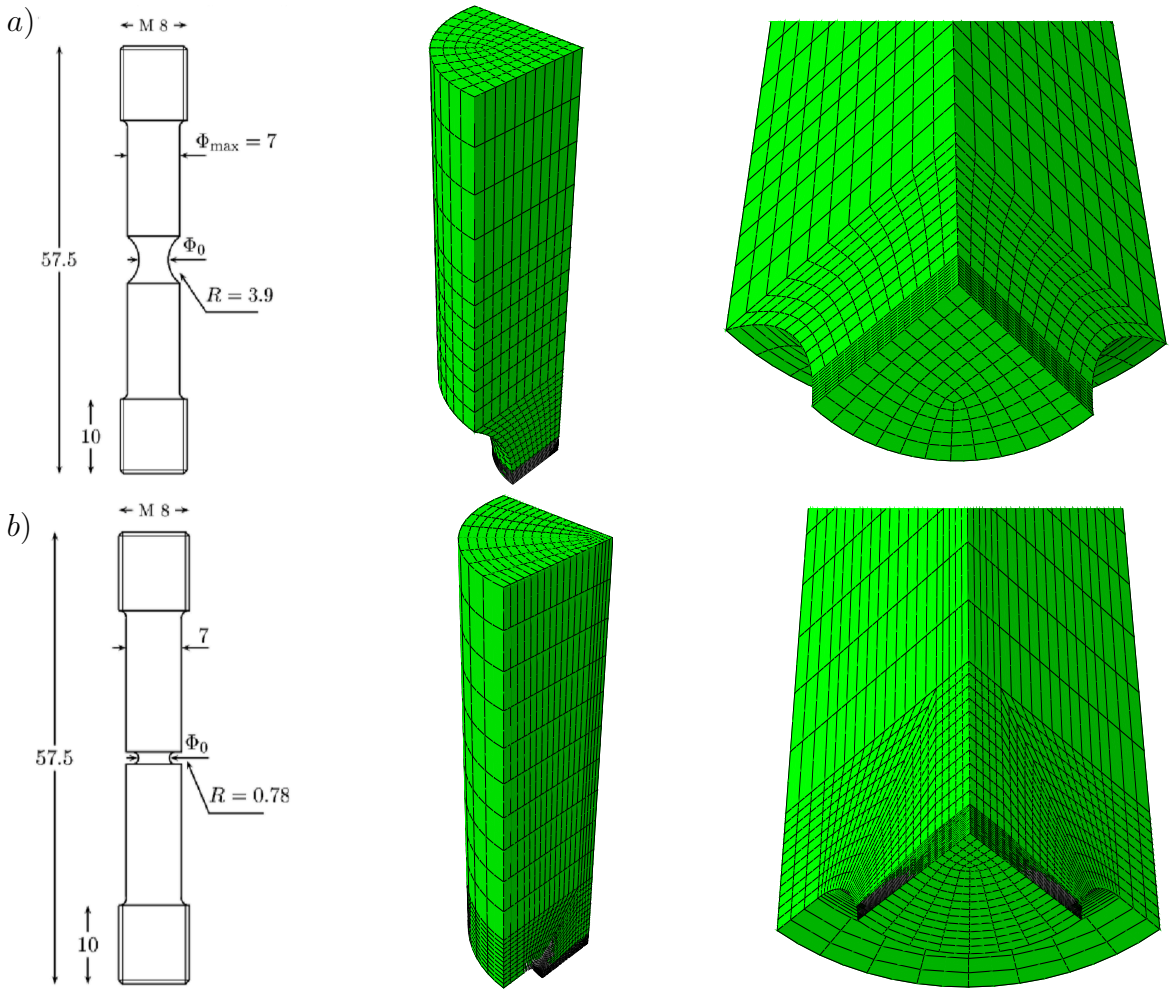

Figure 4.1: Geometries and mesh used for the simulations. a) RN10 and b) RN2

4.3 Results

4.3.1 Code verification

In this section the predictive capability of the KB model is assessed against experimental data. Towards this, simulation results using the KB model are compared with the experimental data reported in [18, 19] for the case of round notched steel bars. Assessment will be carried out at the macroscopic (load versus diameter re-

duction) as well as the microscopic level (critical porosity at failure initiation).

[18]conducted experiments on notched bars made of a low alloy steel which displayed anisotropy in plastic as well as fracture properties. The material parameters were identified following the standard procedure as outlined in Chapter 2. In the steel samples, two major void nucleation sites were identified: elongated MnS inclusions and equiaxed alumina particles. Quantitative metallography was used to identify the initial volume fraction, void aspect ratios and void spacings. The following material properties are used for the simulations: $\sigma_{\mathrm{S}} = 381.23$ MPa is the initial yield stress of the matrix material along $\mathbf{e}_{\mathrm{S}}$, $N = 0.107$ is the hardening exponent and $\epsilon_0 = 0.002$ is a constant strain offset. These values were obtained from the best fit to the experimental uniaxial stress strain curve obtained in tension along the L direction. The initial porosities which was approximated to be of the order of the volume fraction of active nucleation sites. The values reported in [18] as $f_0 = 0.0004$ and $f_0 = 0.00075$ were used in this comparison. Initial aspect ratios of $S_0 = 2.35$ and $S_0 = 3$ were used to model voids nucleated from MnS inclusions and $S_0 = 0$ was used to represent those nucleated from equiaxed particles. For further details see refs.[18, 19].

Three dimensional calculation were carried out using the notched bar geometries corresponding to those tested in [18]. The mesh shown in (Fig.4.1) was used and consists of the 20-noded quadratic quadrilateral elements (C3D20R) with reduced integration (2 x 2 x 2 integration points). The boundary conditions are specified as follows. Due to symmetries and since the loading is kept along the principal axes for all analyses, only 1/8 of the notched bars is modeled. Symmetry boundary conditions are applied on the lateral surfaces and displacement boundary conditions applied on the top and bottom faces.

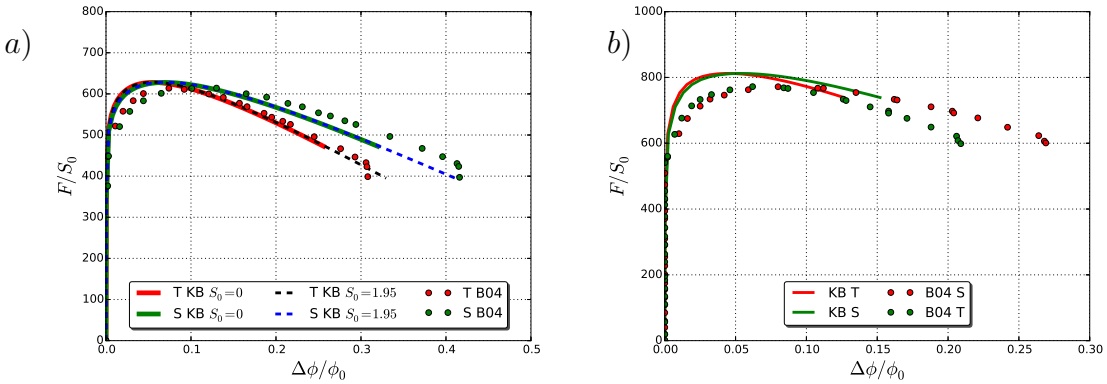

Figure 4.2: Experimental and calculated load vs. diameter reduction for the case of L loading with $f_0 = 0.00075$, $S_0 = 0$ and 3 and $\lambda_0 = 1.5$ for a) RN10 specimen b) RN2 specimen (Fig. 8a, Fig. 8b from [18])

The load versus diameter reduction for the case of L loading of the RN10 and RN2 specimens are shown in Fig. 4.2. It can be seen from Fig. 4.2a that in the case of RN10 bar, the load displacement predicted by the KB model accurately match that of the experimental data for the initial microstructural variables $f_0 = 0.00075$, $S_0 = 1.95$ and $\lambda_0 = 1.5$. For this case, the strength level and the failure initiation are well captured both in L and S directions. For the initial microstructural values of $f_0 = 0.00075$, $S_0 = 0$ and $\lambda_0 = 1.5$, although the maximum load and the softening due to porosity is accurately predicted, early failure initiation is predicted by the KB. It can also be observed that the anisotropy in these steels as evidenced from the load displacement curves from experiments are also accurately captured by the KB model. Note that the values of $S_0 = 1.95$ corresponds to an intermediate value of aspect ratio when both the population of voids (elongated as well as equiaxed) actively contribute to the coalescence process. Using the Benzerga Besson (BB) model from [19] it was hypothesized that at low triaxiality only the equiaxed voids were contributing

to the coalescence process on the basis of BB model quantitatively matching the experimental values when $S_0 = 0$ was used and since it was over predicting ductility for $S_0 = 1.95$. For the RN2 case it is observed that for the initial microstructural values of $f_0 = 0.00075$, $S_0 = 0$ and $\lambda_0 = 1.5$, the KB model accurately captures the maximum strength and softening. However the in this case the KB model predicts early failure. Due to lack of simulation data for the case of $S_0 = 1.95$ in RN2, it is not shown. However starting with an initially elongated void would have clearly resulted in higher ductility and would have better matched the experiments. According to the agreement observed between experiments and simulation using KB model, it is concluded that under low triaxiality conditions, under L loading, both the elongated as well as equaled voids contribute equally to the coalescence process.

In the case of T loading (note here that the void axis was assumed to be along L in simulations) as shown in Fig. 4.3 it was seen that the starting with initial aspect ratio corresponding to elongated voids resulted in better quantitative predictions at the low triaxiality regime. In the case of RN2 specimen, it can be seen that the KB model captures the failure points along L and S from experiments quite accurately with elongated voids and also the trend in anisotropy, although it over predicts strength. Hence in the T loading using the KB model it is concluded that the elongated voids are the major contributing players to the coalescence process.

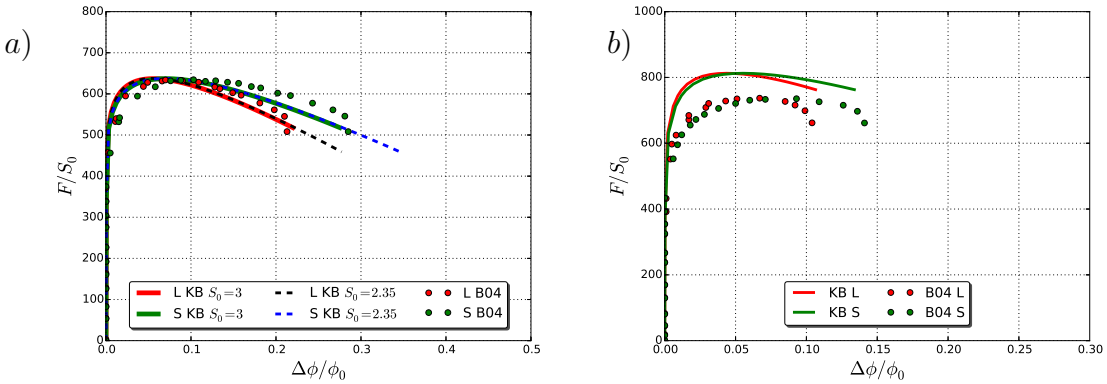

Figure 4.3: Experimental and calculated load vs. diameter reduction for the case of T loading with $f_0 = 0.00075$, $S_0 = 3$ and $\lambda_0 = 1$ for a) RN10 specimen (Fig 10a from [18]) b) RN2 specimen (Fig 10b from [18])

In passing, a comparison between the KB model and the Benzerga Besson (BB) model are shown in Fig. 4.4 for the case of T loading. The load displacement, triaxiality as well as the evolution of microstructural variables predicted by both the models are shown. The KB model predicts higher evolution of triaxiality, ligament parameter, and porosity with the evolution of void aspect ratio reducing at a higher rate, compared to the BB model. Although the ductility is over predicted by the BB model compared to KB model, the porosity at void coalescence (critical porosity) predicted by both the models agree equal.

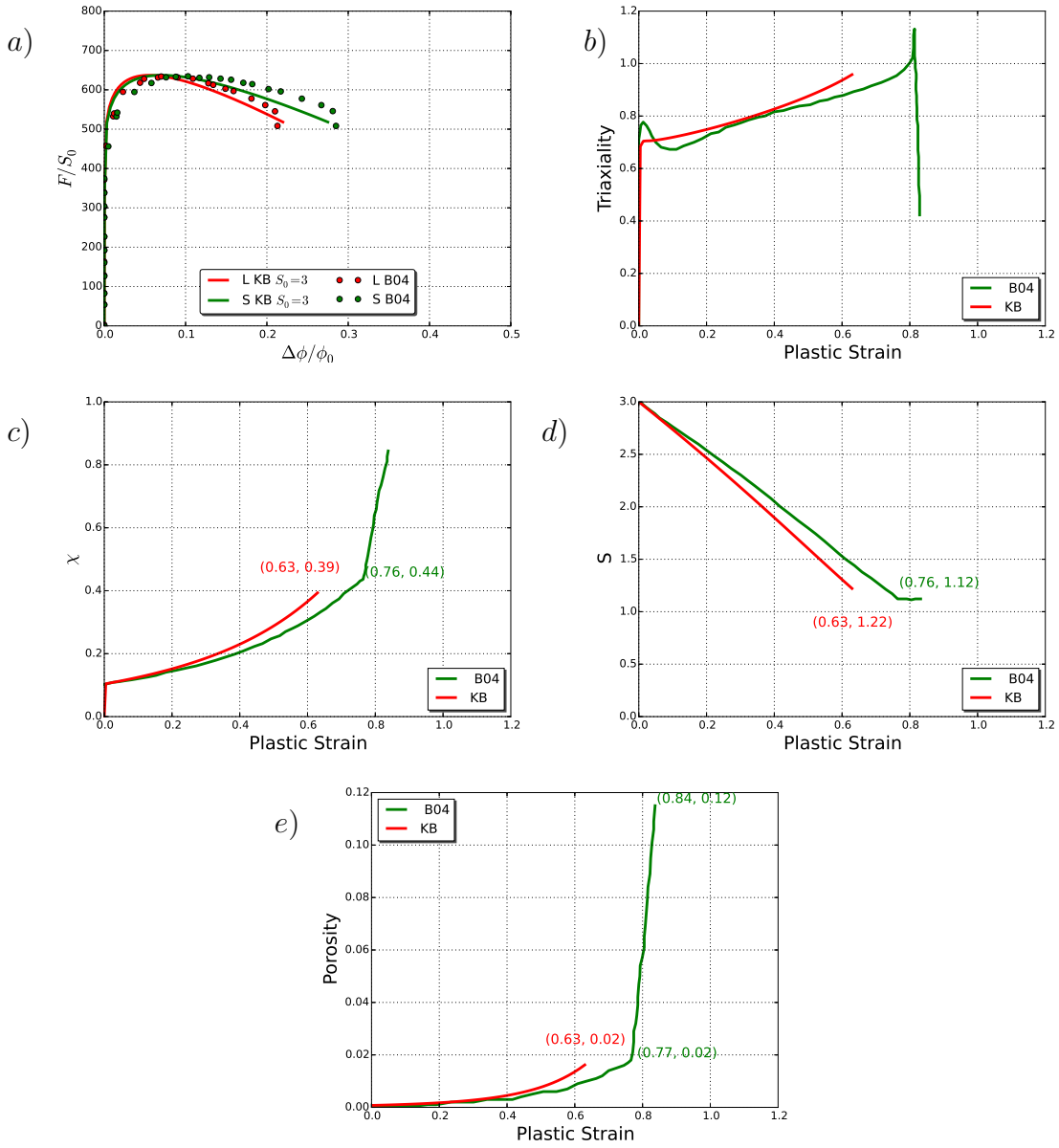

Figure 4.4: Force vs. diameter reduction for the case of T loading for RN10 specimen with $f_0 = 0.00075$, $S_0 = 3$ and $\lambda_0 = 1$ (Fig 10a, 5a, 5b, 5c, 5d from [18])

The measured and predicted strains to failure initiation from the experiments and the simulations using KB model in the L and T directions are compared in

Fig. 4.5a. At higher triaxiality we get lower failure strains as expected. In the RN10 case, in the L loading, the predicted strain to failure are well within the experimental range and for the T loading they are nearby. However in the RN2 case, although the strain to failure in L loading is under predicted by the KB model, that in the T loading is captured well. From Fig. 4.5b, it can be observed that the predicted critical porosities are between the measured maximum and average values from the experiments.

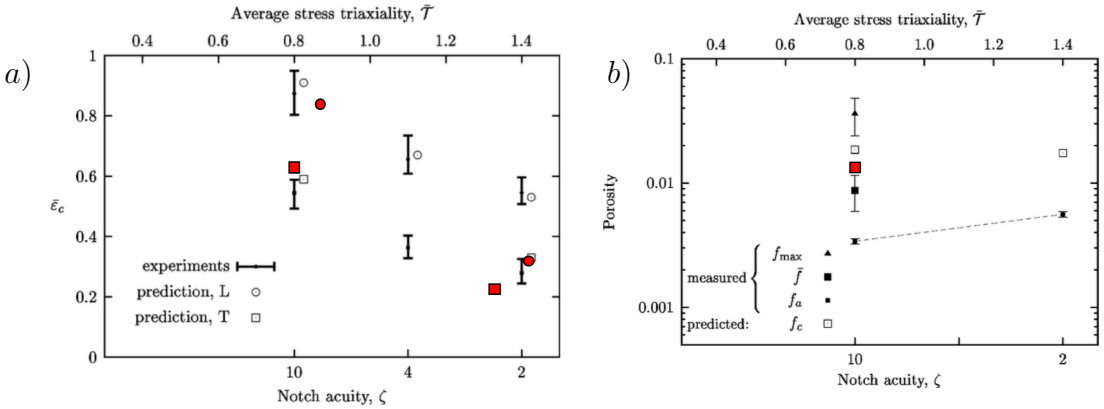

Figure 4.5: Comparison between measured and predicted average strains to failure initiation in notched bars for two loading orientations (Fig 11b from [18]): the red data points corresponds to those obtained by KB model b) Measured and predicted porosities for T orientation at incipient coalescence in notched bars (Fig 12b from [18])

The important aspect to note is that all the above simulations are presented without using any fitting parameters and the simulations are done for the initial values of microstructural parameters extracted form the actual experimental samples. This clearly demonstrates the capability of the KB model to capture the quantitative as well as qualitative aspects of damage and fracture initiation in modeling anisotropic

materials. With the confidence gained from this comparison, we proceed to present results from further simulations conducted using material parameters representative of a variety of real materials and for equivalent microstructural parameters existing in them.

4.3.2 Isotropic matrix material

Fig. 4.6 shows the contours of plastic strain and porosity for the case of RN10 and RN2 specimens for the isotropic matrix material, compared at the same macroscopic applied displacement. It can be seen from Fig. 4.6a and Fig. 4.6b that in the case of RN10 specimen, plastic strain is concentrated at the centre of the specimen whereas in the case of RN2 specimen, the plastic strain is accumulated near the outer circumference of the bar. The distribution of porosity follows the same pattern with more porosity development happening at the centre of the specimen. From Fig. 4.6a and Fig. 4.6c, it can be seen that the value of maximum plastic strain occurring in the RN2 bar is higher than that of RN10 specimen. In the case of porosity, there is one order difference in the maximum values with the porosity evolution in RN2 being much greater than that of RN10. Even for this isotropic material case, the tendency of plastic strain to concentrate along the circumference in the case of RN2 specimen implies that the geometry of the structure or specifically the severity of the notch plays a crucial role not only in controlling the stress/strain state, but also their spatial distribution.

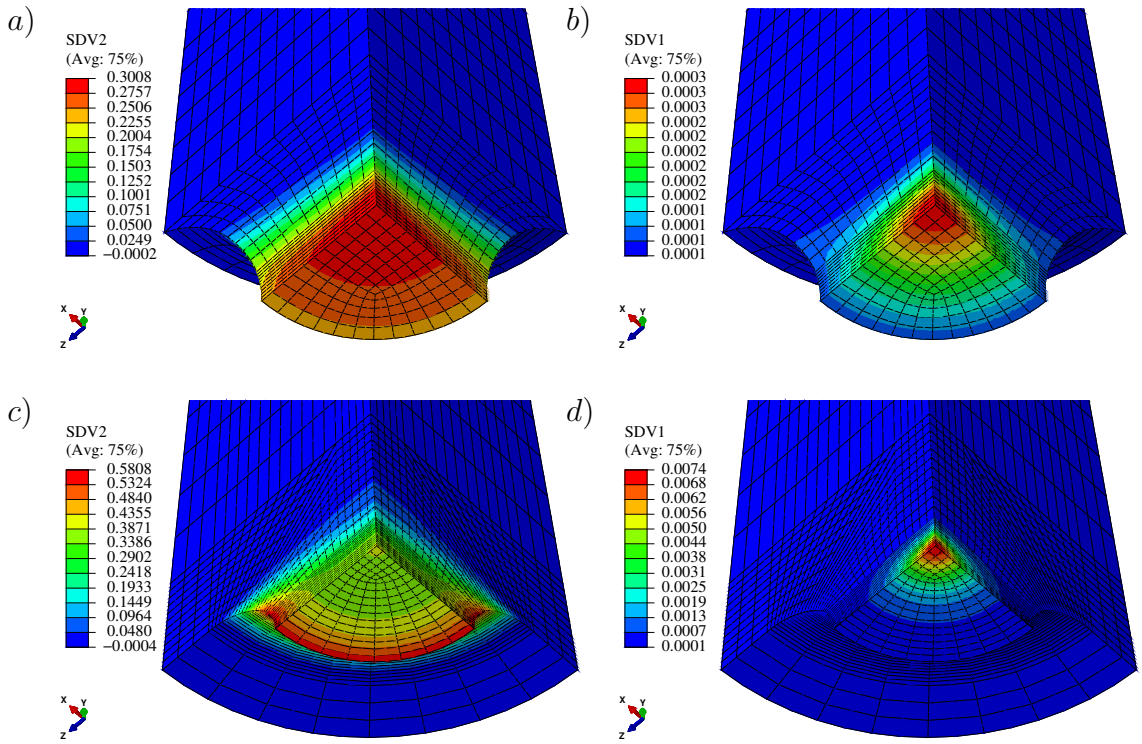

Figure 4.6: For isotropic matrix material with initial void aspect ratio $w_0 = 1$ and initial porosity $f_0 = 10^{-4}$ a) Contours of plastic strain for RN10 specimen b) Contours for porosity for RN10 specimen c) Contours of plastic strain for RN2 specimen d) Contours for porosity for RN2 specimen

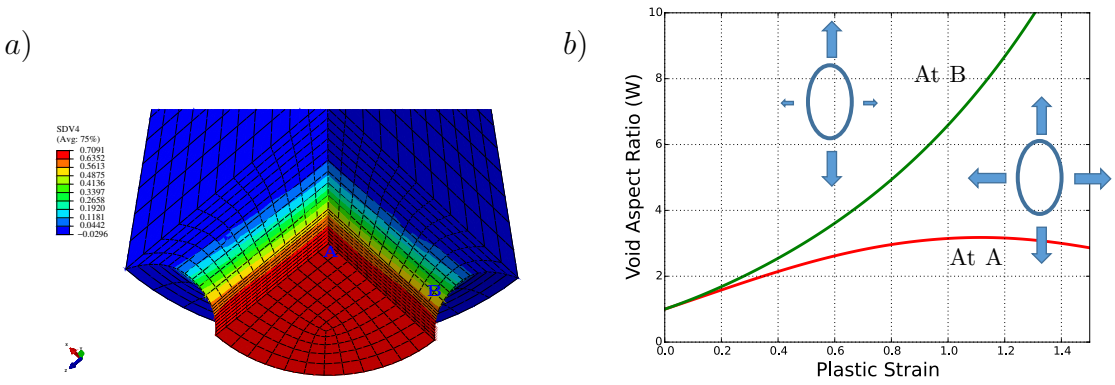

Figure 4.7: a) Contours of void aspect ratio b) Evolution of void aspect ratio vs plastic strain at two locations

The contours of void aspect ratio, evolution of the void aspect ratio at two locations for the isotropic material is shown in Fig. 4.7. It can be observed even for the isotropic case, the void aspect ratio at two locations (one at the centre of the specimen and another near the surface) evolve in entirely different way. For the element A, which is at the center of the specimen, although the void aspect ratio increases initially after some plastic strain has set in, it reaches a maximum and starts to reduce. This is due to the fact that although evolution at both the sites are governed by the plastic strain, at the centre of the specimen, the effect of increased triaxiality sets in and governs the evolution eventually. Increased triaxiality results in lateral growth of the void, thereby reducing the aspect ratio. On the other hand, in the case of element B, the void aspect ratio keeps on increasing as increase in triaxiality near the surface is lower compared to that at centre.

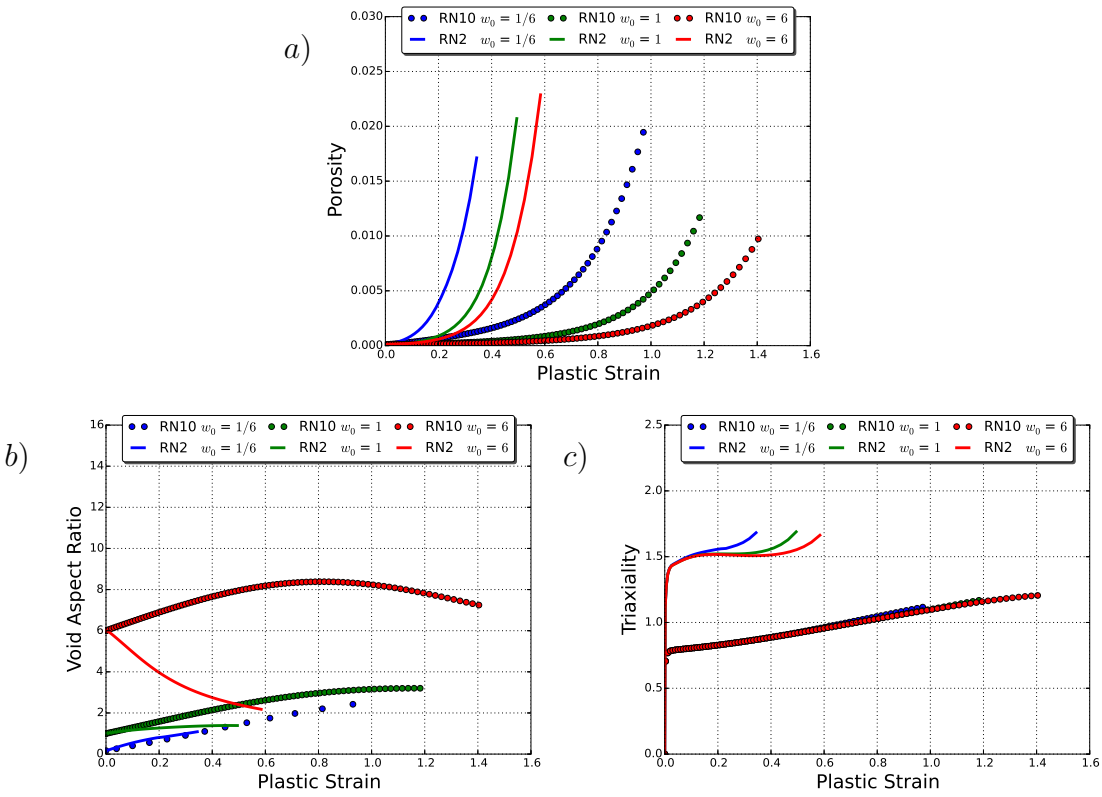

Figure 4.8: Isotropic material loaded along the S direction a) Porosity b) Aspect ratio c) Triaxiality, all extracted at the centre for the cases of $w_0 = 1/6$, 1 and 6 and for RN10 and RN2 samples

In Fig. 4.8, the evolution of porosity, void shape and triaxiality at the centre of the RN10 and RN2 notched bars for the isotropic material for three initial void aspect ratios, namely w_0 =1/6, 1 and 6 are shown. It can be observed that the evolution of porosity is higher for the case of RN2 specimen which is a direct consequence of higher triaxiality existing in the RN2 bars. Among the three void aspect ratios considered, the case with initial prolate void ($w_0 = 6$) displays the most ductile response and the initially oblate void ($w_0 = 1/6$) is the least ductile. It can also be observed that the porosity evolves most in the case of the oblate void in the RN10 case and least in the

case of prolate void. However in the RN2 case, the prolate void favors more porosity evolution and the oblate void leads to lesser evolution of porosity. This is due to the effect of triaxiality overtaking the void shape effects at higher triaxiality existing in the RN2 specimen. In the case of void aspect ratio evolution, it can be observed that for the initially oblate and spherical case, the void aspect ratio keeps on increasing with the plastic strain. However for the prolate case, for the RN10 case initially the void aspect ratio increases and then the effect of increased triaxiality causes the void to expand laterally effecting a reduction in aspect ratio. For the RN2 case, the effect of triaxiality overtakes that of the plastic strain early in the evolution thereby causing reduction of aspect ratio very early on. From the evolution of porosity it can also be seen that in the RN10 specimen, higher value of critical porosities (porosity at void coalescence) occur for the case of oblate voids. However the reverse trend can be seen in the case of RN2 specimen.

4.3.3 Transversely isotropic materials

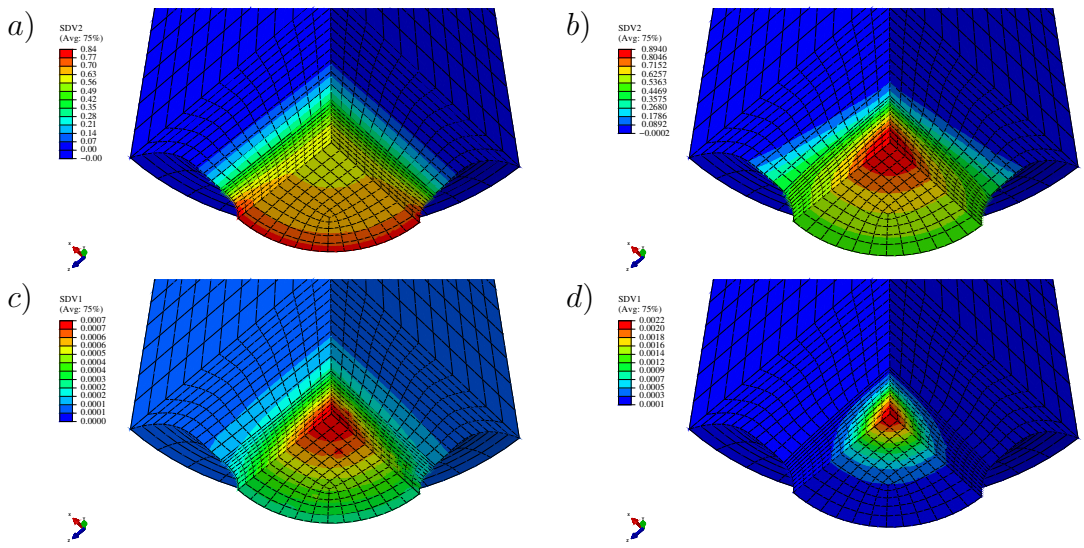

Figure 4.9: For the RN10 specimen when loaded along S (Y) direction with initial void aspect ratio $w_0 = 1$ and initial porosity $f_0 = 10^{-4}$ a) Contours of plastic strain for transversely isotropic material ib b) Contours of plastic strain for transversely isotropic material iii c) Contours of porosity for transversely isotropic material ib d) Contours of porosity for transversely isotropic material iii

The contours of plastic strain and porosity for the transversely isotropic materials ib and material iii are compared in Fig. 4.9. For these materials, the axis of transverse isotropy is the e_S axis and the applied loading is in along the S direction. For this configuration, the response is isotropic as expected in the L (X) and T (Z) directions for both the materials. In the case of material ib, the accumulation of plastic strain is concentrated along the circumference of the specimen (Fig. 4.9a), whereas in the case of material iii, it is concentrated at the centre (Fig. 4.9b). For the RN10 geometry, the plastic strain at the centre of the specimen is lower for the material ib than that

of material iii. The porosity distribution in both materials follows the same pattern. However, it can be seen that value of porosity developed in material iii is much higher than that in material ib. This can be explained by comparing the value of triaxiality existing at the centre of the specimen for the case of both materials as seen from Fig. 4.27a. A higher value of triaxiality and plastic strain existing in in RN10 bar of material iii is the reason behind the higher porosity developed in RN10 bar of material iii when compared to that of material ib which produces lower plastic strain and lower triaxiality at the centre of the specimen.

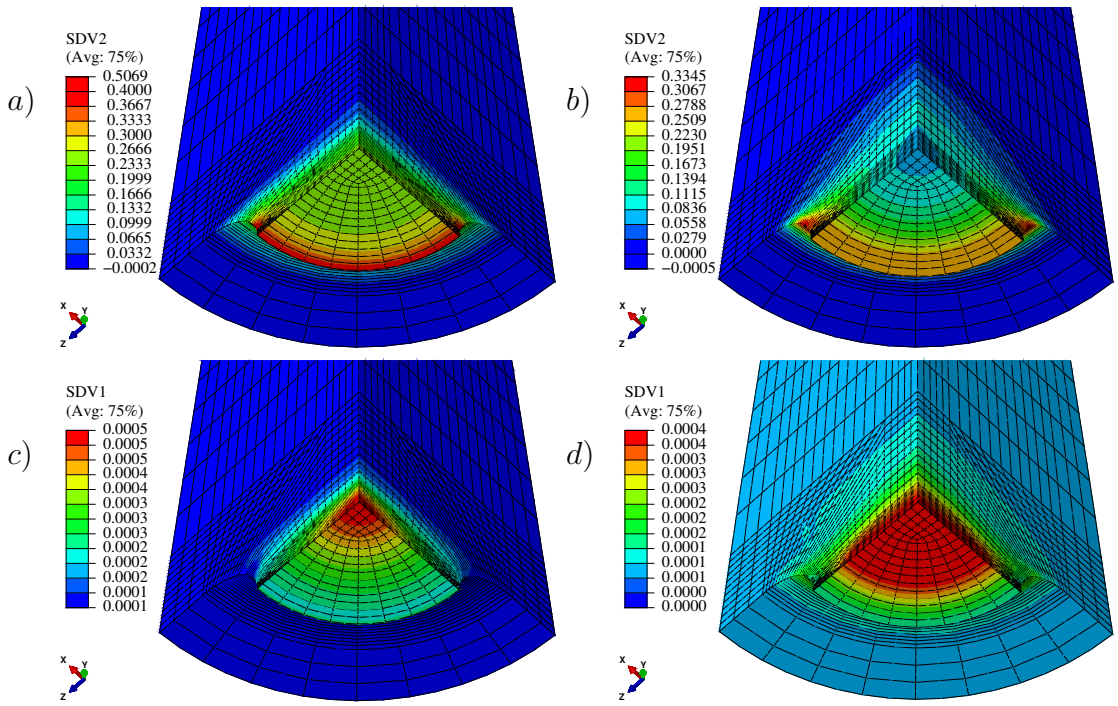

Figure 4.10: For the RN2 specimen when loaded along S (Y) direction with initial void aspect ratio $w_0 = 1$ and initial porosity $f_0 = 10^{-4}$ a) Contours of plastic strain for transversely isotropic material ib b) Contours of plastic strain for transversely isotropic material iii c) Contours of porosity for transversely isotropic material ib d) Contours of porosity for transversely isotropic material iii

In the RN2 specimen of material ib, the accumulation of plastic strain is concentrated along the circumference of the specimen (Fig. 4.10a), whereas in the RN2 specimen of material iii, although it tends to concentrated at the circumference (Fig. 4.10b), the location of maximum accumulation of plastic strain occurs away from the notch root, along the near the free surface. The spatial distribution of plastic strain in RN2 specimen of material iii is thus different from that of RN10 specimen of the same material as can be seen by comparing Fig. 4.9b and Fig. 4.10b. The porosity distribution in both materials follows the same pattern and the value of porosity developed in material iii and material ib are comparable even though the triaxiality existing at the centre of RN2 specimen of material iii is much higher than that of material ib (Fig. 4.27b). However, in addition to triaxiality, the development of porosity is influenced by the amount of plastic strain also. It can be observed from Fig. 4.10a and Fig. 4.10b that the amount of plastic strain existing at the centre of the RN2 specimen of material iii is much lower than that of material ib and this counteracts the increased triaxiality value existing at the centre of RN2 specimen (Fig. 4.27b) of material iii.

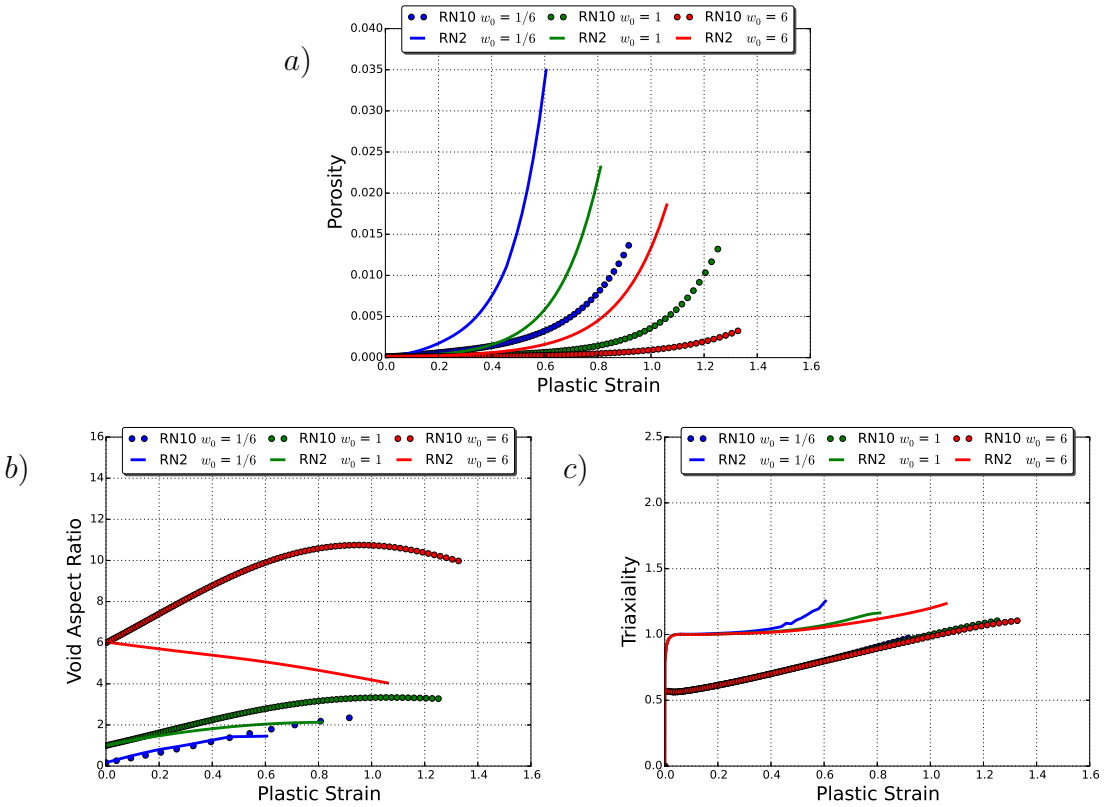

Figure 4.11: Material ib loaded along the S direction a) Porosity b) Aspect ratio c) Triaxiality, all extracted at the centre for the cases of w_0 =1/6, 1, 6 for RN10 and RN2 samples.

In Fig.4.11, the evolution of porosity, void shape and triaxiality at the centre of the RN10 and RN2 notched bars for the material ib for three initial void aspect ratios, namely w_0 =1/6, 1 and 6 are shown. The evolution of porosity in this material follows similar trends as the case of isotropic material. However, one interesting aspect to note in this case is that for this material the prolate void shapes results in higher ductilities with RN2 specimen, even higher than with initially oblate voids in RN10 specimen. This is due to the comparatively lower triaxiality existing in this material for the RN10 and RN2 case, compared to the isotropic material and material iii.

This will be explored further in section 4.3.8.

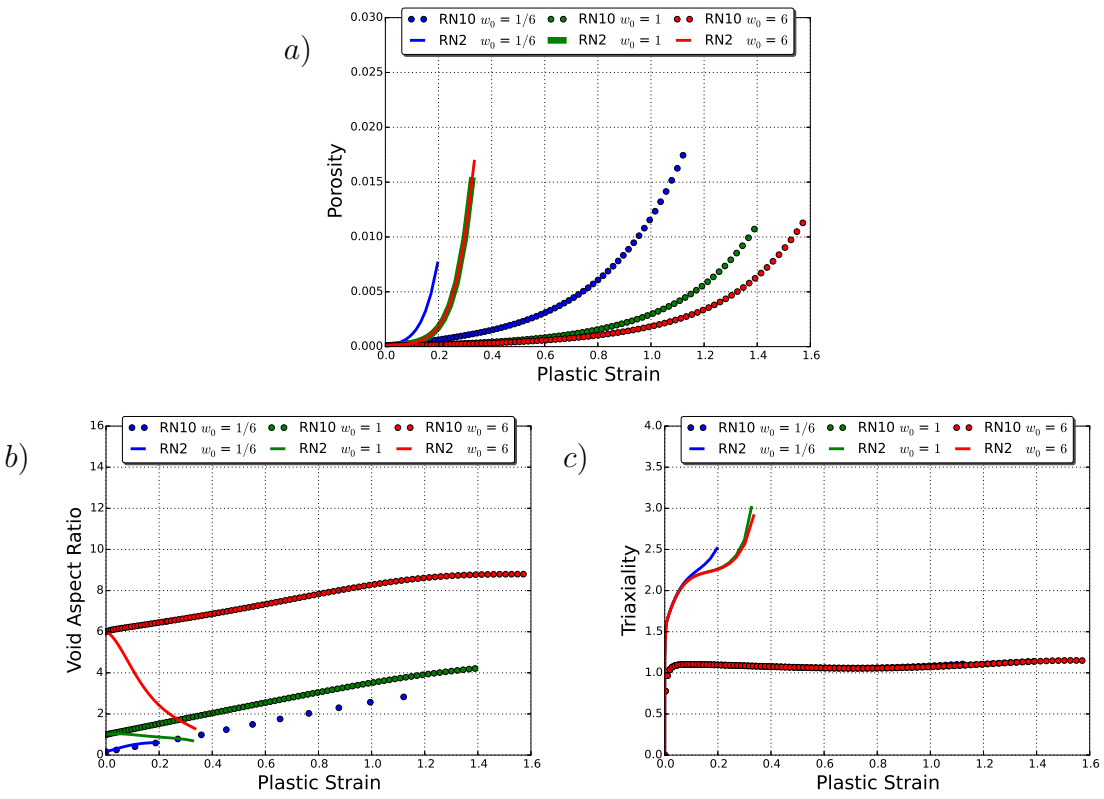

Figure 4.12: Material iii loaded along the S direction a) Porosity b) Aspect ratio c) Triaxiality, all extracted at the centre for the cases of w_0 =1/6, 1 and 6 and for RN10 and RN2 samples

Fig.4.12 shows the evolution of porosity, void shape and triaxiality at the centre of the RN10 and RN2 notched bars for the material iii for three initial void aspect ratios, namely w_0 =1/6, 1 and 6. Although the trends are similar to the case of isotropic material, some significant observations can be made. Triaxiality at the centre is higher than that of the isotropic case for material iii, for both the RN10 and RN2 (much higher) cases. Also, in the case of material iii, the triaxiality is

constant throughout the history of loading whereas in the case of isotropic material (Fig.4.8c), it is linearly varying. Compared to the isotropic case, material iii seems to be more ductile for all the cases of void aspect ratio considered in the RN10 specimen, with higher porosity evolution when the initial shape of the voids are oblate. In [67], using cell model studies, it was shown that in general for materials with $h_{TS} \leq 0.5$, the void shape effects are nullified at high triaxialities. Although this can be observed from Fig.4.12a for the RN2 specimen for initially prolate and spherical voids, this is not the case in general as seen from the porosity evolution in RN2 specimen with oblate voids (w_0 =1/6).

4.3.4 Anisotropic material

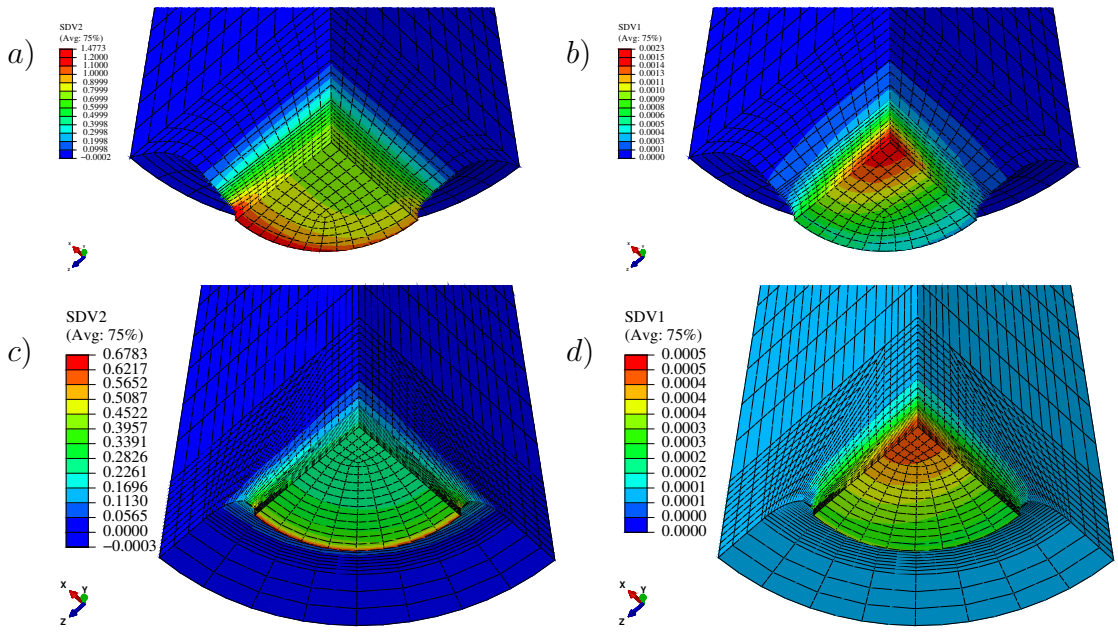

Figure 4.13: For anisotropic material AZ31 when loaded along the S direction a) Contours of plastic strain for RN10 specimen b) Contours of porosity for RN10 specimen c) Contours of plastic strain for RN2 specimen d) Contours of porosity for RN2 specimen

In Fig.4.13, the contours of plastic strain and porosity for the case of RN10 and RN2 specimen of anisotropic material AZ31 are compared. In both cases, the anisotropy in damage evolution is clear by the comparison of porosity and plastic strain contours. In both these geometries, the porosity and plastic strain are accumulated more towards the T (Z) direction when loaded along the S direction. This can be explained on the basis of values of Hill coefficients and geometry. AZ31 has higher shear Hill coefficients when compared to the isotropic case. Similar to plastic strain contours of material ib which also has higher shear Hill coefficients than the isotropic case, the higher shear Hill coefficients of this material contributes to the accumulation of plastic strain near the circumference for the RN10 geometry. In addition, for this material, the h_L and h_T coefficients also contribute in deciding the direction of plastic strain accumulation. The values of h_L and h_T are 1.17 and 0.9 respectively for this material (Table. 5.1). A lower value of principal Hill coefficient implies that the material is stronger in that direction. As a result, the resistance of the material to deformation along that direction will be higher which causes the higher stresses to develop along that direction. This causes the plastic strain to accumulate near the circumference and along the T direction.

4.3.5 Void shape effect at different porosity levels

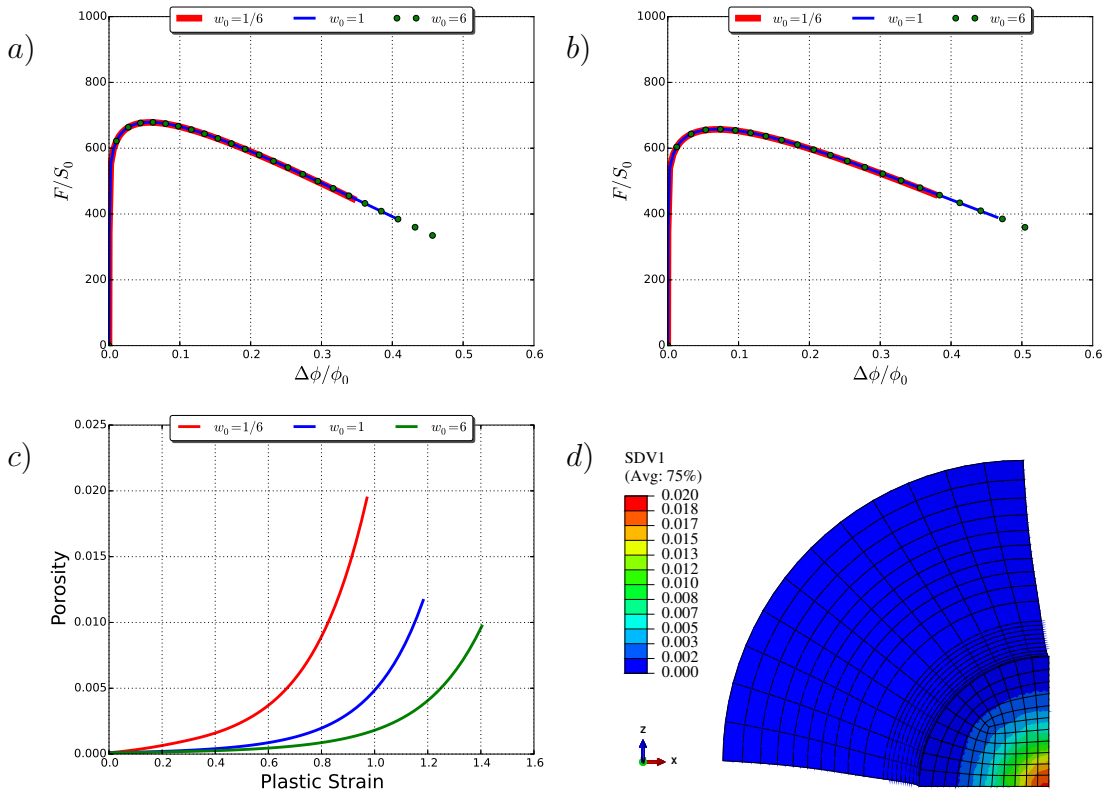

Figure 4.14: Load versus diameter reduction for RN10 samples with $f_0 = 10^{-4}$ for initial void shapes of $w_0 = 1/6$, 1 and 6 a) Isotropic material loaded along S b) Transversely isotropic material ib loaded along L c) Evolution of porosity for the isotropic case d) Contour of porosity for the isotropic case with initially oblate voids

The load versus diameter reduction for isotropic material and transversely isotropic material for an initial porosity of $f_0 = 10^{-4}$ for three different initial aspect ratios are shown in Fig. 4.14a and Fig. 4.14b respectively. Fig. 4.14c and Fig. 4.14d are the corresponding evolution of porosity and void shape with plastic strain, extracted at the centre of the notched bar where first instance of void coalescence was reported.

It can be seen that the macroscopic effect of void shape is limited to that dictating ductility but not strength for both materials. The initially prolate voids results in higher ductility that the oblate ones and this is due to the porosity evolving at a higher rate in the case of oblate voids at the local level (and thus finally dictating ductility), keeping in agreement with the classical cell model studies of [103]. However, if you observe the macroscopic contours of porosity for the case initially oblate voids, it can be observed that the rapid increase of porosity is limited to the area very near to the centre of the notched bar and in the remaining areas the evolution of porosity is not considerable so as to affect the global softening, even in the case of initially oblate voids. This explains why the macroscopic response is not affected in by initial void shape although the ductility is, for a low initial porosity. Similar is the response in the case of RN2 specimens, and for for different materials and along different loading orientation although they are not shown here for brevity.

In Fig. 4.15a, the load versus diameter reduction for an isotropic material for the case of $f_0 = 10^{-2}$ for three different void shapes are given. It can be see that at high porosity, for the case of oblate void, the void shape starts to have an effect on strength also, in addition to ductility. For the spherical as well as prolate void, again the macroscopic effect of void shape is negligible. This behavior in the case of oblate void is due to macroscopic softening induced by the steep rise of porosity starting with the very high initial porosity in the oblate case compared to the spherical and prolate void shapes as seen from Fig. 4.15b and Fig. 4.15c. This shows that even if we start with an initially low porosity, after significant growth has taken place, the effect of initial void shape also may come into play in determining the strength. In any case, ductility is always affected by the initial void shape.

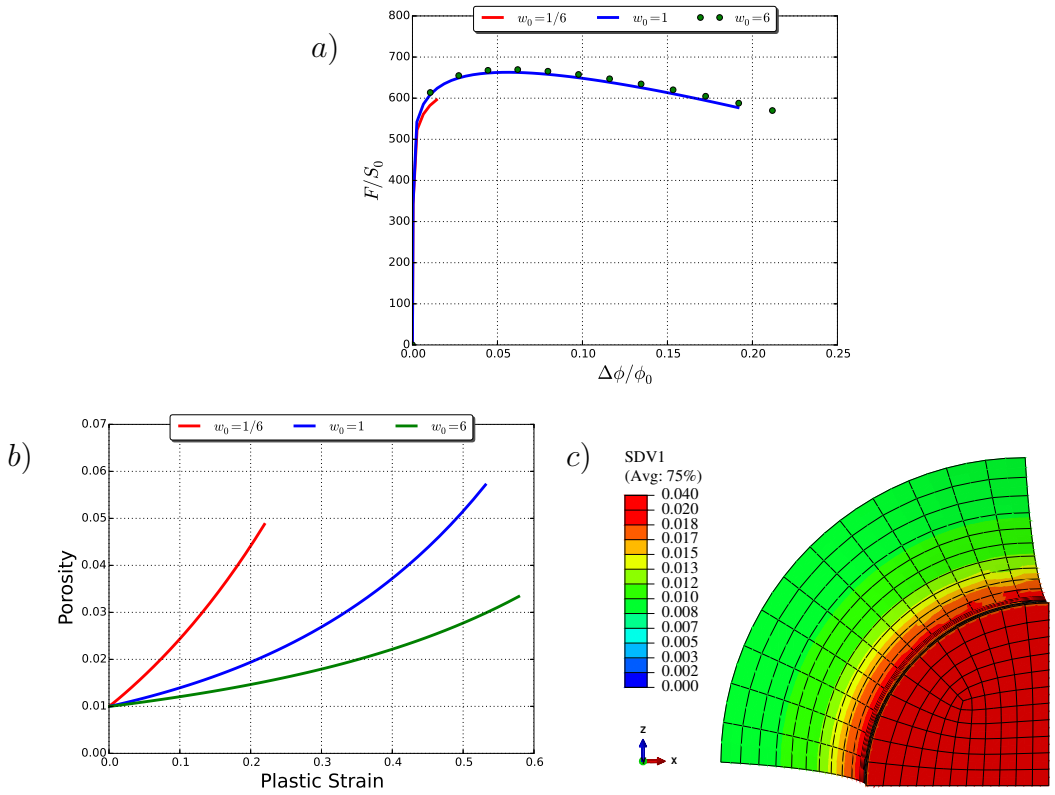

Figure 4.15: Load versus diameter reduction for isotropic RN10 specimen when the major load direction is along the S with $f_0 = 10^{-2}$ a) For $w_0 = 1/6$, 1, 6 b) Porosity evolution at centre d) Contour of porosity for the isotropic case with initially oblate voids

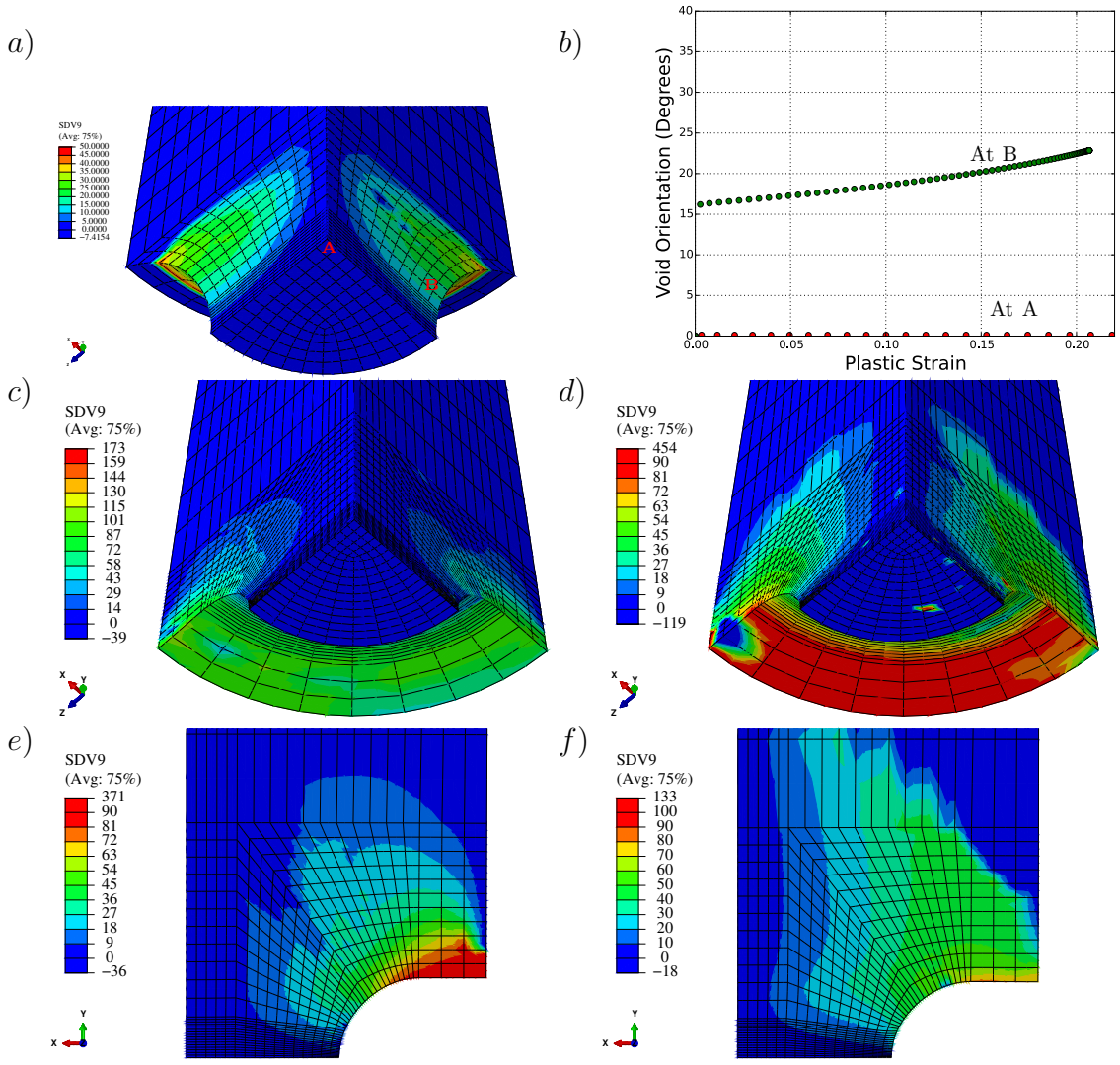

Figure 4.16: For initial void aspect ratio $w_0 = 1$ and initial porosity $f_0 = 10^{-4}$ and initially void orientation along the direction of loading a) Void axis rotation for isotropic RN10 geometry loaded along S b) Evolution of void orientation at two locations for the case of an isotropic RN10 specimen, loaded along the S direction. Void axis rotation for RN2 bar of c) Material iii when loaded along S d) Material ib when loaded along L e) Material iii when loaded along L f) Material ib when loaded along S

4.3.6 Rotation of void axis

Fig.4.16 shows the contours of void orientation its evolution for the case of RN10 and RN2 specimen. In all the cases presented above, the voids were initially aligned along the loading direction. Fig.4.16a and Fig.4.16b show the case of RN10 specimen of isotropic material loaded along the S (Y). The contours of void axis rotation are also isotropic with higher rotations near the surface of the specimen. At the centre of the specimen, the rotation of the void axis is zero as expected. But for an element B near the surface angle of rotation is observed to be in the range of 0-5 degrees. But these are not the highest values of rotations of void axis. In fact from the contour plot of void axis rotation, considerable rotation of even 45 degrees can be observed at some locations which are near the circumference of the specimen. Fig.4.16c shows the case of RN2 bar of material iii when loaded along the S direction. In this geometry, significant void rotations near the free surface of the specimen can be observed. Similar is the case in RN2 bars of material ib loaded along the L direction. Fig.4.16d and Fig.4.16e shows alternate views of of RN2 geometry with the former showing contours for material iii in L loading and latter showing contours for material ib for S loading. It can be seen that near the free surface of RN2 bar rotation of void axis closely follows the curvature of the surface with voids initially along the Y axis getting aligned to X axis with almost rotations of near 90 degrees. The void axes in this case tends to align along the free surface. Thus in both the RN10 and RN2 geometries, there can be significant void axis rotation taking place,especially near the free surface even if the remote loading does not contain any applied shear stress. These are in agreement with the rotations of voids reported experimentally in [17]. In the case of shear stress dominated loadings, the effect of this void axis rotations might be much more significant.

4.3.7 Comparison of loading orientations

In this section the effect of loading along the different directions of orthotropy of the matrix material is presented for the transversely isotropic and anisotropic materials. When the axis of material orthotropy LTS are aligned with the global axes (XYZ axes of Abaqus), depending upon the alignment we can have loading along L, T or S direction. Here two loading directions are focused. The first one is termed as S loading where the S direction is aligned with the global Y axis (major load direction). In this case the L is aligned along X and T is along Z. In the case of second loading which is termed as the L loading, L is along Y, S is along X and T is along Z.

4.3.7.1 Effect of loading on the macroscopic response

The macroscopic response of various materials are presented which showcases the comparison of ductility and strength of the materials at the low triaxiality and high triaxiality cases with respect to the isotropic case.

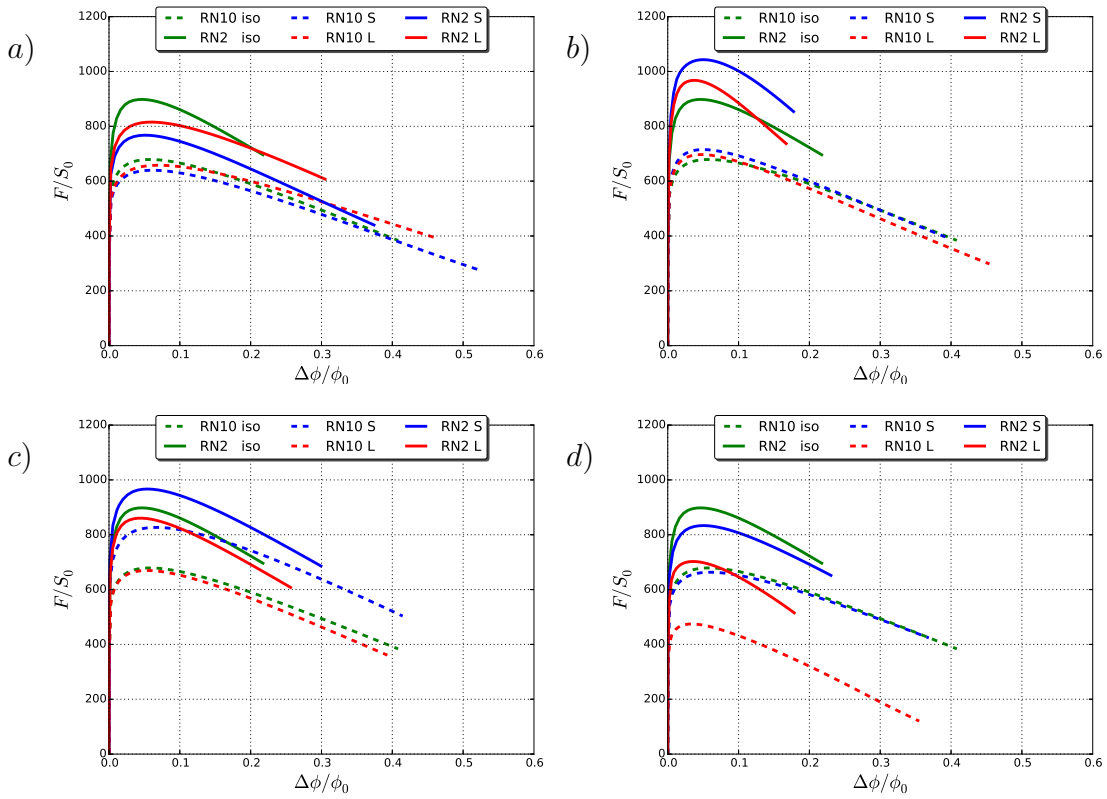

Figure 4.17: Load versus diameter reduction for RN10 and RN2 samples when the major load direction is along the S and L direction of loading for initial void shape of $w_0 = 1$ a) Material ib b) Material iii c) Material AZ31 d) Material ie. Reference isotropic case is also shown in each plot

In Fig.4.17, the load versus diameter reduction when the RN10 and RN2 notched specimen are loaded along the S and L directions are plotted for the transversely isotropic materials ib, iii, ib3 and the anisotropic material AZ31. For comparison the isotropic response is also given. The common trend in all the plots being the response in RN2 being stronger as expected with the difference more pronounced in the case of material iii. In the case of material ib, the response is almost similar in the RN10 specimen whereas in RN2 specimen which has higher triaxiality, the S

direction has a softer response compared to the L direction, with both being softer than the isotropic response. However in material iii, reverse trend is displayed at high triaxiality specimen with the S showing a stronger response compared to the L direction and both the responses happen to be stronger than the isotropic one. In materials AZ31 and ie, the difference between the S and L direction remains comparable between the low triaxiality and high triaxiality cases. For the RN10 geometry, which has lower triaxiality, all the materials considered except for material ie, displays ductility greater than or equal to that of the isotropic case when loaded along S and L direction. This points to the beneficial effect of certain kinds of anisotropy towards increasing the ductility of the material as investigated and confirmed by [10]. Material iii displays higher ductility in the case of S loading and in the case of material ib, it is the L direction which is more ductile. This in itself is interesting since the only difference between these two materials are in the shear hill coefficients which basically captures the behavior of a particular material when loaded in shear.

For the high triaxiality case, however, the trend is the same in the case of material iii, with both directions of loading resulting in higher ductility than the isotropic case; however in material ib, in this case, both the L as well as the S direction shows reduced ductility than the isotropic case. This in itself points to the complex interplay between the effect of anisotropy and triaxiality affecting the local as well as global evolution of micro structural parameters for the cases considered. However although it is beneficial to observe these behaviors, one thing to be kept in mind while interpreting these responses is the different evolution of triaxiality in each material under each direction of loading as can be observed from Fig.4.21d, Fig.4.18d and Fig.4.24d.

4.3.7.2 Effect of loading orientation for transversely isotropic materials

In Fig. 4.18, the evolution of microstructural variables at the centre of the notched bars are compared in for the S and L directions of loading for RN10 and RN2 specimens for initially spherical void shapes for the case of material ib. For comparison, the response for the isotropic material is also given. The corresponding macroscopic contours for the porosity and plastic strain in the case of RN10 specimen are given in Fig. 4.19.

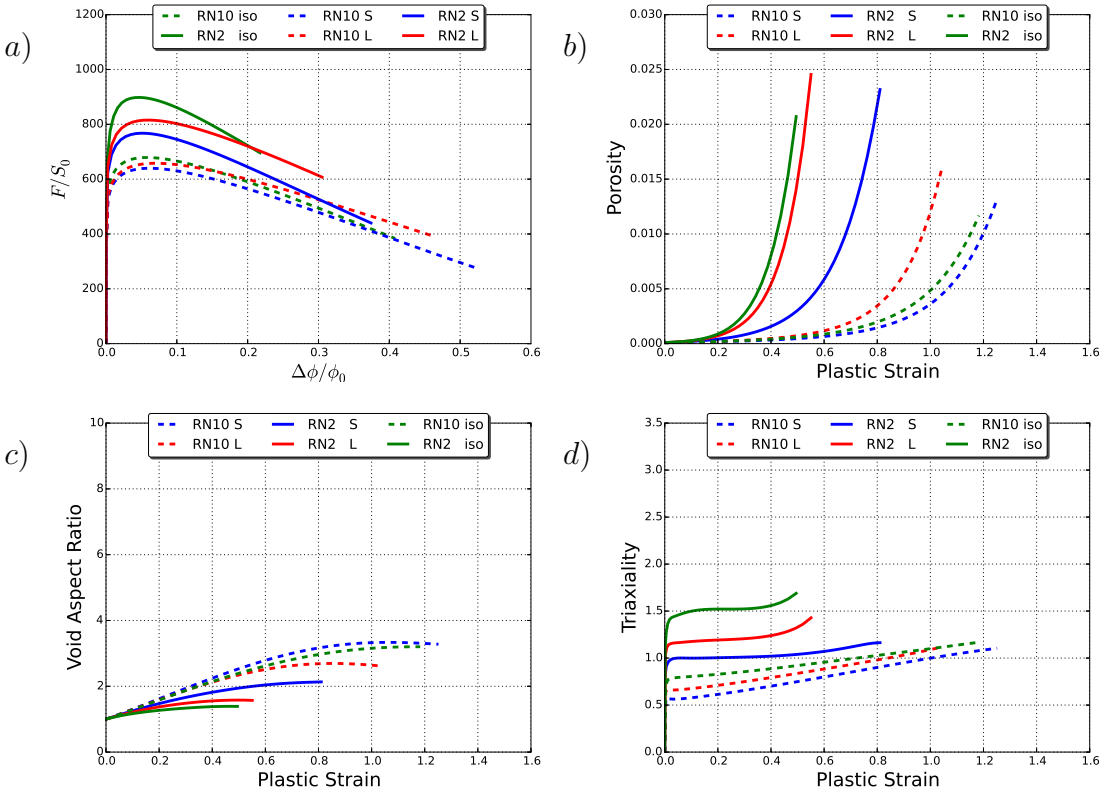

Figure 4.18: For RN10 samples of material ib when the major load direction is along the S and L direction of loading for initial $w_0 = 1$ a) Load versus diameter reduction b) Porosity c) Void aspect ratio d) Triaxiality

In both the S and the L loading for all the calculation reported here, coalescence was first reported at the centre of the notched bar. It can be observed from Fig. 4.18a that the material ib is more ductile when loaded along the S direction, which is its axis of transverse isotropy for the RN10 as well as the RN2 geometry. The ductility difference between the S and the L direction remains almost the same for both the geometries. If the evolution of porosity at the centre of the bars is is examined, the L loading results in higher growth of porosity which can explain its lesser ductility in the case of L, when compared to the S loading where the porosity evolution is at a lesser rate. This holds true for the RN2 specimen also. Since in both directions of loading, the sum $4h_S + h_L + h_T$ and $4h_L + h_T + h_S$, is equal to 6, the equivalent stress existing in both the materials in the S and L direction of loading are the same (see Chapter 2) and it is the mean stress which is different in the materials as evidenced from the different evolution of triaxialities in Fig. 4.18d. In L loading, the triaxiality existing at the centre is higher thereby making the voids grow faster compared the S loading, thereby resulting in a reduced ductility. The evolution of void shape in this material is comparable in the S and L loading case for the RN10 and RN2 cases as shown in Fig. 4.18c.

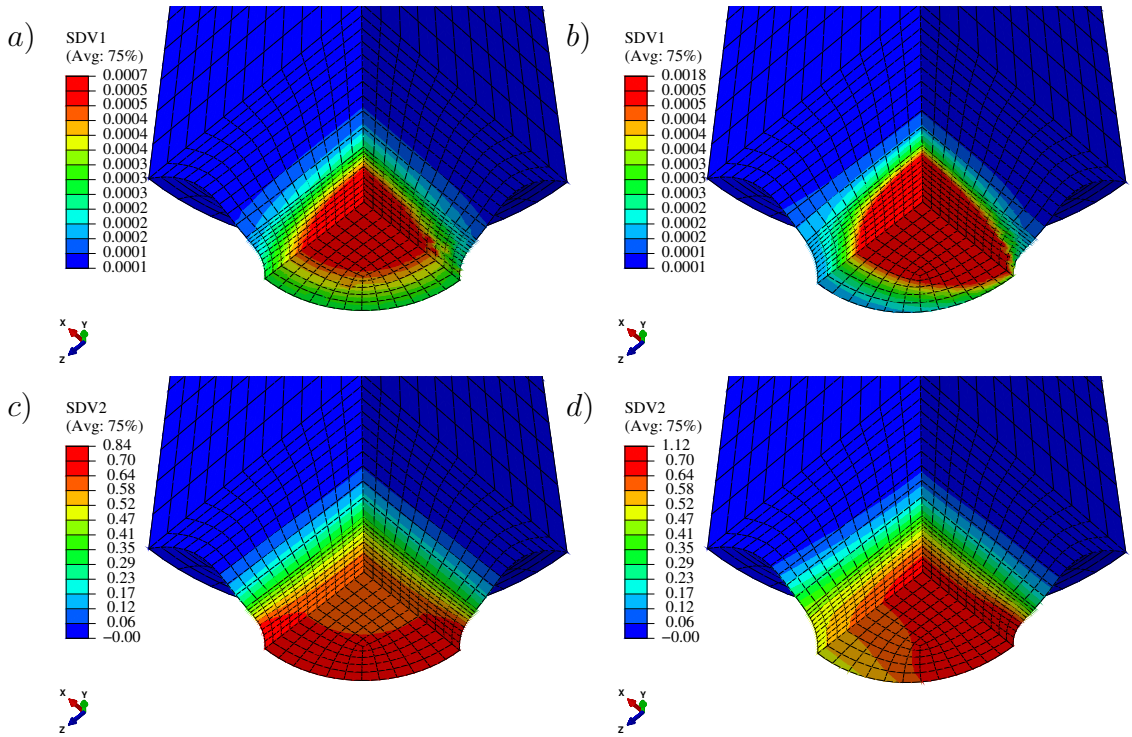

Figure 4.19: For RN10 samples of material ib for initial $w_0 = 1$, contours of a) Porosity for S loading b) Porosity for L loading c) Plastic strain for S loading d) Plastic strain for L loading

If the macroscopic contours of porosity and plastic strain are examined (Fig. 4.19), one can see that in the S loading which is the loading along transverse isotropy, the porosity and plastic strain contours are isotropic with respect to the S axis (Y axis). However in the case of L loading, the plastic strain is concentrated along the S direction with higher porosity evolution along that direction. Also it can be noticed that although higher porosity exists spatially in S loading, ductility is dictated by the local evolution of porosity (resulting in coalescence) which is higher in the L loading as seen from Fig. 4.18b. In addition to this, it can be seen from Fig. 4.19c and Fig. 4.19d that the accumulated plastic strain is higher at the centre in the case

of L loading contributing to its reduced ductility. In the RN2 case also similar trends can be observed from Fig. 4.19a and Fig. 4.19c. However the direction of porosity evolution changes from S direction in RN10 specimen to T direction in RN2 specimen when loaded along L, as can be seen by comparing Fig. 4.19b and Fig. 4.20b.

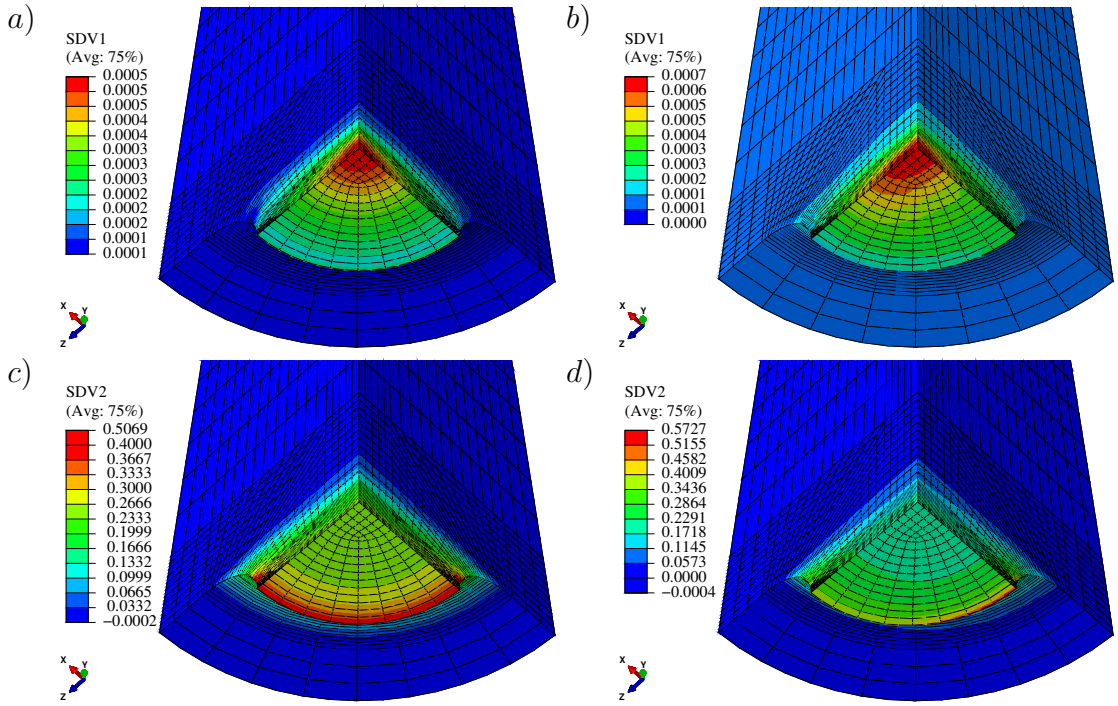

Figure 4.20: For RN2 samples of material ib for initial $w_0 = 1$, contours of a) Porosity for S loading b) Porosity for L loading c) Plastic strain for S loading d) Plastic strain for L loading

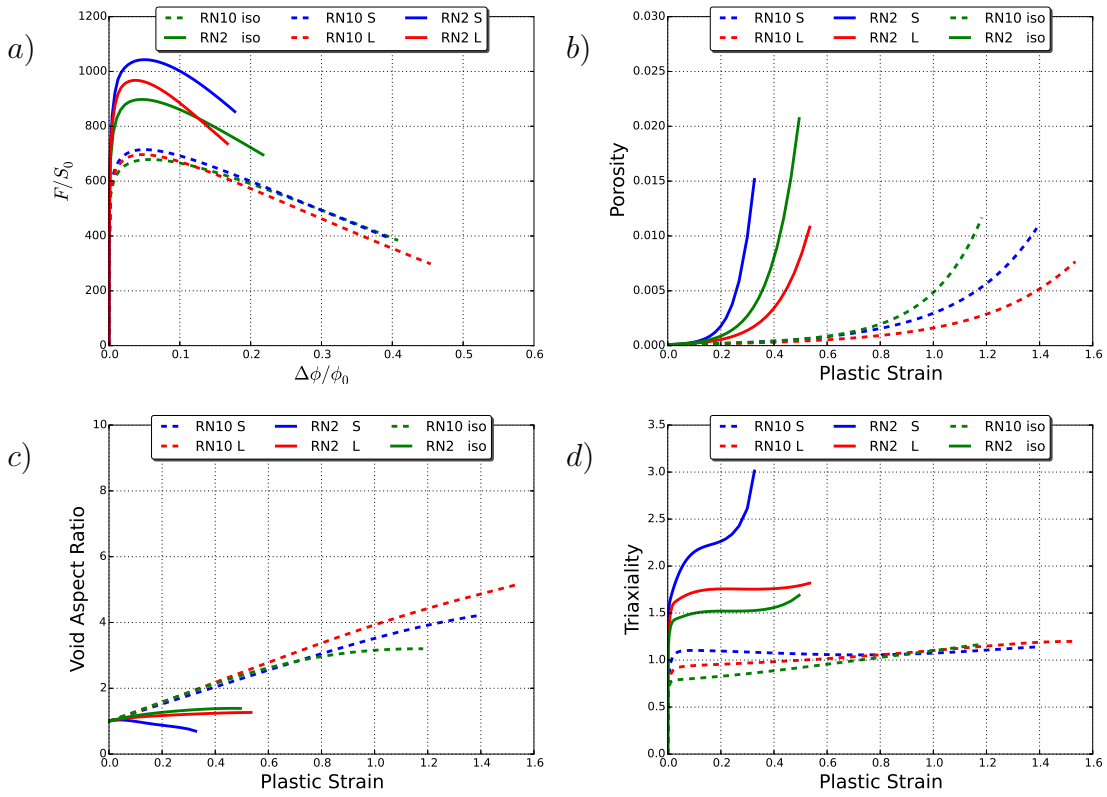

Figure 4.21: For RN10 samples of material iii when the major load direction is along the S and L direction of loading for initial $w_0 = 1$ a) Load versus diameter reduction b) Porosity c) Void aspect ratio d) Triaxiality

In the case of material iii, in the RN10 geometry, loading along the L direction resulted in higher ductility than the isotropic case, with the isotropic and S loading case having similar ductility values. However in the RN2 specimen, the influence of high triaxiality drives the material ductility in both the S and L directions of loading comparatively lower than the isotropic case. Most interesting is the evolution of triaxiality in this material (Fig. 4.21d). In the RN10 specimen the levels of triaxiality existing at the centre are comparable and remains constant throughout the loading history. However in the RN2 specimen, in the L loading it is higher than the isotropic

case and in the S loading it is significantly higher with steep increase after some plastic strain has accumulated.

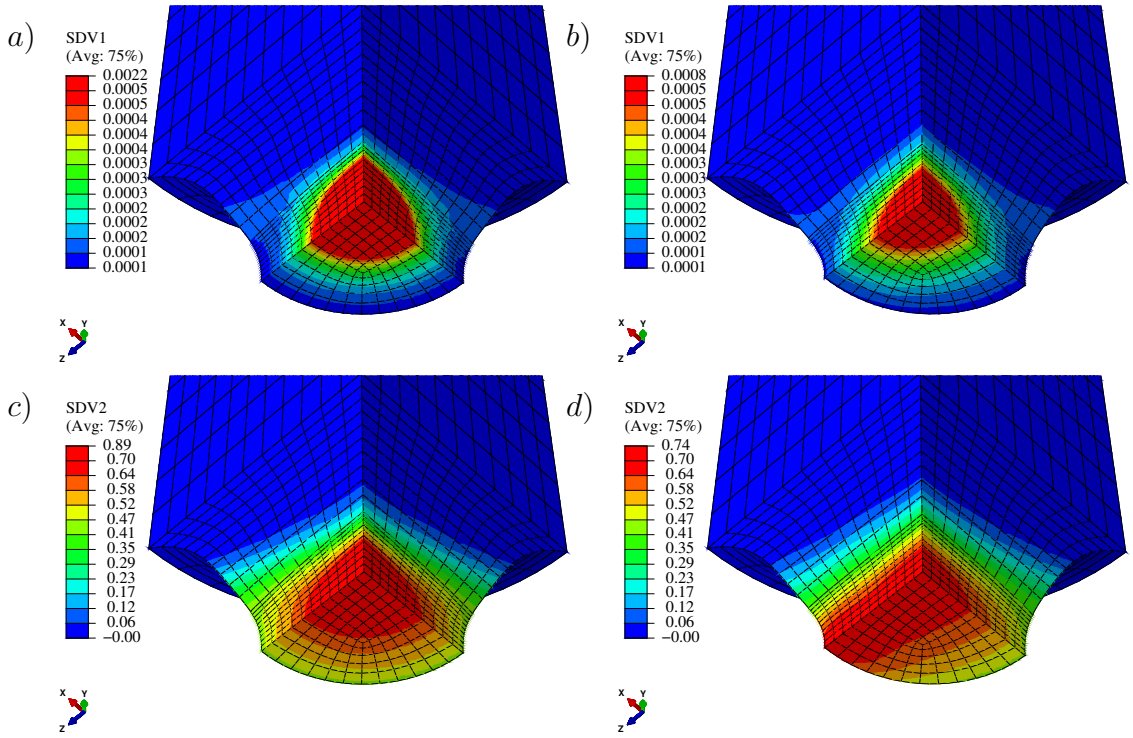

Figure 4.22: For RN10 samples of material iii for initial $w_0 = 1$, contours of a) Porosity S loading b) Porosity L loading c) Plastic strain S loading d) Plastic strain L loading

In the macroscopic contours of material iii, in the S loading it can be seen from Fig. 4.23 that the response is similar to that of material ib and is isotropic with respect to the axis of transverse isotropy which is the S axis. Also in this material, for the S loading, the magnitude of porosity and plastic strain are comparable to that in S loading of material ib. However in the L loading, as can be observed from Fig. 4.23b and Fig. 4.23d, the porosity and plastic strain are concentrated along the T

axis when loaded along the L axis. Thus the change in shear hill coefficient value from a high value of 2.33 in material ib to a value of 0.5 in material iii resulted in significant differences, both in the microscopic as well as spatial evolution of variables for the similar geometries. This itself points to the important role of plastic anisotropy in driving the material behavior and thus, eventually deciding the failure. For example in material ib when loaded along the L axis, first coalescence happens at the centre and then the macroscopic crack will grow and propagate along the S axis whereas in material iii, which has the only difference as the shear hill coefficient value, the crack will propagate along the T axis for the same loading.

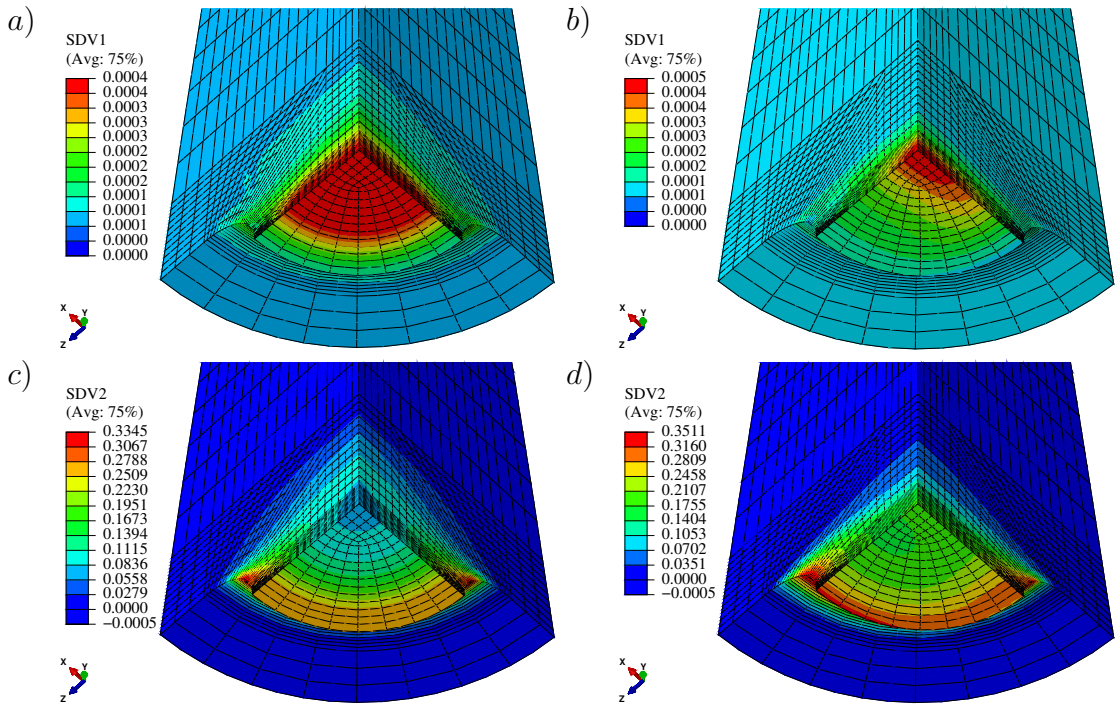

Figure 4.23: For RN2 samples of material iii for initial $w_0 = 1$, contours of a) Porosity S loading b) Porosity L loading c) Plastic strain S loading d) Plastic strain L loading

4.3.7.3 Effect of loading orientation for anisotropic material

For the anisotropic material AZ31, which has all the Hill coefficients different, the macroscopic response and the evolution of microstructural variables are shown in Fig. 4.24. Although it is interesting to note that in the RN10 specimen, the macroscopic response along L and S and also the microstructural evolution at the centre is identical to that of the isotropic case, it is not surprising since the anisotropy characterizing invariant which captures the essence of anisotropy for this material is 2.09 which is very close to the isotropic value of 2.0. However in the RN2 specimen the response is comparatively different from that of the isotropic one with L loading and S loading resulting in higher ductilities. Similar is the trend for evolution of porosity and void aspect ratio. Another factor to note is the lowest triaxiality existing at the centre of the specimen in this material for the RN10 case as seen from Fig. 4.24d and in fact this is the lowest value among all the materials considered here.

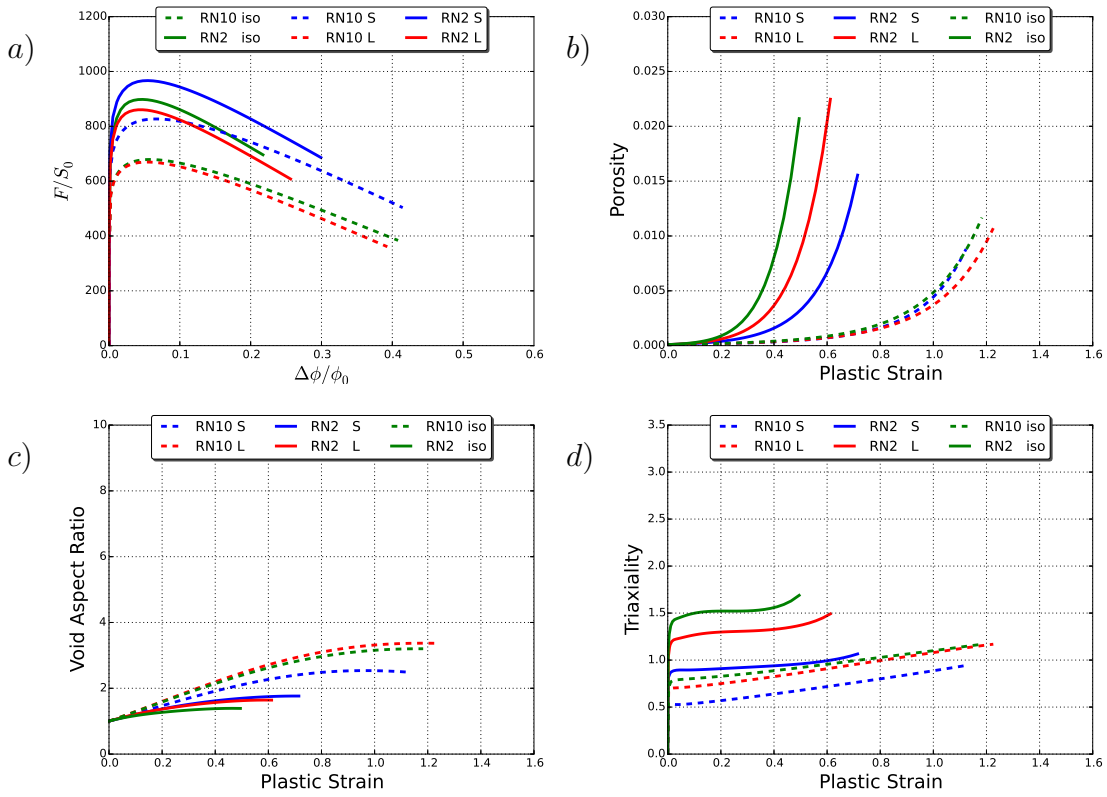

Figure 4.24: For RN10 samples of material AZ31 when the major load direction is along the S and L direction of loading for initial $w_0 = 1$ a) Load versus diameter reduction b) Porosity c) Void aspect ratio d) Triaxiality

If one were to look at the macroscopic response and evolution of porosity at the centre of the specimen in the case of RN10 specimen one might think that the behavior of this material is almost indistinguishable to the isotropic case. However the strong spatial anisotropy existing in the evolution of plastic strain and porosity in this material are evident from the contour plots shown in Fig. 4.25. In the S loading porosity and plastic strain are more evolved along the T direction. However in the L loading we can see that the porosity is concentrated along the S axis and so is the plastic strain. This can be explained by the value of principal Hill coefficient

h_s which is 0.4 for this material and is comparatively lesser than the value for the other two principal directions. A lower value of Hill coefficient means the material is stronger or that it is more difficult to deform the material in that direction compared to the other directions. Thus when the material is loaded along L, the T direction will deform more than the S direction or in other words, the resistance of the material to deform along the S direction will generate more stresses along the S direction causing the plastic strain to concentrate along S which in turn will drive the higher growth of porosity along the same direction. When loaded along the S direction, the same reasoning holds and material chooses the direction of lesser value of Hill coefficient to have more plastic strain which in this case is the T direction. However due to the lesser difference between the h_L and h_T values for this material, it can be observed that in S loading, the porosity growth is comparatively more similar along the L and T direction unlike in L loading where the larger difference between h_T and h_S makes them grow by different amounts.

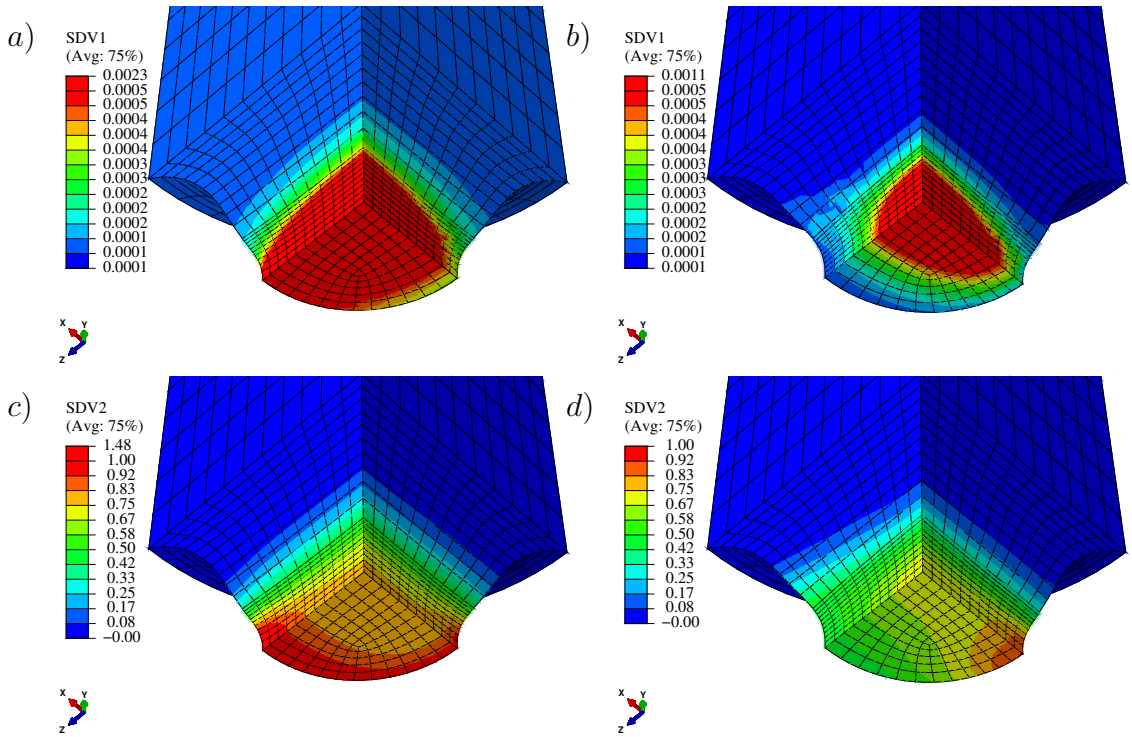

Figure 4.25: For RN10 samples of material AZ31 for initial $w_0 = 1$, contours of a) Porosity for S loading b) Porosity for L loading c) Plastic strain for S loading d) Plastic strain for L loading

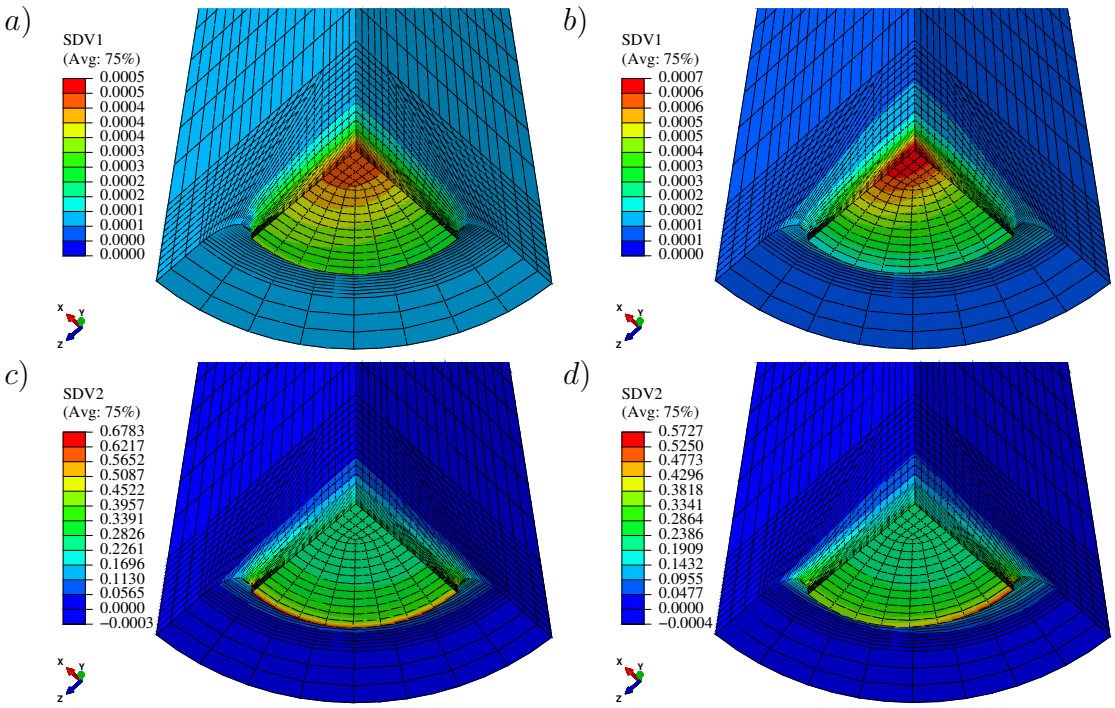

Figure 4.26: For RN2 samples of material AZ31 for initial $w_0 = 1$, contours of a) Porosity for S loading b) Porosity for L loading c) Plastic strain for S loading d) Plastic strain for L loading

4.3.8 Variation of triaxiality for different materials

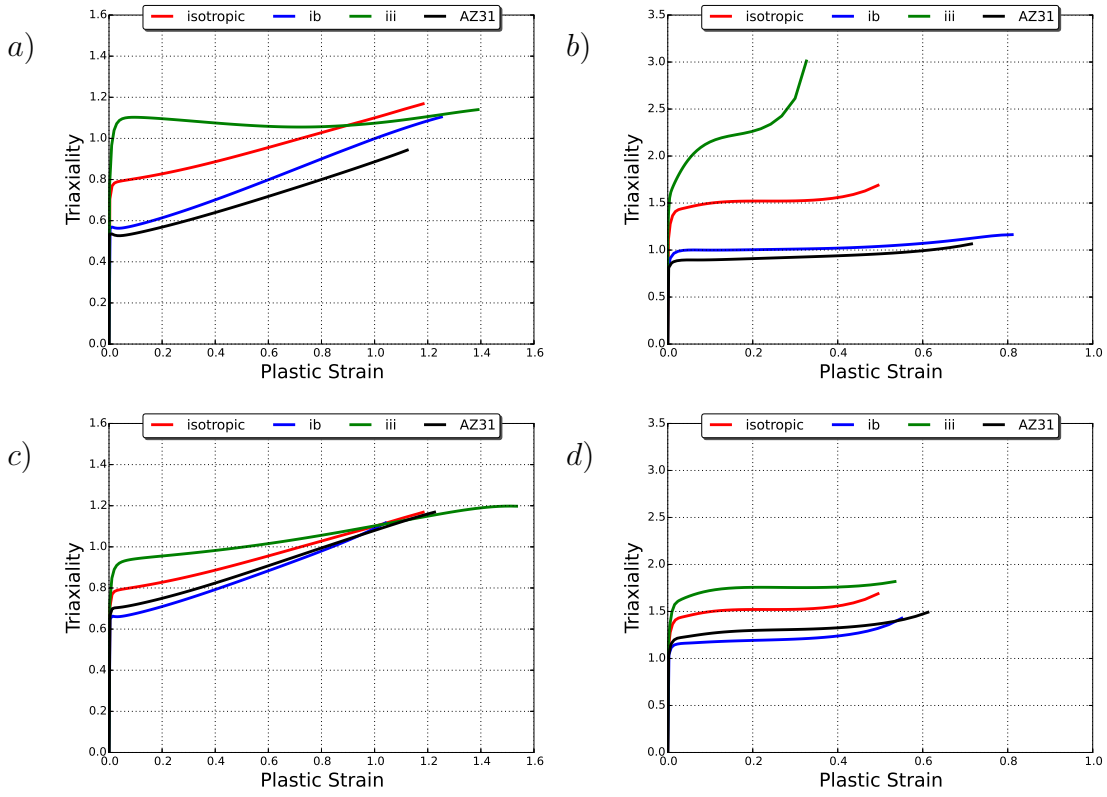

Figure 4.27: Evolution of triaxiality at the centre for materials isotropic, ib, iii and AZ31 for $w_0 = 1$, $f_0 = 10^{-4}$ for a) RN10 S Loading b) RN2 S Loading c) RN10 L Loading d) RN2 L Loading

In this section the effect of plastic anisotropy on the evolution of triaxiality will be examined. The effect of triaxiality on ductile fracture is prominent and well established by previous studies. On examining the evolution of triaxiality at the centre for RN10 and RN2 specimen for various materials it is evident that the evolution of triaxiality is greatly affected by the plastic anisotropy of the material. In the

simulations presented here, triaxiality is not controlled and is an outcome of the solution of the boundary value problem. The response of each material is dependent on the triaxiality existing in the specimen and this value is impacted by the plastic anisotropy.

It can be noticed from the previously presented results that void shape doesn't have any impact on the evolution of triaxiality in the materials considered. This is evident from Fig. 4.8d, Fig. 4.11d and Fig. 4.12d which showcases identical evolution of triaxiality at the centre for materials iso, ib, iii and AZ31 for the three initial void shapes considered here viz $w_0 = 1/6$, 1 and 6. Triaxiality is impacted only by the plastic anisotropy parameters characterizing the material. It can be observed from Fig. 4.27 that material iii has the highest value of triaxiality existing at the centre of the specimen with the material AZ31 having the least value of triaxiality when loaded along the S direction. Material ib has lower triaxiality than the isotropic case but is higher than the AZ31 value. It is also interesting to note the significantly higher increase of triaxiality in material iii in the RN2 specimen, when compared to other materials.

If you consider the materials presented here, for example material ib and material iii differ only in the value of shear Hill coefficient. This says that the response of the materials under shear stress dominated regions will be different. However if you look at the evolution of triaxialities at the centre of the specimen, one can see that although there are no shear stresses existing at the centre of the specimens in question, the evolution of triaxiality is evidently different. This can be explained by the different macroscopic structural response of the materials ib and iii effected by their different shear hill coefficient as elaborated below.

Triaxiality is calculated as $T = \Sigma_m/\Sigma_{eq}$ where the Σ_{eq} is the Von Mises equivalent stress. The Hill coefficients are affecting triaxiality through the stress components

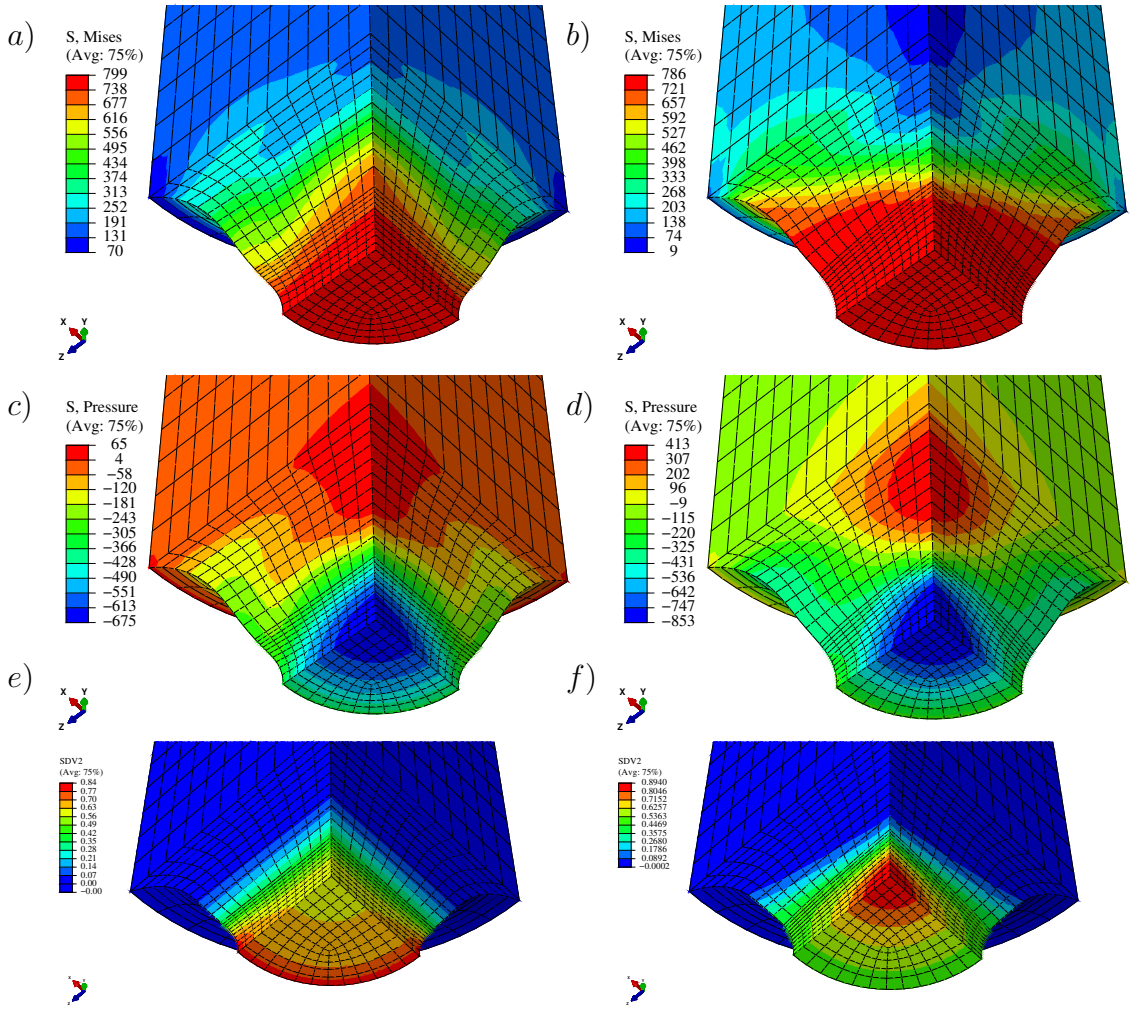

Figure 4.28: For RN10 specimen with $w_0 = 1$, $f_0 = 10^{-4}$ and S loading, contours of a) Von-Mises stress for material ib b) Von-Mises stress for material iii c) Mean stress for material ib d) Mean stress for material iii e) Plastic strain contours for material ib f) Plastic strain contours for material iii

entering Σ_{eq} and Σ_m. Among material ib, iii and iso, only the shear Hill coefficients are varying. For ib, $h_{SL} = 2.33$ and for iso, h_{SL}= 1.0 and for iii $h_{SL} = 0.5$. It can be observed from Fig. 4.28a and Fig. 4.28b that for material ib and iii, the equivalent stress contours displays nearly identical values. Although at the centre of the specimen the shear stresses are absent, it is seen that from Fig. 4.28c that in material ib, compared to material iii, a higher value of shear Hill coefficients results in a lower hydrostatic stress (note that the pressure reported by Abaqus is -hydrostatic stress) at the centre and hence lower triaxiality value in that material. In material iii, the increased hydrostatic stress at the centre is contributing to higher triaxiality evolution as expected. The increased hydrostatic stress in material iii can be explained by a *constraint* effect caused by the plastic flow processes which in turn are modulated by plastic anisotropy. As it can be observed from Fig. 4.28e and Fig. 4.28f, in material ib, the plastic strain is concentrated near the circumference of the notched bar and in material iii, it is concentrated at the centre. As explained earlier, this difference in spatial distribution of plastic strain is due to the effect of shear Hill coefficients of the materials and it imparts a plastic constraint effect. In addition, looking at the mean stress contours (Fig. 4.28c, Fig. 4.28d), it can be seen that in both bars of material iii and ib, compression pockets (or regions of negative mean stress) are created away from the centre. These are similar to the compression pockets forming during necking of a smooth bar and in the case of notched bar, since the notch behaves like a neck, the concurrence of these pockets are even more plausible. However the important aspect is not just the formation of compression pockets, but how the stress values in them are modulated by the plastic anisotropy in general and shear hill coefficients here in particular, affecting the macroscopic stress response of the specimen. This region of compressive stresses are lesser in magnitude in material ib. Although far away from the centre, the presence of these

regions affect the stress response of each material at the centre, indirectly. A change of shear Hill coefficient values (alone) from a low value of 0.5 in material iii to a high value of 2.33 in material ib resulted in significant change in macroscopic stress response between these materials even for the same geometry. This in turn points to how significant the influence of plastic anisotropy is in governing material behavior. Each specimen is a structure and plastic anisotropy plays the crucial role in dictating the overall structural response of the material. Thus depending upon the value of Hill coefficients, although the triaxiality is set on an average by the geometry of the notch, different macroscopic stress responses and thereby values of triaxialities can be realized even in similar geometries of different materials.

In the case of RN2 geometry the differences in the macroscopic spatial variation of stress between materials ib and iii are much more prominent and noticeable when compared to that of RN10 geometry. This can be observed from Fig. 4.29 which compares the equivalent stress contours and mean stress contours for materials ib and material iii. In the case of material ib, the maximum value of equivalent stress is at the centre of the RN10 specimen, whereas in the case of material iii, it is existing away from the centre. At the centre similar to RN10 geometry the equivalent stress values are comparable and similar to each other. However, the difference in hydrostatic stress values between these two materials existing at the centre of RN2 geometry is prominent when compared to the RN10 case. From Fig. 4.29c and Fig. 4.29d, it can be observed that, higher hydrostatic stress exist in RN2 specimen of material iii when compared to that of material ib. Here also it is emphasized that the only difference between these two simulations is the value of shear Hill coefficients, which at the macroscopic level results in significant differences in stress distribution. This variation is reflected in the stress triaxiality contours shown in Fig. 4.29e and Fig. 4.29f. It can be observed that the location of highest triaxiality

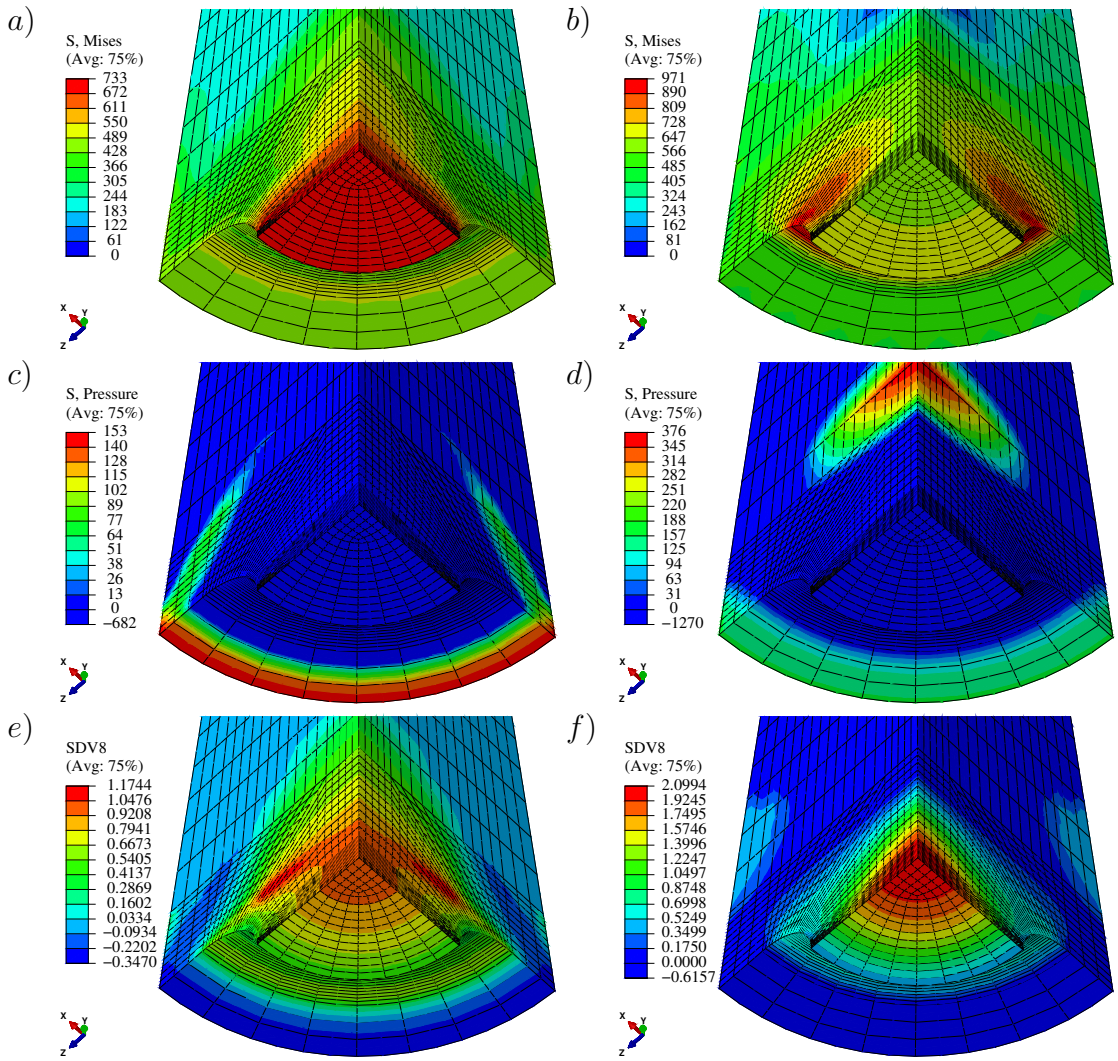

Figure 4.29: For RN2 specimen with $w_0 = 1$, $f_0 = 10^{-4}$ and S loading, contours of a) Von-Mises stress for material ib b) Von-Mises stress for material iii c) Mean stress for material ib d) Mean stress for material iii e) Stress triaxiality contours for material ib f) Stress triaxiality contours for material iii

value in RN2 specimen of material ib exists away from the centre of the specimen whereas in that of material iii, it is at the centre with much higher magnitude. Thus in both RN10 and RN2 specimen, the effect of plastic anisotropy is significant and it influences the damage evolution by dictating the spatial as well as local evolution of triaxiality. This influence has greater consequences as far as the ductility response of the structures are concerned as explained in the next few sections.

4.3.9 Coalescence strains and critical porosities

In this section strains to failure and the porosity at the first instance of coalescence in the RN10 and RN2 specimen are compared of the S loading as well as L loading. This is aimed at demonstrating the combined effect of plastic anisotropy, void shape and stress state (here triaxiality) on ductile failure. Towards this, the critical strains and critical porosities are compared for three materials-material ib, isotropic material and material iii for three different void shapes as a function of the anisotropy characterizing invariant h. In all the materials and for all the cases considered here, failure initiation or the first instance of coalescence was reported at the centre of the notched bar. To complete the picture, as triaxiality evolution in these simulations are not controlled, the results are also presented as functions of strain weighted average triaxialities existing in the specimen so as to provide an idea on the average triaxiality values existing at the centre for each loading and each specimen during the course of deformation.

4.3.9.1 RN10 S loading

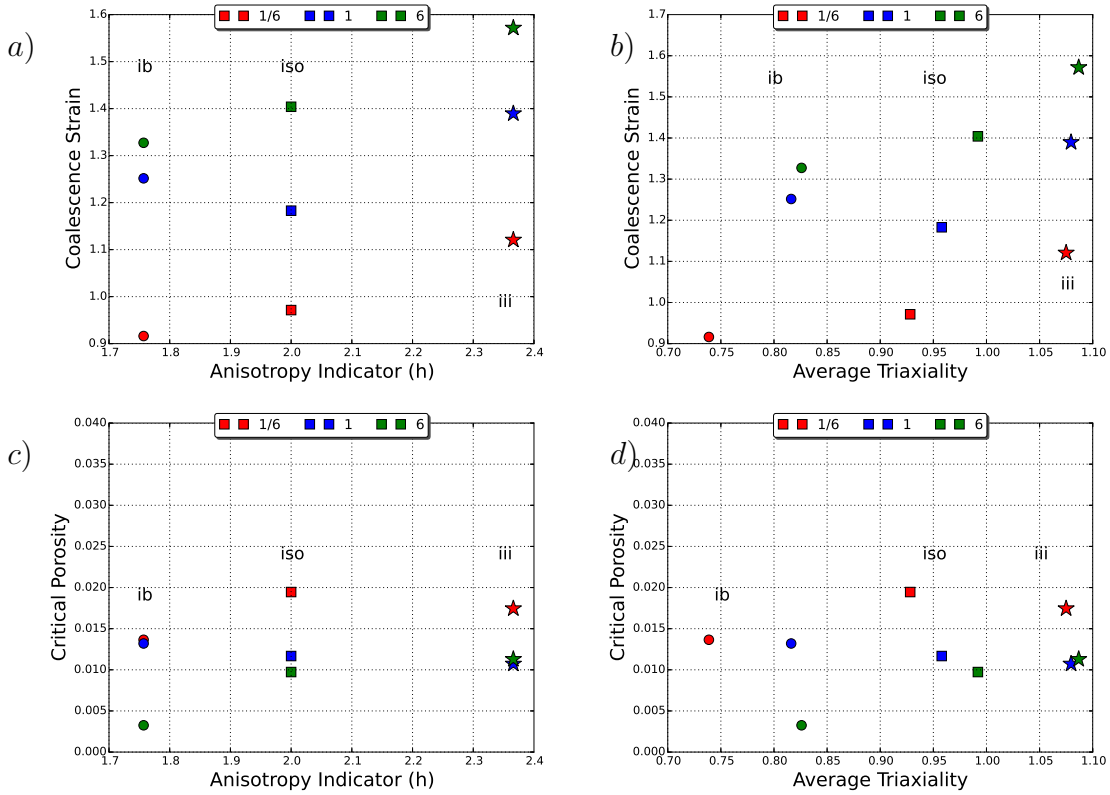

Figure 4.30: For RN10 samples when the major load direction is along the S direction of loading for initial void shapes of $w_0 = 1/6$, 1 and 6 a) Coalescence strains versus h b) Coalescence strains versus average triaxiality c) Critical porosities versus h d) Critical porosities versus average triaxiality

The coalescence strains and critical porosities as a function of average triaxialities and values of anisotropy indicator (h) are shown in Fig. 4.30. It can be seen from Fig. 4.30a that for each material, initially oblate void shapes result in lowest strain to failures with initially spherical void shapes resulting in intermediate strain to failures and the prolate void shapes resulting in highest ductilities which is in

agreement with the previous cell model calculations [67, 103]. The effect of triaxiality on ductile fracture with higher triaxiality resulting in lower strain to failures is also well established and rationalized. However if Fig. 4.30b is examined it is clear that material iii has the highest average triaxiality among all the materials considered for any void shape the rationale for which was explained in section 4.3.8. Hence material iii is expected to have the least strain to failure among the three materials, if triaxiality alone was the driving factor with all other factors kept constant as is done in cell model studies mentioned above. On the other hand, when triaxiality is kept constant, it is shown by previous cell model studies [72] that the strain to failure initiation is directly proportional to the value of anisotropy indicator (h). However it can be observed from Fig. 4.30a that for all the void shapes considered, material iii resulted in higher strain to failures than the isotropic material and material ib. This can be explained on the basis of the influence of plastic anisotropy (characterized by the scalar invariant h) dominating that of triaxiality in the S loading case considered. For the materials considered, the order of h value is $h_{iii} > h_{iso} > h_{ib}$. Higher the value of h, higher is the ductility which established by previous studies [72], [16, 67] and was experimentally confirmed by [10] recently on a highly anisotropic Magnesium alloy AZ31. The higher value of triaxiality existing in material iii is not high enough to overcome this influence of plastic anisotropy for this specimen and the loading considered.

On examining the critical porosities it is seen that except for prolate void in material ib, all other void shapes and materials resulted in critical porosities in the range of 0.01-0.02. This is also in agreement with the usual porosities at coalescence reported by previous simulations [18] in similar materials. In material ib, the oblate and the spherical void shapes resulted in identical porosities at failure whereas in isotropic and material iii, its the spherical and prolate voids which have nearby

critical porosities with identical values in material iii.

4.3.9.2 RN10 L loading

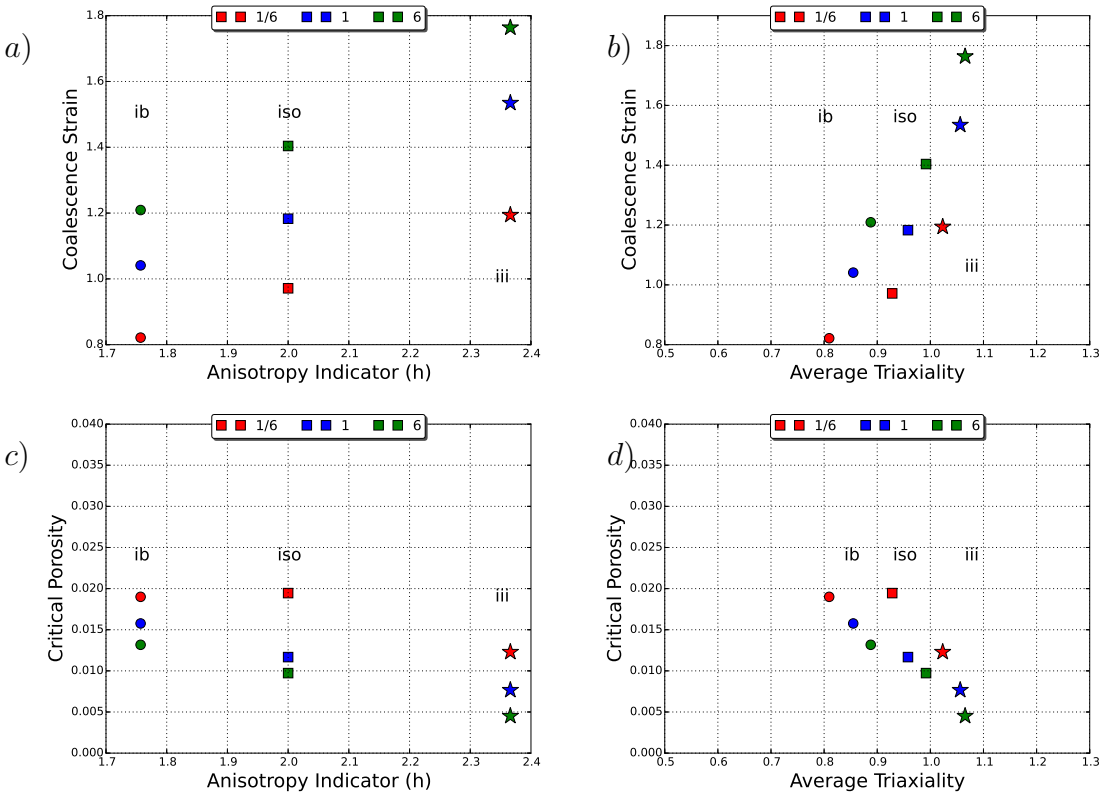

Figure 4.31: For RN10 samples when the major load direction is along the L direction of loading for initial void shapes of $w_0 = 1/6$, 1 and 6 a) Coalescence strains versus h b) Coalescence strains versus average triaxiality c) Critical porosities versus h d) Critical porosities versus average triaxiality

For the L loading also the trends similar to the S loading can be found with the effect of plastic anisotropy dominant than that of triaxiality. The failure strains range from 0.8 for initially oblate void shapes of material ib to about 1.8 for initially prolate void shapes in material iii. From the above two loading configurations, it

can be concluded that the effect of plastic anisotropy is significant at these levels of triaxialities existing in the materials and that this effect is comparable to or even more than that of already known triaxiality effect.

Observing Fig. 4.31b and Fig. 4.31d, looking at the critical strains and critical porosities for the isotropic matrix material (which eliminate the influence of plastic anisotropy), the influence of morphological anisotropy is evident. It should be noted that the initially oblate void shapes resulted in lower triaxiality values existing in RN10 specimens with the highest value of triaxiality in the case of prolate voids. However, at these triaxiality values, the influence of initial void shape is found to be prominent with higher strain to failure initiation with initially prolate voids even though the triaxiality value existing in that case is higher than the initially oblate and spherical void shapes. In the case of critical porosities, the initially oblate voids resulted in higher critical porosity values. This is expected and in agreement with the previous literature. However it is highlighted here so as to provide comparison to the case of materials ib and iii where significant plastic anisotropy exists.

4.3.9.3 RN2 S loading

In the high triaxiality regime, however the picture is different. It can be observed from Fig. 4.32 that in this regime of triaxialities, the effect of triaxiality on the ductility is dominant than that of plastic anisotropy. Material iii although with the highest value of h coefficient, ends up having the lowest ductility due to the significantly higher triaxiality existing in the RN2 specimen of material iii. This demonstrates the influence of *structural effects* which cannot be accounted for in cell model studies. In cell model calculations, usually a homogenized deformation is imposed on the cell, usually with the triaxiality kept constant. However in these calculations, the triaxiality is not imposed. When the triaxiality is not imposed, it

was shown in section 4.3.8, how crucial is the role of plastic anisotropy in determining the evolution of triaxiality in the specimen. In addition, the influence of the notch geometry also brings about non-homogeneity in the stress state. These results point to one important practical consequence that in the case of notched bars of plastically anisotropic materials, the strain to failure does not always scale with the anisotropy indicating factor (h), as expected on the basis of cell model calculations. The results also suggests that in this regime of triaxialities, materials which are weak in shear might be better suited for structural applications which have tensile dominated stress states than materials that are shear resistant. One interesting thing to note is that although the initially oblate shapes of all materials resulted in lowest ductilities, in isotropic material and material iii, this void shape resulted in lower critical porosities unlike in the case of these materials for RN10 specimen (Fig. 4.30c, Fig. 4.31c). The effect of void shape is still persistent even at the average triaxiality value of around 2.3 existing in material iii. However the initially spherical and prolate void shapes of material iii displays identical ductility values.

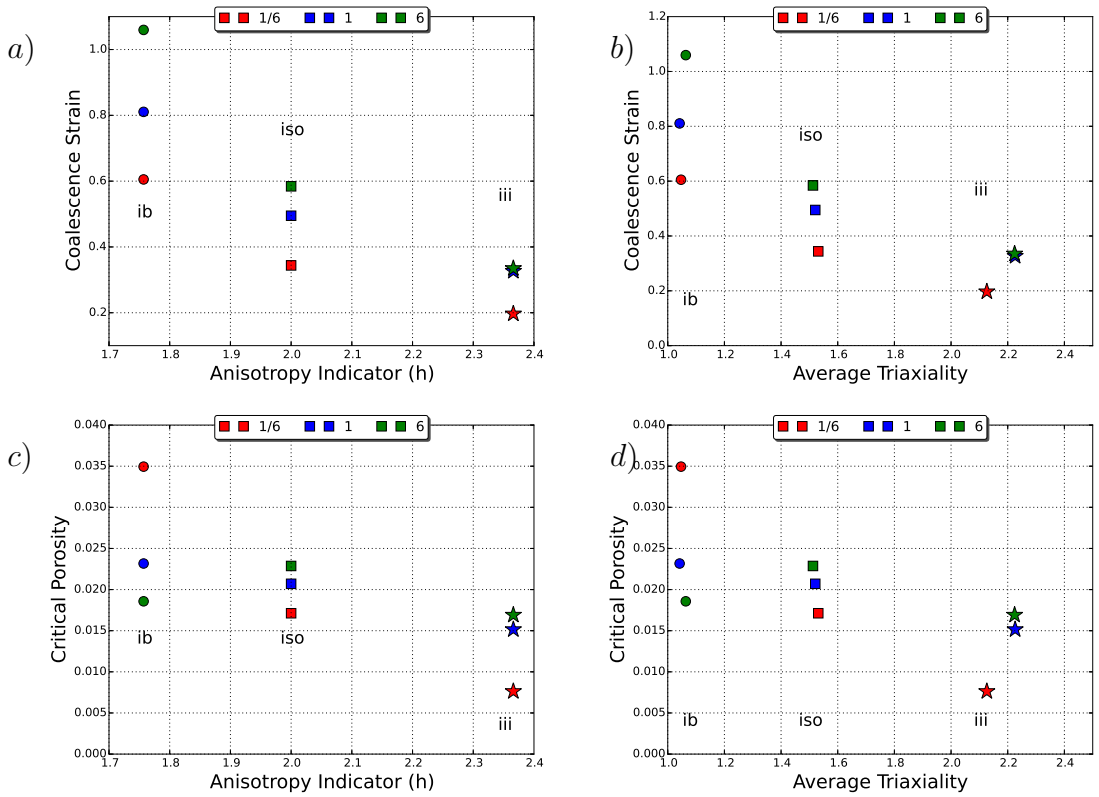

Figure 4.32: For RN2 samples when the major load direction is along the S direction of loading for initial void shapes of $w_0 = 1/6$, 1 and 6 a) Coalescence strains versus h b) Coalescence strains versus average triaxiality c) Critical porosities versus h d) Critical porosities versus average triaxiality

4.3.9.4 RN2 L loading

In the case of RN2 L loading also although similar trends can be found interesting observations can be found. It is worth noting that the competition between the plastic anisotropy effect and that of triaxiality is making the material iii to have better ductilities than in the case of S loading. Hence it must be conjectured that even a very high average triaxiality value of near 1.8 is not high enough to completely overpower the effect of plastic anisotropy. This should be compared to the high triaxiality

value of around 2.2 which was high enough to dominate the plastic anisotropy effect in material iii. The critical porosities however shows a clear trend with material ib having highest critical porosities and material iii having lowest porosity values at failure.

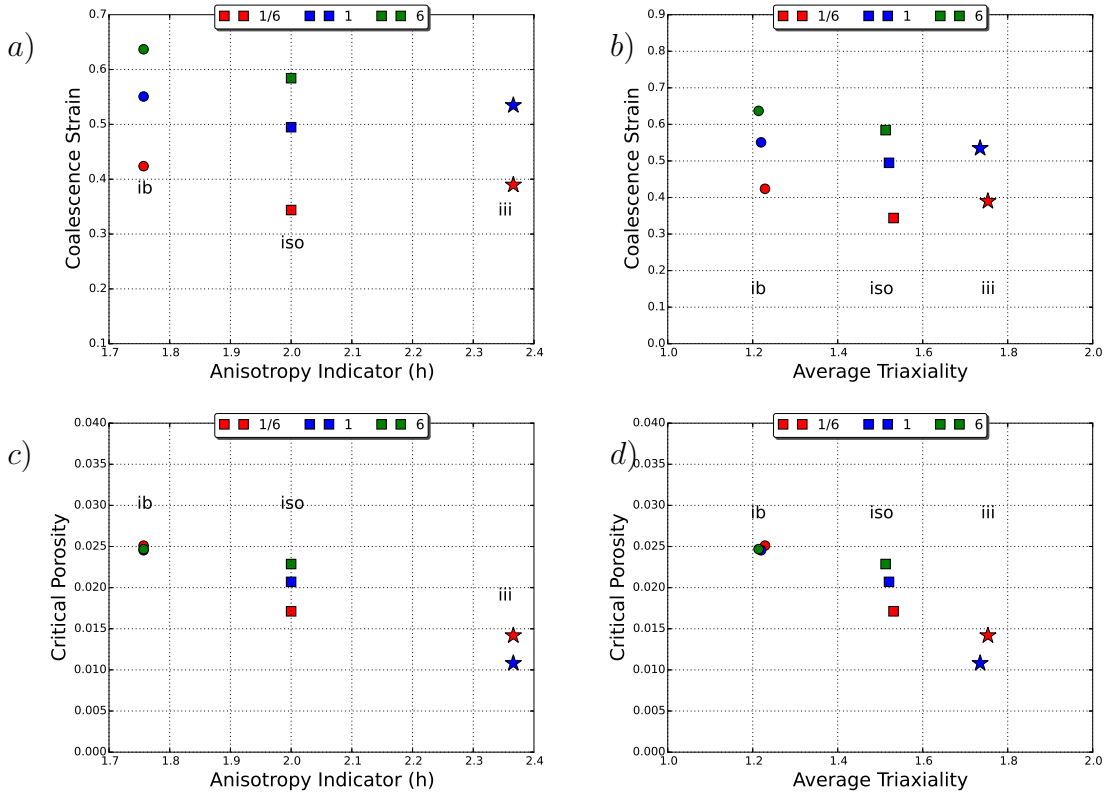

Figure 4.33: For RN2 samples when the major load direction is along the L direction of loading for initial void shapes of $w_0 = 1/6$, 1 and 6 a) Coalescence strains versus h b) Coalescence strains versus average triaxiality c) Critical porosities versus h d) Critical porosities versus average triaxiality

4.4 Discussion

Towards accurate prediction of fracture in ductile materials and for the development of damage tolerant microstructures, a symbiotic approach rooted in sound understanding of mechanisms supplemented with microstructure based simulations is important. However the availability of advanced models of ductile fracture in existing finite element solvers are lacking and there is scope for aggressive improvements. Toward this, new, advanced and improved models of ductile fracture need to be developed and they need to be validated and then implemented in existing finite element solvers. In addition, the simulation of fracture all the way to failure warrants the use of accurate void coalescence models. Three dimensional simulations of ductile fracture using an advanced model of void growth supplemented by an analytical void coalescence condition is employed in the simulations presented here to explore the effects of plastic anisotropy void shape and stress state and also to demonstrate the predictive capabilities of the model. Although the model as such lacks a void nucleation criterion, a stress based or strain based nucleation model can be incorporated easily into the model. In addition, the interaction between different populations of voids, the evolution of material anisotropy parameters etc are not considered in the simulations presented. However this allows parametric studies to be conducted and leads to clean comparisons.

One of the major findings from these simulations is the influence of structural effects happening in notched bars with plastic anisotropy being the driving factor behind it. In all the calculations presented here, unlike in the cell model calculations the triaxiality is not controlled or imposed and evolves naturally as happening in experiments. The presence of notch induces an overall level of triaxiality due to the notch geometry. However, in addition to dependence on geometry, the actual

value of triaxiality generated in the structure depends on the constitutive parameters such hardening law and more importantly as described in section 4.3.8, on plastic anisotropy. Even for the same geometry, the effect of plastic anisotropy can lead to significant variation in evolution of triaxiality both spatial and locally in notched bars. This is an important aspect to be kept in mind since notched bars are usually employed as constant triaxiality specimens in experiments for calibrating fracture strains which are characterized on the assumption of proportional loading paths. Plastic anisotropy in itself can cause significant non-proportionality in triaxiality evolutions whose implications were discussed in the previous chapter. It is interesting to note that in RN10 specimen of material iii, the triaxiality at the centre was constant throughout the deformation history making it an excellent candidate for constant triaxiality specimen. Hence the effect of plastic anisotropy is not always that of inflicting significant variations from proportionality; in some case, it can be beneficial. The application of models such as presented here makes the tracking of triaxiality variations easier in the case of structural materials and informed choices can be made on the assumption of non-proportional loading histories. It should also be kept in mind that in all the cases presented here, damage evolution happened by void growth failure initiation was reported to be taking place by void coalescence. The presence of localization in shear bands were not observed and the non-proportionality imparted were solely due to plastic anisotropy. The presence of instabilities can also impart significant deviations from proportionalities and plastic anisotropy might contribute to this effect either independently or in collaboration with other micro structural variables. More details on this will be presented in the next chapter.

The structural effects happening in the notched bars have important practical implications as demonstrated in the previous sections. For example, in the RN10

specimen, material iii induces a higher triaxiality. At the same time, this material is intrinsically more resistant to void growth. This intrinsic resistance overcomes the counteractive effect (purely structural) of the triaxiality being above that of the isotropic reference case which is demonstrated by its higher ductilities in the RN10 specimen. However in the RN2 specimen, although the triaxiality induced by material iii is again higher than that of isotropic case, the outcome as far as coalescence strains are considered is entirely opposite. This shows that in notched bars, the overall behavior is dictated by the relative influences of intrinsic and structural effects and the ductilities in notched bars of plastically anisotropic materials don't always scale in direct proportion to the anisotropy indicating factor (h) as shown by previous studies [72]. It remains to be seen how significant is the interplay between the intrinsic and the structural effects in low triaxiality regimes.

Another factor to be stressed is the influence of various loading orientation on ductility and possibly on location of fracture initiation. It was shown in previous sections that depending upon the Hill coefficients and loading directions, different ductilities and potential directions of crack propagation can be realized in plastically anisotropic materials. In addition, the spatial variation of major factors such as triaxiality and plastic strain differ significantly between specimens and also between materials. It should be kept in mind that it is the competition between triaxiality and plastic strain which determines the failure initiation site. Although in all the calculations reported here failure was first reported at the centre, significant spatial variations of accumulated plastic strain imparted by different loading directions can potentially cause fracture to initiate in areas where stress triaxiality might not be maximum. Another factor which can be noticed is the large rotations of void axes happening in these geometries near the free surfaces which can also contribute to the above behavior.

4.5 Conclusions

The combined effect of void shape, stress state and plastic anisotropy was investigated by employing an anisotropic void growth model supplemented with a micro mechanically motivated void coalescence condition using three dimensional simulations involving anisotropic materials on round notched bars of varying notch intensity. The materials chosen were representative of those employed in various structural applications. The predictive capabilities of the model were initially demonstrated by comparison with existing experiments and a wide variety of results exploring the parameter space usually not accessible to experimental investigation. Based on the studies the following conclusions can be made:

- The effect of triaxiality on ductile fracture is well established from previous studies. In the simulations reported here, although the triaxiality value for a particular specimen is dictated by the notch geometry, its variation is found to be modulated by plastic anisotropy of the material. The spatial variation at a given time as well as the temporal variation at a given location of triaxiality is indeed a manifestation of the structural effects imparted by plastic anisotropy of the material. This triaxiality variation in turn will also influence the evolution of various microstructural parameters such as void shape, porosity etc and thus eventually affecting ductility response of the material.

- One of the major findings of this study is to reveal an interesting competition between two effects; both imparted by plastic anisotropy, one the intrinsic effect which can be quantified through the anisotropy characterizing scalar invariant **h** and the other being purely structural effect which manifests through the way in which plastic anisotropy affects plastic flow processes and triaxiality evolution in time and space in the structure. Depending upon the geometry

and kind of anisotropy in the material, this can be beneficial or detrimental to the ductility response of the material. In the calculations analyzed in the main text, the structural effect of plastic anisotropy always goes against its intrinsic effect. In RN10 specimens the structural effect of plastic anisotropy is not strong enough to revert the trends obtained from cell model calculations. In RN2 specimens, however, the structural effect overcomes the intrinsic one.

- More generally, whether the structural effect always goes against the intrinsic one is worth investigating. Preliminary results (shown in Appendix) indicate that this is not necessarily the case. Therefore, in general complete boundary-value problem solutions are needed to understand ductile fracture in anisotropic materials.

- The above findings are robust in the sense that they apply not only to initially spherical voids but also initially prolate or oblate voids.

- The effect of loading orientation combined with plastic anisotropy in governing the evolution of various microstructural variables and damage was demonstrated. As shown in the results, this plays a crucial role in deciding the potential direction of crack propagation in various loading orientations.

- It was shown that in notched bars, in addition to that imparted by plastic spin, significant void rotations take place near the free surface due to the curvature-induced shear stresses. This is consistent with experimental observations. The implication of such rotations are important when the loading axes are aligned with the microstructure (either the axes of plastic anisotropy or the damage entities/voids). However, they are expected to play a much more key role under combined tension and shear loading (where rotations imparted by loadings also

might be superimposed in addition to geometry and plastic spin) or under off-axes tensile loadings, which is explored in the next chapter.

5. FAILURE BY SHEAR LOCALIZATION IN DUCTILE MATERIALS

5.1 Introduction

In general, ductile failure may occur mainly in two modes; by micro-void growth and coalescence or by instability [105]. In the previous chapter, the role played by plastic anisotropy in determining the ductility when void coalescence was the primary failure mechanism was demonstrated. Mechanical or plastic instabilities can also result in early failure and drastic reduction of ductility. This mode of failure usually presents itself during static or dynamic loading conditions with the formation of one or more shear bands inside of which the failure concentrates [5] and is found in a wide range of solids from metals to rocks. This can happen even when the remote loading doesn't have any shear component. In this mode of failure, the fracture surfaces are characterized by slanted features such as shear lips as observed in plane strain bars and cup-cone fracture. Understanding localization of deformation is significant to structural applications and in the design of advanced materials as this mode of failure adversely limits ductility and formability.

Failure by shear localization may occur as an emergent behavior of the underlying constitutive relationship, eventually affected by geometric constraints and boundary conditions [5, 17]. In certain kinds of loading such as in torsional loadings it can happen by thermal softening [62] and even without any prior necking. For analyzing localized necking, Hill [56] used rigid plastic $J2$ flow theory under plane stress conditions to demonstrate that necking happens along the direction of least straining in thin sheets. Except when the material has very low strain hardening, shear bands are not predicted at realistic strain ranges by the use of $J2$ flow theory. Rice [107] expressed the necessary condition for localization of plastic deformation into

a planar band in elastic-plastic solids and had shown that the choice of constitutive equation played a crucial role in the prediction of localization. The analysis by [107, 109] proved that within the elastic plastic modeling framework involving associative isotropic plasticity, localization cannot happen in the regime of hardening. However, introduction of damage brings about softening behavior and can cause localization. This makes Gurson-like models with porosity as the damage parameter capable of predicting localization at realistic strain levels, see for example, [128].

Localization analyses following the lines of Rice [107] have pointed out several other constitutive factors that play a major role in triggering localization in rate independent solids. These studies focused on the case of infinite media wherein a band like discontinuity emerges. The study by [12, 61, 120] revealed that in a solid with smooth but high curvature yield surface at the current loading path, predictions of localization more in agreement with experimental observations could be found. This is also the case with solids having vertex on the yield surface which was shown to favor bifurcation behavior as shown by [99] and [61]. For isotropic hardening case, [126] demonstrated that the type of objective stress rate used in the constitutive formulation has no effect on localization. [93, 123] studied the effect of kinematic hardening and found that it adversely affected the ductility. Simulation of real structures in the context of finite element calculation usually employs the relevant constitutive model combined with Rice's bifurcation analysis wherein macroscopic failure is assumed to take place when the first instance of localization condition is met [35]. However [27] showed that the use of Rice's localization condition as a failure criterion might not be adequate as it slightly underestimated the macroscopic load drop. Very recently, [88] employed the GTN model along with the Rice's bifurcation analysis in elucidating the role of damage induced softening in triggering plastic flow localization.

Microstructure also plays a major role in deciding the localization behavior. This effect manifests in different ways. On the one hand, inhomogeneities at the microscopic level may trigger the formation of shear bands. Additionally, the various microstructural parameters entering the constitutive equation can indirectly affect the constitutive behavior thereby contributing to the localization behavior. However, it is important to differentiate between the macroscopic and microscopic modes of localization. One of the factors driving macroscopic mode of plastic instability is the softening induced by void nucleation and growth. On the other hand, the microscopic mode refers to the localization of deformation in the inter void ligament commonly referred to as void coalescence which can happen either through internal necking, shearing or in columns. Since these two modes of localization limits the ductility of the material, it is important to understand the competition between these two modes as in whether these two modes can take place simultaneously or if one preceded the other. This was investigated in detail by [115] who reported that these two modes of localization can exist simultaneously at lower stress triaxialities (for example shear dominated loadings). However at sufficiently high value of stress triaxiality, ($T > 1$) a clear separation was identified to exist between these two localization modes with the macroscopic localization preceding the microscopic one.

Another important factor in governing the formation of shear bands is the role of microstructure/deformation induced texture. Using an orthotropic elastic plastic constitutive model following associative flow rule, [112] analytically and numerically investigated the influence of certain types of orthotropy in aiding the formation of shear bands. The analysis by [112] was limited to plane stress uniaxial tension problem and a plane strain compression problem. [81] demonstrated that the formation and development of shear band in plane strain specimen of an orthotropic material is strongly dependent on the initial orientation of orthotropic axes. [17] found that

plastic anisotropy in synergy with a yield surface vertex can trigger localization. It was also shown that the presence of yield surface vertex alone need not necessarily result in flow localization. In tensile plane stress or plane strain specimens of aluminum alloys [27] or steels [17], shear failure is frequently observed. On the other hand this mode of failure is rarely observed in round tensile specimens. Although axisymmetric stress states are expected to be resistant towards shear localization compared to the plane strain specimens according to the classical localization analysis by Rice [107], and shear failure in axisymmetric specimens are rarely noticed experimentally, some recent experiments on Mg (which is highly anisotropic) and Al alloys by [10, 72] reveals shear failure modes even in round smooth bars and round notched bars. This was attributed to a destabilizing effect of texture induced plastic anisotropy, but with no supporting analysis.

The influence of plastic anisotropy along with other microstructural features in inducing strong yield surface curvatures (kinematic hardening) or yield surface vertex (due to void coalescence) thereby favoring shear band formation is known from previous studies [17, 123]. However, whether plastic anisotropy ***alone***, in the absence of strong yield surface curvature or vertex on yield surface is capable of inducing the formation of shear bands is unexplored. Systematic analyses of effect of plastic anisotropy either independently or combined with damage on shear band localization are still lacking. Therefore it is needed to investigate if plastic anisotropy by itself or in synergy with evolution of relevant microstructure (such as porosity induced softening) provides a sufficient condition for shear localization in ductile materials.

In the present treatment, an anisotropic large strain elastic plastic void growth model [67] is used to numerically investigate the effect of stress state, damage and plastic anisotropy on ductile fracture through macroscopic strain localization. Towards this three dimensional full boundary-value problem solutions of plastic flow

localization in plane strain and notched specimens are carried out for a variety of initial conditions so as to elucidate certain conditions that favor the formation of shear bands in anisotropic materials.

5.2 Formulation

In [67], analytical yield criterion for porous materials having spheroidal voids embedded in plastically anisotropic matrix were developed by following the Hill-mandel homogenization [58, 87] procedure along with limit analysis. The spheroidal representative volume element consisting of confocal spheroidal voids was subjected to kinematic boundary conditions having uniform rate of deformation. To incorporate plastic anisotropy, the matrix material was assumed to be of Hill-type following the works of [16]. In [67], the voids may assume any orientation relative to the axes of orthotropy of the matrix. The yield function was also supplemented with microstructure evolution laws for void shape, void orientation and porosity. This model was implemented in a finite element code after incorporating heuristic extensions for weak elasticity, accurate evolution of void shape and strain hardening effects. A synopsis of the Keralavarma–Benzerga model is recalled in the next section for completeness. For further details, see Refs. [67, 77].

5.2.1 Constitutive model

The deformation of the material is captured by additive decomposition of the symmetric part of velocity gradient and the hypoelastic law is employed for a finite strain formulation.

$$\mathbf{D} = \mathbf{D}^{\mathrm{e}} + \mathbf{D}^{\mathrm{p}} \tag{5.1}$$

where the elastic part is given by:

$$\mathbf{D}^{\mathrm{e}} = \mathbb{L}^{-1} : \overset{\nabla}{\boldsymbol{\sigma}} \tag{5.2}$$

with $\mathbb{L}$ the isotropic tensor of elastic moduli and $\overset{\nabla}{\boldsymbol{\sigma}}$ is the Jaumann stress rate defined by:

$$\overset{\nabla}{\boldsymbol{\sigma}} = \dot{\boldsymbol{\sigma}} + \boldsymbol{\sigma}\boldsymbol{\Omega} - \boldsymbol{\Omega}\boldsymbol{\sigma}, \quad \boldsymbol{\Omega} = \frac{1}{2}(\boldsymbol{\nabla}\mathbf{v} - \boldsymbol{\nabla}\mathbf{v}^T), \tag{5.3}$$

where $\boldsymbol{\Omega}$ is the skew symmetric part of the velocity gradient $\boldsymbol{\nabla}\mathbf{v}$. The plastic part of $\mathbf{D}$ is given by normality to a yield surface $\mathcal{F}(\boldsymbol{\sigma}) = 0$

$$\mathbf{D}^{\mathrm{p}} = \Lambda \frac{\partial \mathcal{F}}{\partial \boldsymbol{\sigma}} \tag{5.4}$$

The Keralavarma Benzerga flow potential for a plastically anisotropic material of the Hill type is written as $\mathcal{F}(\boldsymbol{\sigma}) = 0$ with

$$\mathcal{F}_G(\boldsymbol{\sigma}) = C\frac{\sigma_{\mathrm{eq}}^2}{\bar{\sigma}^2} + 2q_{\mathrm{w}}(g+1)(g+f)\cosh\left(\kappa\frac{\boldsymbol{\sigma} : \mathbf{X}}{\bar{\sigma}}\right) - (g+1)^2 - q_{\mathrm{w}}^2(g+f)^2 \tag{5.5}$$

where σ_{eq} is an equivalent stress that could be based on advanced anisotropic plasticity in the absence of porosity. Here, yielding in the matrix is taken to obey Hill's criterion [55] and σ_{eq} is defined as:

$$\sigma_{\mathrm{eq}}^2 = \frac{3}{2}\boldsymbol{\sigma} : \mathbb{H} : \boldsymbol{\sigma} \tag{5.6}$$

where $\mathbb{H}$ is related to Hill's anisotropy tensor $\mathbb{p}$ through:

$$\mathbb{H} \equiv \mathbb{p} + \eta(\mathbf{X}\otimes\mathbf{Q} + \mathbf{Q}\otimes\mathbf{X}), \quad \mathbb{p} \equiv \mathbb{J} : \mathbb{h} : \mathbb{J}, \quad \mathbb{J} \equiv \mathbb{I} - \frac{1}{3}\mathbf{I}\otimes\mathbf{I} \tag{5.7}$$

Here $\mathbf{Q}$ is a constant tensor and $\mathbf{X}$ a void shape dependent tensor which are both transversely isotropic in the frame associated with the void are are given by:

$$\mathbf{Q} \equiv -\frac{1}{2}(\mathbf{n}_1 \otimes \mathbf{n}_1 + \mathbf{n}_2 \otimes \mathbf{n}_2) + \mathbf{n}_3 \otimes \mathbf{n}_3 \tag{5.8}$$

$$\mathbf{X} \equiv \alpha_2(\mathbf{n}_1 \otimes \mathbf{n}_1 + \mathbf{n}_2 \otimes \mathbf{n}_2) + (1 - 2\alpha_2)\mathbf{n}_3 \otimes \mathbf{n}_3 \tag{5.9}$$

where $\mathbf{n}_3$ is the void axis and $\mathbf{n}_1$ and $\mathbf{n}_2$ are orthogonal base vectors arbitrarily chosen in the transverse plane. Also, in 5.5, $\bar{\sigma}$ is the flow stress of the matrix material in a reference direction. In practice, $\bar{\sigma}$ is selected as the yield strength in one of the principal directions of orthotropy and the components of the anisotropy tensor $\mathbb{p}$ are scaled accordingly. In addition, f denotes the porosity and the criterion parameters C, g, κ in 5.5 as well as η in 5.7 and α_2 in 5.9 are functions of f and eventually the void aspect ratio w and the components of $\mathbb{p}$. In 5.7, $\mathbb{J}$ denotes the deviatoric projection operator and $\mathbb{h}$ denotes the anisotropy tensor in the deviatoric stress space and $\mathbb{I}$ and $\mathbf{I}$ are the fourth and second order identity tensors, respectively. Finally, q_{w} in in 5.5 is a void shape dependent factor that was determined by [46] to fit unit cell results:

$$q_{\mathrm{w}} = 1 + (q - 1)/\cosh S \tag{5.10}$$

where $q = 1.6$ is the value taken by q_{w} for a spherical void. The matrix is considered to obey the power-law strain-hardening law as follows.

$$\bar{\sigma} = \sigma_{\mathrm{S}}(1 + \bar{\epsilon}/\epsilon_0)^N \tag{5.11}$$

where $\bar{\sigma}$ and $\bar{\epsilon}$ are work-conjugate measures of matrix effective stress and plastic strain, respectively. $\bar{\epsilon}$ is defined as the cumulative plastic strain. The evolution of

porosity is given by plastic incompressibility of the matrix as follows.

$$\dot{f} = (1-f)\Lambda \frac{\partial \mathcal{F}}{\partial \boldsymbol{\sigma}} \tag{5.12}$$

where Λ is the plastic multiplier. The evolution of the plastic strain of the matrix $\bar{\epsilon}$ is obtained considering the plastic work equivalence between the macroscopic homogeneous material and the microstructure (matrix); the work done on voids is zero.

$$\boldsymbol{\sigma} : \mathbf{D}^{\mathrm{p}} = (1-f)\bar{\sigma}\dot{\bar{\epsilon}} \tag{5.13}$$

The evolution of void shape is described as

$$\dot{S} = \frac{3}{2} D^{\mathrm{p}'}_{33} + 3\left[\frac{1-3\alpha_1}{f} + 3\alpha_2 - 1\right] D^{\mathrm{p}}_{\mathrm{m}} \tag{5.14}$$

where $'$ indicates the deviatoric component of a second order tensor. Note this equation includes an implicit dependence upon matrix anisotropy through the macroscopic rate of plastic deformation, $\mathbf{D}^{\mathrm{p}}$, which is derived from the yield criterion (5.5) by normality. Introducing the adjusting factor in [18, 45] into Eq.(5.14) leads to

$$\dot{S} = \mathbf{Q} : \left[h\mathbf{D}^{\mathrm{p}} + 3\left(\frac{1}{f}\mathbf{X}^{v} - \mathbf{X}\right) D^{\mathrm{p}}_{\mathrm{m}}\right] \tag{5.15}$$

where tensor $\mathbf{X}^{v}$ is defined similar to $\mathbf{X}$ in (5.9)2. The adjusting factor h is defined as follows.

$$h = 1 + h_{\mathrm{e}} h_{\mathrm{f}} h_{\mathcal{T}} \tag{5.16}$$

$$h_{\mathrm{e}}(e_1) = \frac{9}{2}\frac{\alpha_1 - \alpha_1^{\mathrm{Gar}}}{1-3\alpha_1}, \qquad \alpha_1^{\mathrm{Gar}} = \begin{cases} \dfrac{1}{3-e_1^2} & \text{(p)} \\ \dfrac{1-e_1^2}{3-2e_1^2} & \text{(o)} \end{cases} \tag{5.17}$$

$$h_{\mathrm{f}}(f) = (1 - \sqrt{f})^2 \tag{5.18}$$

$$h_{\mathcal{T}}(\mathcal{T}, \epsilon) = \begin{cases} 1 - \dfrac{\mathcal{T}^2 + \mathcal{T}^4}{9} & \text{for} \quad \epsilon = +1 \\ 1 - \dfrac{\mathcal{T}^2 + \mathcal{T}^4}{18} & \text{for} \quad \epsilon = -1 \end{cases}, \qquad \epsilon \equiv \mathrm{sgn}(\Sigma_{\mathrm{m}} \Sigma'_{33}) \tag{5.19}$$

$$\mathcal{T} = \frac{\Sigma_{kk}/3}{\sqrt{\frac{3}{2}\boldsymbol{\Sigma}' : \boldsymbol{\Sigma}'}} \tag{5.20}$$

$\mathcal{T}$ is the stress triaxiality. e_1 is the eccentricity of the void. h_{e}, h_{f} and $h_{\mathcal{T}}$ correct the mismatch due to eccentricity, porosity and stress triaxiality, respectively, between unit cell simulation results and the model prediction.

The void orientation evolves following the macroscopic spin of the material and the local plastic distortion, which was derived by Kailasam and Ponte Castaneda [64] as follows

$$\boldsymbol{\Omega}^v = \boldsymbol{\Omega} - \mathbb{C} : \mathbf{D}^{\mathrm{p}} \tag{5.21}$$

where $\boldsymbol{\Omega}$ and $\boldsymbol{\Omega}^v$ represent the continuum and void spin tensors respectively. $\mathbb{C}$ is the fourth order spin concentration tensor, which is given by

$$\mathbb{C} = -(1-f)\mathit{\Pi} : \mathbb{A}, \qquad \mathbb{A} = [\mathbb{I} - (1-f)\mathbb{S}]^{-1} \tag{5.22}$$

where $\mathbb{A}$ is the strain concentration tensor and $\mathit{\Pi}$ and $\mathbb{S}$ are the Eshelby tensors [40] for a spheroidal inclusion in an incompressible linear matrix. Then, the evolution of the void orientation is obtained using the following kinematical relationship

$$\dot{\mathbf{e}}_3 = \boldsymbol{\omega} \cdot \mathbf{e}_3, \qquad \boldsymbol{\omega} = \boldsymbol{\Omega}^v + \boldsymbol{\Omega}^l \tag{5.23}$$

where $\mathbf{\Omega}^l$ is an antisymmetric tensor given by

$$\Omega^l_{12} = 0, \quad \Omega^l_{i3} = \frac{w^2+1}{w^2-1} D^v_{i3} \qquad (i = 1, 2, \quad w \neq 1) \tag{5.24}$$

$$\mathbf{D}^v = \mathbb{A} : \mathbf{D}^{\mathrm{p}} \tag{5.25}$$

Combining Eq.(5.21) and (5.23)-2 leads to

$$\boldsymbol{\omega} = \mathbf{\Omega} - \mathbb{C} : \mathbf{D}^{\mathrm{p}} + \frac{1}{2} \sum_{i \neq j,\, w_i \neq w_j} \frac{w_i^2 + w_j^2}{w_i^2 - w_j^2} (\mathbf{e}_i \otimes \mathbf{e}_j + \mathbf{e}_j \otimes \mathbf{e}_i) : \mathbb{A} : \mathbf{D}^{\mathrm{p}} \mathbf{e}_i \otimes \mathbf{e}_j \tag{5.26}$$

The plastic spin tensor is defined as $\mathbf{W}^{\mathrm{p}} = \mathbf{\Omega} - \boldsymbol{\omega}$. Utilizing Eq.(5.26), $\mathbf{W}^{\mathrm{p}}$ is written as follows.

$$\mathbf{W}^{\mathrm{p}} = \mathbb{C} : \mathbf{D}^{\mathrm{p}} - \frac{1}{2} \sum_{i \neq j,\, w_i \neq w_j} \frac{w_i^2 + w_j^2}{w_i^2 - w_j^2} (\mathbf{e}_i \otimes \mathbf{e}_j + \mathbf{e}_j \otimes \mathbf{e}_i) : \mathbb{A} : \mathbf{D}^{\mathrm{p}} \mathbf{e}_i \otimes \mathbf{e}_j \tag{5.27}$$

5.2.2 Finite element model

Using the KB model, the combined effect of plastic anisotropy, void shape, loading orientation on the tendency to localization of plastic strain is systematically investigated for two geometries – a) round notched bars having $\zeta = 10$ with ζ representing the notch severity parameter as explained in Chapter 2 and b) plane strain bars.

In the KB model, the following material properties are used for the simulations in this study: $\sigma_{\mathrm{S}} = 420$ MPa is the initial yield stress of the matrix material along $\mathbf{e}_{\mathrm{S}}$, $N = 0.1$ is the hardening exponent and $\epsilon_0 = 0.002$ is a constant strain offset. For the results shown here, the following materials are selected – isotropic, transversely isotropic material ib which is weak in shear in planes perpendicular to L-T, transversely isotropic material iii which is shear resistant in planes perpendicular to L-T

and material AZ31 (representative of Magnesium alloys) which is an anisotropic material. The isotropic, ib and iii are materials that have equal yield stresses in tension along the principal directions of orthotropy which leads to roughly similar values of effective yield stresses. This can be beneficial while comparing different materials. All Hill coefficients for the isotropic matrix has a value of 1. The transverse isotropy of Mat ib is characterized by the equal values of the hill coefficients h_{TS} and h_{SL} with the direction of transverse isotropy along $\mathbf{e}_{\mathrm{S}}$. For the anisotropic AZ31, all the hill coefficients have different values. In all the results shown here, the void axis is initially aligned along the loading direction unless the void is spherical.

The typical range of porosities generated due to nucleation at second phase particles in materials are between 10^{-4} and 10^{-2}. Although, nowadays, the effective initial porosities existing in various processed alloys can be less than 10^{-4}, for the simulations conducted in this study an initial porosity of $f_0 = 10^{-4}$ is assumed and is considered to be representative of actual porosities in typical engineering materials. In addition, to explore the case localization in a damage free material, an initial porosity value of 10^{-7} is also considered for one particular case of simulation. The values of initial void shapes explored are $w_0 = 1$ and 6, corresponding respectively to spherical and prolate voids. These are representative of void shapes existing in real materials with the void shape as spherical in the case of equiaxed voids, and prolate when they are originate from inclusions previously elongated by a manufacturing process. As an example, prolate voids with aspect ratios even greater than 20 can be found in rolled steel plates with MnS inclusions, see [19].

The meshes used in the simulation (Fig. 5.2, Fig. 5.3) consisted of the 20-noded quadratic quadrilateral elements (C3D20R) with reduced integration (2 x 2 x 2 integration points). The boundary conditions are specified as follows: A uniform displacement U is prescribed on the top surface in the Y direction and the bottom

surface of the bar is fixed. Initially flat elements are used in the regions where necking is expected since the elements therein would undergo significant elongation in the direction of major axial stress. Table.5.1 shows the Hill coefficients for the materials used in the simulations and Table.5.2 shows the different variables and their values used in the simulations. In the calculations presented here, the loading direction is always along the Y axis and the orthotropy axes are misaligned by an angle θ with respect to the loading axes as shown in Figure. 5.1. Also in whichever cases where a shear band is observed, the orientation of the shear band with respect to the loading direction is denoted by the angle ψ in the results of following sections. All the calculations presented here are stopped after void coalescence as predicted by the [21] coalescence criterion is met at 50 integration points.

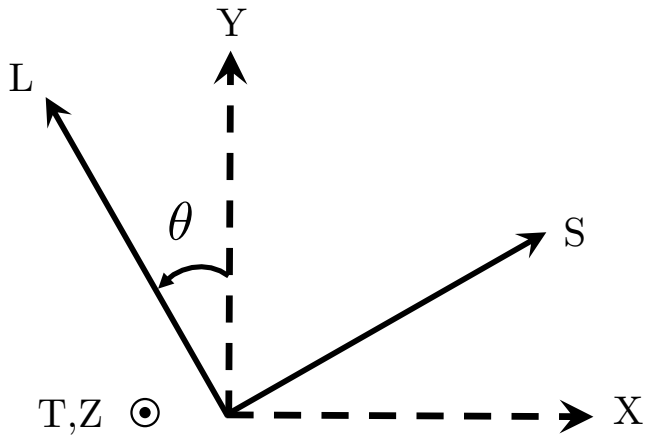

Figure 5.1: Orientation of the orthotropy axes with respect to the loading axes

Table 5.1: Hill coefficients for the materials used in this study

Calculation	h_{L}	h_{T}	h_{S}	h_{TS}	h_{SL}	h_{LT}	h
Isotropic	1.000	1.000	1.000	1.000	1.000	1.000	2.000
Mat ib (trans.iso)	1.000	1.000	1.000	2.333	2.333	1.000	1.757
Mat iii (trans.iso)	1.000	1.000	1.000	0.5	0.5	1.000	2.366
AZ31(anisotropic)	1.170	0.920	0.400	1.780	1.600	1.030	2.090

Table 5.2: Parameter values used in this study

Parameter	Values Employed
f_0	10^{-4}, 10^{-7}
w_0	1, 6
Initial void axis	along the loading (Y) direction
θ	0, 15, 30, 45, 60, 75

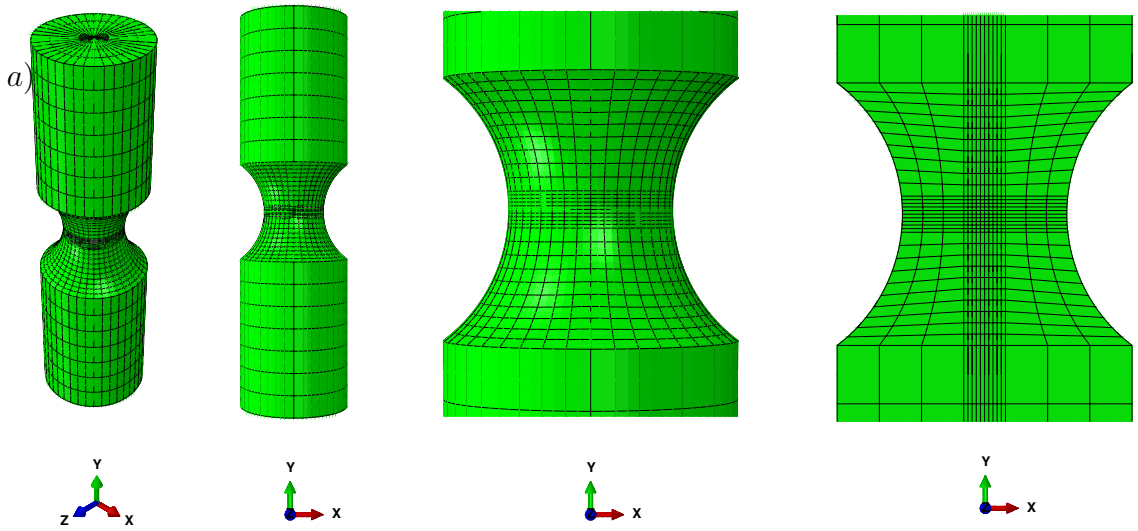

Figure 5.2: Geometries and mesh used for the simulations. a) RN10 bars - respectively the isometric, frontal, zoomed in view of the notch and the inside cut view.

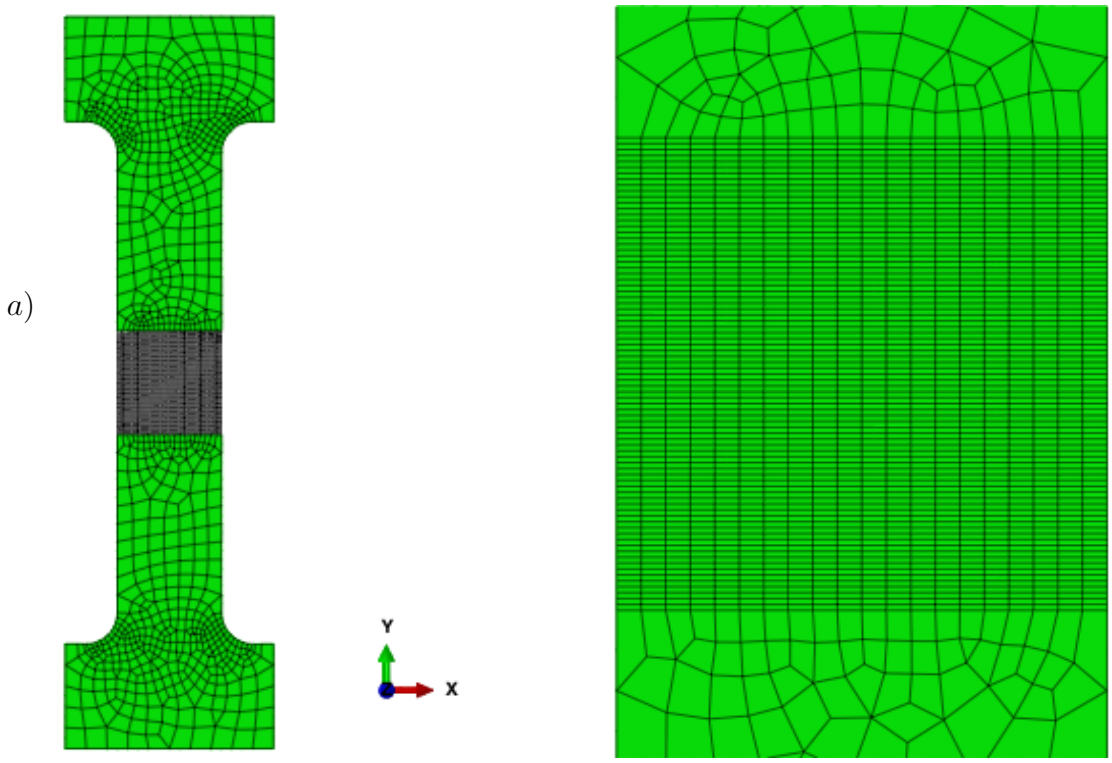

Figure 5.3: Geometries and mesh used for the simulations. a) Plane strain specimen and zoomed in view of centre part of the plane strain specimen.

5.3 Results

In the following sections, the results corresponding to simulations in notched bars are presented first, followed by the case of plane strain bars. For the notched geometry, four different material cases are presented – isotropic, material ib, material iii and AZ31 for different values of θ. For the plane strain case, only one material was considered– transversely isotropic material ib which is weak in shear along the plane of transverse isotropy. In the results for all the geometries, the key question addressed is how crucial is the role of plastic anisotropy in aiding the tendency to

shear localization and if the initial value of damage makes any difference in the localization behavior for the two geometries presented.

5.3.1 Simulations on notched bars

In the simulations of notched bars presented here, three classes of materials are explored-isotropic, transversely isotropic and anisotropic material. Among the transversely isotropic materials ib and iii considered, as indicated by the value of shear Hill coefficients, material ib is weak in shear along the plane of transverse isotropy and material iii is shear resistant along its plane of transverse isotropy. For the case of material ib, six cases of θ are explored, *viz.*, 0°, 15°, 30°, 45°, 60° and 75°.

5.3.1.1 Isotropic matrix material

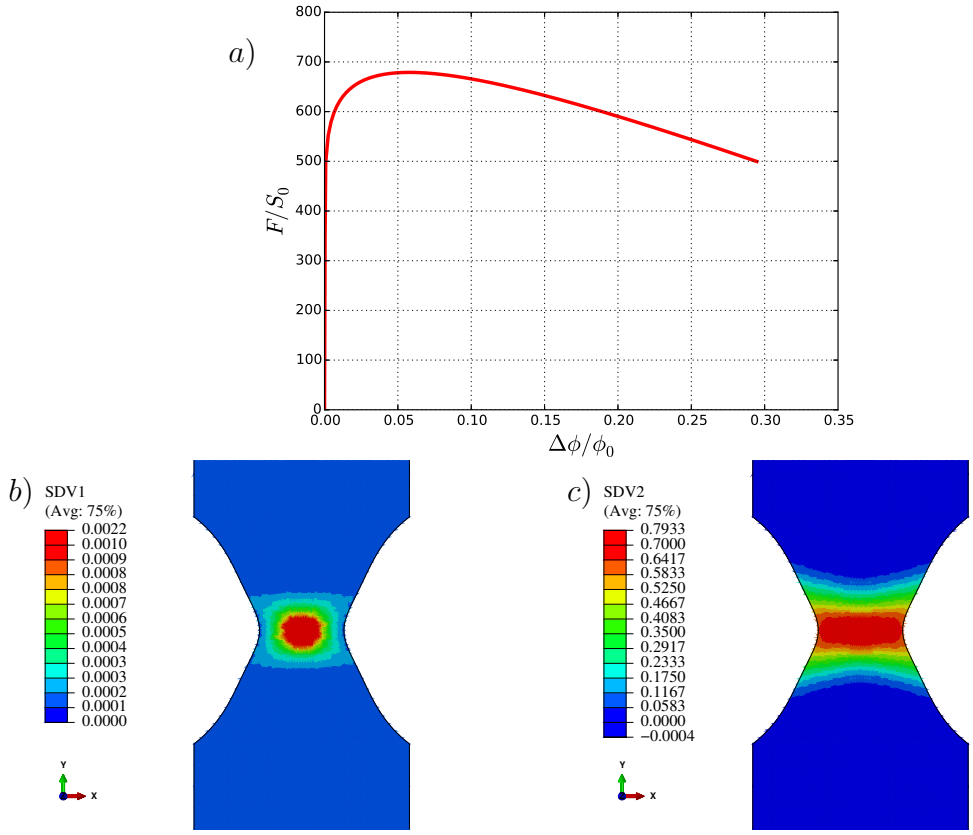

Figure 5.4: For RN10 specimen of isotropic material with initial aspect ratio $w_0 = 1$ and initial porosity $f_0 = 10^{-4}$ a) Load versus diameter reduction b) Porosity c) Plastic strain

The case of isotropic matrix material is first demonstrated so as to enable suitable comparisons with the case of plastically anisotropic materials towards showcasing the role of plastic anisotropy in inducing shear bands. Although a 2D axisymmetric calculation would have sufficed for this case, since a 3D mesh was available, it was employed for the calculation. The load versus diameter reduction and the contours of

porosity and plastic strain in the LS plane for the case of isotropic material properties for an initial porosity of $f_0 = 10^{-4}$ and initial aspect ratio of $w_0 = 1$ are shown in Fig. 5.4. The porosity is concentrated at the centre where the triaxiality and plastic strain are maximum. In the case of plastic strain, it can be observed that it is confined to the minimum cross section of the notched bar with maximum value at the centre. As it can be observed, there are no shear bands occurring in the notched bar for the isotropic material case and the concentration of plastic strain at the centre is brought about by the geometry of the notch. Similar are the contours for for the case of isotropic material with higher initial porosity of $f_0 = 10^{-2}$ and is not shown here for brevity. Thus, for notched bars of isotropic matrix material, tendency for shear localization is not observed and since there is no change in behavior even with higher values of initial porosity, for these cases, initial value of damage does not play a role in aiding localization. The results are consistent with that of Needleman and Tvergaard [100] who presented a wide range of parameter sensitivity analyses using the GTN model. Most of the parameters varied therein are kept fixed in the present study to focus on anisotropy.

5.3.1.2 Case of $\theta = 45°$ for material ib

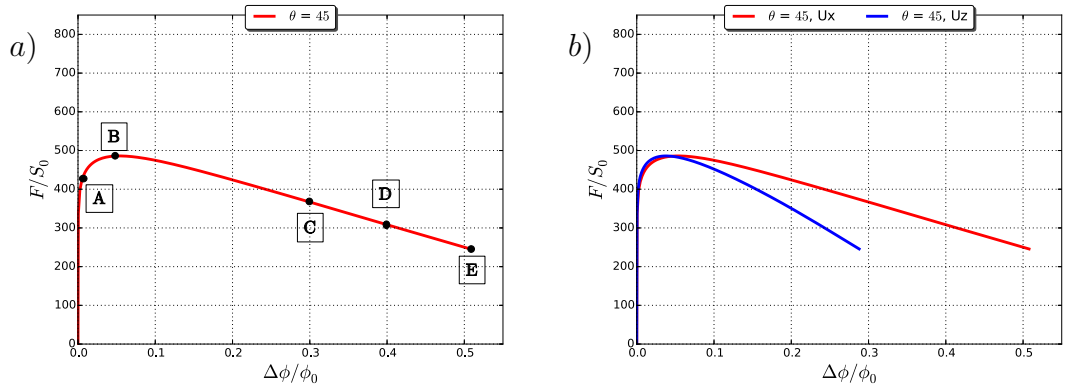

Figure 5.5: Load versus diameter reduction for RN10 specimen of material ib with $w_0 = 1$, $f_0 = 10^{-4}$ for $\theta = 45°$ a) Along X b) Along X and Z

The load versus diameter reduction curve for the case of $\theta = 45°$ for material ib is shown in Fig. 5.5. Various points on the curve are labeled from A–E with A being a point before the limit load is reached and B is the point of maximum load, E is the final point on the load curve with C and D being two intermediate points. The contours of plastic strain and porosity corresponding to these points are shown in Fig. 5.6a and Fig. 5.6b respectively. After the limit load is reached, gradual reduction in the load bearing capacity can be observed from the macroscopic response in Fig. 5.5. Recall that this is material ib whose axis of transverse isotropy is the S axis. Fo this case, given that $\theta = 45°$, the Z axis coincides with T axis with L and T axes rotated at an angle of 45° with respect to the Z axis in the anti clockwise sense when looking down the Z axis. As it can be seen from Fig. 5.6a, the evolution of plastic strain an the concentration of plastic strain occurs in certain

particular directions. Recall that for this material, $h_{\mathrm{TS}} = 2.33$ and $h_{\mathrm{SL}} = 2.33$ with all other Hill coefficients equal to 1. Even though the material is transversely isotropic, since it is not loaded along the axis of transverse isotropy, the material has preferred directions along which the plastic strain concentrates, depending upon the value of Hill coefficients and the values of stress components imparted by remote loading. In this case the response of the material is brought about by the interplay between high shear Hill coefficients and the components of shear stresses along the LS, LT and TS planes. However, the strain concentration bands seen from 'A' to 'E' are not shear bands, but deformation bands which are caused by the plastic anisotropy of the material.

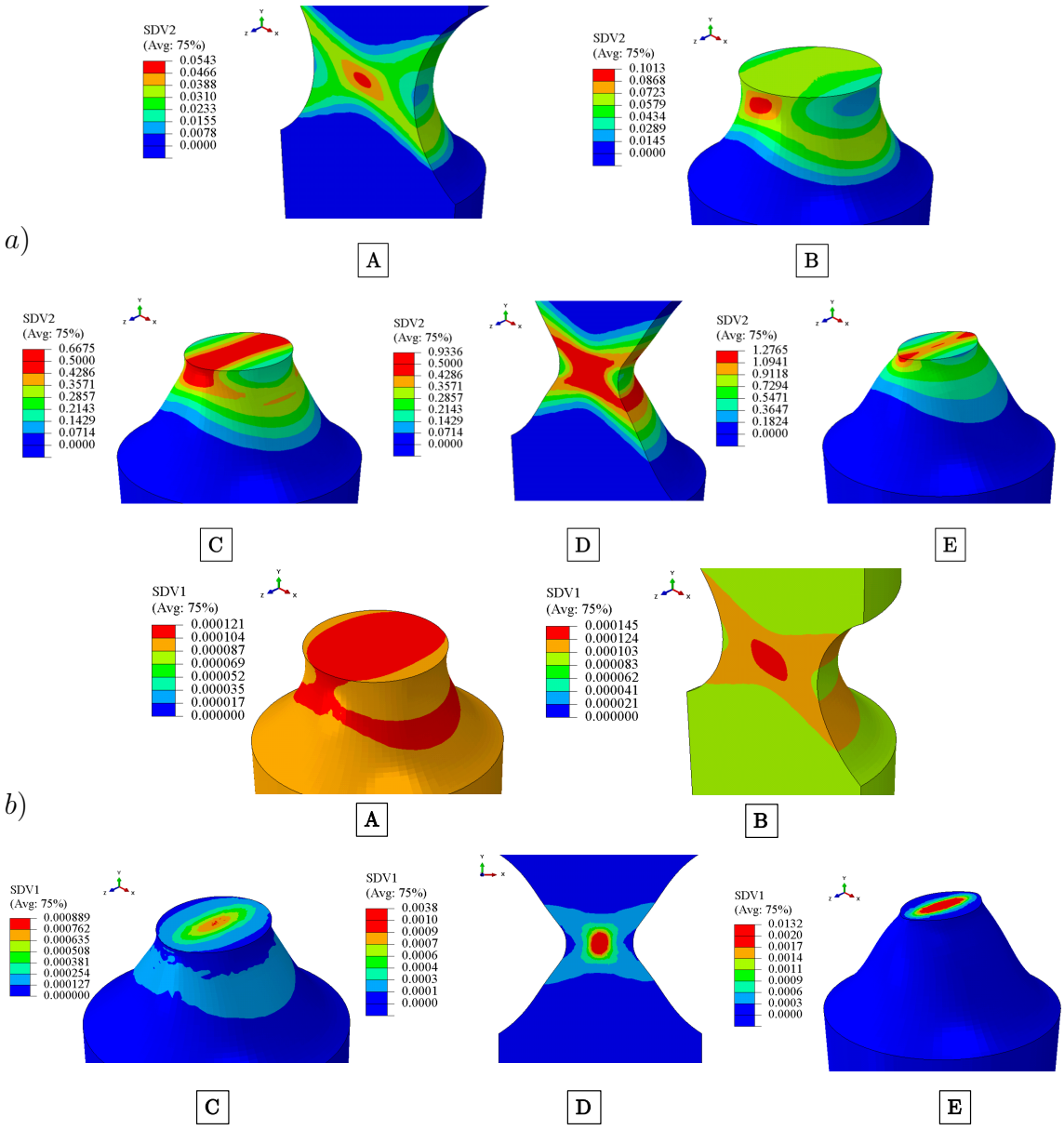

Figure 5.6: For RN10 specimen of material ib with $w_0 = 1$, $f_0 = 10^{-4}$ for $\theta = 45°$, corresponding to various stages of loading A–E as marked on the load displacement curve in Fig. 5.5a a) Plastic strain b) Porosity

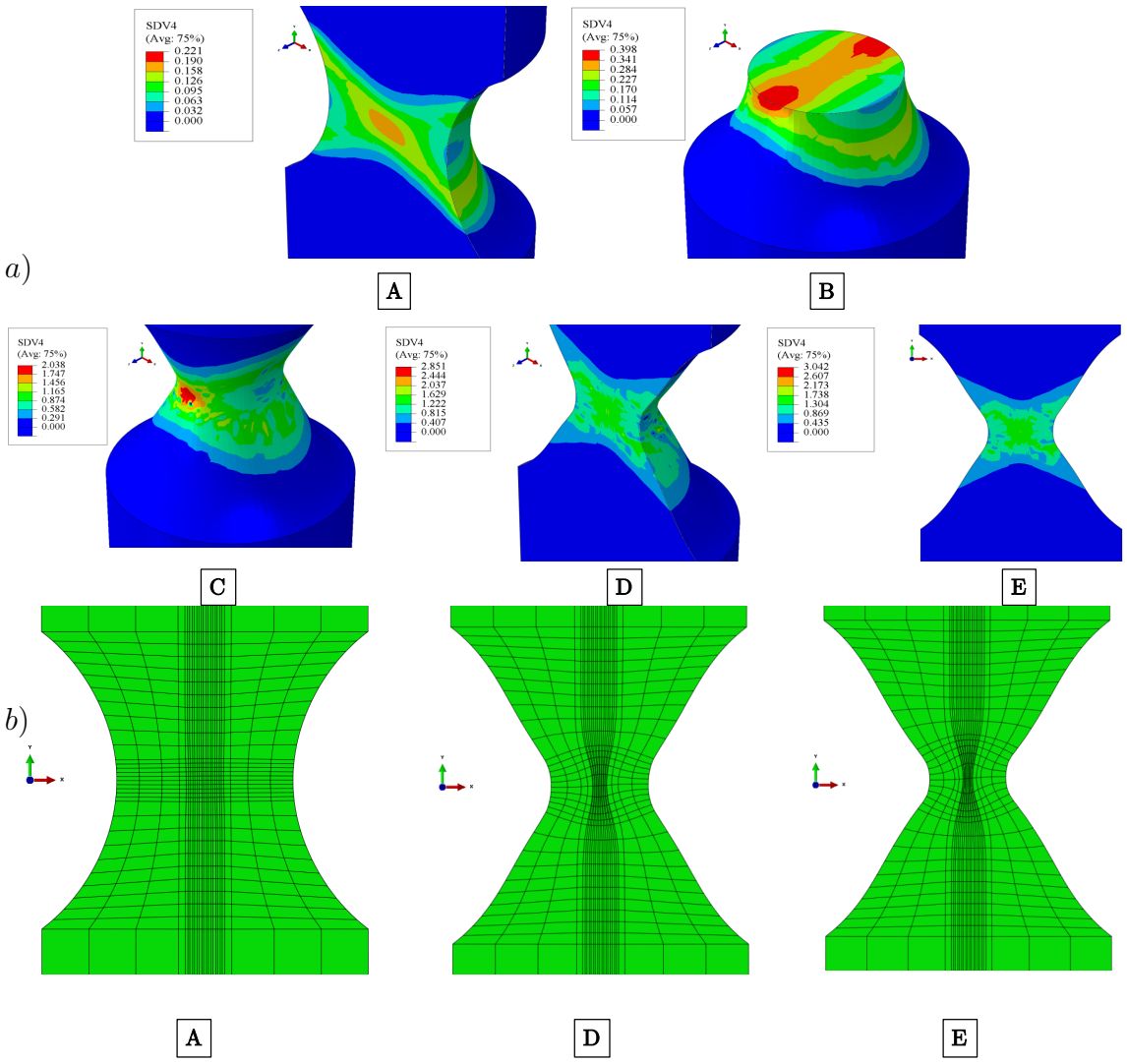

Figure 5.7: For RN10 specimen of material ib with $w_0 = 1$, $f_0 = 10^{-4}$ for $\theta = 45°$, corresponding to various stages of loading A–E as marked on the load displacement curve in Fig. 5.5a a) Contours of $\ln(w)$ b) Deformed meshes corresponding to A, D and E

The deformation bands can be seen very early on in this case as observed form the 3D view of plastic strain contours corresponding to 'A' in Fig. 5.6a. From 'B' and 'C' plastic strain concentration along the T direction also can be observed. Thus in the

cross sectional plane of the notched bar, the plastic strain is concentrated along the T direction, whereas in the LS plane it is concentrated in two deformation bands where the angle made by the less prominent band with respect to the X axis is 35° and the angle of the most prominent band is 145°. This is more evident from the 3D view in 'D'. In the case of porosity also, the development concentrates along two bands in the LS plane as seen from 'A' and 'B' of Fig. 5.6b and in the LT plane, similar to the case of plastic strain, porosity is concentrated along the T direction. In the case of porosity, initially from 'A' and 'B', it can be seen as increasing at the surface as well as the centre and then due to the effect of triaxiality and plastic strain, it develops along two bands in the LS plane and along the T direction in the LT plane. The tendency of porosity to concentrate along these bands is a direct consequence of porosity evolution being driven by plastic strain. In Fig. 5.7a, the contours of logarithm of the void aspect ratio at various stages are shown. It can be seen that elongation of void happens near the surface as well as inside the deformation bands as expected. It is important to keep in mind that for this case of $\theta = 45°$, the loading direction is symmetric with respect to the L and S directions and although plastic deformation bands are observed, no shear localization can be observed as is evident from the deformed meshes shown in Fig. 5.7b. Also it is not clear if the occurrence of these deformation bands in the material can lead to shear localization or development of instability, especially for some other case in which the anisotropy axes L and S are aligned asymmetrically with respect to the loading direction. This will be explored in a later section.

5.3.1.3 Comparison between $\theta = 0°$and $45°$ for material ib

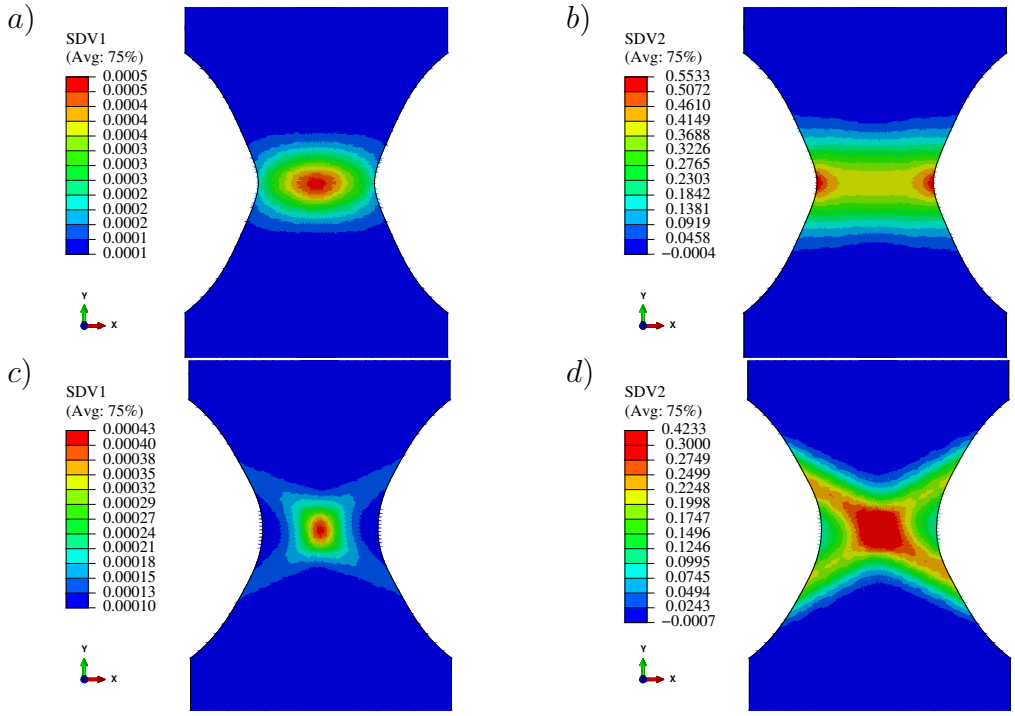

Figure 5.8: For RN10 specimen of material ib with $w_0 = 1$, $f_0 = 10^{-4}$ at $U/L = 0.11$ a) Porosity when $\theta = 45°$ b) Plastic strain when $\theta = 45°$ c) Porosity when $\theta = 0°$ d) Plastic strain when $\theta = 0°$

Fig. 5.8 compares the plastic strain and porosity contours for the matrix material ib when the orthotropy axes are at an angle of $\theta = 0°$ and $45°$ misaligned with respect to the loading direction. In the case of $\theta = 0°$, similar to the case of isotropic material, the porosity is concentrated at the centre. The plastic strain which has maximum value at the notch root and is concentrated at the minimum cross section. However, in the case when $\theta = 45°$, porosity shows clear tendency for evolution in two bands, with maximum value being at the centre. For this case, the plastic strain also shows

two deformation bands with one band tending to have more concentration of plastic strain when compared to the other. These cases demonstrate that for a transversely isotropic material, a misaligned loading configuration (where the loading axes are misaligned with that of the principal axes of orthotropy) can aid the development of deformation bands of plastic strain which are not necessarily shear bands.

5.3.1.4 Comparison between two initial values of void shape for $\theta = 45^\circ$ for material ib

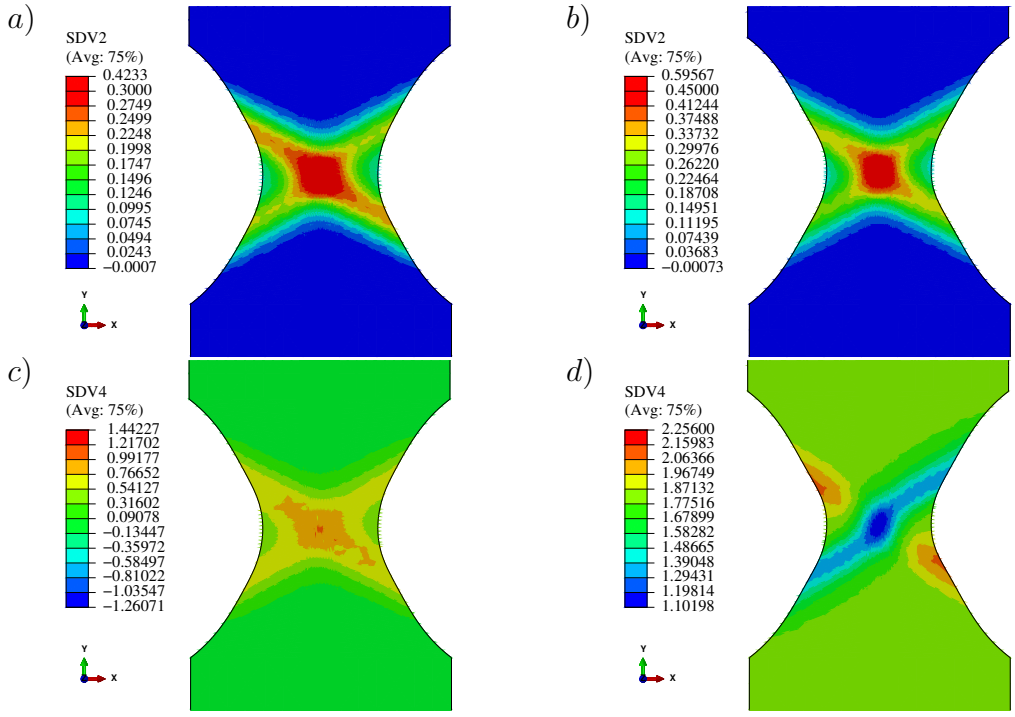

Figure 5.9: For RN10 specimen of material ib with $f_0 = 10^{-4}$ and $\theta = 45^\circ$ at $U/L = 0.11$ a) Plastic strain with $w_0 = 1$ b) Plastic strain with $w_0 = 6$ c) Contours of $\ln(w)$ with $w_0 = 1$ d) Contours of $\ln(w)$ with $w_0 = 6$

Previous result was for the case of initially spherical void shape. However for a case of prolate void shape with initial aspect ratio of $w_0 = 6$ also, deformation bands of plastic strain are observed as seen from Fig. 5.9 which compares the $w_0 = 1$ and $w_0 = 6$ cases for $f_0 = 10^{-4}$ and $\theta = 45°$. Although these bands are a consequence of plastic anisotropy, it is worth noting that the evolution of the void shapes in the LS plane in both the cases is entirely different. In the case of initially spherical voids, the void aspect ratio keeps on increasing in the most prominent deformation band whereas in the case of initially prolate voids, in one of the bands the void aspect ratio keeps decreasing and in the other band it increases. It can be seen from Fig. 5.9c and Fig. 5.9d that in the case of $w_0 = 1$, the void shape evolution is maximum at the centre whereas in the case of $w_0 = 6$, elongation of the void shape happens near the surface. This showcases that although macroscopically the deformation bands looks similar in the case of two void shapes, the microscopic evolution inside the band can be entirely different and this can have implications for ductile failure by coalescence of voids inside these deformation bands.

5.3.1.5 Case of $\theta = 30°$ for material ib

The above results were for the case of material ib for $\theta = 45°$. In this section, the asymmetric case of $\theta = 30°$ is explored in detail to showcase the formation of shear bands in material ib for various stages of loading.

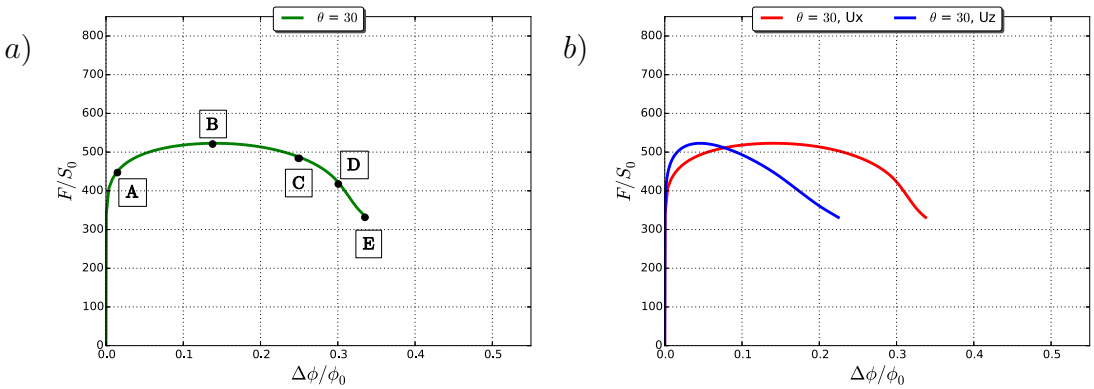

Figure 5.10: Load versus diameter reduction for RN10 specimen of material ib with $w_0 = 1$, $f_0 = 10^{-4}$ for $\theta = 30°$ a) Along X b) Along X and Z

The load versus diameter reduction curve for the case of $\theta = 30°$ for material ib is shown in Fig. 5.10. Various points on the curve are labeled from A–E with A being a point before the limit load is reached and B is the point of maximum load, E is the final point on the load curve with C and D being two intermediate points where the load drop is much more drastic that the previous locations. In the case of $\theta = 45°$, recall that shear bands were not observed and only deformation bands were observed within which plastic strain concentrated. In the case of $\theta = 30°$, similar to the case of $\theta = 45°$, initially the plastic strain concentrates in a band oriented along the TS plane which is inclined at an angle of 30° with respect to the XZ plane. For this material, given the values of $h_{\text{TS}} = 2.33$ and $h_{\text{SL}} = 2.33$ with all other Hill coefficients equal to 1, for the given loading configuration, the resolved shear stress along the TS plane being greater than that of SL plane drives the initial plastic strain deformation bands along the TS plane. This corresponds to 'A' and 'B' in Fig. 5.10a and the macroscopic contours of plastic strain and porosity can be seen from Fig. 5.11a. Then as the simulation progress, the deformation band moves

across the cross section of the notched bar and results in the development of a strong shear band in LT plane as seen from 'C', 'D' and 'E' of Fig. 5.11a. This is reflected by the change of slope of load displacement curve at points corresponding to 'C', 'D' and 'E' in Fig. 5.10a and is more evident from the deformed meshes corresponding to 'A', 'D' and 'E' in Fig. 5.12b. The abrupt reduction of load at 'D' corresponds to the intensification of plastic strain localization inside the shear band.

Comparing the load versus diameter reduction for $\theta = 30°$ and $\theta = 45°$ (Fig. 5.5a), it can be seen that the limit load in the case of $\theta = 30°$ is slightly higher than that of $\theta = 45°$. However the ductility in the case of $\theta = 30°$ is much lesser than that of $\theta = 45°$. In addition to limiting ductility, the sudden load drop also, induced by shear localization in the case of $\theta = 30°$ is much more prominent when compared to that of $\theta = 45°$. More insights into the differences between the case of $\theta = 30°$ and $\theta = 45°$ happening at the macroscopic level can be understood by looking into the microscopic contours of plastic strain and porosity and comparing it to the $\theta = 45°$ case. The orientation of the shear band in the case of $\theta = 30°$ is seen to be $\psi_1 = 50°$. In fact, upon close examination (as portrayed in Fig. 5.13) the shear band can be observed to have a central portion at an angle of 50° and two parallel portions of 60° when approaching the free surfaces of the notched bar. This can be thought of as the result of shear band being influenced by the necking induced material rotation happening in near the surface of the notched bar.

When the deformation band changes to the shear band in the LT plane, the location of accumulation of plastic strain in the cross section of notched bar where plastic strain is accumulated along the T direction, changes from near the boundary of notched bar at stage 'A' to the centre of the notched bar at stage 'E'. This is in contrast to the case of $\theta = 45°$ where the plastic strain accumulation was along the T direction and at the centre of the cross section all through the deformation history.

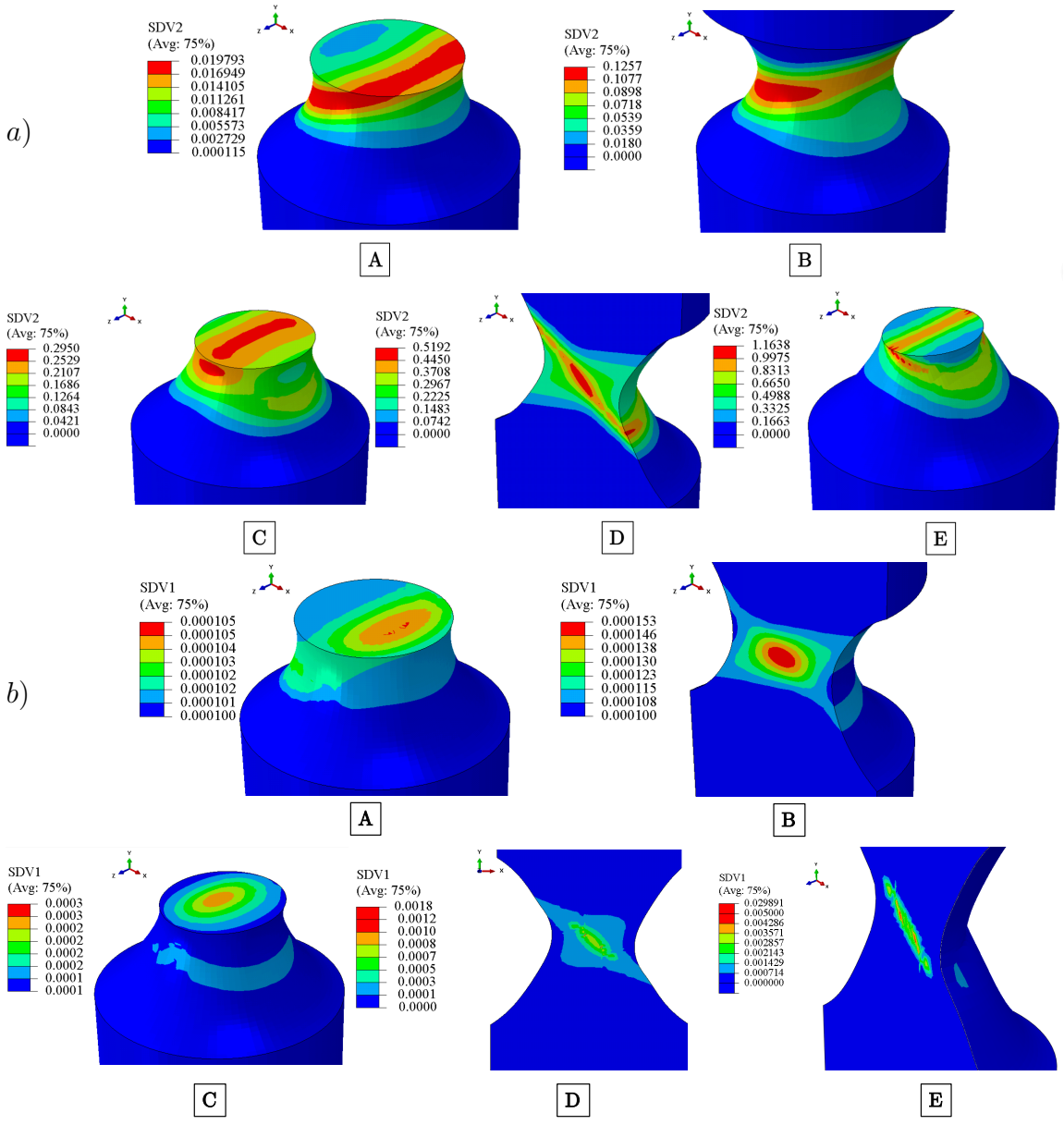

Figure 5.11: For RN10 specimen of material ib with $w_0 = 1$, $f_0 = 10^{-4}$ for $\theta = 30°$, corresponding to various stages of loading A–E as marked on the load displacement curve in Fig. 5.10a a) Plastic strain b) Porosity

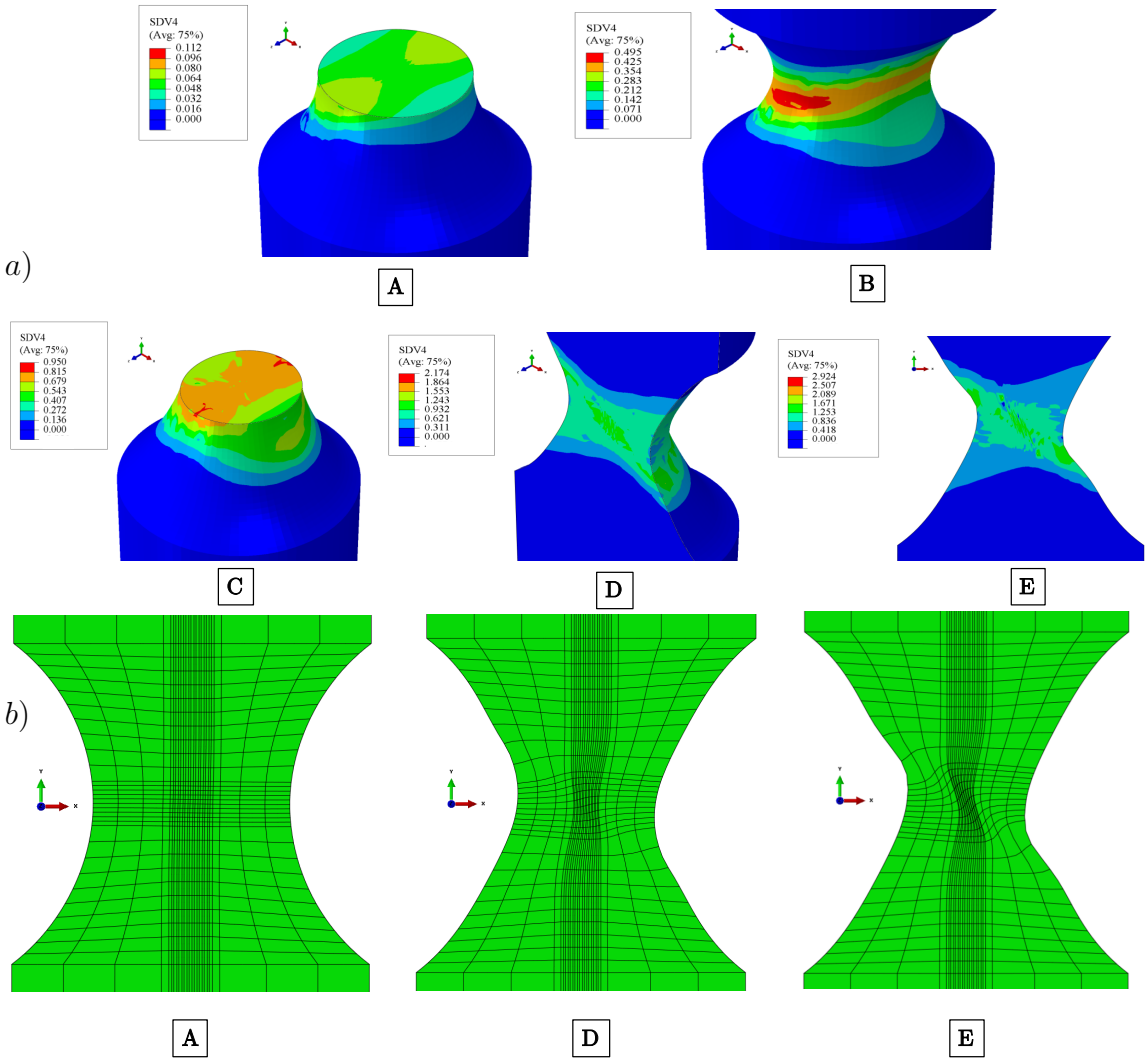

Figure 5.12: For RN10 specimen of material ib with $w_0 = 1$, $f_0 = 10^{-4}$ for $\theta = 30°$, corresponding to various stages of loading A–E as marked on the load displacement curve in Fig. 5.10a a) Contours of $\ln(w)$ b) Deformed meshes corresponding to A, D and E

The contours of porosity as seen from Fig. 5.11b also closely follows that of plastic strain with the maximum near the boundary corresponding to stage 'A' and moving towards the centre corresponding to stage 'E'. For this case also the first instance of void coalescence was reported to take place inside the shear band but away from the centre in the LS plane of the notched bar as seen from the porosity contours corresponding to stage 'E' in Fig. 5.11b.

It is well known that with damage models such as the one employed here, the mechanical response may exhibit mesh sensitivity because of the porosity-induced softening. In notched bars, this effect is small, but not negligible. In addition, when strain localization occurs as in the case of $\theta = 30°$, the thickness of the shear band is dependent on discretization. To investigate this, a calculation was carried out using a finer mesh (halving the mesh element size in the region where shear bands were found to form). At the time of writing, the 3D calculation was still running. The formation of the early deformation band dictated by the initial misorientation was found to be independent of mesh size. The above results were for the case of material ib for $\theta = 45°$ and $30°$. In the next few sections, the effect of the angle of misalignment θ in the formation of shear bands in notched bars of material ib is explored for other values of θ.

5.3.1.6 Comparison between $\theta = 0°$and $30°$ for material ib

The evolution of porosity and plastic strain along a path across the cross section (indicated by red line in Fig. 5.14b) of the notched bar for the case of $\theta = 30°$ and $\theta = 0°$ at the final stage of simulation are compared in Fig. 5.14c and Fig. 5.14d. For the case of $\theta = 0°$, no shear bands were formed and for the case of $\theta = 30°$, shear bands were observed. It can be seen from Fig. 5.14c that the plastic strain is concentrated at the centre of the specimen for the case of $\theta = 30°$ and the presence of

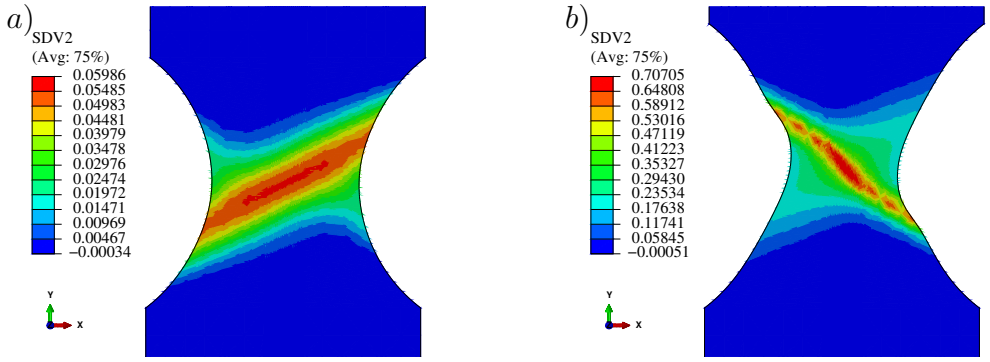

Figure 5.13: For RN10 specimen of material ib with $w_0 = 1$, $f_0 = 10^{-4}$ and $\theta = 30°$ a) Plastic strain at $U/L = 0.01$ b) Plastic strain at $U/L = 0.12$

shear band causes it to have a localized increase in plastic strain inside of the band. Compared to the case of $\theta = 30°$, the maximum value of plastic strain in the case of $\theta = 0°$, is at the free surface of the notched bar. Although the maximum value of plastic strain is more for the case of $\theta = 0°$, the distribution of plastic strain in this case is uniform across the midsection. The distribution of porosity along the path for these two cases also follows the same trend, as seen from Fig. 5.14d, with porosity concentrating in the shear band for the case of $\theta = 30°$. For the $\theta = 0°$, note that the maximum value of porosity is not occurring at the centre, but away from it. The evolution of porosity and void aspect ratio for the case of $\theta = 30°$, at two points, one inside the shear band and another outside the shear band are shown in Fig. 5.14e and Fig. 5.14f respectively. It can be seen that for the case of $\theta = 30°$, the porosity as well as void aspect ratio increases at a much faster rate inside the shear band when compared to that at a location outside of the band.

5.3.1.7 Matrix material ib with $\theta = 15°$

When the angle of misalignment of the orthotropy axes with respect to the loading direction is $\theta = 15°$, as seen from Fig. 5.15, in the initial stages of deformation, the

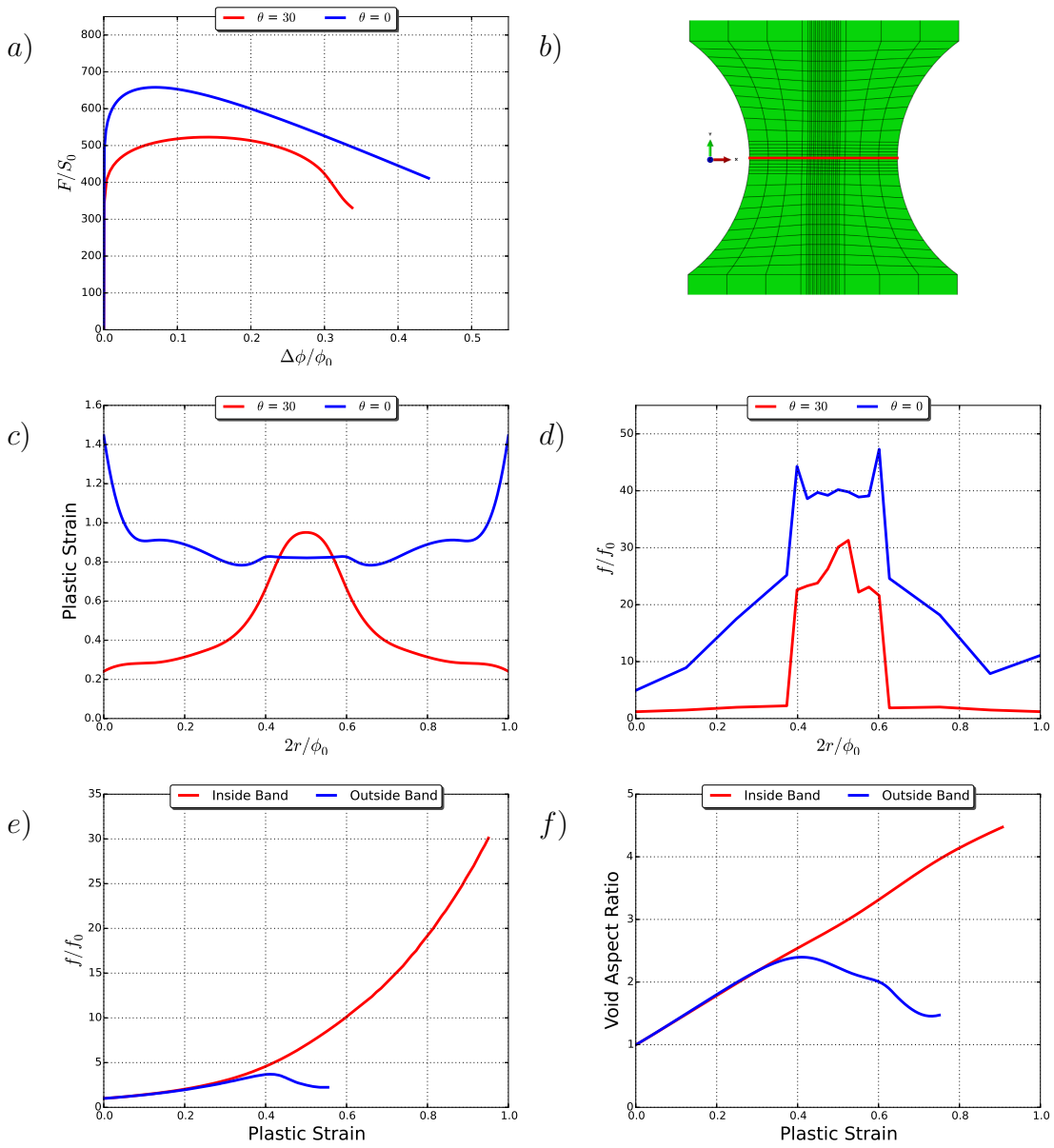

Figure 5.14: For RN10 specimen of material ib with $w_0 = 1$, $f_0 = 10^{-4}$ a) Load versus diameter reduction along X for $\theta = 30°$ and $\theta = 0°$ b) Path across the cross section indicated by red line c) Plastic strain along the path for both cases d) Porosity along the path for both cases e) Comparison of porosity evolution inside and outside of shear band for the case of $\theta = 30°$ f) Comparison of void aspect ratio inside and outside of shear band for the case of $\theta = 30°$

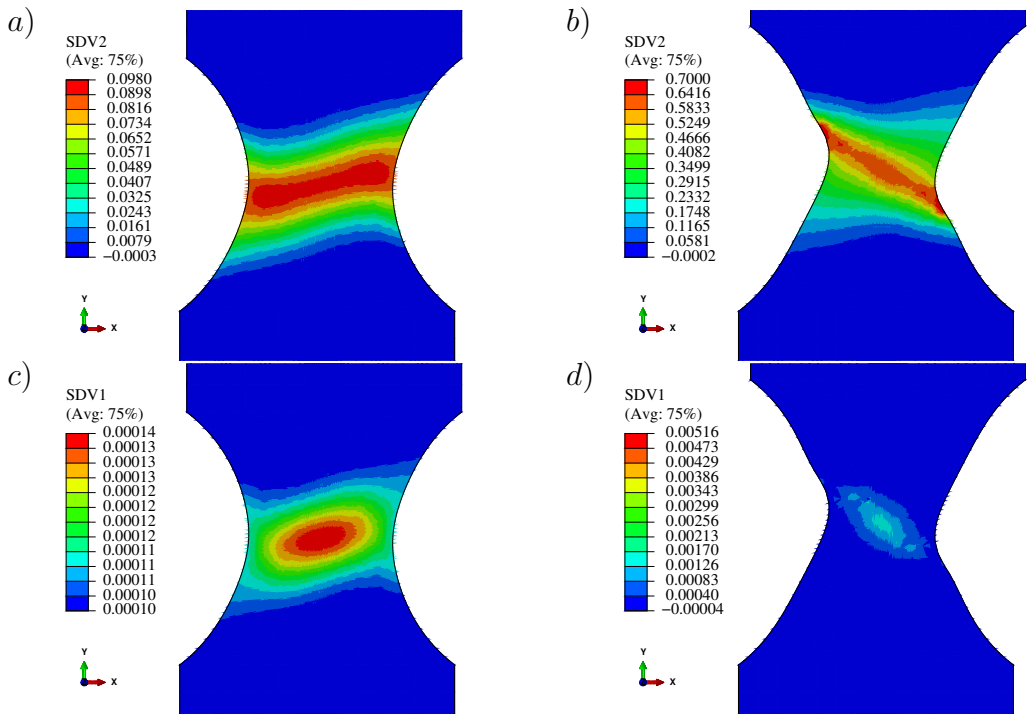

Figure 5.15: For RN10 specimen of material ib with $w_0 = 1$, $f_0 = 10^{-4}$ and $\theta = 15°$ a) Plastic strain at $U/L = 0.03$ b) Plastic strain at $U/L = 0.16$ c) Porosity at $U/L = 0.03$ d) Porosity at $U/L = 0.16$

plastic strain and porosity in the LS plane are inclined at an angle 105° with respect to the loading direction. However in the later stages of deformation, the deformation bands of plastic strain evolve into a shear band that makes an approximate angle $\psi_1 = 30°$ with respect to the loading direction. Also in this case, it must be noted that similar to the case of $\theta = 30°$, only one shear band is observed in the case of $\theta = 15°$. In addition, the location of maximum damage changes from the centre of the notched bar to two locations inside the shear band but away from the centre as seen from Fig. 5.15c and Fig. 5.15d. For this case, after the localization of strain and porosity in the shear band, the first instance of void coalescence was reported not at the centre, but away from the centre where the damage accumulation was maximum. Also in this case, note the fact that in this case the damage has increased by only one order of magnitude from an initial value of $f_0 = 10^{-4}$ which is two orders of magnitude smaller when compared to the case of 30° misalignment for the initial porosity value of $f_0 = 10^{-4}$ and at the similar macroscopic loading stage.

5.3.1.8 Matrix material ib with $\theta = 60°$

The contours of plastic strain and porosity in the case of $\theta = 60°$ is also qualitatively similar to the previous cases. However in contrast to the $\theta = 15°$ and $\theta = 30°$ cases, the initial deformation band in the case of $\theta = 60°$ makes an acute angle with respect to the loading direction. Then upon further deformation this angle changes to an obtuse value and the deformation band evolves into a shear band. The orientation of the shear band at the centre is $\psi_1 = 130°$ and when approaching the free surface, the orientation angle reduces. In the case, however, the maximum plastic strain was not taking place at the centre of the specimen in the LS plane; but on the free surface of the notched bar as seen in the 3D view presented in Fig. 5.16e and Fig. 5.16f. However the first instance of void coalescence was reported at inside the

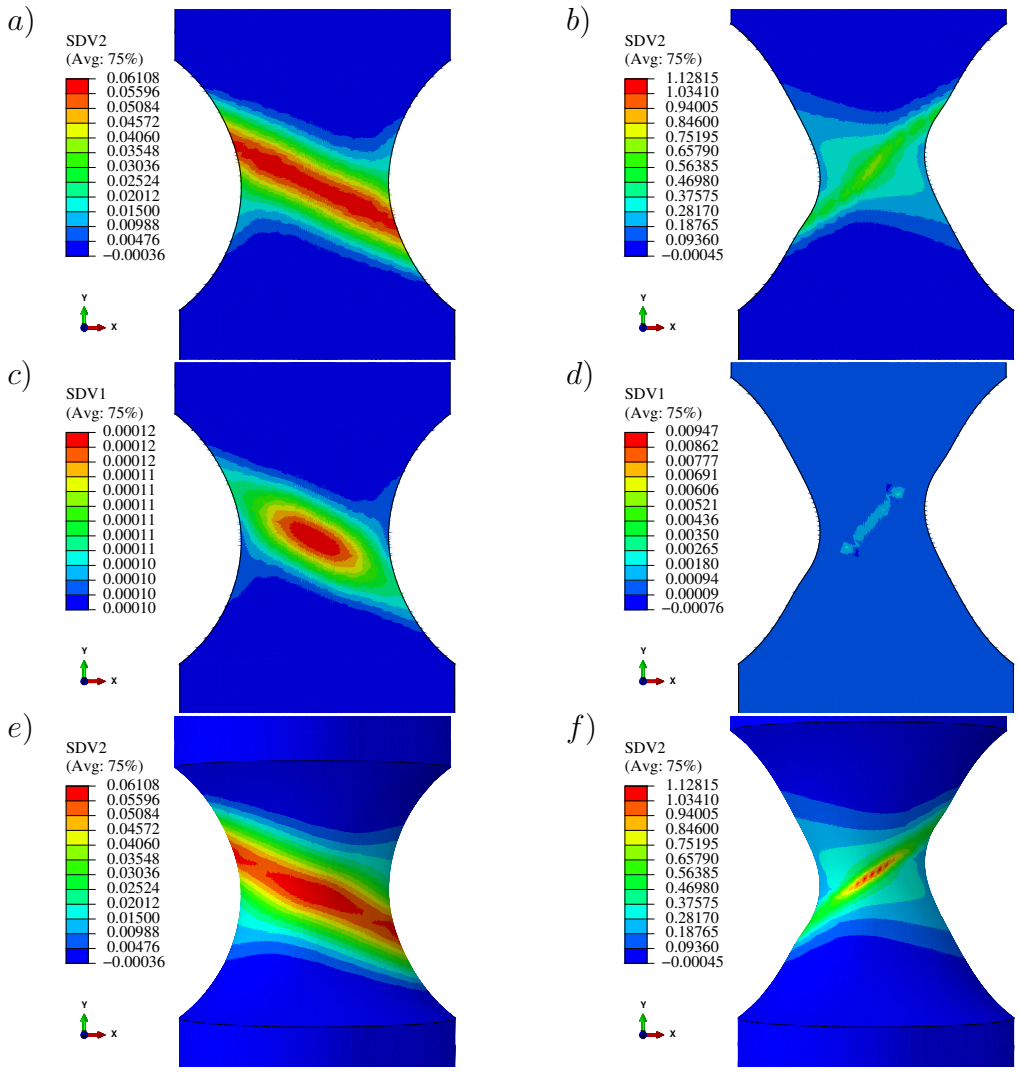

Figure 5.16: For RN10 specimen of material ib with $w_0 = 1$, $f_0 = 10^{-4}$ and $\theta = 60°$ a) Plastic strain at $U/L = 0.02$ b) Plastic strain at $U/L = 0.2$ c) Porosity at $U/L = 0.02$ d) Porosity at $U/L = 0.2$ e) Plastic strain at $U/L = 0.02$ (3D view) f) Plastic strain at $U/L = 0.2$ (3D view)

shear band a little bit away from the centre, in the LS plane where the maximum value of damage was observed (Fig. 5.16d). Another important aspect to note is that this case also presents with considerable shearing along the shear band as seen from Fig. 5.16f, although the remote loading is tensile and only along the Y direction.

5.3.1.9 Matrix material ib with $\theta = 75^\circ$

When $\theta = 75^\circ$, the contours are similar to the case of $\theta = 60^\circ$ with the only difference being the orientation of the initial deformation band and final shear band. The initial deformation band was oriented at an angle of 75° and the shear band appearing at the later stage has a value of $\psi_1 = 120^\circ$ as seen from Fig. 5.17a and Fig. 5.17b. Here also the orientation of the shear band changes when it approaches the free surface of the bar and considerable shearing takes place along the shear band even when the remote loading is tensile. In this case also, the maximum plastic strain is accumulated not at the centre of the notched bar in the LS plane but at the centre and at the surface of the notched bar when looking down the Z direction. (Fig. 5.17e, Fig. 5.17f)

5.3.1.10 Macroscopic response for matrix material ib

The load versus diameter reduction curves in the case of material ib, for all cases of θ considered are plotted in Fig. 5.18. The plot can also be interpreted as the response imparted by the shear Hill coefficients when loaded along various misaligned planes of loading. It can be observed that the aligned configuration or the $\theta = 0^\circ$ resulted in the maximum limit load among all the cases considered here. In all other cases where at least one shear band was observed, reduced strength as evidenced form the load displacement plots can be observed. $\theta = 45^\circ$ resulted in the least limit load among all cases. It should be noted that strong reduction in the load bearing capacity is most prominent for the cases of $\theta = 15^\circ$ and $\theta = 30^\circ$ and occurs in the

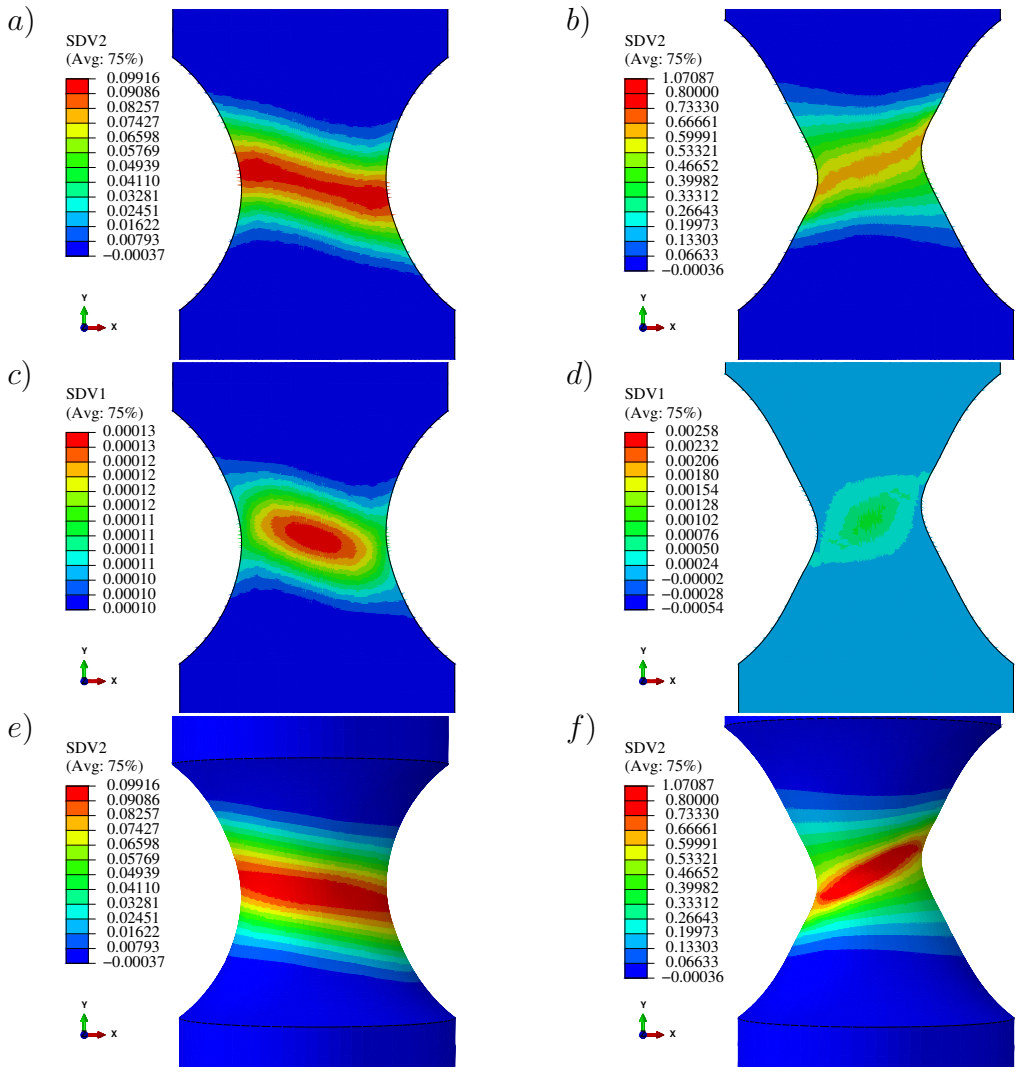

Figure 5.17: For RN10 specimen of material ib with $w_0 = 1$, $f_0 = 10^{-4}$ and $\theta = 75°$ a) Plastic strain at $U/L = 0.03$ b) Plastic strain at $U/L = 0.16$ c) Porosity at $U/L = 0.03$ d) Porosity at $U/L = 0.16$ e) Plastic strain at $U/L = 0.03$ (3D view) f) Plastic strain at $U/L = 0.16$ (3D view)

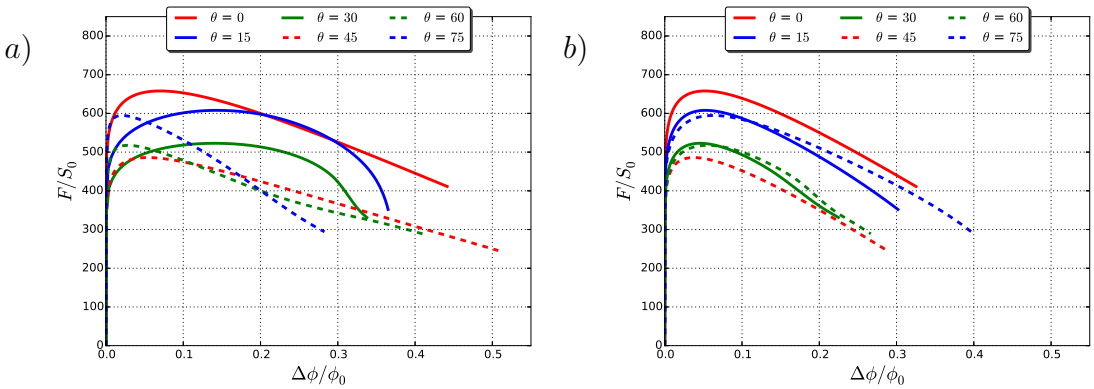

Figure 5.18: Load versus diameter reduction for RN10 specimen of material ib with $w_0 = 1$, $f_0 = 10^{-4}$ a) Along X b) Along Z

later stage of the simulation whereas in the case of $\theta = 60°$ and $\theta = 75°$, softening occurs very early on in the simulation. For these two cases, the rate of softening is much more than the other cases in the early stages of simulation and it keeps on constant in the softening regime. Whereas in the case of $\theta = 15°$ and $\theta = 30°$, the limit load is reached later in the simulation and once the limit load is reached the rate of softening increases drastically due to the intense shearing taking place along the bands.

5.3.1.11 Matrix material iii for $\theta = 45°$

For the matrix material ib which was weak in shear, as shown from the results of the previous sections, when the orthotropy axes where inclined at an angle of $\theta = 45°$ with the loading direction, deformation bands were observed. In addition, for other misaligned angles also at least one shear band was observed at later stages of loading. The large value of the shear Hill coefficients of material ib is what which makes it a weak in shear material. For similar conditions of loading, the contours of material iii which is shear resistant (due to its low shear Hill coefficient values)

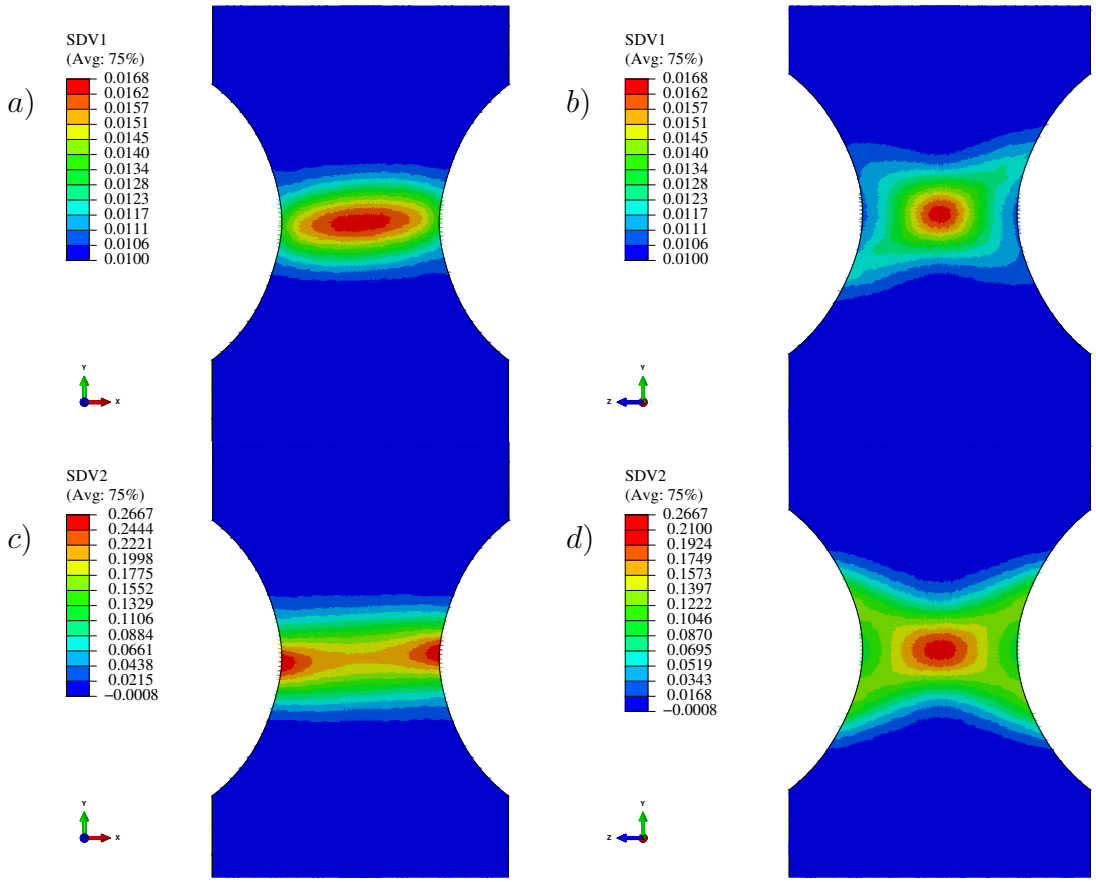

Figure 5.19: For RN10 specimen of material iii with $w_0 = 1$, $f_0 = 10^{-2}$ and $\theta = 45°$ a) Porosity in the LS plane b) Porosity in the LT plane c) Plastic strain in the LS plane d) Plastic strain in the LT plane all at $U/L = 0.05$

is shown in Fig. 5.19. Fig. 5.19a and Fig. 5.19c. The porosity and plastic strain contours in the LS plane demonstrates that for the identical conditions investigated for material ib, shear bands are not formed in material iii. Besides, the plastic strain in this material is concentrated near the surface of the notched bar at the minimum cross section with orientation of the deformation band in the LS plane taking a value very near to an angle of 0°. Recall that in the case of material ib, the deformation bands which were seen in the material had similar inclinations to the inclination of material axes L and S and for that material, for other values of θ, those initial deformation bands evolved into strong shear bands. In material iii, although there is a deformation band, its inclination is very near to an angle of 0° and this band didn't evolve into a shear band at later stages of simulation. However the plots in Fig. 5.19b and Fig. 5.19d which are the porosity and plastic strain contours in the LT plane can be interpreted as displaying a tendency for deformation banding in that plane and this can be attributed to the relative differences between values of h_{TS}, h_{SL} and h_{LT} shear Hill coefficients.

5.3.1.12 Material AZ31 for $\theta = 0°$

For the matrix material AZ31, the porosity and plastic strain contours in the LS plane and LT plane when $\theta = 0°$ (which is pulling along the L direction) are shown in Fig. 5.20. All the Hill coefficients of this material are different from 1 which makes the material anisotropic. However for $\theta = 0°$, ie when the orthotropy axes are aligned with the axes of loading, the plastically anisotropic nature of this material is not seen to be resulting in the formation of shear bands as seen from the plots in two planes. In the LS and the LT planes, the porosity is concentrated at the centre and it is not localizing in a band. Similar is the case with the plastic strain which in the LS plane is concentrated at the minimum crossection with the maximum value

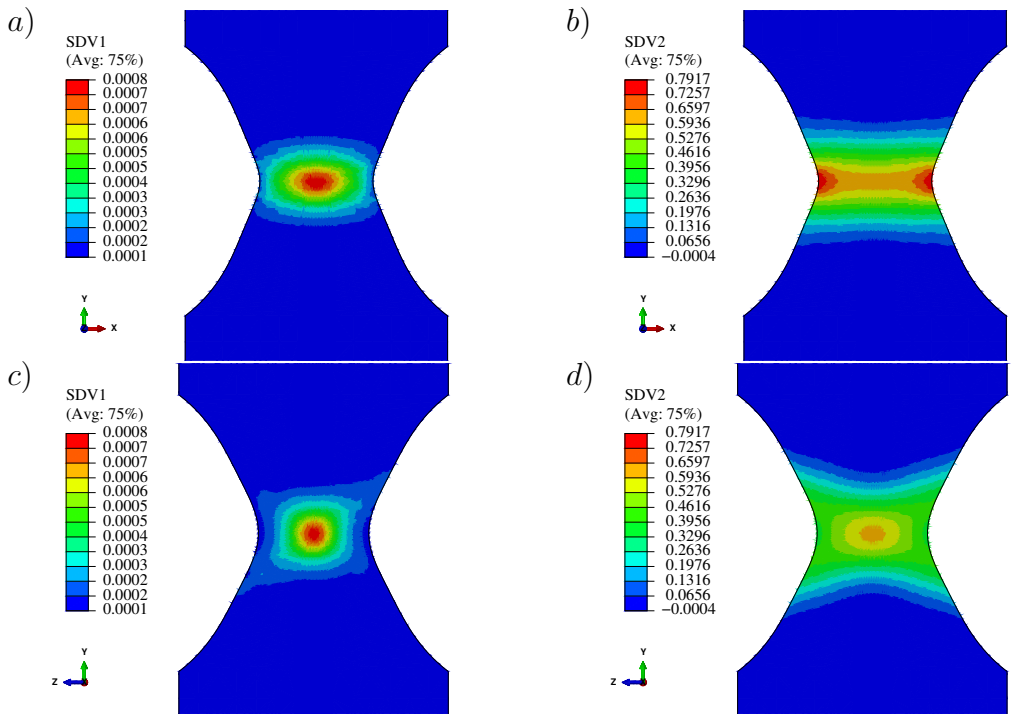

Figure 5.20: For RN10 specimen of material AZ31 with $w_0 = 1$, $f_0 = 10^{-4}$ and $\theta = 0°$ at $U/L = 0.12$ a) Porosity in the LS plane b) Plastic strain in the LS plane c) Porosity in the LT plane d) Plastic strain in the LT plane

occurring near the free surface. In the LT plane, for this configuration the plastic strain is concentrated at the centre of the notched bar and the maximum value of plastic strain is happening in the LS plane and not in the LT plane.

5.3.1.13 Material AZ31 for $\theta = 45^\circ$ and $\theta = 30^\circ$

For AZ31, similar to the case of material ib, in the case of $\theta = 45^\circ$, deformation bands are observed in the initial and later stages of deformation as seen from Fig. 5.21. Fig. 5.21a and Fig. 5.21b show the contours in the LS plane in the early stage of deformation and Fig. 5.21c and Fig. 5.21d show the contours at a later stage of deformation. In the case of material ib, there were two deformations bands observed in the case of $\theta = 45^\circ$. For AZ31, the orientation of the deformation band changes from the initial to the later stages. Initially plastic strain concentrates along the orientation which makes an angle $\psi_0 = 60^\circ$ with respect to the loading direction. Later, the orientation angle increases and reaches a value of $\psi_1 = 130^\circ$. As seen from Fig. 5.21e and Fig. 5.21f, for this material there were no shear bands developed in the LT plane too.

However, similar to the case of material ib, in the case of AZ31, for the $\theta = 30^\circ$, initially deformation band is observed which then evolves into a shear band later in the deformation stage as observed from Fig. 5.22a and Fig. 5.22b. It is worth emphasizing that experiments using RN10 notched bars of AZ31 had reported at least one instance where the notched bars failed in shear (Fig. 5.23). In the experiments also the shear failure happened in the LS plane just as the simulation results in Fig. 5.22 predict.

5.3.2 Simulations on plane strain bars

In the previous sections, the effect of plastic anisotropy alone, in the absence of the various factors which are believed to support shear band formation, in inducing

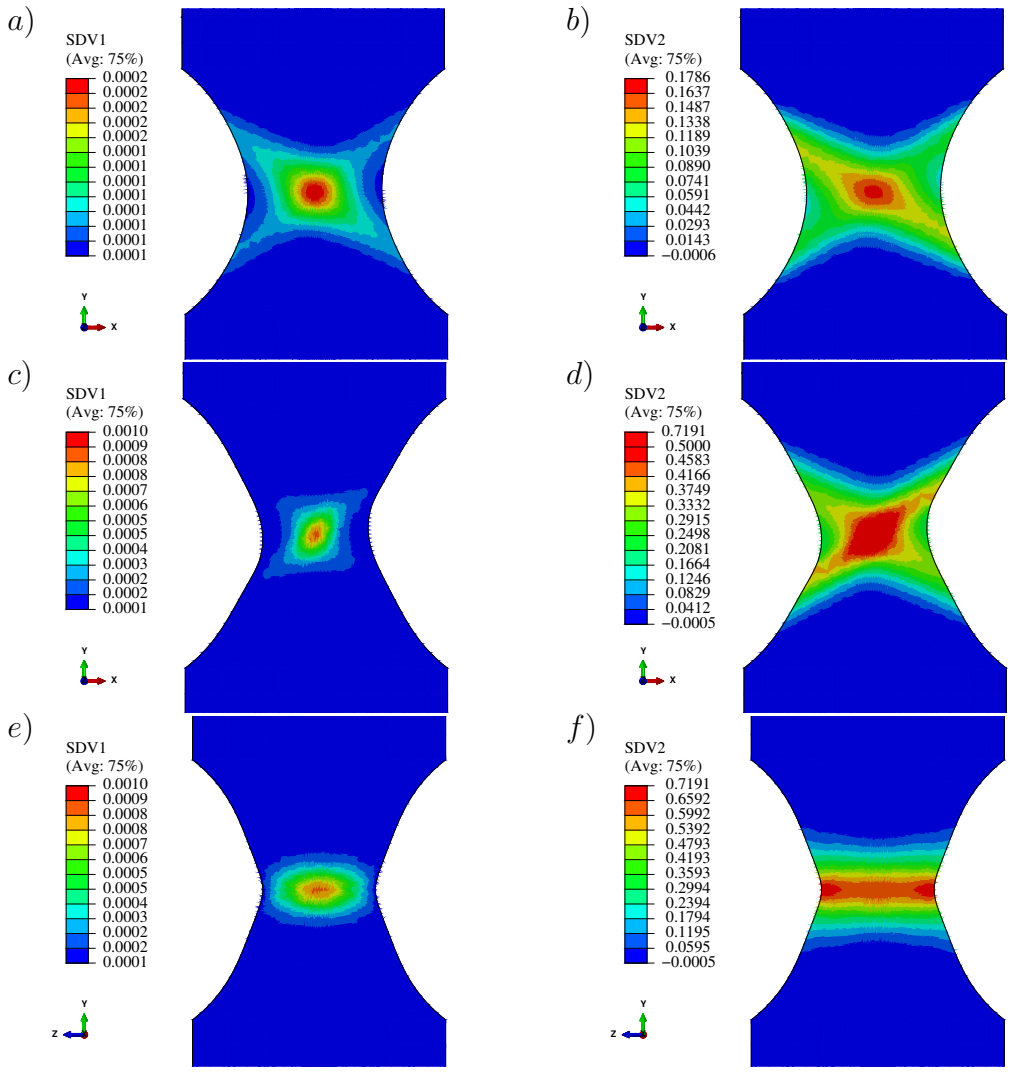

Figure 5.21: For RN10 specimen of material AZ31 with $w_0 = 1$, $f_0 = 10^{-4}$ and $\theta = 45°$ a) Porosity in LS plane at at $U/L = 0.04$ b) Plastic strain in LS plane at at $U/L = 0.04$ c) Porosity in the LS plane at $U/L = 0.12$ d) Plastic strain in the LS plane at $U/L = 0.12$ e) Porosity in the LT plane at $U/L = 0.12$ f) Plastic strain in the LT plane at $U/L = 0.12$

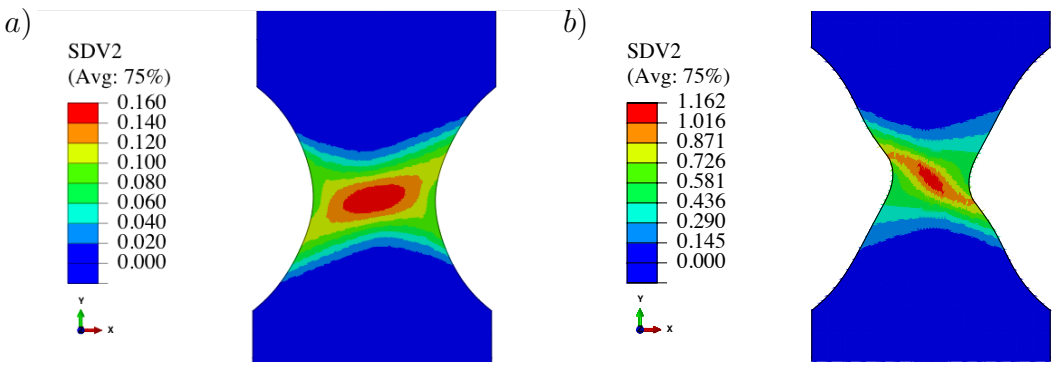

Figure 5.22: For RN10 specimen of material AZ31 with $w_0 = 1$, $f_0 = 10^{-4}$ and $\theta = 30°$ a) Plastic strain in LS plane at at $U/L = 0.04$ b) Plastic strain in the LS plane at $U/L = 0.12$

Figure 5.23: Shear failure observed in RN10 specimen of AZ31 (Basu, S., unpublished research)

the formation of shear bands were illustrated for the particular case of RN10 notched geometry. Previous studies on localization had established that axisymmetric stress states are more resistant towards the formation of shear bands when compared to the case of plane strain geometry. However, those studies were done for the cases of high yield surface curvatures, presence of vertex on the yield surface or with initial imperfections added in the numerical model so as to aid the shear band formation. Hence it is to be seen if for the similar conditions explored in the notched geometry, the formation of shear bands is favored in the case of plane strain conditions and how the evolution of damage contributes to the development of shear bands. In this section the tendency for shear localization in the case of plane strain geometry is explored for the cases of misaligned loading and for the material ib which proved to be highly favorable to shear localization in the axisymmetric case.

5.3.2.1 Effect of initial damage in material ib with $\theta = 45^{\circ}$

In Fig. 5.24, the isotropic matrix material and the case of material ib for $\theta = 45^{\circ}$ for the plane strain specimen are compared. It can be observed from Fig. 5.24a and Fig. 5.24b that, in the case of isotropic matrix with $w_0 = 1$, the maximum plastic strain and porosity are occurring at the centre of the specimen. However, there are no shear bands evidenced in this case. This is similar to the response of notched geometry also where the isotropic case did not show any tendency for shear localization. Now for the case of isotropic material with $w_0 = 6$ with the axis of the voids misaligned at 45° with the loading direction, although damage and plastic strain happens more in a particular inclined direction with respect to the loading direction as seen in Fig. 5.24c and Fig. 5.24d, no shear bands are evidenced.

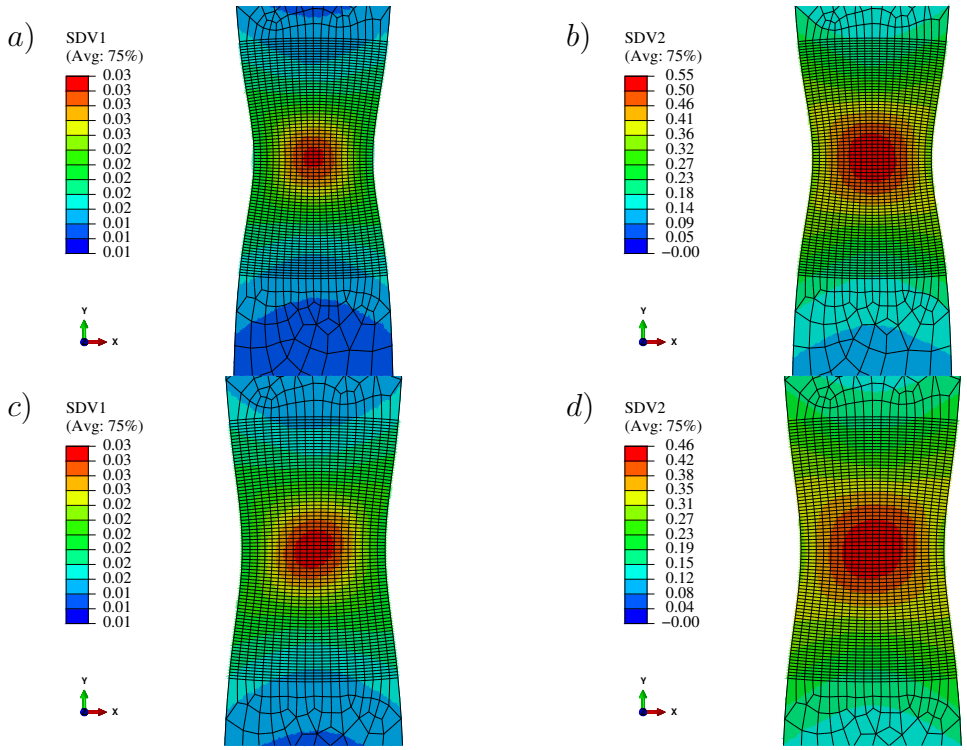

Figure 5.24: For plane strain specimen and isotropic material with $f_0 = 10^{-2}$ a) Porosity for $w_0 = 1$ b) Plastic strain for $w_0 = 1$ c) Porosity for for $w_0 = 6$ d) Plastic strain for $w_0 = 6$

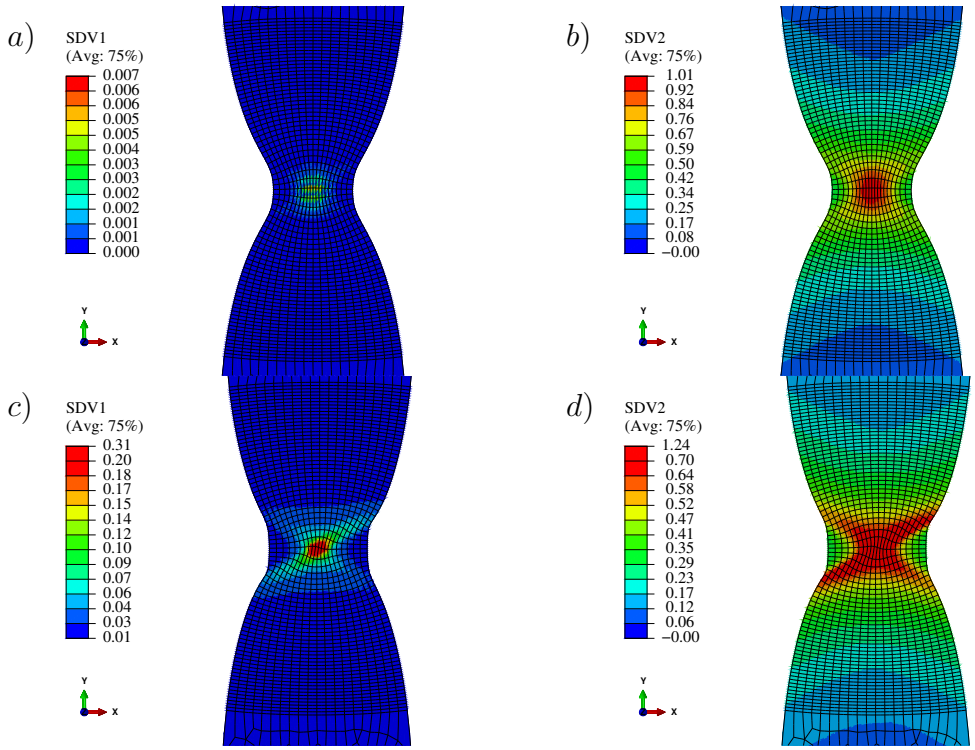

Figure 5.25: For plane strain specimen of material ib with $\theta = 45°$ and $w_0 = 6$ a) Porosity with $f_0 = 10^{-4}$ b) Plastic strain with $f_0 = 10^{-4}$ c) Porosity with $f_0 = 10^{-2}$ d) Plastic strain with $f_0 = 10^{-2}$

The porosity and plastic strain contours for the misaligned case of material ib, with $\theta = 45°$ and for the initial void shape of $w_0 = 6$ for the case of initial porosities of $f_0 = 10^{-4}$ and $f_0 = 10^{-2}$ are shown in In Fig. 5.25. It can be seen that in the case of material ib at low initial porosities as in the case of Fig. 5.25a, no shear bands are evidenced. However, at initial high porosities (Fig. 5.25c and Fig. 5.25d), the plane strain geometry displays shear localization with the plastic strain concentrating in two bands. It can be observed from the contours of porosity for this case that the evolution of damage also localizes along the most prominent among these shear bands. This shows that for the case of plane strain geometry, although plastic

anisotropy combined with misaligned configuration of the orthotropy axes do not result in the formation of shear bands, higher values of initial damage can contribute to the development of shear bands for this case. This shows that damage plays a crucial role in shear localization at realistic strain levels in the case of plane strain geometry.

5.3.2.2 Effect of primary Hill coefficients with a model material with $\theta = 45^{\circ}$

In all the previous sections, it was seen that shear band was occurring in the mis aligned loading of transversely isotropic material ib, for which only the shear Hill coefficients were greater than 1 which makes the material weak in shear along the plane of transverse isotropy. This might point to the influence of shear Hill coefficient along with mis aligned loading or higher value of initial damage as factors contributing to the occurrence of localization in plane strain bars of material ib. Now to explore if in addition to the case of shear Hill coefficient, the primary Hill coefficients are also capable of bringing about localization in the case of plane strain bars. Towards this, a model material with the Hill coefficients as $h_{\mathrm{L}} = 3$ $h_{\mathrm{T}} = 1$ $h_{\mathrm{S}} = 0.4$ $h_{\mathrm{TS}} = 1$ $h_{\mathrm{SL}} = 1$ $h_{\mathrm{LT}} = 1$ are employed as matrix material in the simulation of plane strain bars. Then the material axes are chosen to be $\theta = 0^{\circ}$ and $\theta = 45^{\circ}$ mis aligned with the loading direction to explore if the large difference in primary Hill coefficients $h_{\mathrm{L}} = 3$ and $h_{\mathrm{S}} = 0.4$, when misaligned with the loading direction is promoting a tendency for localization in the case of plane strain bars. The comparison between the case of $\theta = 0^{\circ}$ and $\theta = 45^{\circ}$ is presented in Fig. 5.26.

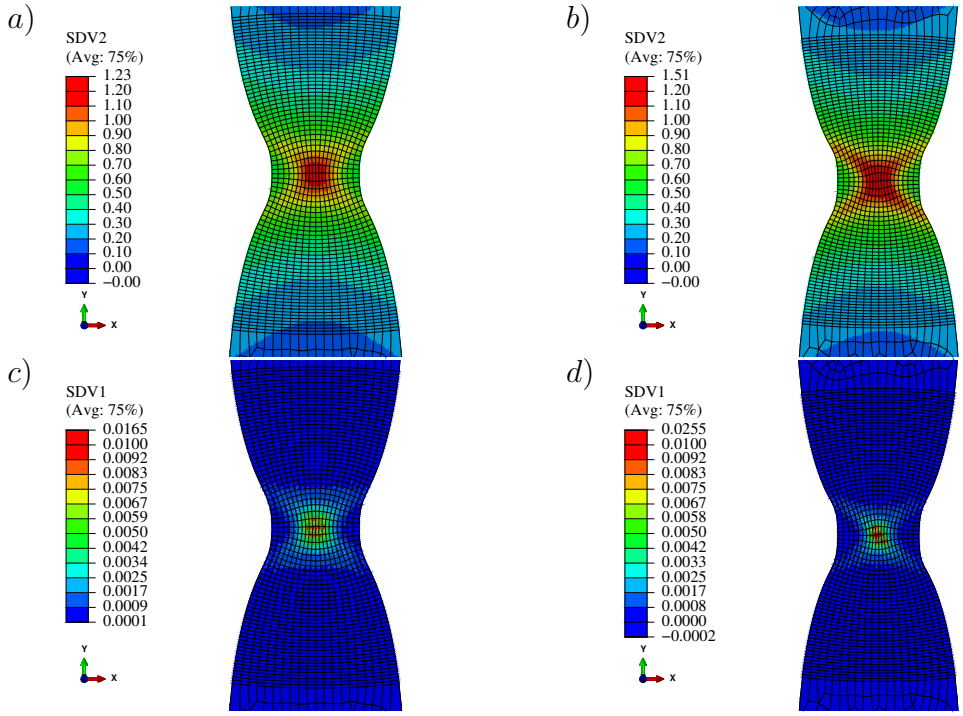

Figure 5.26: For plane strain specimen of a model material with $h_{\mathrm{L}} = 3$ and $h_{\mathrm{S}} = 0.4$ and $f_0 = 10^{-4}$ a) Plastic strain with $\theta = 0^\circ$ b) Plastic strain $\theta = 45^\circ$ c) Porosity with $\theta = 0^\circ$ d) Porosity with $\theta = 45^\circ$

As it can be seen from Fig. 5.26, for the case of $\theta = 0^\circ$, the plastic strain is concentrated at the centre. However there is no tendency for shear localization observed in this case. In contrast, for the case of $\theta = 45^\circ$ there is shear localization happening in the LS plane. In this case of model material, except for the $h_{\mathrm{L}} = 3$ and $h_{\mathrm{S}} = 0.4$, rest of the Hill coefficients are 1. A large value of h_{L} coefficient makes the material weaker along the L direction which is inclined at an angle of $\theta = 45^\circ$ with the Y (loading) axis. This can be thought of as contributing to a de stabilizing effect leading to the shear band. The contours of porosity are also seen in Fig. 5.26c and Fig. 5.26d for the cases of $\theta = 0^\circ$ and $\theta = 45^\circ$ respectively. The porosity in the case of $\theta = 0^\circ$ follows the trend of the plastic strain. Similar is the case of porosity

for the case of $\theta = 45^\circ$ which can be seen developed along the band of localized plastic strain. Also note the fact that the initial porosity in this case was $f_0 = 10^{-4}$ and even for such a low initial value of damage, localized shear bands were observed for this material due to the de-stabilizing effect brought about by the primary Hill coefficients. This points to the fact that not only the shear Hill coefficients, the primary Hill coefficients can also contribute to the tendency for shear localization, in misaligned loading configuration.

5.4 Discussion

Localization of plastic strain in well defined bands in solids can happen under different loading conditions; static as well as dynamic. It can be promoted either by a geometric constraint or as a result of material response. It can emerge as a bifurcation behavior for rate independent constitutive relations. Under this framework, localization is dependent upon the various constitutive features. In this study, the combined effects of damage, void shape and plastic anisotropy and stress state on the propensity for shear localization in ductile materials were investigated by employing an anisotropic void growth model supplemented with a micro mechanically motivated void coalescence condition. Using three dimensional simulations on round notched, plane strain and smooth bars of anisotropic materials, systematic analyses were conducted to study the individual and coupled effects of the above variables on shear localization. Attention was focused on the effect of plastic anisotropy/deformation induced texture on localization. The materials chosen were representative of those employed in various structural applications.The aim of this study was to investigate if plastic anisotropy helps the formation of shear bands and to elucidate under what loading conditions and geometry and whether presence of damage played some role in exacerbating the behavior.

Taking insights from the presented results, it can be conjectured that one of the key factors contributing to formation of shear band is the plastic anisotropy in the material coupled with misalignment of the orthotropy axes. The presence of shear bands in the case of axisymmetric stress state of a cylindrical notched bars suggest that the influence of plastic anisotropy is strong and prominent. It is worth recalling the result of [81] at this point. Although they conducted the study in a plane strain specimen for a fixed orientation of the orthotropic axes, their results suggested that the formation and development of shear band of an orthotropic material is strongly dependent on the initial orientation of orthotropic axes. In the notched bar analyses presented, the orientation of the orthotropy axes were varied systematically. In all the cases where θ was non-zero except for the symmetric loading case of $\theta = 45$, at least one shear band was observed. In the case of notched bars, for the materials investigated, the relative difference in the value of Hill coefficients, specifically the shear Hill coefficients, in unison with the misaligned orthotropy axes resulted in the formation shear bands. This will result in the material to be weaker in an inclined plane and the plastic deformation tend to concentrate along that plane initially as a deformation band which then creates a destabilizing effect leading into a shear band. In the case of material ib, the high value of shear Hill coefficients h_{TS} and h_{SL} and the relative differences between h_{TS}, h_{SL} and h_{LT} were the contributing factors which resulted in shear band. In material iii, however, the lower shear Hill coefficient value resulted in a preventive effect which eliminates the formation of bands. However for this material the relative difference between h_{SL} and h_{LT} can be interpreted as the reason why a tendency for shear bands was observed for this material in the LT plane. In addition, further observations in the case of material ib shows that a high value of shear Hill coefficient also helps in formation of shear bands. Another important aspect to notice is the presence of deformation and shear

bands in the case of notched bar geometry in all the cases analyzed. The orientation of the initial deformation band was closely related with the mis alignment of the orthotropy axes. It is to be noted that since the constitutive model employed here does not incorporate a length scale, the results of these simulations are expected to be mesh sensitive.

Although the plane strain geometry was expected to be more favorable for shear localization, for the same conditions which proved promoting a deformation band in the notched geometry, such bands were not observed in plane strain bars. However, a higher value of initial damage resulted in localization in the plane strain geometry. The relative higher propensity for localization in a notched geometry when compared to that of a plane strain geometry points to the potential influence of triaxial stress state in exacerbating the effect of plastic anisotropy on localization in notched bars. This effect in notched bars was found to be more prominent than the effect of geometric constraint combined with that of plastic anisotropy in plane strain bars. It must also be noted that in addition to the shear Hill coefficients, the principal Hill coefficients can also contribute to the formation of shear bands; an example for a lower initial value of damage and in the case of plane strain geometry was presented in Section 5.3.2.2.

Another point worth mentioning is the comparison between macroscopic and microscopic modes of localization found in the simulations of notched bars. Note that the load displacement curves for all the cases of notched bars of material ib presented in Section. 5.3.1.10 were plotted until the first instance of void coalescence as reported by the Benzerga-Leblond void coalescence condition is met. As explained in the introduction, the competition between macroscopic and microscopic modes of localization is evident in the plots, especially for the case of $\theta = 15^{\circ}$ and $\theta = 30^{\circ}$. For all the cases presented for the notched bar of material ib, as seen from the results of

Section. 5.3.1, macroscopic localization preceded the microscopic (void coalescence) one. The investigation by [115] reported that for axisymmetric stress states, above a triaxiality value of $T > 1$, macroscopic mode of localization occurs prior to void coalescence. For the results presented here, it is worth emphasizing that the average triaxiality existing at the centre of the notched bar of material ib (note that the value of triaxiality is dependent on the material as explained in the previous chapter) is near $T = 1$ and that the results here are qualitatively in agreement with the studies done by [115].

The results of this study have important practical consequences. Notched bar geometries are usually employed in experimental investigations since they are thought of as constant triaxiality specimens decoupled from plastic instabilities such as shear bands [20]. The present results showcase that notched bars of plastically anisotropic materials are prone to localization and suggests that care must be taken while interpreting the fracture strains/results from experiments on notched bars of highly anisotropic materials such as alloys of Mg. Note that in the present study, the remote loading consisted of only tensile component. The influence of plastic anisotropy on causing localization in the case of tension-torsion or shear dominated loadings are yet to be studied. It is expected that the effect will be more detrimental in those cases. Another aspect to keep in mind is the strong non-proportionality brought about by shear bands and the associated path dependence of fracture strains under non-proportional loading conditions [11, 14, 116] (Chapter 3) Another point is that a low value of strain hardening ($n \approx 0.06$) is shown to favor shear fracture [79]. This study points to the chances of localization even at higher values of strain hardening ($n = 0.1$ was used in this study). Also the angle of misalignment chosen in this study was limited to varying in the plane of loading only (allowing for thoroughly exploring how various parameters affect misalignment in a plane) and for these con-

ditions the shear bands were evidenced. It needs to be seen for multiple planes of misalignment with respect to the loading direction, how severe can be the effect of plastic anisotropy.

The current study expands the earlier investigations on shear localizations using Gurson like models where it was established that to predict localization at a realistic strain levels either some initial heterogeneities needed to be introduced in the model or by the introduction of void coalescence model which will bring about a vertex in the yield criterion. In this study, by using a Gurson like void growth model alone, shear localization was captured at realistic strain levels, that too in axisymmetric specimens. The Benzerga-Leblond coalescence condition used in this model was used only to check for the first instance of microscopic coalescence happening in the simulations and was it was not used to help trigger the formation of shear bands as done in previous studies [17]. Another aspect that needs to be mentioned is that the effect of void nucleation is also not included in the simulations. Having said that, it points to the possibility of future directions of exploration, given that improved models of void growth and coalescence are available. These new models that accounts for ellipsoidal void shapes and plastic anisotropy [96] can be combined with models of void coalescence that takes plastic anisotropy also into account [65] to form an integrated ductile fracture model which can then be applied to study various stress states especially the pertinent ones such as the shear dominated stress states.

5.5 Conclusions

In this study, a Gurson like anisotropic void growth model was employed to study the effect of shear localization in plastically anisotropic ductile materials. Simulations on notched bars, plane strain bars and smooth bars were carried out to explore the parameter space and to investigate the combined effect of plastic anisotropy

and damage on promoting strain localization. Based on the results, the following conclusions can be made:

- Notched bars: For the first time, shear bands were captured in axisymmetric notched specimen under tensile loading at realistic strain levels using a Gurson like model, without introducing any initial inhomogeneities in the model or by incorporating any nucleation criterion. Plastic anisotropy was shown to play a very crucial role under misaligned loading conditions, in triggering shear bands in notched bars.

- Plane strain bars: A higher values of initial damage in unison with plastic anisotropy and misaligned loading state was shown to help develop shear bands in plane strain bars. This shows that in the case of plane strain geometry damage plays a crucial role in contributing to localization for misaligned loadings of plastically anisotropic materials.

5.6 Acknowledgements

Partial support from the Lawrence Livermore National Security, LLC under Master Task Agreement No. B575363, LLNL under Contract DE-AC52-07NA27344 and the National Science Foundation under grant CMMI-0748187 is gratefully acknowledged.

6. CONCLUSIONS

6.1 Summary

The overall goal of this research was to elucidate the inevitably coupled effects of stress state, strain/load history and material microstructure on the ductile fracture of engineering materials. Towards addressing these, the focus of this dissertation was on three important topics in ductile failure namely (i) the effect of non proportional loadings on fracture locus in futile materials (ii) anisotropic ductile fracture (iii) ductile failure by shear localization.

In the first topic, a simple fracture theory has been employed which supplements an uncoupled damage model with a constant critical damage parameter in order to investigate ductile fracture under nonproportional loading. Emphasis was laid on that part of the deviations that are related to plasticity-induced damage. When first compared with exact finite-element cell model simulations, the predictions of the theory were shown to be excellent when a variant of the damage model that approximately accounts for void shape effects is used. Then the theory was employed to explore the effect of non proportional loadings for two representative families and the strong deviations in the fracture strains for those loadings as contrasted with that of proportional loadings were demonstrated.

The first topic demonstrated that although simple fracture models are useful, to account for the inherent anisotropic and path dependent nature of ductile fracture, more sophisticated models need to be employed. Towards this, in the second topic, the combined effect of void shape, stress state and plastic anisotropy was investigated by employing an anisotropic void growth model supplemented with a micro mechanically motivated void coalescence condition using three dimensional simulations in-

volving anisotropic materials on round notched bars of varying notch intensity. The materials chosen were representative of those employed in various structural applications. Important findings related to the effects of plastic anisotropy in modulating the stress state and imparting structural effects in ductile materials were elucidated. The thrust of this study was mainly on ductile fracture by void growth and coalescence.

The third topic focused on ductile fracture by shear localization. A Gurson like anisotropic void growth model was employed to study the effect of shear localization in plastically anisotropic ductile materials. Simulations on notched bars, plane strain bars and smooth bars were carried out to explore the parameter space and the role of combined effect of plastic anisotropy and damage in promoting strain localization was shown. Plastic anisotropy under mis aligned loadings was found to be another sufficient condition contributing to shear localization in ductile materials.

6.2 Conclusions

Specific conclusions from the research presented in this dissertation are listed below.

6.2.1 Non proportional loadings

- When the nonproportional loading path involves an increase in stress triaxiality, fracture is invariably found to set beyond the fracture limit curve defining proportional loading. This holds for both a step jump and gradual increase in triaxiality and is thus likely to hold irrespective of the detailed shape of the loading path.

- On the other hand, when the loading path involves a decrease in stress triaxiality, fracture is found to set before the path intersects the (proportional)

fracture limit curve. This situation indicates that one should be concerned about employing critical fracture strain criteria in integrated form.

- A generic shape of the fracture strain versus average triaxiality locus has been rationalized, irrespective of loading type. With this as basis, previously published experimental results have been rationalized without recourse to ad hoc explanations. In addition, the results provide insight into ways to improve the experimental programs previously attempted to tackle this problem.

- Ductile fracture is inherently anisotropic, particularly at low stress triaxialities. The fracture theory accounts only partially and approximately for some effects of anisotropy. Although the authors do not advocate using the model as is to make fracture predictions, it is remarkable that the projections are qualitatively robust for changes in the constitutive damage laws used.

6.2.2 Anisotropic ductile fracture

- The effect of triaxiality on ductile fracture is well established from previous studies. In the simulations reported here, although the triaxiality value for a particular specimen is dictated by the notch geometry, its variation is found to be modulated by plastic anisotropy of the material. The spatial variation at a given time as well as the temporal variation at a given location of triaxiality is indeed a manifestation of the structural effects imparted by plastic anisotropy of the material. This triaxiality variation in turn will also influence the evolution of various microstructural parameters such as void shape, porosity etc and thus eventually affecting ductility response of the material.

- One of the major findings of this study is to reveal an interesting competition between two effects; both imparted by plastic anisotropy, one the intrinsic effect

which can be quantified through the anisotropy characterizing scalar invariant **h** and the other being purely structural effect which manifests through the way in which plastic anisotropy affects plastic flow processes and triaxiality evolution in time and space in the structure. Depending upon the geometry and kind of anisotropy in the material, this can be beneficial or detrimental to the ductility response of the material. In the calculations analyzed in the main text, the structural effect of plastic anisotropy always goes against its intrinsic effect. In RN10 specimens the structural effect of plastic anisotropy is not strong enough to revert the trends obtained from cell model calculations. In RN2 specimens, however, the structural effect overcomes the intrinsic one.

- More generally, whether the structural effect always goes against the intrinsic one is worth investigating. Preliminary results (shown in Appendix) indicate that this is not necessarily the case. Therefore, in general complete boundary-value problem solutions are needed to understand ductile fracture in anisotropic materials.

- The above findings are robust in the sense that they apply not only to initially spherical voids but also initially prolate or oblate voids.

- The effect of loading orientation combined with plastic anisotropy in governing the evolution of various microstructural variables and damage was demonstrated. As shown in the results, this plays a crucial role in deciding the potential direction of crack propagation in various loading orientations.

- It was shown that in notched bars, in addition to that imparted by plastic spin, significant void rotations take place near the free surface due to the curvature-induced shear stresses. This is consistent with experimental observations. The

implication of such rotations are important when the loading axes are aligned with the microstructure (either the axes of plastic anisotropy or the damage entities/voids). However, they are expected to play a much more key role under combined tension and shear loading (where rotations imparted by loadings also might be superimposed in addition to geometry and plastic spin) or under off-axes tensile loadings, which is explored in the next chapter.

6.2.3 Failure by shear localization

- Notched bars: For the first time, shear bands were captured in axisymmetric notched specimen under tensile loading at realistic strain levels using a Gurson like model, without introducing any initial inhomogeneities in the model or by incorporating any nucleation criterion. Plastic anisotropy was shown to play a very crucial role under misaligned loading conditions, in triggering shear bands in notched bars.

- Plane strain bars: A higher values of initial damage in unison with plastic anisotropy and misaligned loading state was shown to help develop shear bands in plane strain bars. This shows that in the case of plane strain geometry damage plays a crucial role in contributing to localization for misaligned loadings of plastically anisotropic materials.

REFERENCES

[1] Abaqus, 2014. Abaqus documentation version 6.14. Dassault Systemes, Providence, Rhode Island, United States 1, 1–1000.

[2] Agoras, M., Castaneda, P.P., 2014. Anisotropic finite-strain models for porous viscoplastic materials with microstructure evolution. International Journal of Solids and Structures 51, 981–1002.

[3] Alves, M., Jones, N., 1999. Influence of hydrostatic stress on failure of axisymmetric notched specimens. Journal of the Mechanics and Physics of Solids 47, 643–667.

[4] Amouzouvi, K.F., Bassim, M.N., 1983. Effect of the type of prior straining on the fracture-toughness of AISI-4340 steel. Materials Science and Engineering 60, 1–5.

[5] Anand, K., Spitzig, W.A., 1980. Initiation of localized shear bands in plane strain. Journal of the Mechanics and Physics of Solids 28, 113–128.

[6] Arndt, J., Majedi, H., Dahl, W., 1996. Influence of strain history on ductile failure of steel. Journal de Physique IV 6, 23–32.

[7] Bai, Y., Wierzbicki, T., 2008. A new model of metal plasticity and fracture with pressure and lode dependence. International Journal of Plasticity 24, 1071 – 1096.

[8] Bao, Y., Wierzbicki, T., 2004. On fracture locus in the equivalent strain and stress triaxiality space. International Journal of Mechanical Sciences 46, 81–98.

[9] Barsoum, I., Faleskog, J., 2007. Rupture mechanisms in combined tension and shear—-Experiments. International Journal of Solids and Structures 44, 1768–1786.

[10] Basu, S., 2016. On the effects of texture and strain path changes on the ductile fracture of Magnesium alloys. Ph.D. thesis. Texas A&M University, College Station.

[11] Basu, S., Benzerga, A.A., 2015. On the path-dependence of the fracture locus in ductile materials: Experiments. International Journal of Solids and Structures 71, 79–90.

[12] Becker, R., Needleman, A., 1986. Effect of yield surface curvature on necking and failure in porous plastic solids. Journal of Applied Mechanics-Transactions of the ASME 53, 491–499.

[13] Becker, R., Needleman, A., Richmond, O., Tvergaard, V., 1988. Void growth and failure in notched bars. J. Mech. Phys. Solids 36, 317–351.

[14] Benzerga, A., Surovik, D., Keralavarma, S., 2012. On the path-dependence of the fracture locus in ductile materials – analysis. International Journal of Plasticity 37, 157 – 170.

[15] Benzerga, A.A., 2000. Rupture ductile des tôles anisotropes. Ph.D. thesis. Ecole Nationale Supérieure des Mines de Paris.

[16] Benzerga, A.A., Besson, J., 2001. Plastic potentials for anisotropic porous solids. European Journal of Mechanics 20, 397–434.

[17] Benzerga, A.A., Besson, J., Batisse, R., Pineau, A., 2002. Synergistic effects of plastic anisotropy and void coalescence on fracture mode in plane strain. Model. Simul. Mater. Sci. Eng. 10, 73–102.

[18] Benzerga, A.A., Besson, J., Pineau, A., 2004a. Anisotropic ductile fracture part i: Experiments. Acta Materialia 52, 4623–4638.

[19] Benzerga, A.A., Besson, J., Pineau, A., 2004b. Anisotropic ductile fracture part ii: Theory. Acta Materialia 52, 4639–4650.

[20] Benzerga, A.A., Leblond, J.B., 2010. Ductile fracture by void growth to coa-

lescence. Advances in Applied Mechanics 44, 169–305.

[21] Benzerga, A.A., Leblond, J.B., 2014. Effective yield criterion accounting for microvoid coalescence. Journal of Applied Mechanics-Transactions of ASME 81.

[22] Benzerga, A.A., Leblond, J.B., 2016. Limit analysis of constrained plastic flow in ductile porous solids. Journal of Applied Mechanics In preparation.

[23] Beremin, F.M., 1980. Elasto–plastic calculations of circumferentially notched specimens using the finite element method. J. Mécanique Appliquée 4, 307.

[24] Beremin, F.M., 1981a. Cavity formation from inclusions in ductile fracture of a508 steel. Metallurgical Transactions A 12, 723–731.

[25] Beremin, F.M., 1981b. Experimental and numerical study of the different stages in ductile rupture: application to crack initiation and stable crack growth, in: Nemat-Nasser, S. (Ed.), Three-Dimensional Constitutive relations of Damage and Fracture, Pergamon press, North Holland. pp. 157–172.

[26] Besson, J., 2010. Continuum models of ductile fracture: A review. IJDM 19, 3–52.

[27] Besson, J., Steglich, D., Brocks, W., 2003. Modeling of plane strain ductile rupture. IJP 19, 1517–1541.

[28] Borvik, T., Hopperstad, O.S., Berstad, T., 2003. On the influence of stress triaxiality and strain rate on the behaviour of a structural steel. part ii. numerical study. European Journal of Mechanics A - Solids 22, 15–32.

[29] Bridgman, J.W., 1952. Studies in Large Plastic Flow and Fracture. McGraw–Hill, New York.

[30] Brown, D., Hancock, J., Thomson, R., Parks, D., 1980. The effect of dilating plasticity on some elastic-plastic stress and strain concentration problems relevant to fracture, in: Numerical Methods in Fracture Mechanics, Swansea, U.

K., July 1980, pp. 309–325.

[31] Castaneda, P.P., Zaidman, M., 1994. Constitutive models for porous materials with evolving microstructure. Journal of the Mechanics and Physics of Solids 42, 1459–1497.

[32] Chae, D., Bandstra, J.P., Koss, D.A., 2000. The effect of pre-strain and strain-path changes on ductile fracture: experiment and computational modeling. Materials Science and Engineering A 285, 165–171.

[33] Chu, C., Needleman, A., 1980. Void nucleation effects in biaxially stretched sheets. Journal of Engineering Materials and Technology 102, 249–256.

[34] Clayton, J.Q., Knott, J.F., 1976. Observations of fibrous fracture modes in a prestrained low-alloy steel. Metal Science 10, 63–71.

[35] Doghri, I., Billardon, R., 1995. Investigation of localization due to damage in elasto-plastic materials. Mechanics of Materials 19, 129–149.

[36] Dunand, M., Mohr, D., 2011. On the predictive capabilities of the shear modified gurson and the modified mohr-coulomb fracture models over a wide range of stress triaxialities and lode angles. Journal of the Mechanics and Physics of Solids 59, 1374–1394.

[37] Dunand, M., Mohr, D., 2014. Effect of lode parameter on plastic flow localization after proportional loading at low stress triaxialities. Journal of the Mechanics and Physics of Solids 66, 133–153.

[38] Enami, K., 2005a. Ductile crack initiation behavior in steels with compressive prestrain. Journal of Marine Science and Technology 10, 41–52.

[39] Enami, K., 2005b. The effects of compressive and tensile prestrain on ductile fracture initiation in steels. Engineering Fracture Mechanics 72, 1089–1105.

[40] Eshelby, J., 1957. The determination of the elastic field of an ellipsoidal inclusion, and related problems. Proceedings of the Royal Society of London A

A241, 357–396.

[41] Gao, X., Kim, J., 2006. Modeling of ductile fracture: Significance of void coalescence. International Journal of Solids and Structures 43, 6277–6293.

[42] Gao, X., Zhang, G., Roe, C., 2010. A study on the effect of the stress state on ductile fracture. International Journal of Damage Mechanics 19, 75–94.

[43] Garrison, W.M., Moody, N.R., 1987. Ductile fracture. Journal of Physics and Chemistry of Solids 48, 1035–1074.

[44] Gologanu, M., Leblond, J.B., Devaux, J., 1993. Approximate models for ductile metals containing non-spherical voids – case of axisymmetric prolate ellipsoidal cavities. Journal of the Mechanics and Physics of Solids 41, 1723–1754.

[45] Gologanu, M., Leblond, J.B., Devaux, J., 1994. Approximate Models for Ductile Metals Containing Non–spherical Voids — Case of Axisymmetric Oblate Ellipsoidal Cavities. Journal of Engineering Materials and Technology 116, 290–297.

[46] Gologanu, M., Leblond, J.B., Perrin, G., Devaux, J., 1995a. Recent extensions of Gurson's model for porous ductile metals. Part I:, in: Suquet, P. (Ed.), Continuum Micromechanics. Springer–Verlag, pp. 61–97.

[47] Gologanu, M., Leblond, J.B., Perrin, G., Devaux, J., 1995b. Recent extensions of Gurson's model for porous ductile metals. Part II: A Gurson-like model including the effect of strong gradients of macroscopic fields, in: Suquet, P. (Ed.), Continuum Micromechanics. Springer–Verlag, pp. 97–130.

[48] Gologanu, M., Leblond, J.B., Perrin, G., Devaux, J., 2001a. Theoretical models for void coalescence in porous ductile solids – I: Coalescence in "layers". International Journal of Solids and Structures 38, 5581–5594.

[49] Gologanu, M., Leblond, J.B., Perrin, G., Devaux, J., 2001b. Theoretical models for void coalescence in porous ductile solids – II: Coalescence in "columns".

International Journal of Solids and Structures 38, 5595–5604.

[50] Graf, A., Hosford, W., 1994. The influence of strain-path changes on forming limit diagrams of Al 6111 T4. International Journal of Mechanical Sciences 36, 897–910.

[51] Gurson, A.L., 1977. Continuum theory of ductile rupture by void nucleation and growth .1. yield criteria and flow rules for porous ductile media. Journal of Engineering Materials and Technology-Transactions of ASME 99, 2–15.

[52] Haltom, S.S., Kyriakides, S., Ravi-Chandar, K., 2013. Ductile failure under combined shear and tension. International Journal of Solids and Structures 50, 1507–1522.

[53] Hancock, J.W., Brown, D.K., 1983. On the role of strain and stress state in ductile failure. Journal of the Mechanics and Physics of Solids 31, 1–24.

[54] Hancock, J.W., MacKenzie, A.C., 1976. On the mechanisms of ductile failure in high–strength steels subjected to multi–axial stress states. Journal of the Mechanics and Physics of Solids 24, 147–169.

[55] Hill, R., 1948. A theory of yielding and plastic flow of anisotropic solids. Proceedings of the Royal Society of London A 193, 281–297.

[56] Hill, R., 1952. On discontinuous plastic states, with special reference to localized necking in thin sheets. Journal of the Mechanics and Physics of Solids 1, 19–30.

[57] Hill, R., 1962. Acceleration waves in solids. Journal of the Mechanics and Physics of Solids 10, 1–16.

[58] Hill, R., 1967. The essential structure of constitutive laws for metal composites and polycrystals. Journal of the Mechanics and Physics of Solids 15, 79–95.

[59] Hopperstad, O.S., Borvik, T., Langseth, M., Labibes, K., Albertini, C., 2003. On the influence of stress triaxiality and strain rate on the behaviour of a

structural steel. part i. experiments. European Journal of Mechanics A - Solids 22, 1–13.

[60] Huang, Y., 1991. Accurate Dilatation Rates for Spherical Voids in Triaxial Stress Fields. Journal of Applied Mechanics 58, 1084–1085.

[61] Hutchinson, J.W., Tvergaard, V., 1981. Shear band formation in plane strain. International Journal of Solids and Structures 17, 451–470.

[62] Johnson, G., Hoegfeldt, J., Lindholm, U., Nagy, A., 1983. Response of various metals to large torsional strains over a large range of strain rates–part 1: Ductile metals. Journal of Engineering Materials and Technology 105, 42–47.

[63] Johnson, G.R., Cook, W.H., 1985. Fracture characteristics of three metals subjected to various strains, strain rates, temperatures and pressures. Engineering Fracture Mechanics 21, 31–48.

[64] Kailasam, M., Ponte Castaneda, P., 1998. A general constitutive theory for linear and nonlinear particulate media with microstructure evolution. Journal of the Mechanics and Physics of Solids 46, 427–465.

[65] Keralavarma, S., Chockalingam, S., 2016. A criterion for void coalescence in anisotropic ductile materials. International Journal of Plasticity .

[66] Keralavarma, S.M., Benzerga, A.A., 2008. An approximate yield criterion for anisotropic porous media. Comptes Rendus Mecanique 336, 685–692.

[67] Keralavarma, S.M., Benzerga, A.A., 2010. A constitutive model for plastically anisotropic solids with non-spherical voids. Journal of the Mechanics and Physics of Solids 58, 874–901.

[68] Keralavarma, S.M., Benzerga, A.A., 2015. Numerical assessment of an anisotropic porous metal plasticity model. Mechanics of Materials 90, 212–228.

[69] Keralavarma, S.M., Hoelscher, S., Benzerga, A.A., 2011. Void growth and

coalescence in anisotropic plastic solids. International Journal of Solids and Structures 48, 1696–1710.

[70] Kim, J., Gao, X.S., Srivatsan, T.S., 2004. Modeling of void growth in ductile solids: effects of stress triaxiality and initial porosity. Engineering Fracture Mechanics 71, 379–400.

[71] Kocks, U.F., Mecking, H., 2003. Physics and phenomenology of strain hardening: the fcc case. Progress in Materials Science 48, 171–273.

[72] Kondori, B., 2015. Ductile fracture of Magnesium alloys : characterization and modeling. Ph.D. thesis. Texas A&M University, College Station.

[73] Kondori, B., Benzerga, A.A., 2014. Effect of stress triaxiality on the flow and fracture of mg alloy az31. Metallurgical and Materials Transactions A 45A, 3292–3307.

[74] Koplik, J., Needleman, A., 1988. Void growth and coalescence in porous plastic solids. International Journal of Solids and Structures 24, 835–853.

[75] Kuna, K., Sun, D.Z., 1996. Three-dimensional cell model analyses of void growth in ductile materials. International Journal of Fracture 81, 235–258.

[76] Kuroda, M., Tvergaard, V., 2000. Effect of strain path change on limits to ductility of anisotropic metal sheets. International Journal of Mechanical Sciences 42, 867–887.

[77] Kweon, S., Sagsoy, B., Benzerga, A.A., 2016. Constitutive relations and their time integration for anisotropic elasto-plastic porous materials. Computer Methods in Applied Mechanics and Engineering 310, 495–534.

[78] Laukonis, J., Ghosh, A., 1978. Effects of strain path changes on the formability of sheet metals. Metallurgical Transactions A 9, 1849–1856.

[79] Lebert, A.A., Besson, J., Gourgues, A., 2005. Fracture of 6056 aluminum sheet materials: effect of specimen thickness and hardening behavior on strain

localization and toughness. Materials Science and Engineering: A 395, 186–194.

[80] Leblond, J.B., Morin, L., 2014. Gurson's criterion and its derivation revisited. Journal of Applied Mechanics 81, 051012.

[81] Lee, H., Im, S.Y., Atluri, S.N., 1995. Strain localization in an orthotropic material with plastic spin. International Journal of Plasticity 11, 423–450.

[82] Li, H., Fu, M.W., Lu, J., Yang, H., 2011. Ductile fracture: Experiments and computations. International Journal of Plasticity 27, 147–180.

[83] Mackenzie, A.C., Hancock, J.W., Brown, D.K., 1977. On the influence of state of stress on ductile failure initiation in high strength steels. Engineering Fracture Mechanics 9, 167–188.

[84] Madou, K., Leblond, J.B., 2012. A Gurson-type criterion for porous ductile solids containing arbitrary ellipsoidal voids – I: Limit-analysis of some representative cell. Journal of the Mechanics and Physics of Solids 60, 1020–1036.

[85] Madou, K., Leblond, J.B., Morin, L., 2013. Numerical studies of porous ductile materials containing arbitrary ellipsoidal voids ii: Evolution of the length and orientation of the void axes. European Journal of Mechanics - A/Solids 42, 490–507.

[86] Mai, Y.W., Cotterell, B., 1980. Effects of pre-strain on plane-stress ductile fracture in alpha-brass. Journal of Materials Science 15, 2296–2306.

[87] Mandel, J., 1964. Contribution théorique à l'étude de l'écrouissage et des lois d'écoulement plastique, in: 11^{th} International Congress on Applied Mechanics, Springer, Berlin. pp. 502–509.

[88] Mansouri, L.Z., Chalal, H., Abed-Meraim, F., 2014. Ductility limit prediction using a gtn damage model coupled with localization bifurcation analysis. Mechanics of Materials 76, 64 – 92.

[89] Marini, B., Mudry, F., Pineau, A., 1985. Ductile rupture of a508 steel under nonradial loading. Engineering Fracture Mechanics 22, 375 – 386.

[90] Martins, P.A.F., Bay, N., Tekkaya, A.E., Atkins, A.G., 2014. Characterization of fracture loci in metal forming. International Journal of Mechanical Sciences 83, 112–123.

[91] McClintock, F.A., 1968. A criterion for ductile fracture by the growth of holes. Journal of Applied Mechanics 35, 363–371.

[92] McMeeking, R.M., 1977. Finite deformation analysis of crack–tip opening in elastic–plastic materials and implications for fracture. Journal of the Mechanics and Physics of Solids 25, 357.

[93] Mear, M.E., Hutchinson, J.W., 1985. Influence of yield surface curvature on flow localization in dilatant plasticity. Mechanics of Materials 4, 395–407.

[94] Mohr, D., Marcadet, S.J., 2015. Micromechanically-motivated phenomenological hosford-coulomb model for predicting ductile fracture initiation at low stress triaxialities. International Journal of Solids and Structures 67-68, 40–55.

[95] Monchiet, V., Cazacu, O., Charkaluk, E., Kondo, D., 2008. Macroscopic yield criteria for plastic anisotropic materials containing spheroidal voids. International Journal of Plasticity 24, 1158–1189.

[96] Morin, L., Leblond, J.B., Kondo, D., 2015. A gurson-type criterion for plastically anisotropic solids containing arbitrary ellipsoidal voids. International Journal of Solids and Structures 77, 86–101.

[97] Nahshon, K., Hutchinson, J.W., 2008. Modification of the Gurson Model for shear failure. European Journal of Mechanics 27, 1–17.

[98] Needleman, A., 1972. A numerical study of necking in circular cylindrical bars. Journal of the Mechanics and Physics of Solids 20, 111–127.

[99] Needleman, A., Rice, J.R., 1978. Limits to ductility set by plastic flow local-

ization, in: Koistinen, D.P. (Ed.), Mechanics of sheet metal forming. Plenum, pp. 237–267.

[100] Needleman, A., Tvergaard, V., 1984. An analysis of ductile rupture in notched bars. Journal of the Mechanics and Physics of Solids 32, 461–490.

[101] Orowan, E., 1945. Notch Brittleness And The Strength Of Metals. Institution of Engineers and Shipbuilders in Scotland.

[102] Papasidero, J., Doquet, V., Mohr, D., 2015. Ductile fracture of aluminum 2024-T351 under proportional and non-proportional multi-axial loading: Bao-Wierzbicki results revisited. International Journal of Solids and Structures 69-70, 459–474.

[103] Pardoen, T., Hutchinson, J.W., 2000. An extended model for void growth and coalescence. Journal of the Mechanics and Physics of Solids 48, 2467–2512.

[104] Pardoen, T., Scheyvaerts, F., Simar, A., Tekoglu, C., Onck, P.R., 2010. Multiscale modeling of ductile failure in metallic alloys. C. R. Phys. 11, 326–345.

[105] Pineau, A., Benzerga, A.A., Pardoen, T., 2016. Failure of metals I. Brittle and Ductile Fracture. Acta Materialia 107, 424–483.

[106] Ponte Castaneda, P., 1991. The effective mechanical properties of nonlinear composites. Journal of the Mechanics and Physics of Solids 39, 45–71.

[107] Rice, J., 1976. The localization of plastic deformation, in: Koiter, W. (Ed.), 14th int. cong. Theoretical and Applied Mechanics, North–Holland, Amsterdam. pp. 207–220.

[108] Rice, J.R., Tracey, D.M., 1969. On the enlargement of voids in triaxial stress fields. Journal of the Mechanics and Physics of Solids 17, 201–217.

[109] Rudnicki, J.W., Rice, J.R., 1975. Conditions for the localization of deformation in pressure-sensitive dilatant materials. Journal of the Mechanics and Physics of Solids 23, 371–394.

[110] Schiffmann, R., Bleck, W., Dahl, W., 1998. The influence of strain history on ductile failure of steel 13, 142–147.

[111] Sivaprasad, S., Tarafder, S., Ranganath, V.R., Ray, K.K., 2000. Effect of pre-strain on fracture toughness of HSLA steels. Materials Science and Engineering A 284, 195–201.

[112] Steinmann, P., Miehe, C., Stein, E., 1994. On the localization analysis of orthotropic hill type elastoplastic solids. Journal of the Mechanics and Physics of Solids 42, 1969–1994.

[113] Suquet, P., 1982. Plasticité et homogénéisation. Ph.D. thesis. Université Pierre et Marie Curie – Paris VI.

[114] Tekoglu, C., 2014. Representative volume element calculations under constant stress triaxiality, lode parameter, and shear ratio. International Journal of Solids and Structures 51, 4544–4553.

[115] Tekoglu, C., Hutchinson, J.W., Pardoen, T., 2015. On localization and void coalescence as a precursor to ductile fracture. Philosophical Transactions of the Royal Society A-Mathematical, Physical and Engineering Sciences 373.

[116] Thomas, N., Basu, S., Benzerga, A.A., 2016. On fracture loci of ductile materials under non-proportional loading. International Journal of Mechanical Sciences 117, 135–151.

[117] Thomason, P.F., 1985. Three–dimensional models for the plastic limit–loads at incipient failure of the intervoid matrix in ductile porous solids. Acta Metallurgica 33, 1079–1085.

[118] Torki, M.E., Benzerga, A.A., Leblond, J.B., 2015. On void coalescence under combined tension and shear. Journal of Applied Mechanics-Transactions of the ASME 82.

[119] Tracey, D.M., 1971. Strain hardening and interaction effects on the growth of

voids in ductile fracture. Engineering Fracture Mechanics 3, 301–315.

[120] Tvergaard, V., 1978. Effect of kinematic hardening on localized necking in biaxially stretched sheets. International Journal of Mechanical Sciences 20, 651–658.

[121] Tvergaard, V., 1981. Influence of voids on shear band instabilities under plane-strain conditions. International Journal of Fracture 17, 389–407.

[122] Tvergaard, V., 1982. Influence of void nucleation on ductile shear fracture at a free-surface. Journal of the Mechanics and Physics of Solids 30, 399–425.

[123] Tvergaard, V., 1987. Effect of yield surface curvature and void nucleation on plastic-flow localization. Journal of the Mechanics and Physics of Solids 35, 43–60.

[124] Tvergaard, V., 1990. Material failure by void growth to coalescence. Advances in Applied Mechanics 27, 83–151.

[125] Tvergaard, V., Needleman, A., 1984. Analysis of the cup–cone fracture in a round tensile bar. Acta Metallurgica 32, 157–169.

[126] Tvergaard, V., Vandergiessen, E., 1991. Effect of plastic spin on localization predictions for a porous ductile material. Journal of the Mechanics and Physics of Solids 39, 763–781.

[127] Wong, W., Guo, T., 2015. On the energetics of tensile and shear void coalescences. Journal of the Mechanics and Physics of Solids 82, 259–286.

[128] Yamamoto, H., 1978. Conditions for shear localization in the ductile fracture of void–containing materials. International Journal of Fracture 14, 347–365.

[129] Yu, H., Olsen, J.S., He, J., Zhang, Z.L., 2016. Effects of loading path on the fracture loci in a 3D space. Engineering Fracture Mechanics 151, 22–36.

[130] Zhalehfar, F., Hosseinipour, S.J., Nourouzi, S., Gorji, A.H., 2013. A different approach for considering the effect of non-proportional loading path on the

forming limit diagram of AA5083. Materials and Design 50, 165–173.

[131] Zhang, K.S., Bai, J.B., Francois, D., 2001. Numerical analysis of the influence of the lode parameter on void growth. International Journal of Solids and Structures 38, 5847–5856.

[132] Zhang, Z.L., Skallerud, B., 2010. Void coalescence with and without prestrain history. International Journal of Damage Mechanics 19, 153–174.